Numerical Analysis of Debonding Mechanisms of Externally Bonded FRP Reinforcement in RC Beams

by

Michael Cohen

A thesis
presented to the University of Waterloo
in fulfillment of the
thesis requirement for the degree of
Doctor of Philosophy
in
Civil Engineering

Waterloo, Ontario, Canada, 2018

Examining Committee Membership

The following served on the Examining Committee for this thesis. The decision of the Examining Committee is by majority vote.

External Examiner	Liying Jiang Associate Professor
Supervisor	Stanislav Potapenko Associate Professor
Internal Members	Giovanni Cascante Professor
	Wei-Chau Xie Professor
Internal-external Member	Grzegorz Glinka Professor

Author's Declaration

I hereby declare that I am the sole author of this thesis. This is a true copy of the thesis, including any required final revisions, as accepted by my examiners.

I understand that my thesis may be made electronically available to the public.

Abstract

There is an urgent need to develop economic and efficient methods to repair and strengthen existing reinforced concrete structures. This demand is motivated by several factors including the aging of concrete structures, the desire to upgrade design standards, and the exposure to severe environmental effects. A particular problem confronting engineers in repairing deteriorated structures is the rehabilitation of reinforced concrete elements. Conventionally, steel plates were utilized to restore and enhance the tensile strength of damaged concrete members. Despite the effectiveness of this practice in terms of improving the structural capacity, it is still considered disadvantageous due to the excessive weight of steel and its susceptibility to corrosion in moist environments. The application of fibre reinforced polymer (FRP) to existing reinforced concrete structures has gained the interest of many researchers in the last few decades. These materials are superior to steel when it comes to comparing the resistance to electrochemical corrosion, strength-to-weight ratio, ease of handling, fatigue resistance, and availability in any length or shape. However, there is still a serious concern regarding the effect of premature debonding of the FRP plates before reaching the desired strength or ductility. This debonding can initiate from the ends of the plate or can be induced by intermediate cracks in the concrete member. Although the end-plate debonding and peeling mechanisms have been studied extensively, there is still a significant lack of data for FRP-strengthened beams in which intermediate crack-induced debonding is the dominant failure mode. On the other hand, the interfacial bond capacity between the concrete and the FRP composite has not been thoroughly investigated. Whereas, there is still need to study the effect of some of the mechanical and physical parameters on the bond strength of FRP-Concrete interface. Moreover, researchers have also shown a keen interest in simulating flexural cracks in concrete beams, and examine their effect on the debonding mechanisms of FRP materials. However, more realistic approach is needed to model cracks and account for their growth.

In this study, a three-dimensional nonlinear finite element model was developed for simulating the flexural behaviour of RC beams externally bonded with FRP systems. The ABAQUS/CAE software version 6.14-2 was used for this purpose. This numerical analysis was performed

based on a comprehensive experimental program conducted by Brena et al. (2003). The simulated RC beams were categorized in two groups: Control Beams (without fibre) and CFRP Beams (with carbon fibre reinforced polymer). During the process of constructing the CFRP beam models, two distinct procedures were followed to simulate the interface between the concrete and the externally attached FRP laminates. Perfect bond was assumed in the first approach, and a Cohesive Zone Model (CZM) was adopted in the second approach. In the latter, cohesive surface technique was implemented in the ABAQUS model through the use of traction-separation law. Despite the lack of quantitative evaluation in the literature as no similar techniques was attempted by others, the results of this numerical analysis were only compared with experimental findings, and the proposed models were found to be reliable.

A parametric study was performed to investigate the influence of various parameters on the flexural capacity of the proposed beam model, and the debonding behaviour of the externally attached FRP laminate. This analysis was conducted by either changing the mechanical properties of some of the constitutive materials (e.g. concrete and reinforcing steel), or altering the geometrical and mechanical properties of the FRP reinforcement. It was then found that the effect of internal steel reinforcement ratio has the most impact on beam ultimate capacity. While changing the FRP bond length beyond a certain value bears no effect on beam strength. Moreover, the numerical model was modified to review the effect of intermediate crack spacings on the overall beam performance. A discrete crack approach was adopted to replicate crack propagation throughout the body of the beam. This technique has shown an approximately 30% improvement in the prediction capacity of this model when compared to a similar specimen in which smeared crack approach is used. The results of this analysis showed that the debonding behaviour of FRP laminates is largely influenced by crack spacing. In addition, the results have also indicated that the initiation of FRP micro-debonding was prolonged as crack spacings were decreased. This response can be attributed to the abrasion effect within the FRP-Concrete interface. Finally, this numerical analysis provides a relatively reliable guidance on the application and the mitigation of externally bonded FRP reinforcement in concrete beams. The predictive capability of the proposed FE models ensures their suitableness for further investigations of FRP effectiveness in civil engineering field.

Acknowledgements

I would like to express my sincere appreciation and gratitude to my supervisor Professor Stanislav Potapenko for his guidance, patience and untiring support. His constant mentorship and suggestions have not only enriched my technical knowledge, but have also provided me with the confidence and determination needed to pursue and complete this research. Also, I like to acknowledge his generous financial support throughout my program, and his kind endeavour to ensure the continuity of such support. I wholeheartedly believe that this work would not have come to fruition without the trust and the encouragement of my supervisor.

Special thanks go to the members of the examination committee for the time they spent on reviewing my thesis, and providing me with their constructive comments and feedback. Their insights have undoubtedly made this work more valuable and practical.

I would also like to extend my words of appreciation to the Department of Civil and Environmental Engineering at the University of Waterloo for their academic and financial support.

Finally, my deepest gratitude and appreciation go to my parents, my sister and my brother for their unconditional love and encouragement throughout these years. Your presence in my life has been nothing short of a continuous inspiration to push forward and achieve my ultimate goals. I truly hope that I will always live up to your expectations, and pay back some of my enteral debt to you for your limitless kindness and compassion. Thank you very much for believing in me and giving me all the support I need to pursue my dreams.

Dedication

I dedicate this thesis to my parents, my sister, and my brother

Table of Contents

List of Figures

List of Tables

Chapter One

Introduction

1.1 Background Information

The need to develop new economic and efficient methods to strengthen or rehabilitate existing reinforced concrete structures has received considerable attention by the engineering community. This desire to produce such innovative techniques was inspired by the deterioration of infrastructures, high demand for increasing structural capacity of exciting concrete structures, and the inadequate design provisions to mobilize these methods. Reinforced concrete structures usually endure various loading and weather conditions throughout their service lives. This becomes more challenging in places where severe environmental exposure is expected such as in North America.

The cost of repairing or replacing deteriorated concrete structures is often tremendous, and such process is time consuming. Therefore, new design methods and materials were studied extensively to overcome the drawbacks associated with using traditional techniques. One of the most effective methods to strengthen and repair reinforced concrete structures is the use of fibre reinforced polymer (FRP) as an alternative to steel reinforcement. This shift to FRP can be attributed to their high tensile strength, high strength-to-weight ratio, fatigue resistance, nonmagnetic electrical insulation, small creep deformation, and corrosion resistance. Moreover, the light weight of FRP and their ease of application result in lowering construction time and labor, and consequently compensating for their relatively high cost. As a result, the use of FRP reinforcement is considered very practical in concrete structures subjected to aggressive environments such as chemical and wastewater treatment plants, sea walls, floating docks, and under water structure (Razaqpur, 2000).

Over the last two decades, the application of fibre reinforced polymer (FRP) as external reinforcement has been introduced as an efficient alternative to steel plates due to their light weight and corrosion resistance. FRP reinforcements were mounted on the surface of beams where tensile stresses are expected. The application of FRP laminate on the beam substrate can increase the flexural strength significantly, control crack growth and ultimately the failure of the reinforced concrete beam. It must be noted that in order for the FRP reinforcement to function effectively, sufficient bond must be maintained between the concrete and the attached FRP laminate throughout the service life of the reinforced structure. This bond is expressed by the resistance of the FRP-Concrete interface to the interfacial shear stresses within that region. Moreover, experimental observations stated that the presence and distribution of multiple cracking in concrete have a tremendous effect on bond mechanisms in FRP-Concrete interface. On the other hand, premature debonding of FRP (i.e. peeling of the plate from the reinforced structure) before achieving the desired capacity or ductility is one of the important issues that might arise in FRP-strengthened beams (Bocciarelli & Pisani, 2017). The catastrophic nature of FRP debonding can be the result of several failure mechanisms in the reinforced concrete structure. Experimental data have shown that such debonding can initiate at the plate end and moves towards the middle of the beam. However, several studies have indicated that FRP debonding can also be the result of intermediate flexural and flexural/shear cracks within the midspan vicinity of the beam. Extensive review of the literature shows a considerable lack of effective numerical representation of concrete beams where intermediate crack-induced debonding of FRP composite is the dominant cause of failure (Nour, et al., 2007) . Moreover, many studies have shown a need to develop a numerical model that is capable of accounting for the interfacial properties between the concrete and the bonded FRP laminate, and explore possible methods to increase and protect the bond between the these materials (Wei, et al., 2017). Furthermore, there has been a significant interest in examining the influence of multiple cracks in concrete beams on the debonding mechanisms of FRP reinforcement (Monteleone, 2008). Previous studies often overlooked the need to simulate concrete cracking discretely, and focused only the effect of cracking by smearing the damage over the entire structure (Lu, et al., 2005).

Therefore, advanced analytical and numerical methods are employed in this study to simulate the behaviour of FRP-reinforced structures. The effect of flexural cracking and interfacial properties, mentioned, earlier, were explicitly considered in the proposed numerical program.

1.2 Research Objectives and Scope

This thesis presents the results of an extensive numerical analysis of the flexural behaviour of FRP-strengthened beams, in which intermediate flexural cracks are the main cause of FRP debonding. Moreover, the interfacial parameters of the FRP-Concrete interface were also considered in the current research. It is worth mentioning that the effect of flexural cracking on the debonding of FRP system was incorporated in the proposed model. This was achieved by presenting each crack schematically and mechanically. Therefore, the contribution of this research allows for the effective utilization of the numerical model in the design of experimental tests and prediction of beam response. In addition, the conclusions made in this study can be used toward developing more reliable design procedures in the field of FRP

A finite element analysis (FEA) was performed using ABAQUS to simulate the flexural response of FRP beams. Experimental study, which was performed by Brena, et al. (2003) on concrete beam externally bonded with FRP, was used to validate the numerical findings. Concrete Damaged Plasticity Model (CDPM) provided by ABAQUS was used in the analysis. In addition, the interfacial mechanical properties of the FRP surface were taken into consideration in the ABAQUS model. The principal steps that were pursued to achieve the research objective are summarized as follows:

1. Introduce a comprehensive literature review to elaborate on the application and behaviour of FRP materials in RC beams.
2. Perform a sound numerical analysis of concrete beams externally reinforced with FRP reinforcement, where intermediate debonding of FRP laminate is the cause of failure.
3. Include the effect of concrete plasticity by utilizing the Concrete Damage Plasticity Model as provided by ABAQUS.

4. Investigate the interfacial response within the vicinity of concrete-FRP interface. This was achieved by utilizing the cohesive surface modelling techniques in ABAQUS.
5. Validate the numerical results with the experimental data available in the literature.
6. Conduct a thorough parametric study to examine the effect of different mechanical and physical parameters on beam capacity and the debonding behaviour of FRP reinforcement.
7. Study the effect of multiple flexural cracks on the load capacity and debonding mechanisms in FRP beams, by incorporating a discrete crack approach.
8. The findings of this research can add to the limited literature on the numerical modelling of concrete structures reinforced by FRP composites.

1.3 Thesis Organization

This thesis consists of eight chapters as can be seen in Figure 1.1. A brief outline of the remaining seven chapters is summarized as follows:

- Chapter Two starts with a comprehensive literature review of the development of FRP materials in structural fields, their manufacturing process, and their applications. Moreover, it presents an overview on the potential failure modes of concrete structures that are reinforced with FRP composites.
- Chapter three elaborates on the finite element analysis used in this study, and the numerical formulation techniques supported by ABAQUS. It also provides an insight on the Concrete Damaged Plasticity Model implemented by ABAQUS software. The interfacial relations between the external FRP and the surrounding concrete material will be illustrated by the use of Traction-Separation response provided by ABAQUS.
- Chapter four introduces a detailed report on the numerical analysis procedure that was followed to construct the finite element model. The chapter presents the steps necessary to create the FRP beam model in ABAQUS. It explains the modelling techniques used

to implement the geometries, material definitions, contact simulation for every model part within the ABAQUS environment.

- Chapter five reviews the results obtained from the numerical analysis, and cover the validation of these results with the experimental data. The modelling results of the main constitutive materials such concrete, main steel rebars, and FRP composite are also calibrated against the corresponding materials in the experimental program.
- Chapter six presents the parametric analysis that was performed using the proposed FE model to examine the effect of several parameters on beam capacity and FRP debonding response.
- Chapter seven covers the effect of multiple cracks on the overall debonding mechanisms of externally bonded FRP in RC beams. The method to simulate the cracks in RC beam is explained, and the effect of various crack spacing is also considered.
- Chapter eight summarizes the conclusions and the recommendations drawn from this research. This chapter, also, suggests some of the future work that can be built on the findings of this study.

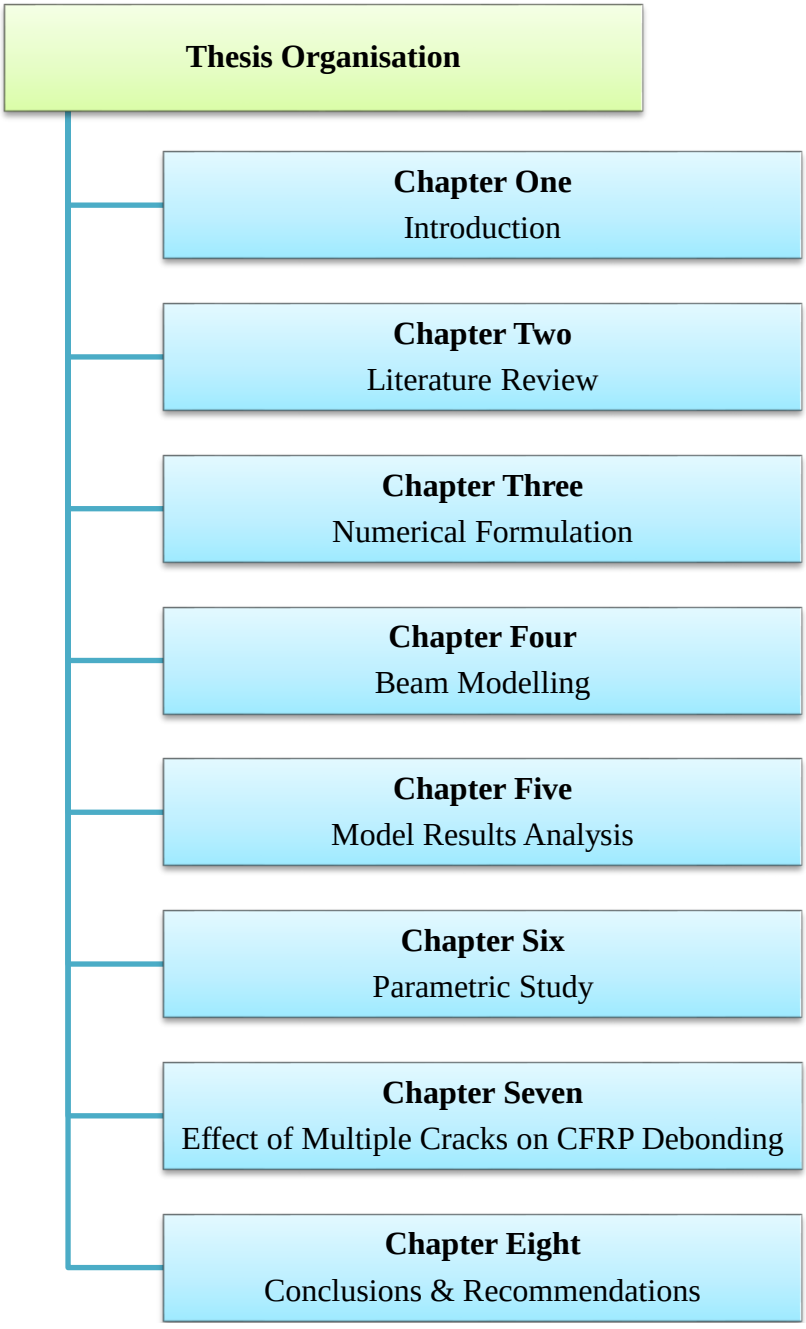

Figure 1.1: Thesis organization

Chapter Two
Literature Review

2.1 Overview

This chapter presents a comprehensive review of the existing knowledge of reinforced concrete beams strengthened with fibre reinforced polymer (FRP). The subsequent sections review the definition of the FRP composites, their components, manufacturing methods, mechanical properties, and applications in civil engineering structures. It also covers some of the advantages and disadvantages associated with use of FRP in concrete structures. It is proven that there are various forms of failure in reinforced concrete beams which are eternally-bonded with FRP materials. This chapter details the differences between failure modes and their effect on the flexural capacity of FRP beams. The significance of each failure mode which is not fully studied or reflected in the existing literature is then discussed based on the limited studies.

It is evident that the performance of reinforced concrete member, both the ultimate state (strength) and the serviceability state (crack and deflection), relies on the transfer capacity of the interfacial regions between the concrete and the reinforcement. The transfer forces, in turn, depend on the bond quality between the two materials (Quayyum, 2010). Therefore, this chapter concentrates on the bond mechanisms between the FRP and the surrounding concrete. This review starts with an introduction to the bond behaviour of the interface elements, and the factors influencing their response, and hence the capacity of RC beams. In addition, this section reviews the perfect bond assumption adapted in some of the common studies. Moreover, a meso-scale finite element approach, introduced in the literature, is explained with attention to its relativity to the current study. The ultimate bond strength is also investigated in terms of

existing models to calculate this parameter. Moreover, the fundamentals of finite element analysis are also covered in the form of historic development of this method to predict the structural behaviour of FRP beams. Nevertheless, an overview of the nonlinear fracture mechanics of concrete is also presented, in order to provide an understanding of the various mechanisms that govern crack pattern and damage evolution in concrete composite. Finally, an introduction to the plasticity of concrete is given with reference to some of the existing studies available in the literature.

2.2 Historical Information

Historically, the use of fibres to reinforce brittle materials is not a new concept. Early applications of straws used to reinforce clay brick was recorded in ancient Egyptian constructions. Similar techniques were found in ancient construction sites in Asia (Cohen, 2012). It is clear that one of the advantages of using fibre is to support and enhance brittle matrices to which it is added. The brittle nature of concrete under tension prompted the need to develop efficient materials that could increase the resistance, and enhance the post-cracking response of concrete members. (Li, 2000).

The high mechanical properties and light weight of fibre reinforced polymer (FRP) materials has prompted their use in the aerospace and automotive industries. They were used as pressure vessels and in airplane parts due to their light weight (Stoner, 2015). The application of FRP in civil engineering goes back to the 1950's, but they have not been considered as practical reinforcement for concrete structures until the 1970's (ISIS Canada, 2007). In addition, the high strength and light weight characteristics of FRP motivated sport industries to consider this material as a building tool for tennis rackets, golf equipment, etc.

2.3 Fibre Reinforced Polymer

Fibre reinforced polymers (FRP) can simply be defined as composite materials that typically consist of organic or nonorganic fibres embedded in a resin matrix. The matrix is a polymer resin, often with some fillers and additives of different nature. FRP reinforcement forms a group of products rather than being one reinforcement type. The characteristics of each group depends on fibres and resin types and properties, volume fractions, production parameters, shape and surface texture. The main components of FRP and their properties will be outlined in the subsequent sections. The fibres strength and stiffness contribute to the performance of the composite and generally carry most of the applied loads. The bond between the fibres and the surrounding structures is induced by the epoxies, polyesters, and vinylesters, which also help protect the fibres (ACI Committe 440, 2007). There are various types of FRP materials used in engineering structures. Some of which are glass (GFRP), carbon, (CFRP), and aramid (AFRP), as can be seen in Figure 2.1. Each type of FRP has its unique characteristics and applications. For example, GFRP is known for its durability in harsh environments and its light weight. It also has a high tensile strength, but a relatively low resistance under shear loading. It is advisable not to use GFRP in applications that are exposed to high content of alkaline. CFRP is more ductile than GFRP, but does not perform well under cyclic loading. AFRP has high resistance against heat, but it is less common than the other two due to its weakness against moisture and ultraviolet radiation. Therefore, painting and coating is required to protect and improve AFRP performance (Minouei, 2013).

Figure 2.1: Different types of FRP (Quayyum, 2010)

2.3.1 FRP Constituents: Fibres

There are different types of fibres with wide range of material properties that suit a variety of structural demands. In another word, the selection of FRP reinforcement is governed by their characteristics such as corrosion resistance, tensile strength, ultimate strain, fatigue resistance, and their dimensional stability. Fibres have high tensile strength and relatively small diameter, which allows them to efficiently transfer the load between fibre composites. Their dimeter usually ranges from 3 to 25 micrometers (ISIS Educational Committe, 2003). However, there are three main types of fibres used in FRP reinforcement: glass, carbon and aramid (the following sections detail the properties of these fibres). The tensile strength of these fibres is significantly higher than that of steel, and their response can be idealized as linearly elastic up until failure, and hence no ductility is expected. The mechanical properties vary considerably between fibres (see Figure 2.2) and may vary for a given type of fibre as well. Table 2.1 summarizes some of the typical properties of different fibres.

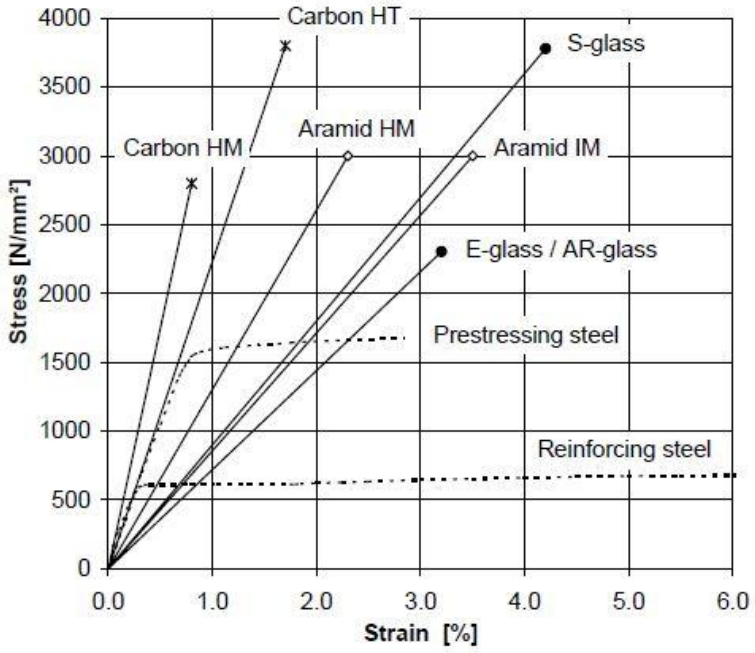

Figure 2.2: Stress-strain response of various types of fibre and steel (ACI Committee 440, 1996)

Table 2.1: Typical properties of fibres (Mathys, 2000)

Fibre type	Tensile strength [N/mm^2]	Modulus of elasticity [kN/mm^2]	Ultimate strain [%]	Density [kg/m^3]	Fibre diameter [µm]
Aramid – IM	2700-4500	60-80	4.0-4.8	1400-1450	12-15
Aramid – HM	2700-4500	115-130	2.5-3.5	1400-1450	12-15
Carbon – Pitch HM	3000-3500	400-800	0.4-1.5	1900-2100	9-18
Carbon – PAN HM	2500-4000	350-700	0.4-0.8	1800-2000	5-8
Carbon – PAN HT	3500-5000	200-260	1.2-1.8	1700-1800	5-8
E-glass(1)	1800-2700	70-75	3.0-4.5	2550-2600	5-25
S-glass	3400-4800	85-100	4.5-5.5	2550-2600	5-25

IM: intermediate modulus, HM: high modulus, HT: high tensile strength

(1) Properties of AR-glass fibres are similar to those of E-glass

2.3.1.1 Glass Fibres

The chemical process, used to manufacture glass fibres, involves the mixing of the main gradient "silicon oxide" with small quantities of other oxides. The formation and shaping of glass fibres is achieved by extruding liquefied glass and fibre stretching. Individual glass fibres are immediately coated by a sizing agent due to their active surface and hydrophilic nature. The sizing also plays a role in restraining abrasion damage and improve coupling with polymer matrices. The categorization of glass fibres is dependent on their chemical composition. The most commonly used are E-glass fibres, which are based on calcium-aluminoborosilicate glass. This type of fibres is known for its low cost and high strength and electrical resistance. On the other hand, S-glass fibres are composed of magnesium-aluminosilicate, and it has higher strength, stiffness, and thermal stability. C-glass is made of soda-lime-borosilicate composition that is used for its higher chemical stability against acids. Alkali-resistant glass fibres (AR) consist of high amount of zirconium oxide to improve resistance against alkalis, particularly in cement matrices (Mathys, 2000).

Despite the high strength, good electrical and thermal resistivity and low cost, glass fibres suffer from considerable degradation in moist environments, and in the presence of acid and alkaline solutions. Moreover, their creep response is not very desirable under long term

loading, thus their tensile strength degrade considerably under constant stress. These drawbacks have prompted the need to better protect the surface of glass fibres. This can be done by using protective matrices (such as in AR-glass fibres) to enhance fibres durability in aggressive environments.

2.3.1.2 Carbon Fibres

The main ingredients of carbon and graphite fibres are polyacrylnitrile (PAN), and pitch or rayon. Low modulus carbon fibres ($E \approx 50000\ N/mm^2$) are generally made of isotropic pitch and rayon. Whereas carbon fibres with high modulus and strength are mainly manufactured from PAN or liquid crystalline pitch (see
Table 2.1). PAN fibres are made through a rigorous chemical process that involves separating a chain of carbon atoms from polyacrylnitrile through heating and oxidation. While pitch fibres are fabricated by using refined petroleum or coal pitch that is passed through a thin nozzle and stabilized by heating (Mathys, 2000). Carbon fibres are known to be the strongest and stiffest between other types of fibres. They exhibit high resistance to creep and fatigue comparing to other fibre composites. They also resist chemical, ultraviolet light and moisture very well. These characteristics makes carbon fibres very durable materials with excellent mechanical properties. However, carbon fibres are electrically conducting materials, and hence they can induce galvanic corrosion in contact with metals. Moreover, the wetting process of fibres by resins is not an easy task, so special surface treatments are suggested. Therefore, carbon fibres are generally provided with an epoxy size treatment that improves the fibres resistance to abrasion, and offers an epoxy matrix compatible interface.

2.3.1.3 Aramid Fibres

Aramid fibres (also known as aromatic polyamide) are manufactured by extrusion process as a liquid crystal polymer and by fibre stretching. The main chemical component of aramid fibres is para-phenylene-terephthalamid. These organic fibres have an anisotropic fibrillar structure. Along the axial direction, fibres have an aligned molecular chain with strong covalent bond. While in the transverse direction, these chains are cross-linked by weaker hydrogen bond.

Therefore, the high tensile strength and stiffness are dominated by the longitudinal direction of the fibres.

aramid fibres are also known for their high energy absorption and toughness, good vibration damping and fatigue resistance, low thermal conductivity and stability, moderate to fairly good chemical resistance, low compressive strength and moderate adhesive properties. Under tension, aramid fibres behave elastically, but show non-linearity and ductility when subjected to compressive loads (Mathys, 2000).

Aramid fibres resistance to acid and alkalis ranges between low to moderate, but poor against ultraviolet radiation. These fibres are also sensitive to water and wet surfaces. To overcome these drawbacks, attention must be given to selecting the appropriate matrices in which fibres are embedded. Surface treatment might be required to enhance the bond strength between fibres and matrix.

2.3.2 FRP Constituents: Resins

Resins binder is one of the components that compose the polymer matrix, and it can be made of thermosetting or thermoplastic polymers. When cured, the former solidifies or sets irreversibly due to the high degree of cross-linking of molecules (polymerization). These cured resins do not experience melting under high temperature, but rather exhibit decomposition. Thermoplastic polymers are composed by more linear macromolecules, and hence can be repeatedly softened when exposed to heat and hardened upon cooling.

When thermosetting polymer resins are used, no high pressure or temperature is needed to process fibre wet-out. Thus, it makes them a suitable choice when processability is a factor. These types of polymers also provide relatively good thermal stability, chemical resistance, creep and stress relaxation. Nonetheless, their storage life and ultimate strain are limited. On the other hand, thermoplastic polymers are more ductile and tough, and consequently, they offer higher impact strength, fracture resistance and micro-cracking resistance than thermosetting polymers. In addition, thermoplastics have a better post-formability, shorter fabrication time and long storage life. However, embedding of continuous fibres into the thermoplastic polymers, and hence composite production, is a challenging task due to the high

viscosity of thermoplastics (Mathys, 2000). There are various types of polymer binders such as: unsaturated polyester, vinyl ester and epoxy. For these thermosetting resins, polyesters are the most commonly used for general-purpose applications because of their good processability, properties and low cost. Vinyl esters process essentially like polyesters, but they have superior mechanical and chemical properties. On the other hand, epoxy resins are more expensive than the last two, but are largely used in high-performance composites due to their excellence mechanical performance, good adhesion properties and resistance to chemical and solvents. Table 2.2 shows some the properties of these polymers.

Table 2.2: Typical properties of polymer resins (Malek & Saadatmanesh, 1996)

Resin type	Tensile strength [N/mm^2]	Modulus of elasticity [kN/mm^2]	Density [kg/m^3]	Cure shrinkage [%]
Polyester	35-104	2.1-3.5	1100-1400	5-12
Vinyl ester	73-81	3.0-3.5	1100-1300	5-10
Epoxy	55-130	2.8-4.1	1200-1300	1-5

2.3.2.1 Unsaturated Polyester

Unsaturated ester polymer is considered a main ingredient of thermosetting polyesters. They are a condensation polymerization product of dihydroxyl derivatives and dibasic acids or anhydrides, dissolved in a cross-linking monomer such as styrene. The process also involves adding a free-radical initiator (in the case of elevated temperature cure) or a promoter (in the case of room temperature cure). This results in a non-reversible chain polymerization reaction which, in turn, induces a cross-linked styrene-polyester copolymer (cured polyester resin). Inhibitors may be introduced to limit premature cure during storage of the unsaturated polyester (Mathys, 2000).

A wide range of polyester resins properties can be obtained through their formulation process. For example, higher stiffness can be achieved by formulating a higher cross-link density, which also can lead to better glass transition temperature and thermal stability. However, this type of formulation results in low ductility. Polyester resins are also known for their low cost,

moderate chemical resistance, good processability (as a result of their low viscosity and fast cure time) and dimensional stability. Nevertheless, polyesters suffer high volumetric shrinkage during curing, which produces undesired residual stresses in the composite.

2.3.2.2 Vinyl Ester

These materials are produced from combining an unsaturated carboxylic acid (such as methacrylic acid) and an epoxy resin. Similar to unsaturated polyester, vinyl esters are mixed with styrene for cross-linking. Consequently, this similarity extends to their process and cure. However, vinyl esters are more superior to polyesters in term of their chemical and temperature resistance, but they cost more. Moreover, they have better workability and fracture toughness because there are few cross-links in their molecular structure. They also promote better wet-out and good adhesion with the surface of glass fibres due to the presence of hydrogen bonds in their chemical composite. When epoxy resins are presented, vinyl esters promote high heat resistance and thermal stability, but their tensile strength does not change dramatically. Vinyl esters have low viscosity and short curing time, and the drawback of having a high volumetric shrinkage during curing process.

2.3.2.3 Epoxy

These resins are made of low-molecular weight organic liquid resins containing epoxide groups (rings of two carbon and one oxygen atom). The most commonly used epoxy resins are based on diglycidyl ethers of bisphenol A (DGEBA). The impact resistance of the cured epoxy can be enhanced by adding diluents to reduce viscosity and agents to improve flexibility. The addition of hardeners contributes to the cross-linking or curing of the epoxy. These hardeners are generally reactive curing agents of the amine, anhydride or Lewis acid type. The mechanical and physical properties and the processing conditions of epoxy resins are influenced by variety of input materials. Therefore, they are the most versatile polymer binder for fibre composites. Their cost, however, is higher than that of polyester and vinyl ester resins. Epoxy possesses excellent strength, good creep resistance, strong adhesion to fibres, good resistance to chemicals and solvents and low volumetric shrinkage during cure. Their

disadvantages lie in their relative high cost, long curing time and the need for careful processing to maintain moisture resistance.

2.3.3 FRP Constituents: Fillers and Additives

Fillers are inorganic materials added to the polymer resin for a range of purposes. Fillers are used to reduce matrix costs by diluting the expensive resin materials. They can also improve fire resistance of FRP by reducing the organic content of the composite, and hence its flammability. Some of the mechanical properties of the composite, such as hardness, shrinkage, fatigue and creep response, can be improved by adding fillers to the matrix. There are different types of fillers which are commercially available such as: clay (alumina silicate), calcium carbonate, wollastonite and glass microspheres (Bai, 2013).

Additives are incorporated in the FRP composite to enhance the matrix resistance and improve the processing of FRP production. They also play a role in enhancing certain mechanical properties of the composite. Different kinds of additive s may be used, such as ultraviolet inhibitors, flame retardants, anti-oxidants, initiators (catalysts), wetting agents, colour pigments, and mold release materials (Mathys, 2000).

2.4 Adhesives

The main purpose of using adhesive is to connect two materials and initiate a full composite act in the composite. In the case of externally bonded FRP, the adhesive works as a gluing agent between the FRP reinforcement and the supported concrete. It allows a load path between the two materials which exhibits bond stresses in transverse directions (along the surface) of the adhesive layer. Although, peel stresses (normal the bonded surface) might occur as well. The selection of the appropriate adhesive materials is determined by many factors, such as the type of substrate on which the adhesive is applied, the desired mechanical response, and the environmental conditions. Adhesives employed in structural applications are generally based on thermosetting polymers. Examples of which are: epoxies, polyesters, cross-linkable acrylics

and polyurethanes. Epoxies are considered the most widely acceptable adhesive in civil engineering structures because of their high surface activity and good wetting properties for a variety of substrates. Epoxies also provide high cohesion (failure in the adhesive) and adhesion (failure in the bond interface) strength which limits the debonding by the adherent strength. As mentioned earlier, their creep and shrinkage are relatively low. Some of the typical mechanical properties of epoxy adhesive are summarized in Table 2.3, and compared to those of concrete and steel.

There are several requirements in order for the adhesives to perform well in the externally bonded FRP reinforcement. Some of the general requirements are outlined below (Hutchinson & Quinn, 1999):

- Careful application methodologies related to mixing, curing and placing of adhesives should be implemented to maintain adequate adhesion to the concrete and the FRP (wetting ability), gap-filling properties and workability. The adhesives should be attached to FRP with no temporary fixings required.
- Maintain good bond quality and workability regardless of the surface quality or environmental conditions.
- Adhesives must be very durable in terms of resistance to moisture, creep, thermal instability, and alkaline presence in concrete.
- High glass transition temperature compared to service temperature must be obtained.
- Adhesives modulus of elasticity (Young's modulus) must be within the range of 2000 to 15000N/mm^2. Whereas the lower limit restricts the creep effect, and the upper value minimizes stress concentrations.
- The minimum allowable shear strength of the adhesive should be 12N/mm^2 at 20^{o}C.
- Good permeability and maximum moisture absorption of adhesives must be achieved. The equilibrium moisture content should not be larger than 3% by weight after immersion in distilled water at 20^{o}C.

Though choosing the suitable adhesive is crucial, extra care must be given to the gluing process and a quality control is required (CEN, 1999).

Table 2.3: Comparison between the mechanical properties of epoxy adhesives, concrete and steel (Shaw, 1982)

Property		Epoxy adhesive	Concrete	Steel
Compressive strength	[N/mm^2]	55-100	25-150	200-2000
Tensile strength	[N/mm^2]	9-20	1-6	200-2000
Modulus of elasticity	[N/mm^2]	500-20000	20000-50000	≈ 200000
Coefficient of thermal expansion	[10^{-6}/°C]	25-30	8-12	≈ 10
Density	[kg/m^3]	1450-1550	≈ 2400	≈ 7800
Poisson ratio	[-]	≈ 0.30	0.15-0.20	0.30

2.5 Manufacture of FRP Reinforcement

FRP reinforcement can be manufactured through various techniques, such as lay-up methods, moulding methods (e.g. injection, compression, resin transfer, vacuum bag and autoclave moulding), pultrusion and filament winding. The following sections summarize some of the typical manufacturing methods for both "pre-cured" and "in-situ curing" types of externally bonded FRP reinforcement.

2.5.1 Pultrusion

This method can simply be defined as a continuous moulding process that combines fibres and a thermosetting matrix to form a straight composite element that has a constant cross section. First stage involves feeding roving-shaped fibres through a resin bath where they are impregnated with the polymer matrix. Then after, the saturated fibres go through a heated metal die to form their shapes and dimensions. The temperature of the heating station is set accurately to control the curing (polymerization) of the FRP matrix. The FRP composites are continuously driven through the pultrusion machine by a system of pullers located between the die exit and the cut-off station (see Figure 2.3). The pultrusion process generally produces FRP composites with high fibre content. The initial cost associated with this method is relatively high, but the

processing cost is considered reasonable for high volume production. The process quality is influenced by many factors such as machine speed, die temperature, and resin reactivity.

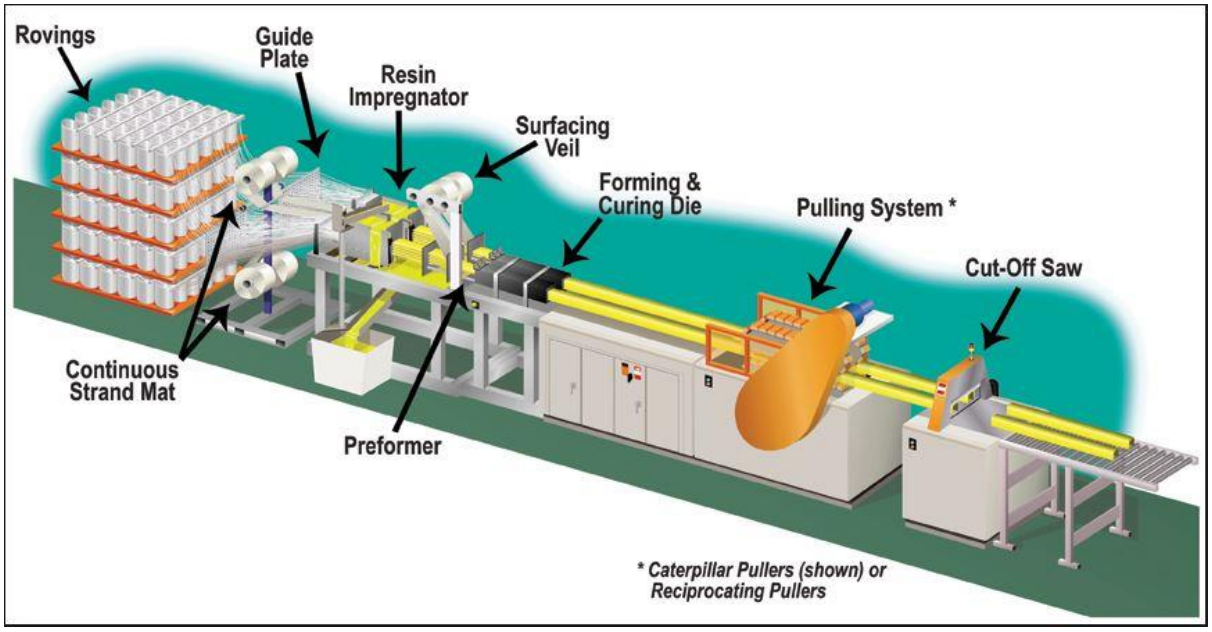

Figure 2.3: Pultrusion process (Pultrusions, 2015)

2.5.2 Moulding

The simple moulding method (also called open-mould method) involves a manual lay-up of FRP composites, then consolidating and curing of laminas in one-sided mould. On the other hand, more complex moulding techniques may consist of vacuum/pressure compacting process (see Figure 2.4) and matched mould process (which can be compression moulding, resin transfer moulding, injection moulding, etc.). Vacuum/pressure compacting moulding applies compression force on the uncured laminate to release the entrapped air, and densifies the resin at the start of the curing and cure the laminate by one of the typical curing methods. This method is more versatile than pultrusion and does not need high production volume. However, the produced laminates cannot be delivered in quasi-continuous lengths (Mathys, 2000).

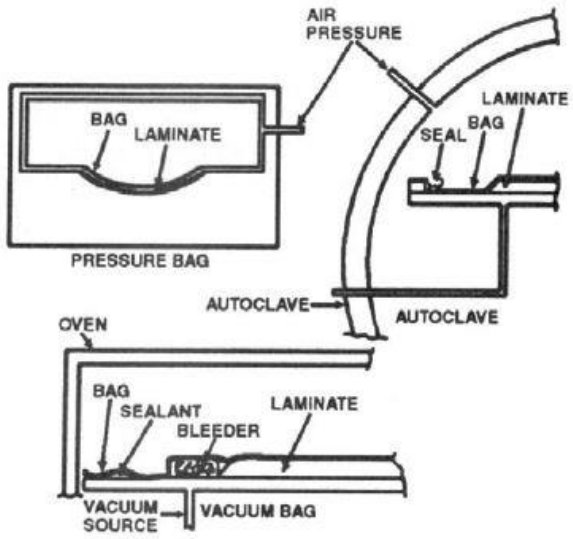

Figure 2.4: Vacuum bag, autoclave and pressure bag moulding (Schwarz, 1992)

2.5.3 Manufacturing of Dry-Fibre Sheets and Fabrics

There are two types of dry-fibres that are commercially available in the industry: unidirectional and multidirectional dry-fibres. The former are made of parallel fibres, tows, yarn or rovings, and as the name suggests, are aligned and straightened in one direction. The produced sheets are characterized by very small thickness and a variety of widths. However, the multidirectional nature of the latter is obtained by weaving, knitting, stitching or braiding continuous fibres (tows, yarns) into a fabric. The stability of fabric is essential for the handling and the wetting process. Multidirectional fabrics are provided in different patterns and having certain fibre orientations in the sheet. Woven fabrics have fibres in the 0^o (wrap) and 90^o direction (wet or fill) and may be produced with different weave patterns. Moreover, the unidirectional fibres are characterized by a high degree of fibre alignment when compared to the multidirectional fabrics.

Following a similar method used to produce multidirectional fabrics, quasi-unidirectional fabrics can be made of only a small amount of fibres normal to the axial direction of the sheet. These products are generally used as alternatives to the unidirectional fibres.

The dry-fibre sheets and fabrics can also be formed as prepreg, where the polymer matrix is already impregnated into the fibres and partially cured to a tack-free state, the so-called B-

stage. During the polymerization reaction of a thermosetting resin, the material is softened with heat until it become plastic and fusible (see Figure 2.5). The final cure of the prepreg is done by a heat source in order to harden the resin and reach the final form (C-stage).

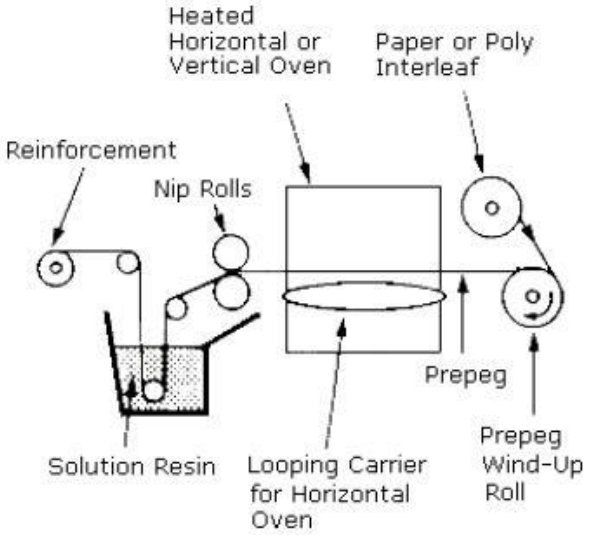

Figure 2.5: Prepregging process (Mathys, 2000)

2.6 Externally Bonded FRP Reinforcement

This reinforcement system consists of both the FRP composites that can be attached to the concrete surface, and the adhesive materials which is used to glue the FRP to the concrete. There are various systems of externally bonded FRP reinforcement depending on their material properties, the shape of the FRP and application techniques. These systems can be divided into either “prefab” (pre-cured) or “wet lay-up” (in-situ curing) (Matthys, 1997). The prefab FRP laminates are produced as a fully cured composite, with final shape, strength and stiffness. The volume fraction of fibres in this system is about 70% and its thickness ranges from 1.0 to 1.5 mm (where the larger thickness refers to the global thickness of the strip). As mentioned earlier, this system of fibres is installed on the concrete surface using adhesive agents, which in turn provide the necessary bond strength between the two materials (concrete and FRP).

The wet lay-up or the in-situ curing systems can take the form of dry-fibre or prepreg sheets and fabrics. The main difference between this system and the prefab technique is that an exact thickness of the FRP strips, after in-situ curing, may be difficult to obtain. In such case a nominal thickness is used, which can be an equivalent to the dry-fibre thickness. This thickness is taken as the ratio of fibre mass per area (kilogram of fibres provided per unit area) and fibre density. The thickness of sheets and fabrics used in this system varies from 0.1 to 0.5mm. It should be noted that after impregnation wet lay-up types generally have a much smaller fibre volume fraction (magnitude of about 30%) than prefab systems. Finally, Table 2.4 outlines some of the typical properties of the two systems.

Table 2.4: Some typical properties of externally bonded FRP systems (Mathys, 2000)

	PREFAB (PRE-CURED)	**WET LAY-UP (IN-SITU CURING)**
Shape of FRP	Strips or laminates	Sheets or fabrics
Thickness	About 1.0 to 1.5 mm	About 0.1 to 0.5 mm
Bonding agent	Thixotropic adhesive for bonding	Low viscosity resin for bonding and impregnation
Fibre volume	About 70 %	About 30 % (after impregnation)
Application	Simple bonding of the factory made elements with adhesive	Bonding and impregnation of the sheets or fabrics with resin (shaped and cured in-situ)
Applicability	If not pre-shaped only for flat surfaces	Regardless of the shape, sharp corners should be rounded
Number of layers	Normally 1 layer, multiple layers possible	Often multiple layers
Surface unevenness	Stiffness of strip and use of thixotropic adhesive allow for certain surface unevenness	Often a putty is needed to prevent debonding due to unevenness
Ease-of-application	Simple in use, higher quality guarantee (prefab system)	Very flexible in use, needs rigorous quality control
Quality control	Wrong application and bad workmanship = loss of composite action between FRP EBR and substrate/structure, lack of long term integrity of the system, etc.	

2.7 Mechanical Properties of FRP Reinforcement

The geometric and mechanical properties of the FRP reinforcements are dependent on their shape and formulation, constituents, and the manufacturing methods. Experimental tests are usually used to obtain the properties of the FRP composites. These tests and data recording follow particular procedures and provisions such as CSA S806, ACI 440.3 and various ASTM standards. However, the properties reported by most manufacturers are typically in the longitudinal direction (the basic direction of the fibres). Therefore, the strength and stiffness are significantly higher in axial direction than in the transverse direction (Quayyum, 2010).

As indicated previously, the FRP reinforcements are considered efficient alternatives to several of the conventional reinforcing materials due to their superior characteristics. Some of the FRP special properties reside in their high strength, corrosion resistivity, light weight, fatigue and creep resistance, non-magnetic nature, and electrical insulation. However, the tensile stress-strain response of all FRP reinforcement is seen as linear elastic without yielding or ductility. Except for some carbon fibre reinforced polymer (CFRP) composites, most of the FRP systems have a lower stiffness than steel rebars (see Figure 2.6). Typical properties of the FRP rebars, strips and sheets are listed in (Table 2.5), (Table 2.6) and (Table 2.7) respectively.

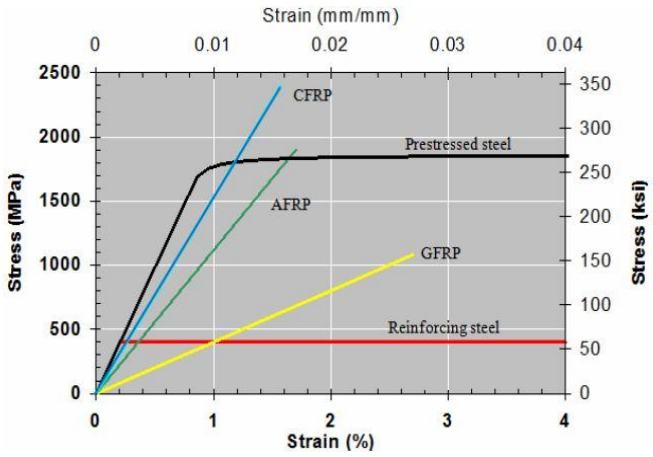

Figure 2.6: Comparison of stress-strain response of FRP and steel (ACI Committee 440, 1996)

Table 2.5: Typical properties of different FRP reinforcing rebars (Bank, 2006)

	GFRP-vinylester	CFRP-vinylester	CFRP-epoxy
Fibre volume (%)	50-60	50-60	50-60
Fibre architecture	unidirectional	unidirectional	unidirectional
Tensile strength, longitudinal (MPa)	500-700	2070	2255
Tensile modulus, longitudinal (MPa)	41-42	124	145
Shear strength, out of plane (MPa)	22-27	--	--
Bond strength (MPa)	1.7	9	--
Coefficient of thermal expansion, longitudinal (10^{-6} °C^{-1})	6.7-8.8	-7.2-0	0.7
Coefficient of thermal expansion, transverse (10^{-6} °C^{-1})	22.0-33.7	73.8-104.4	--
Density (g/cm^3)	2.1	--	1.6

Table 2.6: Typical properties of different FRP reinforcing strips (Bank, 2006)

	Standard modulus CFRP epoxy	High modulus CFRP epoxy	GFRP epoxy	CFRP vinylester
Fibre volume (%)	65-70	65-70	65-70	60
Fibre architecture	Unidirectional	unidirectional	unidirectional	unidirectional
Nominal thickness (mm)	1.2-2.9	1.2	1.4-1.9	2.0
Width (mm)	50-100	50-100	50-100	16
Tensile strength, longitudinal (MPa)	2690-2800	1290	900	2070
Tensile strain (max), longitudinal (%)	1.8	--	2.2	1.7
Tensile modulus, longitudinal (MPa)	155-165	300	41	131

Table 2.7; Typical properties of FRP reinforcing sheets (Bank, 2006)

	Standard modulus CFRP	High modulus CFRP	GFRP epoxy
Thickness (mm)	0.165-0.33	0.165	0.35
Width (mm)	600	600	1200
Fibre architecture	Unidirectional	Unidirectional	Unidirectional
Tensile strength, longitudinal (MPa)	3790	3520	1520-3240
Tensile strain (max), longitudinal (%)	1.67-1.7	0.94	2.1-2.45
Tensile modulus, longitudinal (MPa)	230	370	72

2.8 FRP Applications in Structural Engineering

Over the past 20 years, there has been a need to develop new construction materials that are both economically and structurally viable, for buildings and bridges. Therefore, FRP composites can been seen today as reinforcement alternatives in new structures, and repairing tools in existing structural members. As discussed before, FRP can be utilized as internal reinforcement which can, partially or fully, replace conventional steel rebars in concrete structures due to the FRP superior properties (Massimiliano, et al., 2017). The surface of external FRP reinforcement can be either sand coated, helically wound spiral outer surface, indented, braided, or with ribs (see Figure 2.7). The main purpose of finishing the outer surface of FRP rebars if to improve their bonding performance and add extra protection to the FRP composite. In the 1980's, FRP was used as prestressing tendons due to their ability to resist corrosion compared to the conventional steel reinforcement. However, FRP potentials in prestressed concrete structures were not fully achieved due to the fact that steel anchors could not be used because of the low transverse strength of FRP (Soudki, 1998). Nonetheless, FRP has been used in structures made of concrete, steel, masonry, and timber to enhance their flexural and shear capacity, and hence prolong their service life significantly. In recent years, near-surface mounted methods started to be adapted mainly in existing concrete structures,

where FRP tendons or strips (prestressed or non-prestressed) is inserted and then bonded adhesively into a machined groove at the surface of the concrete member (Quayyum, 2010).

In the last few decades, FRP laminates were introduced as external reinforcement materials bonded to the top, sides, or bottom of the concrete beams to increase their flexural or/and shear capacity.

It must be noted that FRP sheets are relatively more expensive comparing to steel plate. However, their light weight makes the installation process much easier, and this decreases the associated labor time and cost. FRP laminates possesses more resistance to aggressive environments which makes them more practical alternative than conventional steel. Structures that are externally reinforced with FRP sheets exhibited a noticeable improvement in their performance and durability.

FRP reinforcement can be used as column confinements in structures that are susceptible to seismic activities. FRP wraps can largely increase the ductility of the confined column and improve their seismic resistance. Reggio Emilia Soccer Stadium in Italy and Aigaleo Soccer Stadium in Greece are well known examples where FRP wraps where used as column confinement. In masonry structures, FRP sheets and rods are used to rehabilitate shear walls and improve their resistance to seismic loads. They are also used to repair historical masonry structures such as the Basilica of St. Francis of Assisi and Vercelli Castle in Italy (Minouei, 2013).

It can be seen that FRP composites play a great role in civil engineering applications mainly as retrofitting/strengthening agent in new or existing structures. They can also be considered an attractive alternative to conventional steel rebars, or they can be combined with other materials such as steel or concrete to create hybrid structures (e.g. concrete-filled FRP tubes) (Chen, 2010).

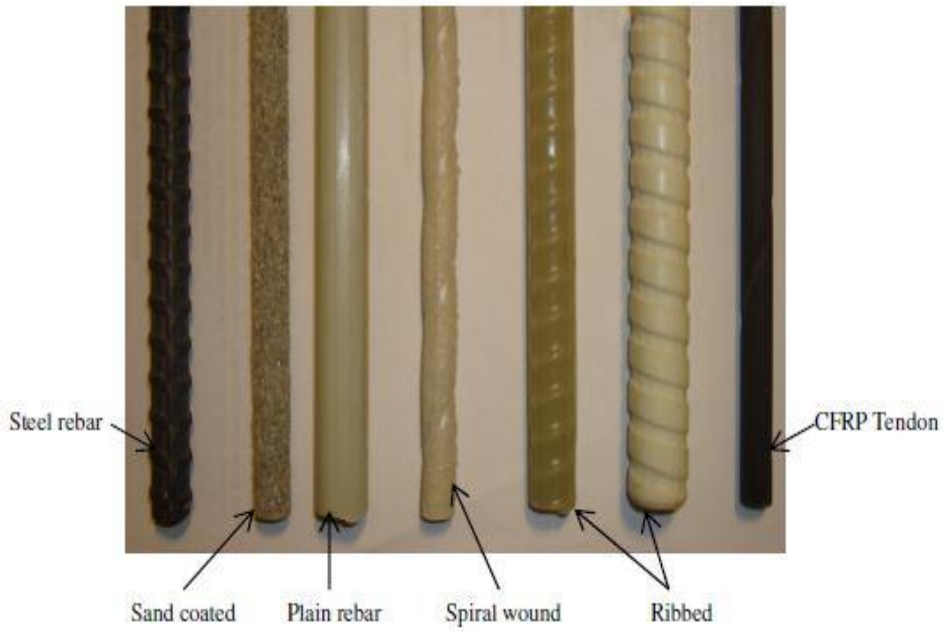

Figure 2.7: Different types of FRP rebars (Quayyum, 2010)

2.9 Advantages of FRP Reinforcements

As mentioned in previous sections, FRP reinforcements have been utilized in engineering applications for quite some time due to their superior durability and performance comparing to conventional steel reinforcements (Namasivayam, et al., 2013). It is noted that corrosion has a very damaging effect on the overall performance and service life of a structure. This effect is characterized by the induced tensile stresses in the affected areas of concrete structure which often leads to spalling and delamination of concrete. The area of steel reinforcements tend to be reduced due to corrosion built up, which results in a significant drop of the reinforcement capacity to transfer loads. The destructive impact of corrosion, both aesthetically and mechanically, has prompted the urge to develop more durable and efficient alternatives to steel reinforcements. Therefore, FRP rebars have been introduced as very effective reinforcing systems for structures in corrosive environments such as underground concrete tanks, roads

and bridges, etc. Moreover, FRP elements are characterized by their resistance to electromagnetic activities. This property is very advantageous for structures that are used to store equipment that uses magnetic fields which are very sensitive to steel (Goldston, et al., 2017). Nano-technology laboratories, hospitals using magnetic resonance (MRI), and toll booths are common structures where the electromagnetic resistivity of FRP materials is benefitted from. In addition, FRP reinforcing rebars have a very high strength-to-weight ratio. Their tensile strength is significantly higher than the yield capacity of conventional steel rebars. In another word, FRP rebars are approximately one fifth the weight of steel. This low weight of FRP materials influences the shipping and application time dramatically (ISIS Educational Committe, 2003).

Steel plates were originally used as a repair method for deteriorated structures, where they are bonded to the beam surfaces that are subjected to tension. Though the flexural capacity of concrete beams is improved by using this method, there are some disadvantageous effects related to the use of steel plate. As indicated earlier, steel is vulnerable to corrosion and its weight becomes a burden in long-span structures. Therefore, externally bonded FRP reinforcements were considered for the same purpose of strengthening new and existing structures, with the added benefits of high strength and stiffness-to-weight ratio, durability, low maintenance costs and applications, high strength in elevated temperatures, and high impact resistance. Therefore, external FRP systems are largely used in civil engineering infrastructures applications where dead weight, space, or time restrictions apply (Ross, et al., 1999).

It should be stated that the initial cost of manufacturing FRP composites is higher than steel reinforcements. However, this cost is shifted by the saving in labor time, and the low maintenance cost required during the life-cycle of FRP reinforcements. In spite of the high tensile strength of FRP materials, their stiffness is relatively lower than steel rebars. Therefore, larger tensile strains, and hence wider cracks, are expected in structures supported by FRP reinforcements. As a result, serviceability limits are adopted in designing FRP strengthened concrete structures instead of strength limits (Zhao, 1999).

2.10 Failure Modes in FRP-Strengthened Concrete Beams

In the last decade, several researchers have conducted excessive experimental studies to investigate the failure mechanisms of concrete structures reinforced with FRP laminates (Esfahani, et al., 2007), (Ashour, et al., 2004), (Garden & Hallaway, 1998), and (Smith & Teng, 2002). It was observed that there are three main modes of failure in FRP-reinforced concrete structures. During the first two types of failure, the composite action between the concrete and the FRP reinforcement is achieved. During the first failure mode, the steel reinforcement yields, followed by rupture of FRP. Whereas in the second mode, the failure occurs due to the crushing of concrete before or after the yielding of tensile steel reinforcement, and without any damage to the FRP laminate.

However, the third mode involves a significant loss of this composite action mainly due to the debonding of FRP laminates. In such case the external FRP reinforcements seize to contribute to the beam capacity, which ultimately results in a brittle failure of the concrete structure (Majid, et al., 2017). The detailed description of each mode as well as some of the literature gathered about this topic are given in the following sections.

1. FRP Rupture: as seen in Figure 2.8(a) this failure is characterized by a flexural failure with yielding of tensile steel reinforcements followed by the rupture of FRP. in this mode, the FRP laminate is fully utilized into the concrete beam response
2. Concrete Crushing: the crushing of concrete in the compressive region initiates this type of failure, which occurs before or after the yielding of tensile steel rebars. While the FRP laminate remain intact (see Figure 2.8(b)).
3. Concrete Shear Failure: typically, in the externally bonded FRP concrete members, the FRP plates do not extend along the entire span of the beam. As a result, a region of stress concentrations exist at the end of the plate. This leads to the formation of nearly vertical cracks at the plate end which could propagate into inclined shear cracks in the concrete body and result into a sudden failure of the structure (see Figure 2.8(c)).
4. Plate-End Interfacial Debonding: this failure is originated within the concrete surface close to the concrete-adhesive interface due to the high interfacial normal and shear

stresses. When these stresses exceed the concrete strength near the plate end, cracking initiates and starts moving toward the midspan region (Smith & Teng, 2002). However, this mode is characterized by the failure of the adhesive layer and the presence of a very thin layer of concrete attached to the fibre plate as shown in Figure 2.8(d).

5. Concrete Cover Separation: in this mode the entire cover of concrete is separated as a result of the crack formulation at or near the plate end, due to the high concentration of normal and shear stresses. The cracks first initiates in the concrete near the plate end and then travel to the level of the tensile reinforcement. Once it reaches that level, it moves horizontally along the bottom of the reinforcement (Garden & Hallaway, 1998). As the load increases, the horizontal cracks will cause the concrete cover to peel off and ultimately the failure of the structure (see Figure 2.8(e)).
6. Midspan Deboning Induced by Flexural Cracks: this mode is initiated by the crack propagation in the vicinity of concrete parallel to the FRP plate and adjacent to the concrete-adhesive interface. The initial debonding is induced by the flexural cracks at the midspan region (Mostafa & Razaqpur, 2017), and propagate toward one of the ends of the beam which results in failure as illustrated in Figure 2.8(f).
7. Midspan Debonding Induced by Flexural/Shear Cracks: similar to the mechanism in the previous mode, the debonding of the FRP plate is triggered by the flexural/shear crack. These types of cracks start as flexural cracks located farther away from the center of the beam. Initially, they grow vertically into a small segment of the concrete cover, then they shift to become inclined (Bizindavyi & Neale, 1999). The debonding also start in the midspan region and move to the ends of the plate leading to a brittle failure of the entire structure. Some concrete residues can be found on the debonded plate after failure (check Figure 2.8(g)).

In summary, FRP rupture and concrete failure (crushing or shear failure) are categorized as "Flexural Failures". As mentioned in the previous section, a complete composite action between concrete and FRP external reinforcement is achieved. However, failures due to loss of composite action such as plate end debonding, concrete cover separation, and both types of intermediate crack-induced debonding are classified as "Local Failures". The latter is very

essential to be considered in designing FRP reinforced concrete beams to ensure safety and structural integrity. The following sections will cover some of the previous research conducted to investigate the flexural and local failure.

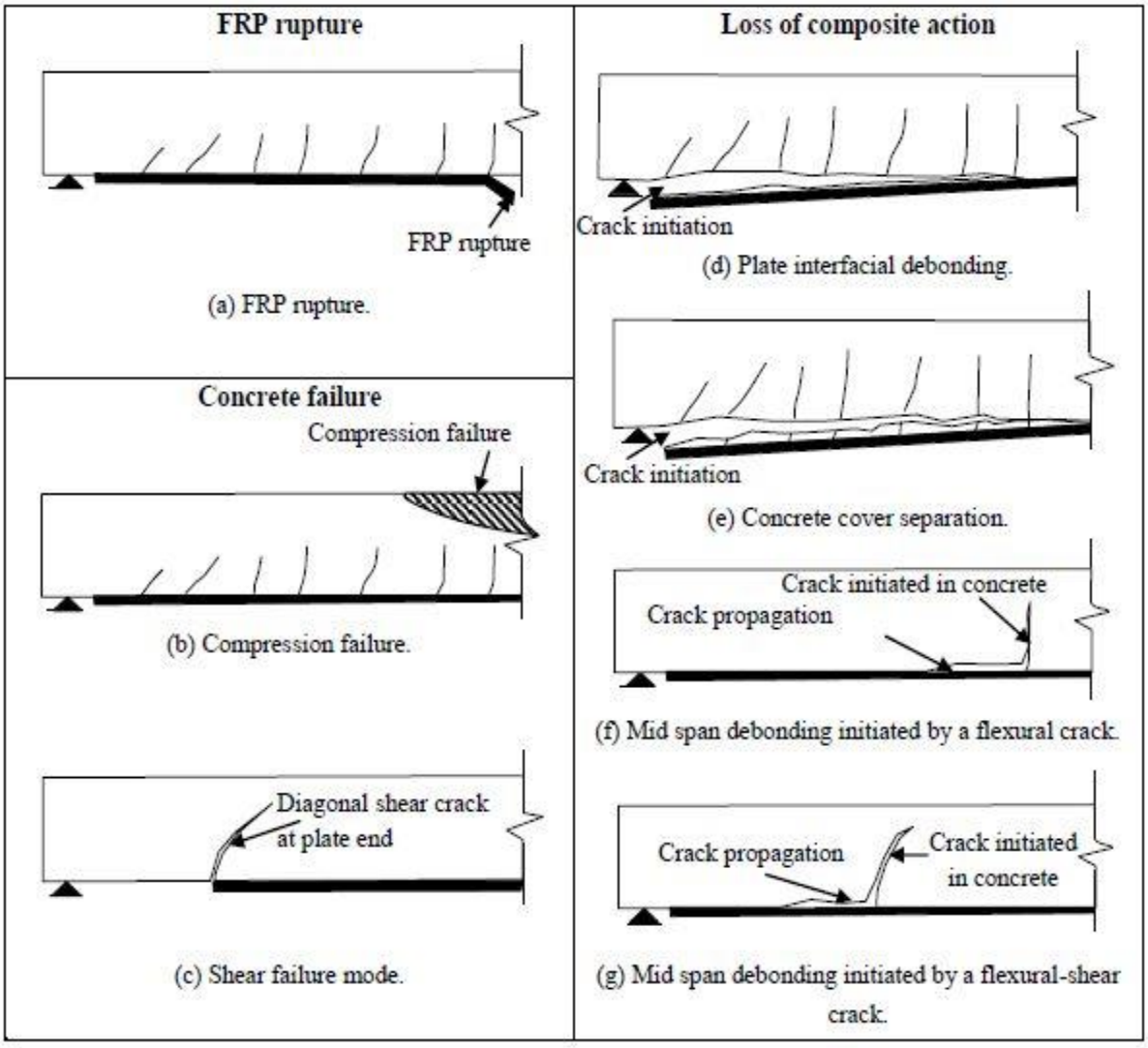

Figure 2.8: Various modes of failure in externally bonded FRP reinforced concrete beams (Obaidat, 2011)

2.10.1 Flexural Failures

Early studies regarding the FRP rupture and concrete failure in FRP-strengthened beams started in the 1990's. Although most of these studies were experimental in nature, there has been a new shift toward the analytical and numerical analysis of the mechanisms related to flexural failures of FRP concrete beams. An extensive parametric study was conducted by Arduini and Nanni (1997) to investigate the effect of various FRP parameters (such as bond length, thickness, and FRP and adhesive stiffness) in the case of applying FRP reinforcement as repair systems in concrete beams. The authors have used an analytical model, which they created in a previous study, to predict the mode of failure of the concrete beams repaired by FRP laminates. This model involves various constitutive laws for each of the main components in the studied structures. Concrete behaviour in compression was taken as nonlinear and affected by the confinement action provided by closed stirrups according to CEB-FIP Model Code 90. While the tensile response of concrete was characterized by a bilinear elasto-softening relation. The steel rebars was modelled by a bilinear elasto-hardening response. On the other hand, FRP and adhesive are both considered perfectly linear elastic materials. This study has produced a prediction tool for the mode of failure of concrete beams externally bonded with FRP sheets if certain conditions are met as explained in Table 2.8. Moreover, the results of the analysis are depicted in Figure 2.9 in the form of ultimate load of the FRP repaired beam (F_{ur}) to the ultimate load of the unrepaired beam (F_u). The plots are characterized by four curves for a given FRP stiffness at the variation of the FRP bonded length-to-shear span (p/a) ratios. For ratios less than 0.65, there is no visible improvement in the strength of the repaired beams. There are five distinct points on the plots at FRP thickness values of 0.0, 0.1, 0.5, 1.0, and 2.0. These points are labeled with a letter that indicates the mode of failure where C, R, S, and D denotes crushing, rupture, shear-tension, and debonding failure, respectively. As it is expected, when no FRP material is present($t_p = 0$), the beam is expected to fail due to the crushing of concrete. While for FRP thickness of 0.1mm, the dominant failure mode is rupture of FRP laminates, regardless of the (p/a) ratio. In the case of 0.5mm thickness of FRP, rupture failure was only observed for the (p/a) ratio of 0.95mm. While shear-tension failure was the dominate mode for all other ratios at that thickness. The authors also stated that

increasing the FRP stiffness leads to a reduction in deflection at service loads. Nonetheless, the onset of shear-tension or debonding failure prevents any possible increase of flexural capacity of the concrete beam by increasing FRP stiffness and/or thickness (Arduini & Nanni, 1997).

Table 2.8: Predictions of failure modes (Arduini & Nanni, 1997).

Condition	Failure Mechanism
Ultimate strain of material is reached	FRP Rupture
Shear stress, τ, reaches τ_u	Shear Failure
Maximum tensile stress, σ_m ,reaches f_t	Tensile Fracture of Concrete
Ultimate tensile strain, ϵ_u, is reached	Local Adhesive Failure

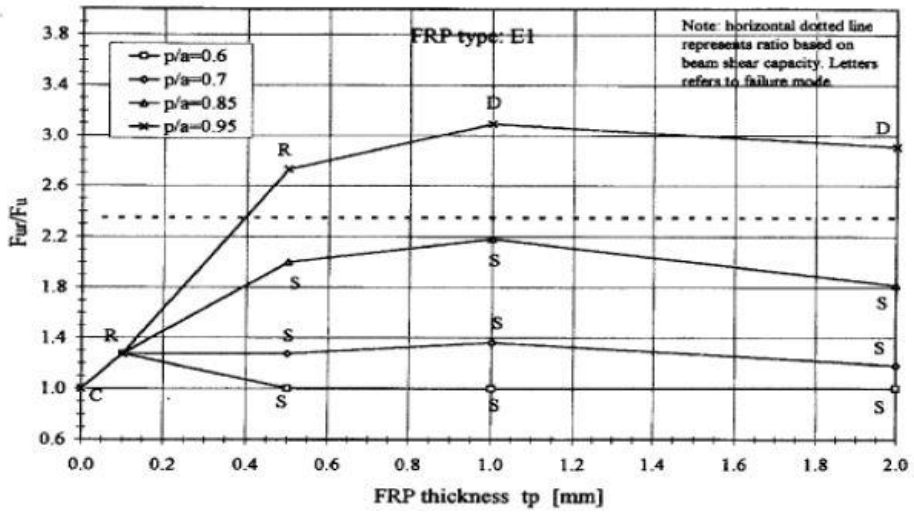

Figure 2.9: Analysis results of Arduini and Nanni (1997) in terms of F_{ur}/F_u ratio vs FRP plate thickness (Monteleone, 2008)

Grace et al. (1999) have investigated the behaviour of reinforced concrete beams strengthened with different types of FRP laminates. The proposed 14 simply supported beams have a rectangular cross section and were loaded beyond the cracking load limit. Then the damaged beams were repaired with CFRP or GFRP laminates and tested to their ultimate capacity. Five configurations of FRP reinforcements were used, to study the effect of FRP addition on the

flexural and shear capacity of the repaired beams (see Figure 2.10). The materials consisted of two types of CFRP sheets, bi and unidirectional GFRP sheets, and CFRP plates. In this study, the effect of FRP reinforcement on deflection, failure load and mode, strain and beam ductility were discussed. The authors also examined the effect of some of the FRP parameters, such as the number of FRP layers, type of epoxy, and reinforcement configuration, on the beam capacity. It was observed that using a combination of longitudinal and U-shaped FRP reduces beam deflection and increase load capacity. Moreover, the use of vertical FRP sheets along the entire span length prevents the rupture of the longitudinal FRP sheets. It was concluded that a combination of vertical and horizontal sheets, together with proper epoxy, can lead to a doubling of the ultimate load strength of the beam. Nevertheless, the authors suggested using a higher factor of safety in the future design of similar beams as all of the strengthened beams have failed in a brittle manner (Grace, et al., 1999).

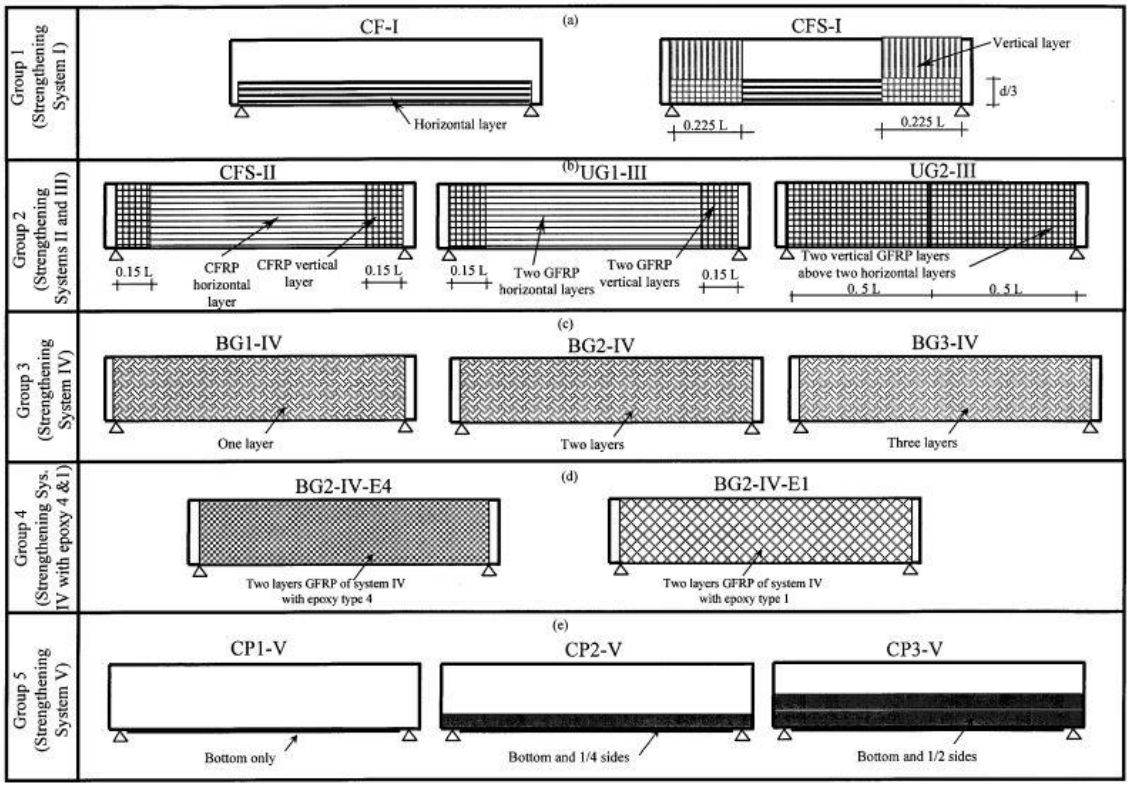

Figure 2.10: FRP reinforcement configuration (Grace, et al., 1999)

Large-scale CFRP externally reinforced concrete beams were tested by Ross, et al. (1999), where three-ply uniaxial CFRP laminates were attached to the longitudinal sides of the beams. The authors have used an inelastic section analysis procedure to predict the beams behaviour, and correlate the results with the experimental data obtained from the tests. In addition, a nonlinear finite element model was employed to analyze the beams, and have a full comparison between the three methods. This study comprises of twenty-four rectangular RC beams, divided into six groups of four depending on the used reinforcement ratio (ρ). It was noticed that for lightly to moderately reinforced beams ($\rho < 1.5\%$) the dominant failure mode was the debonding of the CFRP plates, otherwise known as mod II failure. While for the heavily reinforced beams ($1.8\% < \rho < 3.3\%$) the failure of beams was determined by the crush of concrete in the compression zone and some horizontal cracking along the tensile reinforcement. This kind of failure is also known as mode I failure. In the inelastic section analysis used in this study, a multilinear load-displacement relationship was obtained as depicted in Figure 2.11. As seen in this plot, each element is divided into four regions which are identified by similarly numbered points. These points are defined by using the appropriate assumptions for the beam's behaviour within each region. The concrete response was idealized by a trilinear stress-strain relationship. An elastic-plastic response was assumed for the steel reinforcement, and CFRP is taken as perfectly linear elastic until failure. Although, point 4 in Figure 2.11 is not necessary reached, it is used to calculate the load displacement curve in region 4. The failure of CFRP represented in point 4 could be preceded by the crushing of concrete under compression stress, the debonding of FRP-adhesive interface due to inadequate bond strength, or the debonding of the concrete-adhesive interface due to low interfacial shear strength.

The nonlinear finite element analysis was conducted using the commercial software ADINA to predict the behaviour of the experimental specimens, and to verify the results obtained from the section analysis. The FE model consists of two-dimensional, eight-node plane stress element to represent the concrete, and three-node truss elements used for the reinforcing steel and FRP plates. A hypo-elastic model based on a uniaxial stress-strain relation was used to simulate the concrete response, with considering the biaxial and triaxial conditions. The

material constitutive models for steel and FRP composites were the same as those used in the section analysis. The load displacement curves plotted from the experimental program, section analysis, and FE model are compared in Figure 2.12 for lightly and heavily reinforced beams, respectively.

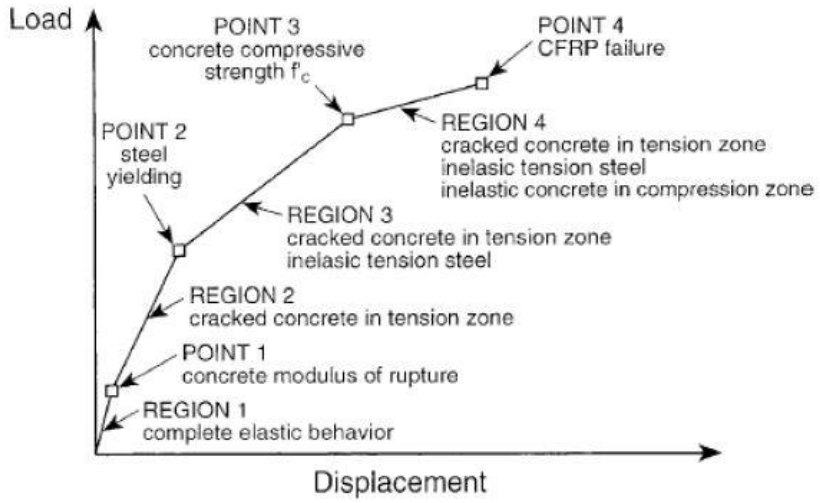

Figure 2.11: Load-displacement assumptions used in the section analysis model (Ross, et al., 1999)

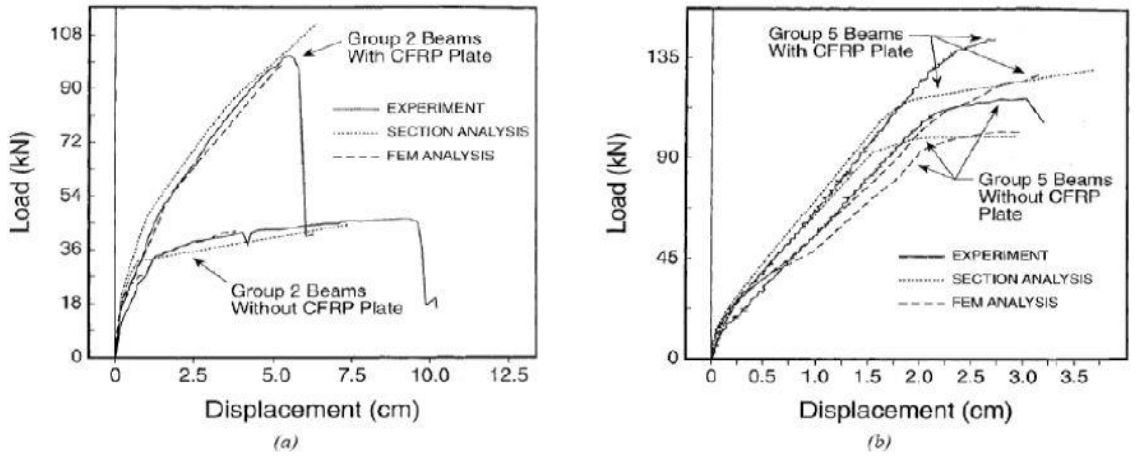

Figure 2.12: comparison of load-displacement plots for (a) lightly reinforced beams (b) heavily reinforced beams (Ross, et al., 1999)

2.10.2 Local Failures

As previously mentioned, this failure is categorized by the loss of composite action between the concrete and FRP reinforcement systems. This can be attributed to the concrete cover separation, plate-end interfacial debonding, and intermediate crack-induced debonding. In FRP-strengthened RC beams, the tensile stresses initiate in the FRP plates and are transferred to the beam by interfacial shear and normal stresses. Therefore, plate-end and intermediate debonding may take place when the interfacial shear strength is reached. The following subsections review some of the literature on the local failure mode in RC beams strengthened by external FRP plates.

2.10.2.1 Plate-End Interfacial Debonding

This type of failure is instigated by the high concentration of normal and shear stresses at the end of the bonded plate in RC beams. Thus, the localization of these stresses results in the delamination of FRP laminate and adjacent concrete cover. Generally, the FRP composites endures tensile stresses under loading, and theses stresses are transfer to the adhesive layer through shear forces. Hence, the crack development is similar to fracture mode II. Triantafillou & Plevris (1991) have proposed an equation to calculate the release rate of the critical strain energy for the interface (G_{IIC}) which is shown in equation (2–1). This quantity can be simply defined as the fracture energy required to cause the plate-end debonding of the FRP external reinforcement.

$$G_{IIC} = \frac{kP^2}{b}\frac{\partial C}{\partial a} \qquad (2\text{–}1)$$

where, k is a constant, P is the applied load, b is the member's width, C is the inverse of the gradient of the load-deflection curve, and a is a crack length.

Malek, et al. (1998) have proposed a closed form analytical model to predict the distribution of normal and shear stress localizations at the plat-end point. The material behaviour in this model was assumed linear-elastic and of an isotropic nature. A perfect bond (no slip) was considered between the concrete and the FRP plate. A discrete crack approach was adapted to model the crack pattern in concrete. Then after, the results obtained from this model were

verified using a finite element analysis conducted by the software ABAQUS. As shown in Figure 2.13 a reasonable correlation was found between the results from both the analytical and the numerical model.

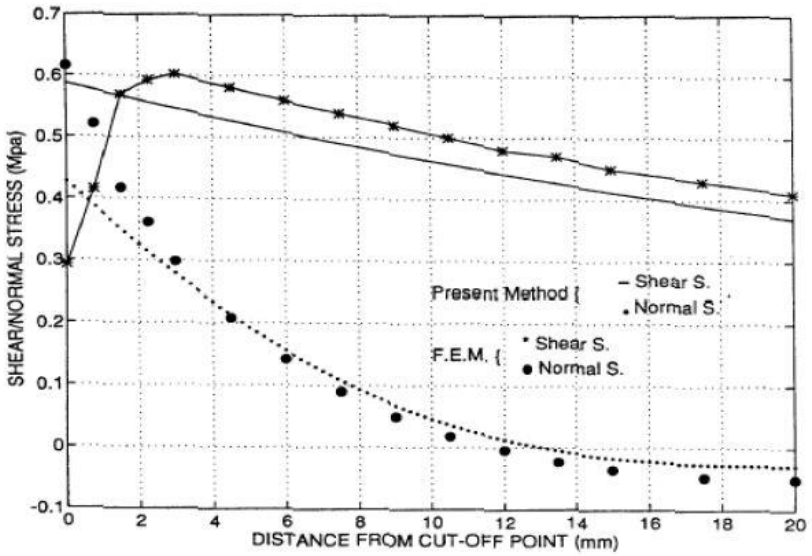

Figure 2.13: Comparison between the predictions of the analytical and the numerical model (Malek, et al., 1998)

Mukhopadhyaka and Swamy (2001) have reviewed some of the existing models to predict the plate-end debonding of FRP laminates in RC beams. The authors suggested that the analytical models proposed by other scholars such as Roberts and Haji-Khazemi (1989), Roberts (1989), Arduini and Di Leo (1996), Taljsten (1997), and Malek, et al. (1998) are not very reliable in practical design, and do not produce consistent results when compared to existing experimental studies. Therefore, there has been a need to develop a more rational model to predict the plate-end debonding mechanism of FRP composites. While the majority of previous research concentred on predicting shear and normal stress concentrations near the FRP plate end, the approach conducted by Mukhopadhyaka and Swamy (2001) presents the concept of interfacial shear stresses to predict plate debonding failure. The debonding occurs when the shear stress at the interface between the concrete and the FRP plates reaches a certain limit. This value

becomes very critical near the plate cut-off end as depicted in Figure 2.14 the critical interfacial shear value can be calculated using equation (2–2).

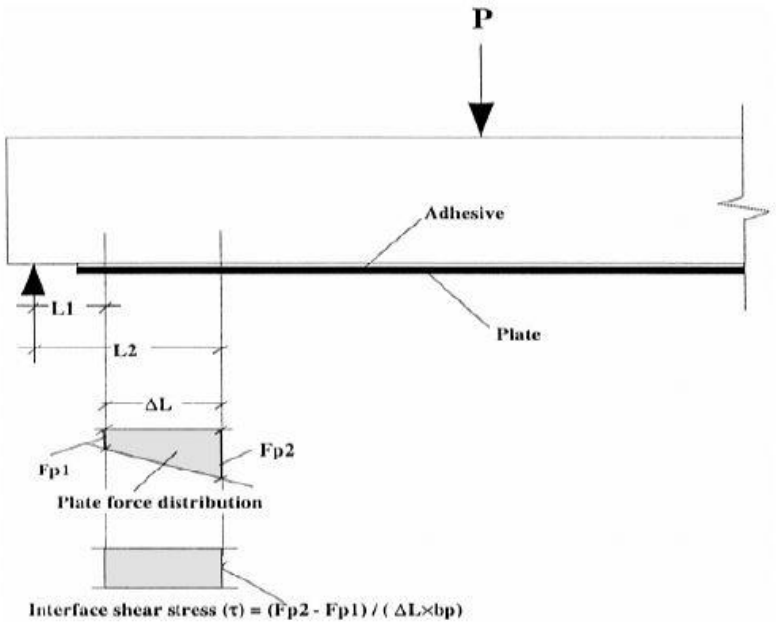

Figure 2.14: Shear stresses at the interface between the concrete and the FRP plate (Mukhopadhyaka & Swamy, 2001)

$$\tau = \frac{F_{p2} - F_{p1}}{(\Delta L) b_P} \qquad (2\text{–}2)$$

where, τ is the ultimate interfacial shear stress, F_P is the force resisted by external plate, $\Delta L = L_2 - L_1$, b_P is the width of externally bonded plate.

This model was verified against a large library of publications focused on the plate-end FRP debonding. The review has reported that the critical interface shear stress ranges between 0.33 and 1.35MPa for CFRP plates, and from 0.26 to 0.90MPa for GFRP plates (Monteleone, 2008). The effect of several other parameters were studied by the authors, such as the concrete strength, FRP stiffness, moment resistance capacity, and size of beam in relation to the interface shear stress. The effect of concrete strength on the interfacial shear stress was found to be minimal as shown in Figure 2.15(a). On the other hand, the increasing the values of the

moment capacity and the FRP stiffness causes the interface shear stress to increase as well (see Figure 2.15(b) and Figure 2.15(c)). The authors stated that FRP plate is more likely to debond in beams with depth to width ratio equal or larger than 2.0, or in beams with shear span to depth ratio equal or greater than 6.0.

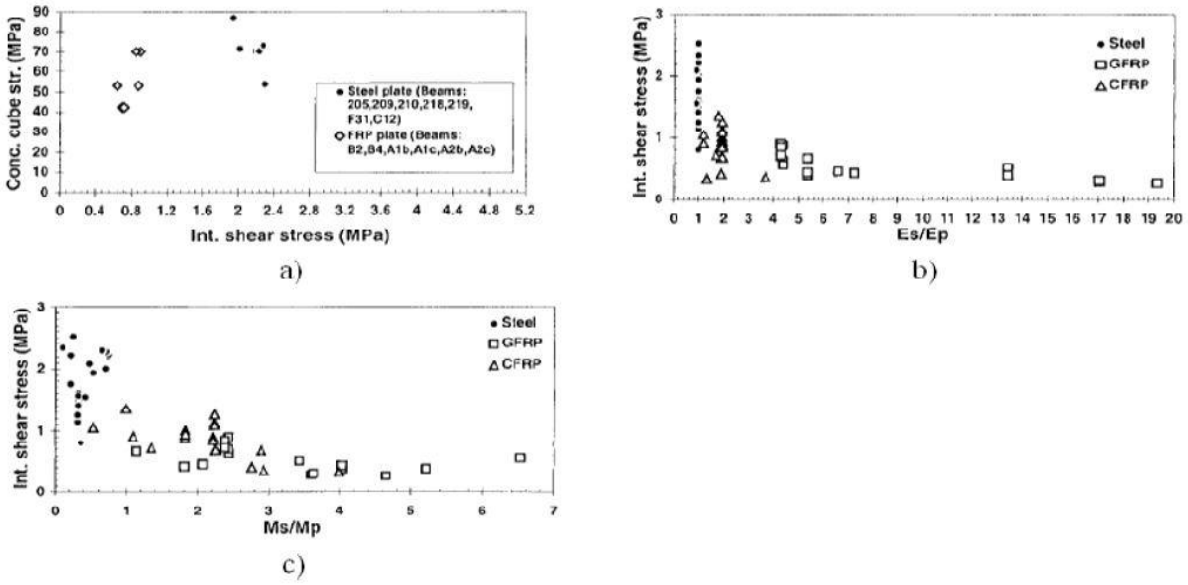

Figure 2.15: Interfacial shear stress plot versus: (a) concrete strength; (b) FRP stiffness; (c) FRP moment resistance (Mukhopadhyaka & Swamy, 2001)

Maalej and Bian (2001) have performed a large experimental program to investigate the shear stress concentrations at the interfacial region between the concrete and the FRP plate. This experimental program isolate the effect of FRP sheet thickness by constructing five RC beams with various number of FRP layers. The first beam was control (no FRP reinforcement was used in this beam). While the remaining four, beam 2 to 5, have one, two, three, and four layers of externally bonded CFRP, respectively. The beam was set up in four-point loading configuration, and the deformations were measured by applying strain gauges to the longitudinal and transverse reinforcement. The tests have shown two types of failure modes: CFRP tensile rupture, and plate-end interfacial debonding. The former was recorded in beam 2, while latter was the dominant mode in beam 3, 4, and 5. The load versus midspan deflection was plotted in Figure 2.16. Although, the area of CFRP external reinforcement was increase in

beam 4 and 5 (by increasing the number of CFRP layers), the CFRP beams did not exhibit larger strength capacity comparing to beam 3. It is, then, concluded that there is an optimum thickness of CFRP which could result in a higher load resistance. This phenomenon can be explained by inability of thick FRP plates to maintain strain compatibility throughout their bonded length (Monteleone, 2008). Nevertheless, FRP plates tend to deform and maintain cross-sectional strain compatibility under small loads. In another word, this tendency to maintain strain compatibility becomes more rigorous as the thickness and/or the applied deflection is increased due to high normal and shear stress concentration (Maalej & Bian, 2001). Therefore, the authors recommend modelling the interfacial normal and shear stress concentration as functions of displacement instead of loads.

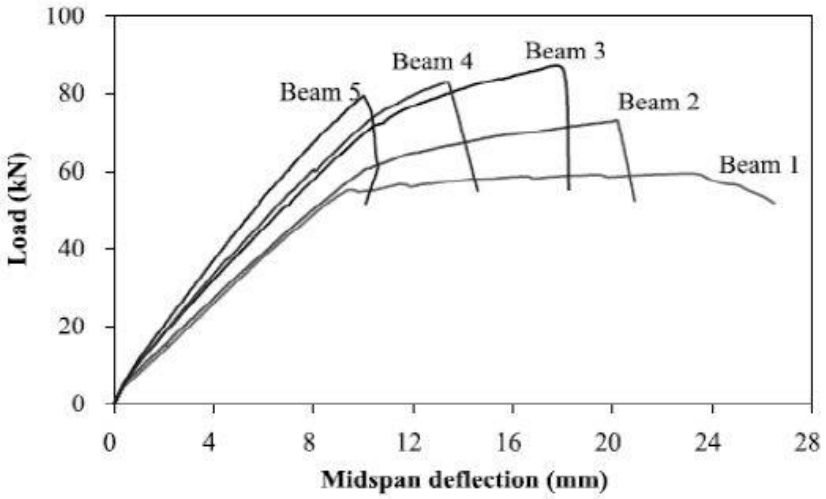

Figure 2.16: Load vs midspan deflection of the five beams (Maalej & Bian, 2001)

2.10.2.2 Concrete Cover Separation

The separation of concrete cover is prompted by the shear failure of the concrete beneath the tensile steel reinforcement, which eventually leads to the debonding of FRP laminates. The debonding of the external FRP reinforcement usually starts from the end of the plate due to the high concentration of shear stresses around this vicinity. A study was conducted by Triantafillou and Plevris (1991) to calculate the ultimate value of the interfacial shear stress, at which the debonding of FRP plate from the anchorage zone commences. This quantity was

set as a function of concrete compressive strength. Some researchers have reported this value to be around 8MPa for normal strength concrete. (Triantafillou & Plevris, 1991).

Another study was done by Ngujen et al. (2001) to predict the failure load of externally bonded CFRP beam due to concrete cover separation. The authors examined the composite action between the RC beam and the FRP plate analytically. As mentioned before, the plate end is a region of concentrated bond stresses at which the peeling of the FRP plate initiates. However, the ripping of concrete is generated at the tensile steel level after shear crack have developed at the plate ends. These shear stresses result in an eccentricity between the tensile stresses in the FRP plates and the steel rebars, which in turn, cause the spalling of concrete cover. The authors have several experimental investigations and they concluded that the composite action of the externally bonded FRP beam can be divided into three zones: (1) a "de-stressed" zone at the end of the plate where strain are approximately zero; (2) a "bond –development" zone where strains increase linearly; and (3) a "composite" zone where the plate acts compositely with the concrete beam. The three zones are schematically shown in Figure 2.17.

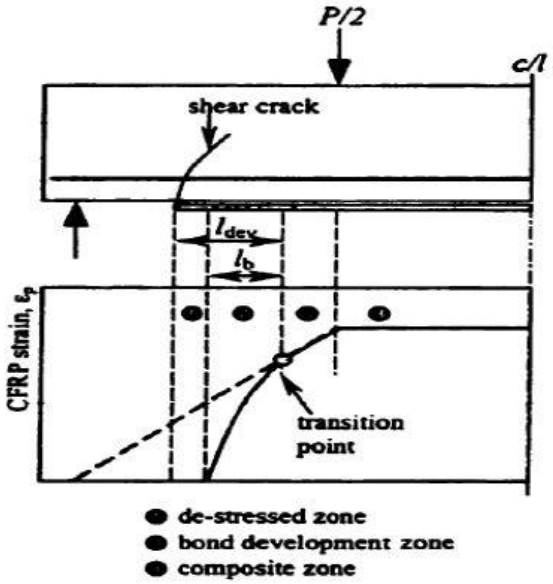

Figure 2.17: Composite model of externally-bonded FRP concrete beams (Ngujen, et al., 2001)

The study has suggested that the concrete cover separation can be prevented if the plate strain at the transition point between the bond-development and the composite zones did not exceed 0.0017 in this case. Moreover, the axial strain in the plate at the transition point, ε_{pe}, is calculated using the equation:

$$\varepsilon_{pe} = \frac{1}{E_c}\frac{M_e}{I_c}(d_p - x) \quad (2\text{–}3)$$

where, M_e is the applied bending moment at the transition point, E_c is the elastic modulus of concrete, I_c is the cracked equivalent moment of inertia of composite beam, d_p is the distance between the top of the beam to the centre of the plate, and x is the distance from the top of the beam to the neutral axis.

The location of the transition point can be identified by evaluating the bond development length (l_{dev}) from the following equations:

$$l_{dev} = c_m + \frac{d_p}{2} + \frac{4.61}{\lambda} \quad (2\text{–}4)$$

$$\lambda^2 = \frac{1}{E_p t_p}\frac{G_a G_c}{G_c t_a + G_a c_m} \quad (2\text{–}5)$$

where, c_m is the thickness of concrete cover, E_p is the elastic modulus of FRP, G_a is the shear modulus of adhesive, G_c is the shear modulus of concrete, t_p is the FRP plate thickness, and t_a is the adhesive thickness.

A finite element analysis was conducted by Yang et al. (2003) based on the discrete crack analogy of concrete. The propagation of multiple discrete cracks during the loading were simulated by using a mixed-mode, linear elastic fracture mechanics program. A combination of four-node isoparametric elements and three-node constant strain elements were employed to model the concrete, adhesive, and FRP plate. However, two-node truss elements were chosen to model the internal steel reinforcement. Typical crack propagation is illustrated in Figure 2.18(a) through Figure 2.18(d). Under the initial load, uniformly-spaced cracks are formed at the tension side of the beam as shown in Figure 2.18(a). The original flexural cracks in the midspan start travelling upward past the reinforcing steel, and new cracks simultaneously

initiate between the major cracks as shown in Figure 2.18(b). As the loading continues, new flexural-shear cracks form and start moving toward the loading point. At this stage, the crack initiated at the plate-end can develop into another major crack that has the largest width. When this crack meets the tensile reinforcement, a new horizontal crack is formed (check Figure 2.18(c)). As the load continues to increase, the major cracks widen, and the horizontal crack propagates rapidly along the interface between the concrete cover and the tension steel reinforcement. At this level, the other cracks do not exhibit noticeable changes, and the beam fails when the horizontal crack intersects with existing major flexural-shear crack which causes the concrete cover to delaminate as shown in Figure 2.18(d).

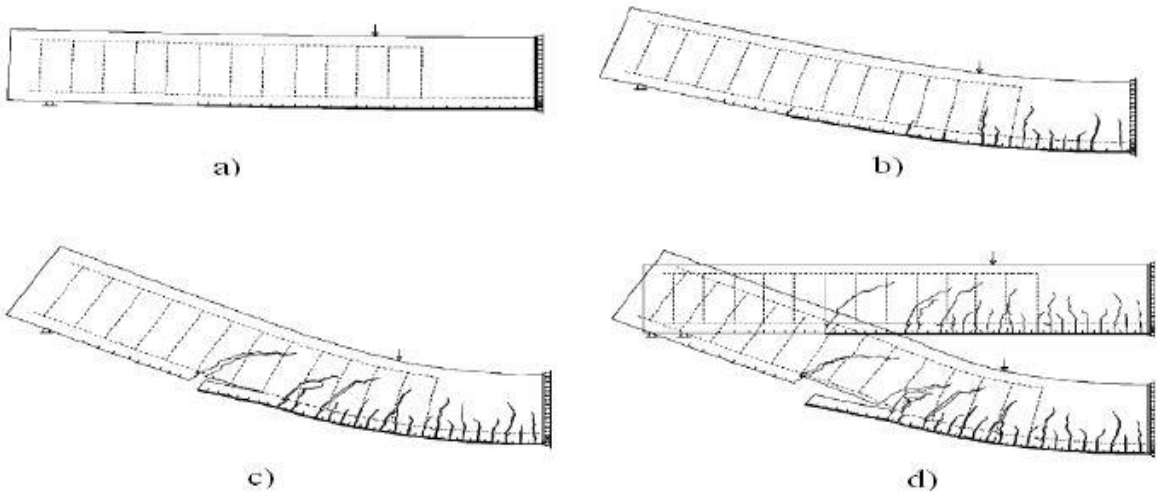

Figure 2.18: Crack propagation in externally bonded FRP concrete beam: (a) uniformly-spaced cracks at the initial loading; (b) migration of major crack and initiation of new cracks; (c) initiation of horizontal crack; (d) plate-end debonding (Yang, et al., 2003)

2.10.2.3 Midspan Deboning Induced by Flexural Cracks

It has been proven that the debonding of the FRP plates can be generated either at the plate end or the mid region of the concrete beam. Although, enormous number of previous research have suggested that the FRP plate delamination occurs exclusively at the end points, many recent studies have found that debonding of FRP laminates can be induced by intermediate cracks as a result of high interfacial shear and normal stresses under loading.

One of the first pioneer to address this kind of debonding mechanism (midspan debonding) was Sebastian (2001). The author has examined a large data gathered from an experimental program that was conducted at Bristol University in UK. The program involved the testing of large-scale FRP-strengthened RC beams under four-point loading. In each specimen, a crack inducer in the form of thin lubricated steel plate was implemented in the midspan, to ensure the initiation of flexural cracks. In addition, the effect of corrosion of steel was simulated by reducing the cross section of all main steel rebars within the midspan length. As shown in Figure 2.19, the debonding of FRP plates were prompted by the high interfacial shear stresses. These stresses are attributed to tension stiffening in cracked concrete and corrosion of internal steel reinforcement. After the onset of first midspan debonding, the process is then self-propagating until the collapse of the entire concrete member as depicted in Figure 2.20.

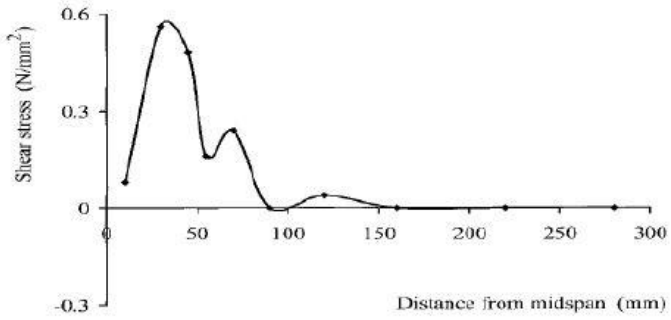

Figure 2.19: Shear stress variation along the midspan of the beam (Sebastian, 2001)

Figure 2.20: Debonding failure: (a) inclined cracks and concrete fracture near the midspan region; (b) the bottom of the beam at the midspan after failure (Sebastian, 2001)

An analytical study on the midspan debonding of FRP plate was presented by Leung (2001). This model was initially created to relate the bonding stress in an FRP plate to the crack opening width. Then, it was further developed into a fracture mechanics-based equation to include moment, crack length, and crack width. This analytical model allows a relationship between the ultimate interfacial shear stress, τ_{max}, and the applied moment to be drawn for different material and geometric properties. This model was verified with data from a finite element analysis, and the results shows that FRP plate debonding is more probable in the case of large crack space, low adhesive thickness, low plate stiffness, and small contact area between the plate and the adhesive (Monteleone, 2008).

Niu and Wu (2005) have examined the effect of multiple flexural cracks on the debonding behaviour of FRP-strengthened RC beams. The authors investigated this particular debonding mechanism by studying the effect of crack spacing, local bond capacity, interfacial stiffness, and interfacial fracture energy. A nonlinear fracture mechanics based finite element model was developed in this study. The crack growth of concrete was modelled using discrete crack approach. While the FRP-concrete interface was modelled by a bilinear bond relationship with a softening behaviour. The authors identified the debonding failure as the instance when the delamination of FRP plate passes through two flexural cracks with a spacing equal to the effective bond length. Therefore, crack spacing has a noticeable effect on the debonding mechanism, and hence the concrete beam structural response. However, if the provided bond length of FRP plate is longer than the effective bond length, the ultimate load capacity of the RC beam is characterized by debonding failure from a single flexural crack. It was also shown that when the crack spacing is larger than the effective transfer length of the FRP sheets, the debonding response and the structural capacity of RC beam can be idealized by the case of a single localized crack.

The relationship between the stress in reinforcement and midspan deflection for different crack spacing is plotted in Figure 2.21. It is seen that the stress in the FRP increases at high rate when the reinforcing rebars start yielding. Then this stress becomes constant at the onset of the FRP plate debonding. The debonding propagates easier along the FRP-concrete interface in the case of large crack spacing, which allows the stresses to remain constant until the final debonding

failure. Nonetheless, a higher beam ultimate capacity is observed in the presence of small crack spacing due to stress redistribution in the FRP plate after cracking.

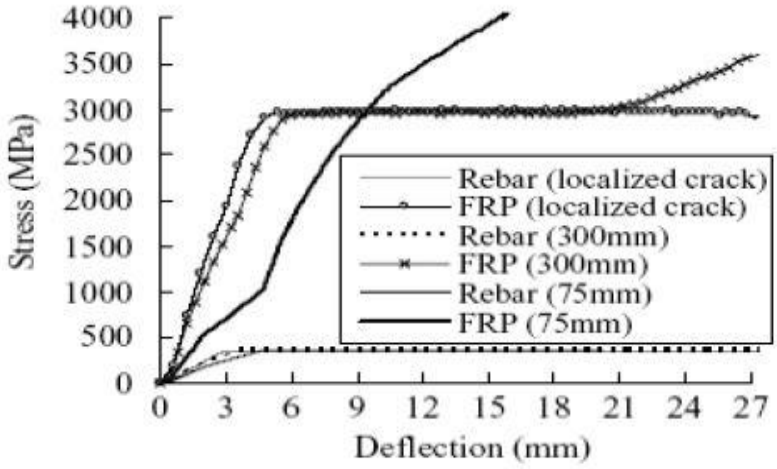

Figure 2.21: Stress in reinforcement vs midspan deflection for different crack spacing (Niu & Wu, 2005)

2.10.2.4 Midspan Deboning Induced by Flexural/Shear Cracks

One of the overlooked FRP debonding mechanisms is that induced by the critical diagonal cracks in reinforced concrete beams. Kishi et al. (2005) have presented a three-dimensional elasto-plastic finite element model. This numerical model aimed to study the debonding behaviour of externally attached FRP sheets in RC beams under the effect of diagonal flexural-shear cracks. Interface elements were employed to model crack openings, rebar slippage, and debonding of FRP sheet. The effect of diagonal crack presence in RC beams on the FRP debonding was further elaborated by making a comparison between those beams with and without diagonal cracks (see Figure 2.22). It is evident from the plots that critical diagonal cracks influence the debonding behaviour of FRP sheet in concrete beams. The case where diagonal cracks were not considered, the load carrying capacity of the beam increases linearly after the rebars have yielded, and the FRP sheet tends to achieve full capacity until rupture. However, the opening of diagonal cracks have impacted the beam load capacity due to the resulted debonding of FRP sheets. Therefore, this study suggested that limiting the initialing

or propagation of diagonal cracks is critical to enhance load-carrying capacity and ductility of concrete beams externally reinforced with FRP laminates.

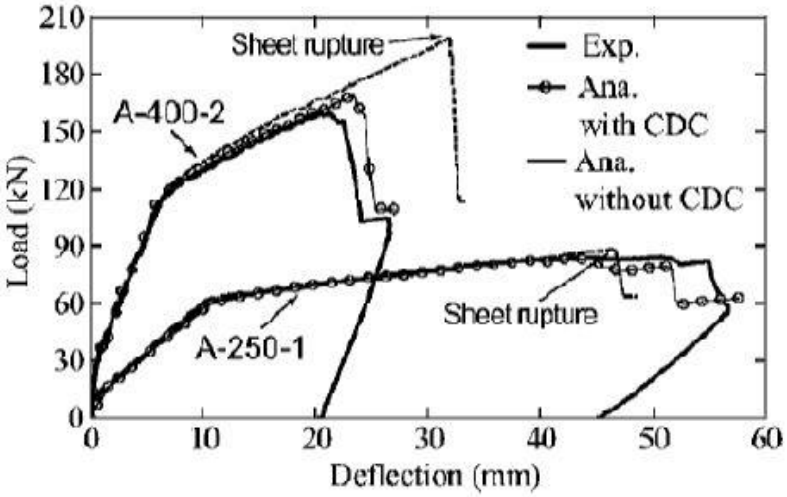

Figure 2.22: Comparison between beams response with and without the presence of diagonal crack (Kishi, et al., 2005)

Another study was conducted by Niu et al. (2006) to examine the effect of diagonal macro-cracks on the debonding of FRP reinforcements in RC beams. The authors have developed a finite element model using the commercially available software DIANA-8 to simulate the RC beam structural response. The concrete parts were modelled with 4-node quadrilateral and 3-node triangular plane stress elements. 2-node beam elements were used to model the FRP reinforcement. The FRP interfaces and the crack planes were modelled using zero-thickness interface elements. The model also includes a predefined midspan crack and two diagonal flexural-shear cracks. These localized cracks were modelled by using the discrete crack method to replicate the crack growth and discontinuity under three-point bending loads. The FRP interface capacity was simulated by a linear shear stress-slip relationship with softening behaviour. As indicated before, the aim of this study is to examine the debonding mechanisms due to diagonal macro-cracking. Therefore, shear retention was ignored once the diagonal crack widens. The effect of interfacial bond strength was also investigated, and it was found that has a tremendous impact on the pre-cracking, post-cracking, and initiation of debonding response until beam failure (Niu, et al., 2006). As seen in Figure 2.23, a set of four bond

strength values, 0.5, 2, 8, and 16MPa were used to study the effect of interfacial bond parameter on the load-deflection response of RC beams. Low interfacial bond strengths, as in 0.5 and 2MPa case, shows premature crack opening, lower beam capacity, and low rates of stress transfer. Consequently, this leads to the debonding of FRP sheets from the midspan flexural crack without the presence of the diagonal cracks causing only mode II response. However, increasing the interfacial bond strength results into a higher load-carrying capacity and ductility, faster load transfer, and the occurrence of diagonal crack induced debonding of FRP sheet. It was suggested that there is a threshold value of interfacial bond strength, beyond which no increase in ultimate load capacity is expected as observed in the case of 8 and 16MPa levels. On the other hand, the authors have investigated the influence of interfacial fracture energy on the debonding failure of FRP sheets. It was concluded that low interfacial fracture energy contributes to the initiation and growth of FRP debonding within the midspan region towards the end of the FRP laminate. Moreover, the low value of interfacial fracture energy constrains stress transfer and hence the capability to distribute the effect of cracking on the overall response of beams (Niu, et al., 2006).

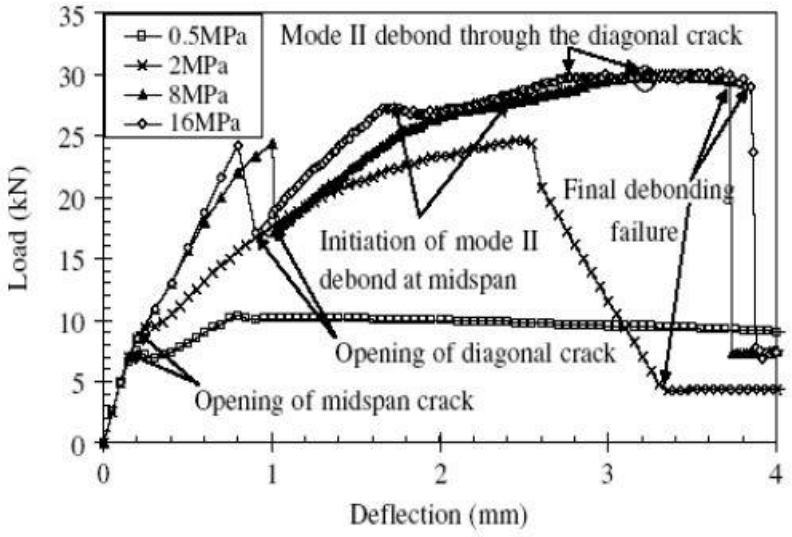

Figure 2.23: Effect of interfacial bond strength parameter on load-deflection response (Niu, et al., 2006)

2.11 Bond Mechanism

The bond strength at the FRP-concrete interface is one of the crucial parameters that influence the debonding behaviour of the externally attached FRP sheets in RC structures. This bond strength is characterized by the load transfer capacity of the FRP-concrete interface region (Xu, et al., 2015). The mechanism of this load transfer is, somewhat, similar to that between concrete and steel plates. In another word, the ability to transfer shear stresses can be induced by the epoxy which is provided at the interface of the concrete and the FRP. Moreover, depending on the roughness of surface, the interfacial load transfer can be carried by the frictional forces generated at the FRP-concrete interface. Finally, mechanical interlocking is also a major element in producing bond strength between the concrete and the FRP reinforcement. This type of interlocking can be identified in different forms, such as gluing aggregate on the surface of the FRP, or by applying mechanical anchors on the FRP reinforcing sheets. Hence, the FRP laminates are mechanically fastened to the external body of concrete beam by steel fasteners and bolts (Yingwu, et al., 2017).

The main difference between the bond behaviour of FRP-concrete interface and the steel-concrete interface is the anisotropic nature of FRP as opposed to the isotropic behaviour of steel. The anisotropic characteristic of FRP is attributed to the type and orientation of the fibre and the resins used primarily in manufacturing FRP composites (Cosenza, et al., 1997). Furthermore, the method of processing FRP sheets results in various characteristics in the surface texture of FRP, as well as, the mechanical properties in both longitudinal and transverse directions.

2.11.1 Factors Affecting Bond Strength

The debonding failure at the FRP-concrete interface was investigated by Triantafillou and Deskovic (1992). The authors have observed that the main cause of failure in the studied specimens was crack propagation in the vicinity of the FRP-concrete interface. Therefore, it was suggested that bonding concrete should not have any loose particles to prevent any

fracture. The authors have also presented empirical models to predict the bond strength between the concrete and the FRP sheets.

Another study was conducted by Yoshizawa et al. (1996) to investigate the effect of different bonding conditions on the bond capacity between concrete and CFRP sheets. Some of the bonding conditions; such as the surface preparation, type of CFRP sheets, and debonding area; were tested using double-face shear specimens. The surface preparation condition was assessed by studying the effect of using water jet or sander for preparing the substrate of the FRP-strengthened concrete members. It was concluded that surfaces prepared with water jet treatment provided better bonding response. This treatment allows the removal of very fines articles that may constrain the bond between concrete and epoxy. It was also observed that bond strength can be enhanced by providing CFRP plates with high tensile strength or stiffness. Moreover, increasing the number of CFRP layers helps improve the bond capacity at the interfacial region.

The effect of surface preparation on the interfacial bond strength of FRP plates was examined further by Chajes and Finch Jr. (1996). Three different methods to prepare the specimens: (a) no surface preparation; (b) grinding with a stone wheel; and (c) mechanically abrading with a wire wheel. The authors have set the bond strength of the FRP laminates as the ultimate load that the bond can sustain divided by the bonded area. The failure of the tested specimens was mainly characterized by the shearing of the concrete under the adhesive layer. From the test results, the mechanical abrasion of the concrete surface was considered the most efficient procedure to maintain a high bond strength. The authors have also proposed that in the case of the failure due to cracking at the concrete-adhesive layer, the ultimate bond strength varies proportionally with the square root of the compressive strength of concrete.

A pullout tests were performed by Taljsten (1997) on concrete prisms which were externally bonded by steel or CFRP sheets. The researcher has defined the anchor length as the minimum length of steel or FRP plate that contributes to the ultimate load capacity, and beyond which no real impact on ultimate bond strength is observed. This study focused on determining the optimum anchor length of steel and FRP plates, in addition to the critical strain level in the concrete at ultimate capacity. Nevertheless, results from the tests suggested that defining the

anchor length depends on the material used in building each specimen. Additionally, the author has concluded that the interfacial bond failure was essentially governed by the strain in the concrete. This failure takes place in the thin concrete layer beneath the adhesive. Finally, the study presented a load response of the bond stress, and the debonding behaviour was related to the strain distribution in the FRP reinforcement.

Bizindavyi and Neale (1999) have examined the load transition mechanism of FRP laminates bonded to concrete surface. The researchers have conducted several pull-out tests in which various parameters were investigated. The type, thickness, and geometrical properties of FRP were assessed, as well as different types of concrete were included in the tests. The study has also presented an empirical model to predict the ultimate load. However, it has been noted that surface preparation is the dominant factor influencing the bond behaviour. It is worth mentioning that the proposed empirical model has some significant restrictions and drawbacks when used to simulate stiff composite laminates (Ueda & Dai, 2005).

Coronado and Lopez (2006) have performed an experimental program by conducting several single lap pull-out tests. The study evaluated the load and strain distribution at failure of specimens with various geometries of FRP sheets. It was found that the bond width is the most critical parameter in increasing the bond strength of FRP-reinforced structure. Moreover, the experimental data were validated against different empirical models. It was concluded that the best agreement between the experimental and numerical results can be achieved by using a model proposed by De Lorenzis et al. (2001).

The effect of moisture on bond behaviour of FRP-concrete interface was investigated by Ouyang (2007). The author presented a new concept, called “Residual Thickness of Concrete-RTC”. In this method, the residual thickness of concrete that was still attached to the peeled FRP plate was measured. Nonetheless, it was concluded that RTC is inversely proportional to the relative humidity of the interface region. Therefore, a higher thickness of residual concrete attached to the plate is expected in dry condition.

2.11.2 Numerical Modelling of Bond Behaviour of Concrete and FRP Interface

It is proven that understanding the complete response of the interfacial load transfer in FRP-reinforced beams is rather complicated. Therefore, thorough experimental programs are needed to fully comprehend the effect of all relevant parameters, which can be expensive and time-consuming. Alternatively, numerical analysis emerges as a practical method, both in cost and time, to simulate the behaviour and predict the ultimate capacity of RC beams strengthened with FRP laminates. In another word, finite element analysis can be employed to analyze the nonlinear behaviour of FRP-concrete interface. Nevertheless, more research is still required in the field of numerical analysis, and the focus needs to be shifted towards developing more rational models that can be used in design provisions (Wei, et al., 2017).

It must be noted that crack simulation is very crucial in any numerical analysis. Coronado and Lopez (2009) have used the cohesive element approach to simulate the behaviour of the FRP-concrete interface. In this analysis, numerical results shows a reasonable agreement with experimental data, and the dominant debonding failure took place within the concrete but close to the interface.

Arduini and Nanni (1997) have proposed analytical models to predict the different failure mechanisms in concrete beams reinforced with externally attached FRP sheets. The results from the model were then validated against an experimental study of RC beams supported with CFRP strips and sheets conducted by the same authors, as well as a commercial finite element program based on smeared crack approach of concrete. Two-dimensional mesh was used to simulate the beams with CFRP strips. While beams strengthened with CFRP sheets were modelled by a three-dimension mesh. Perfect bond assumption was used to simulate the interfacial behaviour between concrete and FRP laminates in both the analytical and numerical models. Figure 2.24 depicts the load-deflection response for the beams bonded with CFRP strips, along with the results from the analytical and numerical analysis. The failure mode of beam A1 and A2 was identified by the crushing of concrete long after the steel rebars have yielded. While beam A3, A4, and A5 collapsed in a brittle manner due to shear failure. As discussed before, this mode of failure is characterized by the onset of crack at one of the plate ends, and the propagation of that crack along the tensile steel reinforcement. Beam A6 also

exhibited a brittle failure due to the delamination of FRP plate from the concrete body. It can be seen that the analytical and numerical analysis has produced a stiffer response comparing to the experimental results. This can be justified by the possible slippage between the concrete and the FRP laminates in both vertical and horizontal direction. Such slippage was disregarded when perfect bond was assumed at the FRP-concrete interface in the analysis.

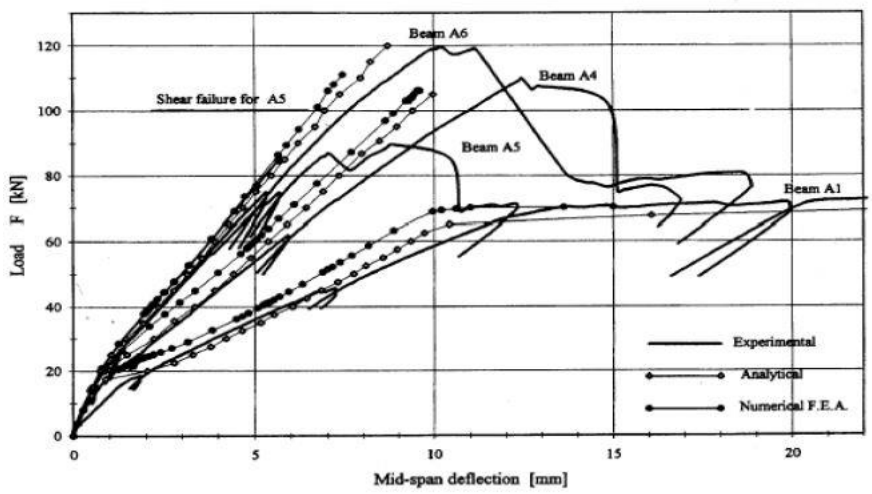

Figure 2.24: Load vs midspan deflection curves of results obtained from experimental, analytical, and numerical FE analysis of RC beams strengthened with CFRP (Arduini & Nanni, 1997)

Nitereka and Neale (1999) have proposed a nonlinear finite element model to predict the full load-deformation response of RC beams externally strengthened with FRP laminates. In this study, the concrete under compression was modelled by a nonlinear relationship with a post-cracking tension stiffening effect. The behaviour of steel reinforcement was simulated by an elastic-plastic model, while a perfect linear elastic curve was adopted for the FRP materials. The presence of the steel rebars and the FRP laminates was smeared into the model in the form of layers of equivalent area. Full bond was assumed between the concrete and the steel reinforcement. On the other hand, a bond slip model was used to replicate the interaction between the concrete and the FRP laminates. Shear strains are ignored in this model, and equal displacements were applied within the interfaces of adjacent layers to maintain compatibility. Experimental programs published by M'Bazaa (1995) and Chicoine (1997) were used to

validate the proposed finite element model (see Figure 2.25). As it can be seen from the comparison, the beam tested by M'Bazaa (1995) has failed due to concrete delamination at about 60% of the predicted ultimate load. However, the specimen tested by Chicoine (1997) exhibited a higher performance due to the application of U-shaped composite anchors at the end of the beam. This beam reached an approximately 95% of the ultimate capacity predicted by the numerical model.

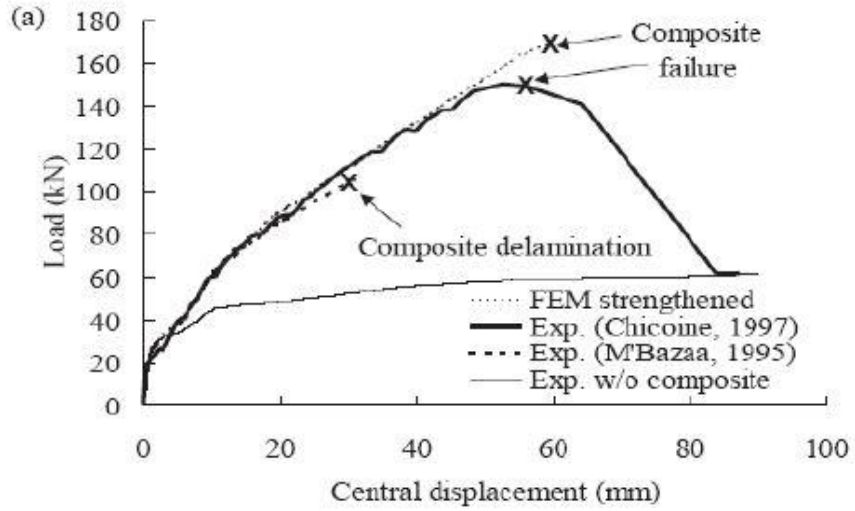

Figure 2.25: Comparison between numerical and experimental results (Nitereka & Neale, 1999)

Another numerical study was performed by Wong and Vecchio (2003) to examine the interfacial bond-slip response between the concrete and the FRP composite. A two-dimensional nonlinear finite element model was adopted in this study, in which two constitutive models were used for bond interface: elastic-plastic and linear-elastic as presented in Figure 2.26. The interfacial connection between the concrete and the FRP elements was presented by a one-dimensional contact bond element as shown in Figure 2.27. The nodes of the concrete and the adjacent FRP elements were connected by bond elements to ensure relative displacement or slip between the two materials. In another word, the differential displacement between the concrete node and FRP node represents the nodal slip of the bond element. Accordingly, the bond stress is calculated by using one of the constitutive relationships. The

bond force is then found by multiplying the bond stress by the bonded surface area represented by the element.

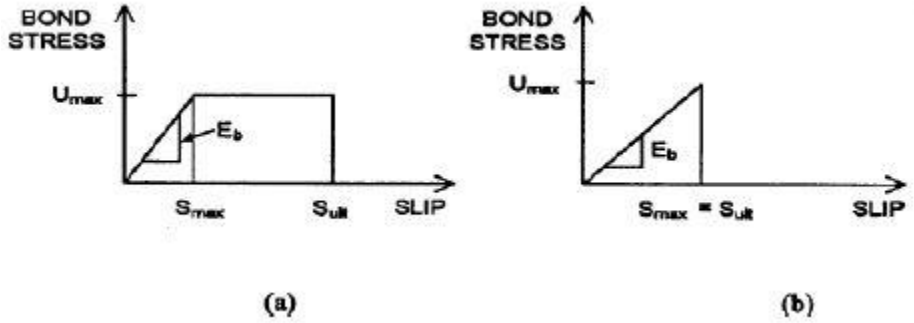

Figure 2.26: Constitutive relationship for bond interface: (a) elastic-plastic; and (b) linear elastic (Wong & Vecchio, 2003)

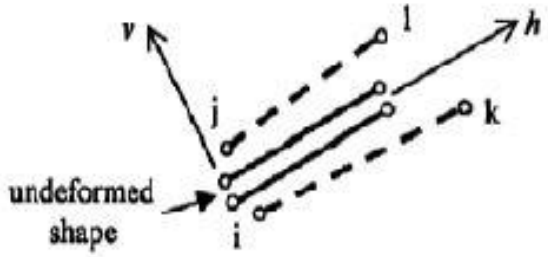

Figure 2.27: One-dimensional contact element (Wong & Vecchio, 2003)

Vecchio and Bucci (1999) have presented a nonlinear finite element model, in which a perfect bond was assumed at the FRP-concrete interface. The results from the numerical analysis were then validated against two sets of published experimental data. The first set involves flexural RC beams strengthened with CFRP plates and tested by Zarnic et al. (1999). The mode of failure exhibited by those specimens was dominated by the delamination of the FRP plates under the concentrated load region. Figure 2.28 illustrates the load-deflection curves obtained from the experimental and numerical analyses. The comparison shows that the perfect bond model (FE-P) overestimated the failure load by 19%, with a corresponding midspan deflection that is 66% larger than the experimental value. While, the elastic-plastic bond model (FE-EP)

has overestimated the ultimate load and deflection by 17% and 59%, respectively. On the other hand, the linear-elastic bond relationship (FE-LE) provides the closest prediction, with an ultimate load of 111kN, which is 5% lower than the experiment value.

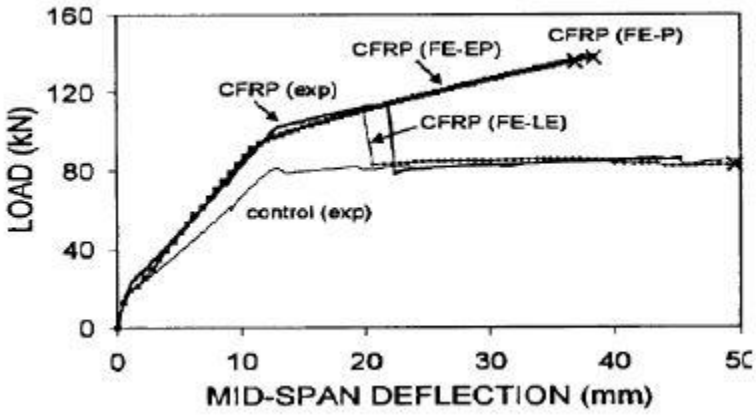

Figure 2.28: Load vs deflection curves of the numerical and experimental results from first set (Wong & Vecchio, 2003)

The second set of experimental data, which was used in the comparison, was tested by De Rose and Sheikh (1997). It should be noted that shear failure was dominant in this set of specimens. The numerical results and the experimental data were compared in terms of load and midspan deflection in Figure 2.29. The perfect bond model (FE-P) resulted in a higher post-yielding stiffness, and underestimated the deflection at the ultimate point by 75%. Whereas, the linear elastic bond relationship (FE-LE) predicted a premature ultimate deflection at around 65% of the tested value. Nonetheless, the specimen modelled with elastic-plastic bond law (FE-EP) exhibited a flexural-shear failure at a load of 2465kN, which is 2% lower than the real ultimate load.

It can be observed that selecting the appropriate bond constitutive model governs the accuracy of the numerical prediction. Therefore, linear-elastic bond relationship was found most suitable to model specimens in which sudden delamination of FRP plate due to weak epoxies is expected. However, specimens with higher epoxy strength, peeling of the concrete cover is more dominant, and hence elastic-plastic bond law was found to produce more realistic prediction. The researchers have suggested that the ultimate bond stress can be taken as a

function of the concrete modulus of rupture, and the maximum slip as a function of the shear modulus of the epoxy. They also noted that the existence of the plastic range in the bond law is dependent on the shear strength of the epoxy (Wong & Vecchio, 2003).

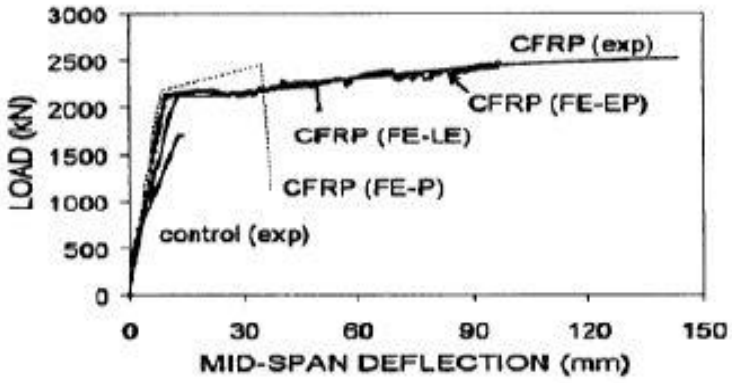

Figure 2.29: Load vs deflection curves of the numerical and experimental results from second set (Wong & Vecchio, 2003)

2.11.3 Meso-Scale Finite Element Approach

It has been already established that the external FRP plates or sheets are counted as a practical alternative to the typical reinforcing methods of concrete beams. However, additional care must be given to designing such members against debonding failure modes that were identified in pervious sections. Therefore, to maintain the integrity and the safety of concrete beams externally reinforced with FRP laminates, a sound understanding to the bond mechanism at the FRP-concrete interface needs to be developed. In particular, a reliable interfacial bond-slip is necessary to understand the debonding failure in FRP-strengthened RC structure.

Lu et al. (2005) have studied the potential of creating a bond-slip curve at any point along the FRP-concrete interface through a comprehensive numerical analysis. This study was driven by the difficulty in obtaining reliable bond-slip curves directly from the strain measurements in pull tests. The authors noted that debonding in pull test generally initiates in the concrete. As such, if the failure of concrete can be accurately modelled, a reliable shear stress-slip relationship can be attained from a finite element model. Moreover, an accurate modelling of concrete failure near the adhesive layer is critical in this numerical analysis. The analysis also

considered that the delamination of the FRP laminates usually takes place within a concrete layer of 2 to 5mm thickness, which is adjacent to the adhesive material. The proposed meso-scale finite element model consists of very small elements that are one order smaller than the thickness of the fracture zone of concrete. The implementation of small elements in this model prompts the ability to trace crack paths as deformations progress. The numerical analysis also employs a fixed angel crack model (FACM), which allows for a clear representation of material parameters (Rots & Blaauwendraad, 1989). The three-dimensional FRP-concrete interface was modelled with a two-dimensional plane stress model with four-node isoparametric elements to reduce computational effort. However, there could be some discrepancies between the width of the FRP plate and the concrete prism. To overcome this issue, the applied load and the axial stresses and strains were adjusted in this model by using a width ratio factor, β_p, proposed by Chen and Teng (2001) as shown in the equation below:

$$\beta_p = \sqrt{\frac{2 - b_f/b_c}{1 + b_f/b_c}} \qquad (2\text{–}6)$$

where, b_f and b_c are the widths of the FRP plate and the concrete prism, respectively. The authors have implemented their numerical model into the general-purpose finite element software MSC.Marc as a user subroutine. The results predicted by the finite element model were then verified by experimental data obtained form 10 pull tests conducted by Wu et al. (2001), Ueda et al. (1999), Tan (2002), and Yuan et al. (2004). The predictions of the finite element model were in a reasonable agreement with all of the actual tests data. In this study, a Fast Fourier Transform smoothing procedure was used to process the raw finite element interfacial shear stresses. The smoothened results were then used to obtain local bond-slip curve (Lu, et al., 2005). As can be seen in Figure 2.30 a smoothing length of 10mm is suitable and this length was used in this numerical analysis. Moreover, all of the finite element models in this numerical study have included an unbonded zone of 25mm.

It ought to be noted that the authors have presented their numerical model in three forms: Precise, Simplified, and Bilinear model. The predicted results from each model was then compared with actual data from extensive experimental programs. The predictions were in a

close agreement with the test results and performs better than existing bond-slip models. Although the prediction of the precise and the simplified models were practically similar, the former was observed to perform slightly better (Lu, et al., 2005).The three forms of the proposed models are elaborated further in the following sections.

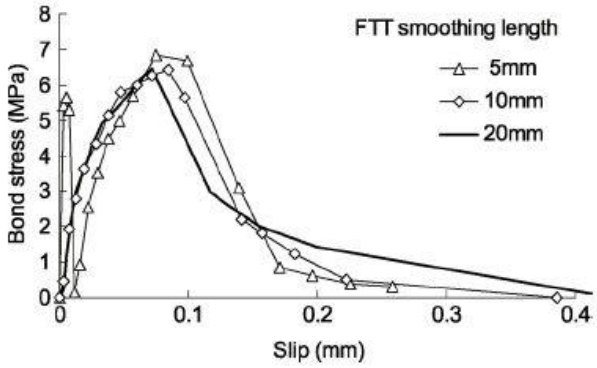

Figure 2.30: Different FFT smoothing lengths used to smoothen bond-slip curves (Lu, et al., 2005)

2.11.3.1 Precise Model

The initial meso-scale finite element model adopted some of the constitutive relationships provided by the Chinese code for the design of concrete structures (GB 50010, 2002). These models were used to calculate the mechanical properties of concrete as shown in the following equations.

$$f_c = 0.76 f_{cu} \qquad (2\text{–}7)$$

$$f_t = 0.395 (f_{cu})^{0.55} \qquad (2\text{–}8)$$

$$E_c = \frac{100\,000}{2.2 + 34.74/f_{cu}} \qquad (2\text{–}9)$$

Where, f_{cu} is the cube compressive strength of concrete, f_c, f_t, and E_c are the compressive strength, the tensile strength, and the modulus of elasticity of concrete, respectively.

A comparison between the typical bond-slip curves, obtained from the three forms of the proposed finite element model, is illustrated in Figure 2.31. It is observed that all of the curves

comprise of an ascending and descending branch, with the bond stress reducing to zero when the slip is sufficiently large. Moreover, in the precise and the simplified models the initial stiffness of the bond-slip curve is much higher than the secant stiffness at the peak stress point. This initial high stiffness reflects the linear elastic state of the interface prior to debonding. However, the interfacial stiffness starts to drop with onset of micro-cracking in concrete as the bond stress propagates (Lu, et al., 2005). The authors also indicated that the maximum bond stress, τ_{max}, and the corresponding slip, s_o, increase almost linearly with f_t. On the other hand, the interfacial fracture energy, G_f, increases almost linearly with $\sqrt{f_t}$.

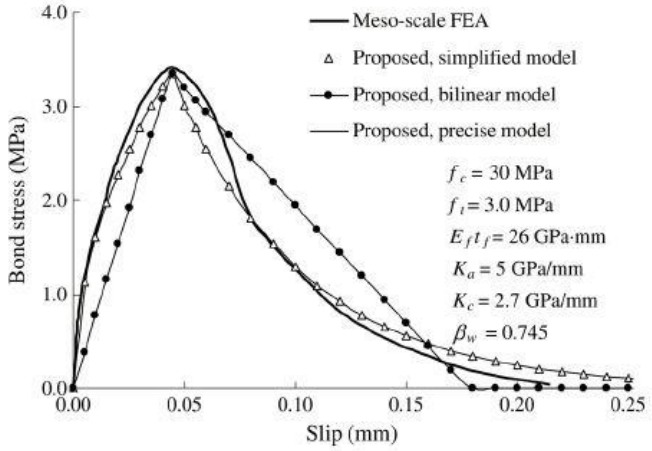

Figure 2.31: Three forms of bond-slip curves simulated by meso-scale finite element model (Lu, et al., 2005)

Based on the above observations, the precise bond-slip model was proposed, and the following series of equations were introduced to describe the local bond-slip relationship of RC beam externally bonded with FRP sheets/plates.

$$\tau = \tau_{max}\left(\sqrt{\frac{s}{s_o A} + B^2} - B\right) \quad \text{if } s \le s_o \qquad (2\text{–}10)$$

$$\tau = \tau_{max}\, exp[-\alpha(s/s_o - 1] \quad \text{if } s > s_o \qquad (2\text{–}11)$$

$$A = (s_o - s_e)/s_o \qquad (2\text{–}12)$$

$$\text{B}=s_e/[2(s_o - s_e) \qquad (2\text{–}13)$$

The maximum bond stress, τ_{max}, and the corresponding slip, s_o, are calculated by the following equations:

$$\tau_{max} = \alpha_1 \beta_w f_t \qquad (2\text{–}14)$$

$$s_o = \alpha_2 \beta_w f_t + s_e \qquad (2\text{–}15)$$

$$s_e = \tau_{max}/K_o \qquad (2\text{–}16)$$

$$K_o = \frac{K_a K_c}{K_a + K_c} \qquad (2\text{–}17)$$

where K_o is the initial stiffness of the bond-slip model, $K_a = G_a/t_a$ and $K_c = G_c/t_c$. The elastic shear modulus of concrete and adhesive is represented by $G_c$and G_a, respectively. t_c and t_a are the effective thicknesses of concrete and adhesive layer, respectively.

The ascending branch of the bond-slip curve is represented in Figure 2.32, which allows the initial stiffness to be approximated. It can be observed that concrete thickness, t_c, of 5mm leads to close prediction of the bond-slip curve. However, the exact value of t_c requires more rigorous analysis, and the effect of such precision on the overall bond-slip model is insignificant for practical purposes. Therefore, this approximate value of thickness was implemented in the precise bond-slip model. In addition, the other two meso-scale finite element models do not include the t_c parameter in their procedures.

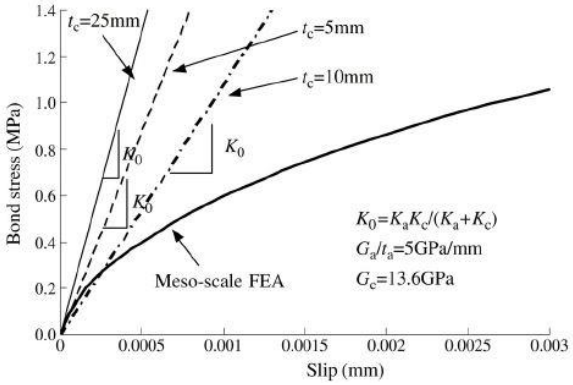

Figure 2.32: Initial stiffness of bond-slip curve (Lu, et al., 2005)

The parameter α in equation (2–11) affects the shape of the descending branch of the bond-slip curve and can be computed using the following equation:

$$\alpha = \tau_{max} s_o / \left(G_f - G_f^a\right) \qquad (2\text{–}18)$$

where the interfacial fracture energy, G_f, can be expressed as follow:

$$G_f = \alpha_3 \beta_w^2 \sqrt{f_t} f(K_a) \qquad (2\text{–}19)$$

where the function $f(K_a)$ is introduced to account for the future extension of the model to interfaces with very soft adhesive layers. However, for normal adhesive layers with $K_a \geq$ 2.5GPa/mm, the value of $f(K_a)$ is taken as 1 because finite element results have shown that the effect of the adhesive layer stiffness on G_f is minimal for such normal adhesives (Lu, et al., 2005).

While the fracture energy of the ascending branch of the bond-slip curve, G_f^a, can be calculated by:

$$G_f^a = \int_0^{s_o} \tau ds = \tau_{max} s_o \times \left[\frac{2A}{3}\left(\frac{1+B^2A}{A}\right)^{3/2} - B - \frac{2}{3}B^3A\right] \qquad (2\text{–}20)$$

As indicated before, the parameter A and B can be calculated using equations (2–12) and (2–13).

The authors have also proposed an iterative procedure to determine the three coefficients in the bond-slip model α_1, α_2, and α_3. This procedure assumes the values of K_a and $\beta_w$equal to 5GPa/mm and 1, respectively. The final values obtained from this process for the three coefficients are: α_1= 1.50, α_2= 0.0195, and α_3= 0.308. While the refine expression of the width ratio factor, β_w, is given by:

$$\beta_w = \sqrt{\frac{2.25 - b_f/b_c}{1.25 + b_f/b_c}} \qquad (2\text{–}21)$$

This term presented in the previous equation is slightly different than the expression originally proposed by Chen and Teng (2001), and as shown in equation (2–6). However, the difference between the two expressions is very small and both formulae are applicable in practical applications (Lu, et al., 2005).

2.11.3.2 Simplified Model

It is evident that the procedure in the precise model is somewhat complicated and time consuming. Thus, more simplified form was proposed by the authors without a significant loss of accuracy. Similar to the observation made in precise model, the initial stiffness of the bond-slip curve is considered much larger than the secant stiffness at the peak point. Hence, the initial stiffness can be approximated as infinity and the following simplified bond-slip model can be presented:

$$\tau = \tau_{max}\sqrt{\frac{s}{s_o}} \qquad if\ s \le s_o \qquad (2\text{–}22)$$

$$\tau = \tau_{max} e^{-\alpha\left(\frac{s}{s_o}-1\right)} \qquad if\ s > s_o \qquad (2\text{–}23)$$

$$s_o = 0.0195\beta_w f_t \qquad (2\text{–}24)$$

$$G_f = 0.308\beta_w^2\sqrt{f_t} \qquad (2\text{–}25)$$

$$\alpha = \frac{1}{\frac{G_f}{\tau_{max}s_o} - \frac{2}{3}} \qquad (2\text{–}26)$$

where the values of τ_{max} and $\beta_w$can be determined by using equations (2–14) and (2–21). Though the simplified model is simpler and shorter than the precise model, the bond-slip curve predicted by this model is very similar to that calculated by the precise model. Therefore, the simplified model is considered in many practical applications in which normal adhesive joints with $f(K_a)$ = 1 is used (Lu, et al., 2005).

2.11.3.3 Bilinear Model

The bond-slip curve in this model is generated by adopting a bilinear relationship which can be used to induce a simple design equation for the bond strength. This model uses the same local bond strength and total interfacial fracture energy as in the simplified model. As a result, the bond strength is unaffected by the simplification made in the bilinear model if the bond length is longer than the effective bond length. The bilinear model can be summarized by the following series of equation:

$$\tau = \tau_{max}\sqrt{\frac{s}{s_o}} \qquad if\ s \le s_o \qquad (2\text{–}27)$$

$$\tau = \tau_{max}\frac{s_f - s}{s_f - s_o} \qquad if\ s_o < s \le s_f \qquad (2\text{–}28)$$

$$\tau = 0 \qquad if\ s > s_f \qquad (2\text{–}29)$$

$$s_f = 2G_f/\tau_{max} \qquad (2\text{–}30)$$

where τ_{max}, s_o, and G_f are calculated by using equations (2–14), (2–24) and (2–25), respectively. Moreover, the predictions of the bilinear bond-slip model are also depicted in Figure 2.31in comparison with the last two models.

2.11.4 Ultimate Bond Strength

In order to better understand the debonding mechanism of the externally bonded FRP plates in RC beams, more rational models are required to assess the ultimate bond strength of the FRP-concrete interface. Some researchers such as Chen and Teng (2001) have reviewed and validated the existing empirical models by comparing them to relative experimental data gathered from literature. This study has exposed the insufficiencies of the existing models and presented a more rational approach based on fracture mechanics analysis and experimental observations. In this approach the bond-slip relationship was presumed linear in a decreasing fashion, whereas the bond stress drops as the displacement grows until it reaches zero at the ultimate allowable slip, δ_f, as shown in Figure 2.33.

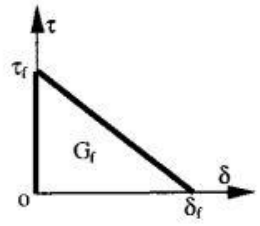

Figure 2.33: Shear-slip model for plate to concrete bonded joints (Chen & Teng, 2001)

The authors have examined a large library of experimental data, and hence concluded that the width ratio of the bonded plate to concrete has a noticeable effect on the ultimate bond strength. This effect is very pronounced when there is a difference between the width of the bonded plate and the concrete member. In another word, if the plate has a smaller width compared to the concrete beam, a non-uniform stress distribution will be induced across the width of the concrete member. This may also lead to a higher shear stress in the adhesive at failure, which can be the attributed to the contribution of the concrete outside the bonded area.

This study has revealed that the ultimate bond strength varies linearly with the width ratio, β_p, in the form of equation (2–6). Accordingly, the following model was proposed to evaluate the ultimate bond strength:

$$P_u = 0.427\beta_p\beta_L\sqrt{f_c'}b_pL_e \qquad (2\text{–}31)$$

where, P_u is the ultimate bond strength, β_p is the width ratio factor, and β_L is calculated by:

$$\beta_L = \begin{cases} 1 & L \geq L_e \\ \sin\dfrac{\pi L}{2L_e} & L < L_e \end{cases} \qquad (2\text{–}32)$$

f_c' is the compressive strength of concrete, b_p if the FRP plate width, and finally L_e, effective bond length, is calculated by the following expression:

$$L_e = \sqrt{\frac{E_p t_p}{\sqrt{f_c'}}} \qquad (2\text{–}33)$$

The E_p and t_p represent the modulus of elasticity and the thickness of the FRP plate, respectively.

It should be noted that this model is more convenient for practical application because it uses the cylinder concrete compressive strength, f_c', which is available in most cases (Chen & Teng, 2001). The authors have validated their model by constructing a comprehensive comparison with six other well-known models as shown in Table 2.9. As indicated in the comparison, the proposed model produces an overall average of 1.05 for the ratio of experimental to predicted ultimate bond strength, and a corresponding standard deviation of 0.18 which is considered reasonably low.

Table 2.9: Comparison between the measured and predicted bond strength ratios (Chen & Teng, 2001)

Source	Average	Standard Deviation	Coefficient of Variation
Hiroyuki and Wu (1997)	2.87	0.95	33%
Tanaka (1996)	2.92	1.65	56%
Van Germert (1980)	2.19	1.12	51%
Chaallal et al. (1998)	1.81	0.89	49%
Khalifa et al. (1998)	1.07	0.24	23%
Neubauer and Rostasy (1997)	0.82	0.15	18%
Chen and Teng (2001)	1.05	0.18	17%

2.12 Finite Element Modelling of FRP-Strengthened RC Beams

In recent decades, finite element method has been vastly considered an effective tool in the analysis of both simple concrete structures, such as RC beam, column, slab, etc., and complex concrete structures, such as deep beam, shear wall, offshore wall, FRP-strengthened RC structures etc. However, the advancement in the computers industries, in terms of memory capacity and speed, has pushed further for the use of finite element analysis in modelling more complex concrete structures with both material and geometric nonlinearities. Many researchers have dedicated their effort to review and develop accurate finite element models for RC beams. Their work and findings are well established in recent literature, and some of which is discussed in this study (Hoque, 2006).

As mentioned earlier, FRP materials have emerged as an effective reinforcing agent in RC structures due to their advantages over steel reinforcement. Over the last decade, many experimental programs were conducted to examine the behaviour of RC structure where FRP reinforcement are employed. However, a considerable number of studies have also concentrated on the development of finite element models for the analysis of FRP-strengthened RC structures. A two-dimensional non-linear finite element computer program was developed by Shahawy et al. (1996) for analyzing beams reinforced with CFRP. Moreover, Nitereka and Neale (1999) predicted the full load-deformation response of RC beams reinforced in flexure with FRP composites. For that purpose, the researchers have developed a nonlinear finite element layered model in which both material and geometric nonlinearities are considered. The numerical results obtained from this model have reflected the effectiveness of FRP laminates when used as external reinforcement against flexure in RC beams. Ferreira et al. (2001) have developed a finite element model for analyzing RC beams that are internally-reinforced with FRP rebars. The first order shear deformation theory was used in the analysis of concrete shells reinforced with internal unidirectional FRP rebars. The concrete was modelled using smeared crack approach, while the compressive response of concrete was analyzed by a perfect plastic and a strain-hardening plasticity approach. A dual criterion for yielding and crushing in terms of stresses and strains were adopted. The effect of cracked concrete zone was considered in the analysis of concrete under tension. The tensile response of concrete was assumed to be linear elastic until the fracture of surface is reached. Post-cracking behaviour was idealized by the sudden and total release of normal stresses in the affected directions, or its gradual relaxation according to the tension-stiffening diagram. Cracking in two principal stress directions in the plane of structure was considered in this model. On the other hand, the reinforcing bars were modelled as layers of equivalent thickness, with strength and stiffness in the bar direction only. Finally, the finite element was applied in the degenerated shell element by considering the modelling techniques mentioned before. The numerical results of the model were then validated against experimental data of simply supported RC beams strengthened with FRP rebars. The predictions of the proposed finite element model were found in a good agreement with the actual beam data. Supaviriyakit et al. (2004) proposed a finite element model to predict

the behaviour of RC beams strengthened with externally bonded FRP plates. The concrete and steel reinforcement were modelled by 8-node 2D isoparametric plane stress elements. In this model, the effect of cracks and reinforcing steel was smeared over the entire element. In addition, perfect compatibility was considered between cracked concrete and steel reinforcement. The FRP composite plate was modelled as a 2D elasto-brittle element. A full compatibility between the concrete and the FRP plates was assumed due to the expected higher strength of bonding agents such epoxies. The numerical predictions of the model were then verified against some experimental data. In this analysis, load-deformation, load capacity, and failure mode of FRP-strengthened beams were recoded. Hu et al. (2004) presented a finite element model to analyze nonlinear response of FRP-strengthened concrete beams using ABAQUS software. The authors relied on the constitutive models available in the material library of ABAQUS program to simulate the nonlinear behaviour of concrete and reinforcing steel. Nonetheless, the nonlinearity of FRP composites was introduced to the ABAQUS model as an external subroutine. The nonlinear in-plane shear behaviour was simulated by the nonlinear stress-strain relation for composite lamina proposed by Hahn and Tsai (1973). Moreover, perfect bond was assumed between the concrete and the FRP in this model. Finally, the numerical results were verified against experimental data of similar FRP-strengthened RC beams.

2.13 Nonlinear Fracture Mechanics of Concrete

Fracture mechanics can be simply defined as the study of the response and failure process in structures as a result of crack onset and growth. This branch of science is effectively used in concrete structures to predict and evaluate various crack patterns and damaging effects on these structures (Shi, 2009). The subsequent sections covers the cracking process of concrete, and place an emphasis on the fracture energy and tension-softening laws which will be adopted in the finite element model proposed in this research. Moreover, plasticity of concrete is reviewed to introduce some of the crucial parameters related to modelling the concrete section.

2.13.1 Cracking of Concrete

Concrete is a heterogeneous material that comprises of cement, fine aggregate, coarse aggregate, water, and sometimes admixtures and supplementary cementitious materials. In another word, concrete consists of two main composites: cement matrix and aggregates. Therefore, the interface between the two composites is seen as the most susceptible environmental for cracks to occur due to bleeding or segregation of fresh concrete. Shrinkage of hardening concrete can also cause non-uniform distribution of strains and hence cracking of concrete materials. These internal cracks in concrete, which occurs before loading, govern the mechanical behaviour of the entire concrete structure (Shah, et al., 1995).

The concrete response under uniaxial tension loading was broadly examined by several researchers, including Hughes and Chapman (1966) and Evan and Marathe (1968). The data collected from these tests were used to set the fundamental concepts of concrete fracture mechanics.

Moreover, Li et al. (1993) have performed several uniaxial tension tests on concrete plates. The displacements in each specimen were measured by four linear variable differential transducers (LVDTs) positioned symmetrically on each plate as shown in Figure 2.34(a). While Figure 2.34(b) depicts the displacements measured by each LVDT, Figure 2.34(c) shows the stress-displacement curves for LVDT-3 and LVDT-4.

From the last two figures, four distinct regions of crack growth can be specified. The first stage is identified by point A, and in which negligible internal cracks were observed by the four LVDTs. However, disparities in the displacements recorded by each LVDT were found in the second stage, between point A and point B. This change reflects the initiation of internal cracks, which in turn are isolated and uniformly-distributed. In stage three, between point B and point C, some internal cracks were observed by LVDT-4, and translated as an increase of displacement rate experienced by LVDT-4. This stage sets the limit for damage localization (also known as strain localization) and internal micro-cracks propagation. Finally, stage four is identified at the region beyond the peak load at point C. At this stage the displacement in LVDT-4 continues to increase while the displacements of all other LVDTs decreases. This can be attributed to the instability of major cracks even after decreasing the applied load. In

summary, the discussed phenomena reflects the typical concrete response under tension. The concrete specimen is expected to experience strain localization before the peak load is reached, which triggers the initiation of a major crack. In addition, strain-softening response is also observed as this major crack propagates and the loading decreases (Shah, et al., 1995).

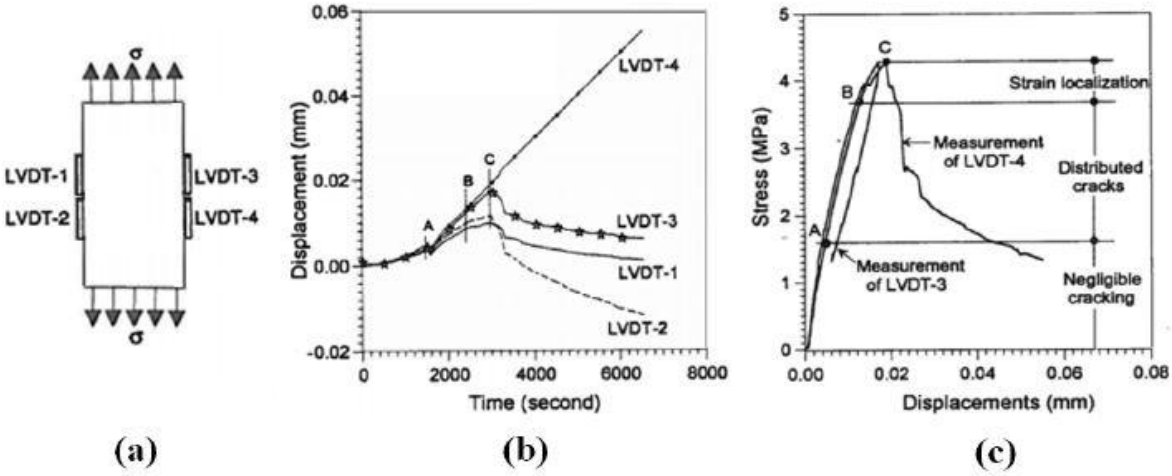

Figure 2.34: Testing of concrete plates under uniaxial tension (Shah, et al., 1995)

2.13.2 Fracture Process Zone

According to the linear elastic theory in fracture mechanics, the stress usually approaches an infinite value at the crack tip. However, this phenomenon is realistically unacceptable, and hence an inelastic zone must exist at the crack tip. When analyzing the structure numerically using discrete crack approach, the inelastic zone around the crack tip is referred to as the Fracture Process Zone (FPZ). The latter is classified as a tension zone which is formed ahead of the pre-existing crack tip and experiences various toughening mechanisms as the crack grows. Figure 2.35 illustrates these mechanisms which include: (a) micro-crack shielding; (b) crack deflection; (c) aggregate bridging; (d) cracked surface interlock; (e) crack tip blunting; (f) crack branching.

Micro-crack shielding is characterized by the formation of micro-cracks at weak spots close to the crack tip which causes high stress state. Crack deflection refers to the mechanism of altering crack path around large aggregate or along weak interface. While, aggregate bridging takes

place when a crack has moved beyond an aggregate that continues to carry stress across the crack. Crack surface interlock is defined as the friction that occurs between two cracked faces which results in energy dissipation. Crack tip blunting is when a crack tip is terminated by an internal void, resulting in a blunted crack tip which in turn requires a large amount of energy to propagate. Finally, crack branching occurs when a crack grows into multiple branches, and hence more energy is needed in this mechanism (Shah, et al., 1995).

It can be concluded that the FPZ consumes a noticeable amount of energy from the applied external loads, and hence the propagation of cracks is somewhat stable before reaching the peak load. Moreover, the toughening mechanisms associated with FPZ are the main factor in creating the quasi-brittle response of concrete after peak load. While, brittle materials are linear elastic up to the peak stress followed by a catastrophic and complete loss of strength, quasi-brittle materials behave nonlinearly before the peak load, followed by strain softening. Nevertheless, some crack surfaces might still maintain some contact, and thus mechanisms such as friction and aggregate interlock could restrain brittle failure after peak load and lead to a more gradual and softening response. In summary, due to the existence of such complex mechanisms in cracked concrete, the use of nonlinear fracture mechanics approach seems more appropriate than linear elastic response (Shah, et al., 1995).

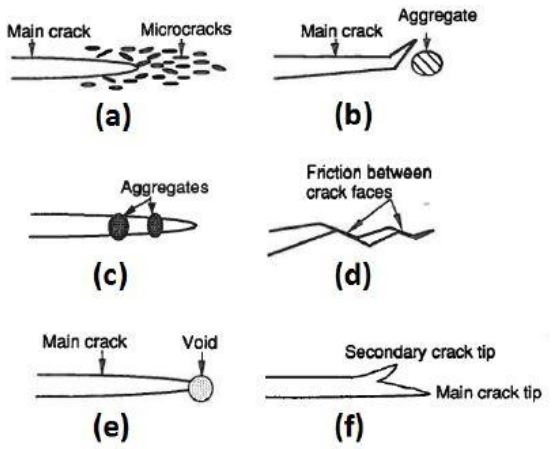

Figure 2.35: Toughening mechanisms of Fracture Process Zone (Shah, et al., 1995)

2.13.3 Fictitious Crack Model

One of the drawbacks of the Fracture Process Zone (FPZ) is that it cannot be classified as a continuous region nor as a discontinuous region, which imposes an analytical challenge to the modelling of concrete fracture. Furthermore, this region is seen as a partially damaged zone that retains some stress transfer capability through the toughening mechanisms discussed previously. This region is characterized as a transition zone between the open crack which is completely discontinuous and the intact concrete composite that is completely continuous. Many researchers have suggested that concrete fracture occurs in this region, and thus the analysis of cracking requires a comprehensive modelling of the FPZ (Shah, et al., 1995). Hillerborg et al. (1976) is one of the first pioneers in proposing a nonlinear theory of fracture mechanics in the form of the Fictitious Crack Model (FCM). In this approach, the FPZ is modelled as a fictitious crack that extends beyond the physical, traction free, crack. This fictitious crack is subjected to closure stresses, $\sigma(w)$, as seen in Figure 2.36 (Karihaloo, 2003).

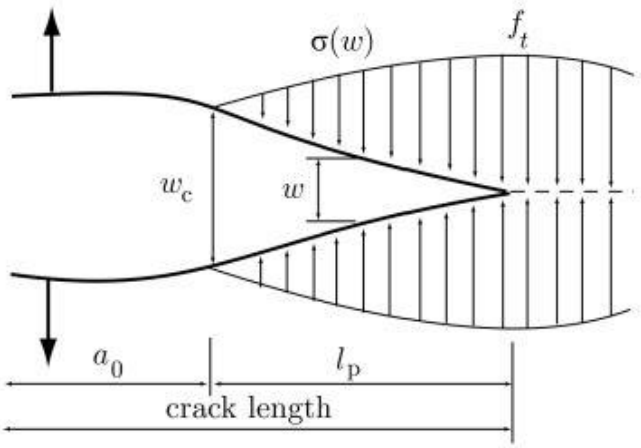

Figure 2.36: Fictitious Crack Model (Malm, 2006)

From Figure 2.36, a_o represents the length of the open crack; l_p is the length of the fracture process zone (FPZ); and w is the crack-opening-displacement within the FPZ. Moreover, the closure stresses (also known as the cohesion stresses) is not constant and varies with the crack-opening-displacement. The closure stresses are equal to zero at the tip of the pre-existing open crack, which is also the location of the critical crack-opening-displacement, w_c. These stresses

tend to increase until it reaches the ultimate uniaxial tensile strength of the materials, f_t, at the location of the fictitious crack tip (extent of the FPZ). The tension softening behaviour within the FPZ is well depicted in Figure 2.37. Region AB represents the fraction of the load-deflection curve prior to peak load. The concrete in this region exhibits micro-cracking but is not yet subjected to the fracture process zone. Within the post-peak region, BC, the presence of toughening mechanisms in the FPZ induces closure stresses that are a function of the crack-opening-displacement, w. The crack-opening-displacements continues to develop until it reaches point D, where stress is equal to zero and crack-opening-displacement has reached the critical value, w_c (Stoner, 2015).

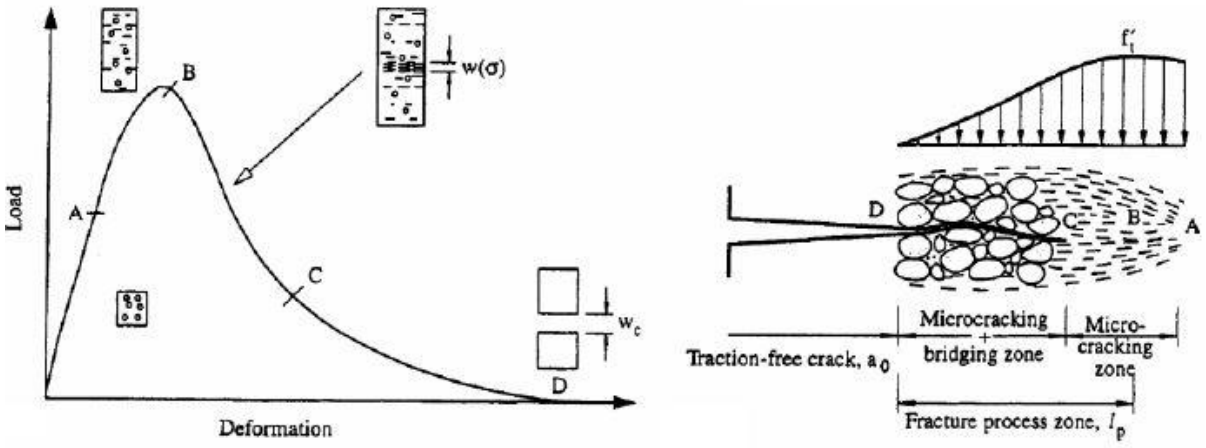

Figure 2.37: Tension softening response within the FPZ (Karihaloo, 2003)

2.13.4 Tension Softening

It is noted that some regions of a concrete specimen subjected to tension exhibit strain localization at ultimate load. While other portions of that concrete section experience unloading. Figure 2.38(a) illustrates a generalized stress-deformation response of a concrete member subjected to tension.

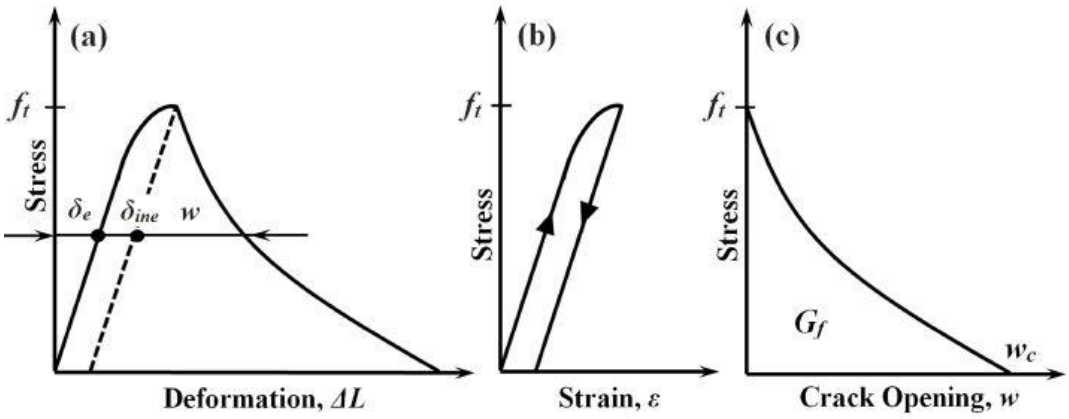

Figure 2.38: Derivation of fracture energy (Shah, et al., 1995)

However, the total change in a member's length can be calculated using the following equation:

$$\Delta L = \delta_e + \delta_{ine} + w \qquad (2\text{–}34)$$

where δ_e is the elastic deformation, δ_{ine} is the inelastic deformation, and w is the crack-opening-displacement of the fictitious crack (Shah, et al., 1995). Figure 2.38(b) shows a typical stress-strain behaviour of an uncracked concrete member, and thus the unloading at the peak point follows a linear-elastic pattern. However, Figure 2.38(c) represents the stress-elongation response for the additional deformation, w, within the damage section (Hillerborg, 1985). It is also observed that the area under the stress-deformation curve in Figure 2.38(c) refers to the energy that is absorbed by the damaged concrete. In another word, this parameter represents the energy needed to overcome some of the resistance of different toughening mechanisms and hence initiate a crack of unit area. This quantity is known as the Mode-I fracture energy, or simply the fracture energy G_f. The following formula depicts the mathematical description of the relationship between the stress-elongation response and the fracture energy:

$$G_f = \int_0^{w_c} \sigma(w)dw \qquad (2\text{–}35)$$

where w_c is the critical crack-opening-displacement when the softening stress is equal to zero. As it is shown in Figure 2.38(c), the tensile stress decreases as the crack-opening-displacement increases, and this phenomenon is referred to as the tension-softening law. This law is used to

characterize the tensile response within the fracture process zone, $\sigma(w)$, and the fracture energy, G_f. These two parameters are material properties and considered independent of structural shape or size (Shah, et al., 1995). The softening curve, $\sigma(w)$, requires only three parameters to be drawn: the ultimate tensile strength of the material, f_t, the fracture energy, G_f, and the shape of the curve. Figure 2.39 depicts some of the common shapes of the softening curves proposed by many scholars, including linear, bilinear, and exponential relationships (Stoner, 2015).

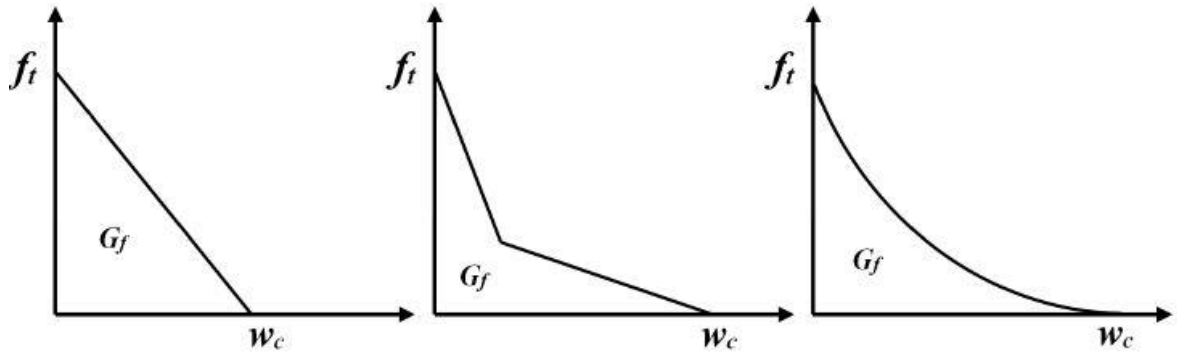

Figure 2.39: Different tension-softening relationships (Stoner, 2015)

2.14 Plasticity Theory

Plasticity is a tool for describing the behaviour of ductile materials that experience permanent deformations. Nevertheless, plasticity theory can also be used in finite element analysis of brittle behaviour. Originally, plasticity theory is developed to model metals which undergo different mechanisms of deformation compared to conventional concrete. However, concrete experiences a nonlinear stress-strain behaviour during loading and exhibits a noticeable irrecoverable strain when it is unloaded (Hany, et al., 2016). Concrete also shows some ductility under compression loading and confining pressure. Therefore, the theory of plasticity is considered a suitable tool to model that type of behaviour in concrete composites (Chen & Han, 1988).

It ought to be noted that when tension is present, such as shear in reinforced concrete structures, plasticity theory is usually employed in the compression zone. On the other hand, regions subjected to tensile stresses are treated with one of the different versions of fracture mechanics (Lubliner, et al., 1989). However, there are three main components of any plasticity model: Initial yield criterion, Hardening/softening rule, and Flow rule. The plasticity models that have been proposed by several researchers might vary in terms of the shape of the yield surface, the hardening/softening rules and the flow rule used in each model.

2.14.1 Initial Yield Criterion

It has been concluded by various biaxial tests on concrete that different critical surfaces in stress spaces are similar. A large volumetric change is expected in concrete members that are subjected to enormous inelastic states. Figure 2.40(a) reflects an increase in volume which is more than twice as large for the hydrostatic compressive stress state (shown as $\sigma_1/\sigma_2 = -1/-1$) as for uniaxial compression ($\sigma_1/\sigma_2 = -1/0$). The bold points on each curve in Figure 2.40(a) represents the limit of elasticity, the point of inflection in the volumetric strain, the point of strain localization, and the ultimate load. While in Figure 2.40(b) the depicted critical surfaces of these material states reflect the onset of the expansion of failure surface. In another word, the amount of concrete strength from the point it entered the plasticity zone until the level of ultimate capacity (Karihaloo, 2003).

The initial yield surface can be simply defined as the limit of elastic response and the onset of plastic behaviour. Therefore, when the applied stresses are within the initial yield surface, the material is said to behave in a linear-elastic manner. However, if those stresses exceeded the initial yield surface, the material would be described as plastic and new yield surface is developed. This new created surface replaces the initial yield surface and is called a loading surface. If the additional stresses remain within this new loading surface, no additional plastic deformations are expected. Conversely, if the loading is increased beyond the loading surface, another new loading surface will develop, and the material will exhibit an increase in plastic strain (Chen & Han, 1988). Consequently, the subsequent loading surfaces are counted as yield functions for the deformed material.

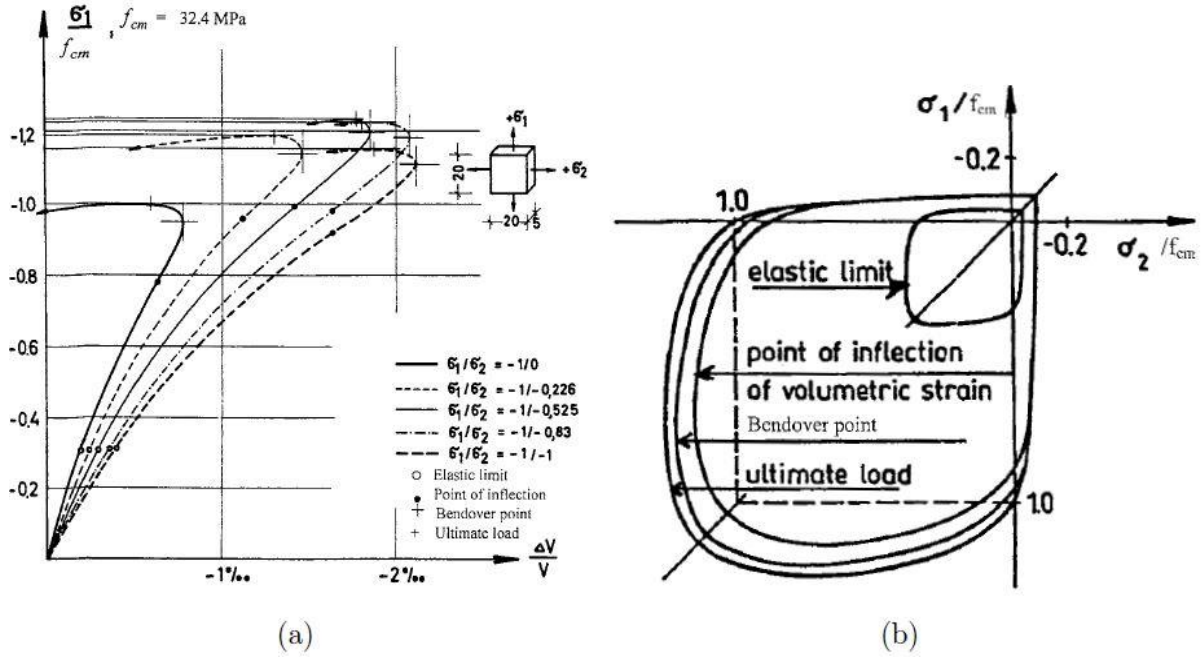

Figure 2.40: (a) Volumetric strain in biaxial compression; (b) Loading curves under biaxial stresses (Karihaloo, 2003)

There has been a significant progress in the field of material plasticity and the constitutive models of concrete. Many yield criterions can be found in recent literature, and some of the commonly used models are presented in Figure 2.41. The von Mises failure criterion, shown in Figure 2.41(a), is most suitable for steel materials. However, the yield criterion often used for concrete are the Drucker-Prager and Mohr-Coulomb criteria (see Figure 2.41(b) and (c), respectively). Nevertheless, Lubliner et al. (1989) suggested that these failure models do not represent the experimental results for concrete efficiently unless appropriately modified. For instance, one effective modification would be the use of a combination of the Mohr-Coulomb and the Drucker-Prager yield functions, where the latter is used for biaxial compression and former is more suitable for other stress states. Moreover, a modified hyperbolic Drucker-Prager yield criterion is proposed by Lubliner et al. (1989), and has been vastly implemented in ABAQUS software package.

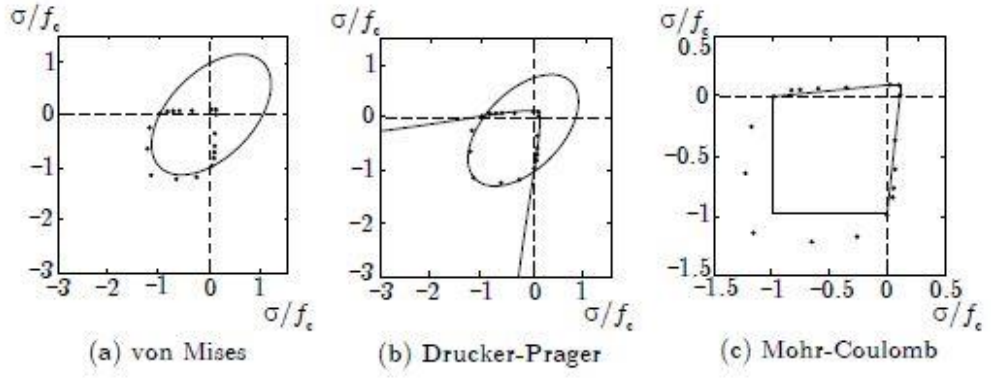

Figure 2.41: Yield criteria for biaxial stress state (Jirasek & Bazant, 2002)

2.14.2 Hardening

The strain parameter in plasticity-based models is usually comprised of an elastic part and plastic part. Moreover, the dependence of material strain on its load history is characterized in plasticity theory by the use of internal scalar variable, here defined as k. This internal variable reflects the irreversible material behaviour and its evolution is evaluated by means of rate equations which are functions of the plastic strain rate: $dk = f(d\varepsilon^p)$. Nevertheless, the scalar hardening variable, k, is obtained by integrating the hardening parameter along the loading path in both the work-hardening and strain-hardening hypotheses. The hardening rule is mainly used to define the expansion of the subsequent yield surfaces during plastic loading. The yield condition usually presents the concept of yield stress as multi axial stress states and includes the history dependence through the scalar hardening variable. Therefore, the dependence of yield function on the loading history through the hardening variable, k, permits this function to only expand or shrink in the stress space, and not translate or rotate. Such hardening is called "isotropic hardening", in the case of using work-hardening or strain-hardening theory. As can be seen in Figure 2.42, the direction of the plastic strain tensor, $d\varepsilon^p$, is determined from the derivative of the plastic potential function (Karihaloo, 2003).

Isotropic hardening is usually adopted in models where plastic deformation exceeds initial yield state and the Bauschinger effect is insignificant. The Bauschinger effect refers to one particular type of directional anisotropy generated by plastic deformation. In another word, the

initial plastic deformation of one sign reduces the resistance of the materials when subjected to a subsequent plastic deformation in the opposite sign. To elaborate further, when a rode is stretched beyond its yield strength in tension, plastic deformation will be recorded. However, subsequent compressive stresses applied to the same rod will result in a significantly lower compressive yield value than the initial tensile yield point due to Bauschinger effect.

It is rather convenient to use the isotropic hardening theory in materials where large plastic strain is expected and in which the plastic strain rate does not continuously reverse direction sharply. Therefore, this theory is intended for problems involving essentially monotonic and proportional loading. On the other hand, in "kinematic hardening" approach the yield surface translates as a rigid body in the stress space, without changing shape, size, or orientation of the initial yield surface. Thus, kinematic hardening approach is usually employed in materials that are subjected to cyclic and reversed cyclic loading with a present Bauschinger effect (Chen, 1982). In the third type of hardening rule, known as "independent hardening", the hardening in compression is independent of that in tension. This rule is more effective in modelling hardening effect in concrete, and is a combination of the both isotropic and kinematic hardening rules (Chen & Han, 1988). It must be noted that the independent hardening rule is implemented in the plasticity model used by ABAQUS.

2.14.3 Flow Rule

As discussed in the previous section, the hardening rule can be used to define the shape of the yield surface at any given loading condition. The relationship between the yield surface and the stress-strain curve is determined with a flow rule.

Concrete undergoes enormous volumetric changes under large inelastic stress states. This change in volume, resulted from plastic deformation, is referred to as "dilation" and can be reproduced by using an adequate plastic potential function, G (Lubliner, et al., 1989). The evolution of the inelastic displacements in the fracture process zone is defined through the flow rule which can be expressed by the following equation:

$$d\varepsilon^p = dk\frac{\partial G}{\partial \sigma} \qquad (2\text{–}36)$$

where dk is a scalar hardening parameter which varies throughout the straining process. This parameter uses positive values, and is nonzero only when plastic deformations occur. The gradient of the potential surface, $\frac{\partial G}{\partial \sigma}$, defines the direction of the plastic strain increment vector, $d\varepsilon^p$, and the hardening parameter, dk, determines the length (Chen & Han, 1988).

When the plastic potential function shares the same shape as the yield surface, the flow is classified as "associated flow rule" (i.e. the plastic flow is connected with the yield criterion). If the associated rule is used, the plastic flow develops along the normal to the loading surface. However, the "non-associated flow rule" refers to the approach of using two separate functions, one of the plastic flow and the other for the yield surface. In this rule the plastic flow develops along the normal to the plastic flow potential and not to the yield surface (Galvez, et al., 2002). Figure 2.42 depicts an example of a plastic potential function known as Drucker-Prager hyperbolic function. This figure also illustrates the hardening process through the scalar hardening parameter. Finally, the Drucker-Prager hyperbolic plastic potential function is utilized in modelling concrete material through damaged plasticity model in ABAQUS.

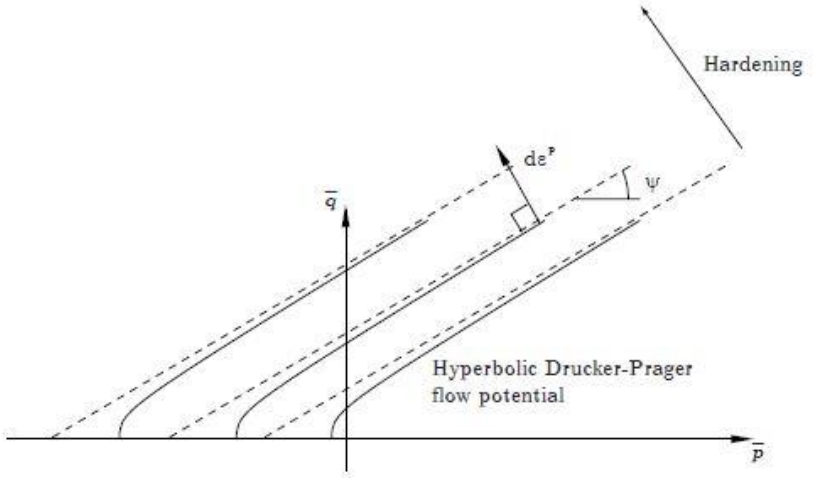

Figure 2.42: The Drucker-Prager hyperbolic function (Hibbitt, et al., 2004)

Chapter Three

Numerical Formulation

3.1 Introduction

It is now a common practice to strengthen the vulnerable faces of reinforced concrete beams with external FRP materials in order to increase the load-carrying capacity of the structure. As it has been previously discussed, extensive research was conducted on the application of FRP composites in RC beams. However, most of these studies have been experimentally based and only a very limited amount of research is available on the numerical modelling of such beams. Structural members such as reinforced concrete beams externally bonded with FRP are classified as heterogeneous composite structures. This type of members usually comprises of three major components: concrete, steel reinforcement, and FRP materials. The composite nature of such structures imposes an enormous nonlinear analysis challenge due to the expected extensive cracking, local effects, and failure modes. There has been several research attempts to overcome this issue and reach a reliable modelling methodology. One common approach is to model each of the components individually by using a suitable numerical method, and then obtain their combined effects by imposing the condition of material continuity. In another word, a complete analysis typically involves selecting an appropriate numerical method, modelling each material using the relative constitutive laws, and finally modelling the interaction between the composite materials.

There are various methods which can be used to analyse the behaviour of a reinforced concrete structural element and investigate the internal forces and displacements in the member. The following section highlights some of the common methods available in literature.

3.2 Methods of Analysis

Structural analysis is typically performed for any given structure to evaluate local effects such as internal forces or stresses, or global effects which involve displacements and reactions. For this analysis to function properly and produce decent results, well defined geometry, material properties, and boundary conditions of the studied member have to be provided. There are three analysis methods which are commonly used by researchers: empirical, analytical, and numerical. Although empirical investigations make up the majority of data compiled on FRP-strengthened RC beams, there are some shortcomings related to the feasibility of testing large-scale specimens and being very expensive and time-consuming. Conversely, analytical methods are generally used to model simple elements due to the difficulty of reproducing the boundary conditions and any geometry limitations. Additionally, most of the analytical methods used to model the interfacial bond between FRP and concrete assumed linear approach and are not reliable in nonlinear settings (Li & Chua, 2009). Therefore, many complex engineering problems cannot be analyzed using the last two methods, and more practical analysis is usually carried out using numerical approaches. This method involves breaking down a structure (domain) into smaller pieces (sub-domains). The common numerical solution techniques are provided in the coming sections.

3.2.1 Finite Difference Method (FDM)

This method generally involves breaking the structure into nodal regions and the governing equations are replaced by finite difference equations, then these equations are solved simultaneously to obtain a solution. However, some of the major drawbacks of this method are that it is impractical to apply the procedure to structures with complicated geometries, boundary conditions, and problems of fast changing variables as in the case of stress concentration. Therefore, this technique is more suitable for problems where heat transfer and fluid flow are to be studied.

3.2.2 Boundary Element Method (BEM)

As implied by the method's name, elements are only formed on the boundary of the structure. The method applies Green's theorem as the response of the differential equation to determine quantities of interest such as displacements and stresses within the closed boundary. Despite the efficiency of this method in terms of computation, large matrices are sometimes expected which makes the techniques difficult to use in nonlinear problems and structures with non-homogeneous media.

3.2.3 Finite Element Method (FEM)

This method is based on the laws of mechanics, and depending on the nature of the problem, it can be associated with solid or structural mechanics, fluid mechanics, or thermomechanics. The modelling procedure of the finite element analysis can be simply described as a loop. The first step involves modelling the physical problem numerically by using the appropriate differential equations (also known as shape functions) to create the finite element model that is a close representation of the structure. Loads are then applied to the model and displacements are quantified at the nodes, followed by stress and strain analyses of the system. The results obtained from this numerical modelling is validated against real data. Based on the review of the analysis results, the numerical model might need further refinement and improvement, and the system is reanalyzed for the same applied loads. Another review of the results is performed, and more refinement might be required until the results closely reflect the experimental response of the system under similar loading conditions.

In summary, the finite element method involves the choice of elements (such as truss, beam, 2D or 3D continuum), mesh, and boundary conditions. The combined solutions of all the elements form the solution of the entire part. This method is typically utilized to analyse structures with complex features and various material properties. It also offers an effective analytical tool for studying structural behaviour of reinforced concrete members. Cracking, tension stiffening, nonlinear material properties, interface behaviour, and other mechanisms that are ignored or treated approximately by other numerical methods can be modelled rationally using finite element method. Nevertheless, the reliability of this method relies on the

accuracy of the original model and the degree of agreements between the numerical results and the actual data from the prototype structure (Monteleone, 2008). Finally, the tremendous advantages of this technique made it the method of choice in the numerical analysis segment of this research study.

3.3 Finite Element Procedure

The principal characteristics of a finite element are embodied in the element "stiffness matrix". For a structural finite element, the stiffness matrix comprises the geometric and material behaviour information that defines the element resistance to deformation when subjected to external loading. These deformations may include axial bending, shear, and torsional effects. On the other hand, in finite elements used in non-structural analyses, such as fluid flow and heat transfer, the stiffness matrix is also used, since the matrix reflects the resistance of the element to change when external effects are present (Hutton, 2004).

In the early applications of finite element method, and without the benefit of modern computers, force analysis was used to develop the matrix in what is called "flexibility method". In this procedure, the unknowns are the forces and the knowns are displacements. However, the finite element method often corresponds to the "displacement method", in which the unknowns are system displacements in response to applied loads. The structural stiffness matrix typically takes the form:

$$[K]\{U\} = \{F\} \qquad (3\text{–}1)$$

where $[K]$ is the assembled global stiffness matrix, $\{U\}$ is the vector of global displacement, and $\{F\}$ is the vector of applied nodal forces. These forces may include directly applied external forces at nodes, the work-equivalent nodal forces attributed to body forces and pressure forces applied on element faces.

After calculating the displacements, stress and strain can be evaluated for the entire structure. As indicated previously, the equations involved in the analysis are derived from the related

structural theory and stratify the following conditions: equilibrium (relate stress to applied forces), compatibility (strains to displacement), and constitutive equations (stresses to strains). Shape functions (also knowns as interpolation functions) are utilized to formulate finite element equations for different types of physical problems in one, two, or three dimensions. These functions are created through the use of Lagrangian interpolation in order to relate the local coordinate position to global coordinate position.

3.3.1 Eight-Node Brick Element

The most common element used in three-dimensional finite element modelling is the eight-node brick element (rectangular parellopiped) shown in Figure 3.1. The global Cartesian coordinates in this element are transformed to the natural (serendipity) coordinate system by the following in order to simplify the derivation of the shape functions:

$$r = \frac{x - \bar{x}}{a} \qquad (3\text{–}2)$$

$$s = \frac{y - \bar{y}}{b} \qquad (3\text{–}3)$$

$$t = \frac{z - \bar{z}}{c} \qquad (3\text{–}4)$$

where $2a$, $2b$, and $2c$ are the dimensions of the element in the x, y, z, coordinates, respectively, and the $\bar{x}$, $\bar{y}$, and $\bar{z}$ are the centroids of the element. The natural coordinates varies between -1 and +1 over the domain of the element.

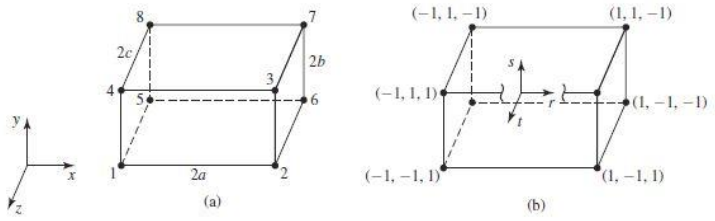

Figure 3.1: Eight-node brick element: (a) Global Cartesian coordinates; (b) Natural coordinates with an origin at the centroid (Hutton, 2004)

The eight shape functions are necessary to express the three directions of displacements as a function of the eight nodes when 3D modelling is used. These eight interpolation functions are defined in the forms:

$$N_1 = \frac{1}{8}(1-r)(1-s)(1+t) \quad (3\text{–}5)$$

$$N_2 = \frac{1}{8}(1+r)(1-s)(1+t) \quad (3\text{–}6)$$

$$N_3 = \frac{1}{8}(1+r)(1+s)(1+t) \quad (3\text{–}7)$$

$$N_4 = \frac{1}{8}(1-r)(1+s)(1+t) \quad (3\text{–}8)$$

$$N_5 = \frac{1}{8}(1-r)(1-s)(1-t) \quad (3\text{–}9)$$

$$N_6 = \frac{1}{8}(1+r)(1-s)(1-t) \quad (3\text{–}10)$$

$$N_7 = \frac{1}{8}(1+r)(1+s)(1-t) \quad (3\text{–}11)$$

$$N_8 = \frac{1}{8}(1-r)(1+s)(1-t) \quad (3\text{–}12)$$

and the field variable (such as displacement) is described by:

$$\emptyset(x,y,x) = \sum_{i=1}^{8} N_i(r,s,t)\emptyset_i \quad (3\text{–}13)$$

where $\emptyset$ corresponds to the global displacement in three dimensions, N_i and $\emptyset_i$ are the nodal shape function and displacement, respectively.

3.3.2 Finite Element Formulation for General 3D Stress Elements

Although the conditions of plane stress, plane strain, and axisymmetry are frequently met, sometimes the geometry of a structure and the applied loads are such that a three-dimensional state of stress is present. Generally, there are three displacement components in that case: *u*, v, and *w* in the directions of *x*, *y*, and *z* axes, respectively. The six components of strain are derived from simple solid mechanics rules and given by:

$$\{\varepsilon\} = \begin{Bmatrix} \varepsilon_x \\ \varepsilon_y \\ \varepsilon_z \\ \gamma_{xy} \\ \gamma_{xz} \\ \gamma_{yz} \end{Bmatrix} = \begin{Bmatrix} \dfrac{\partial u}{\partial x} \\ \dfrac{\partial v}{\partial y} \\ \dfrac{\partial w}{\partial z} \\ \dfrac{\partial u}{\partial y} + \dfrac{\partial v}{\partial x} \\ \dfrac{\partial u}{\partial z} + \dfrac{\partial w}{\partial x} \\ \dfrac{\partial v}{\partial z} + \dfrac{\partial w}{\partial y} \end{Bmatrix} \qquad (3\text{–}14)$$

For convenience, the strain-displacement relations in the previous equation can be expressed as:

$$\{\varepsilon\} = \begin{bmatrix} \dfrac{\partial}{\partial x} & 0 & 0 \\ 0 & \dfrac{\partial}{\partial y} & 0 \\ 0 & 0 & \dfrac{\partial}{\partial z} \\ \dfrac{\partial}{\partial y} & \dfrac{\partial}{\partial x} & 0 \\ \dfrac{\partial}{\partial z} & 0 & \dfrac{\partial}{\partial x} \\ 0 & \dfrac{\partial}{\partial z} & \dfrac{\partial}{\partial y} \end{bmatrix} \begin{Bmatrix} u \\ v \\ w \end{Bmatrix} = [L] \begin{Bmatrix} u \\ v \\ w \end{Bmatrix} \qquad (3\text{–}15)$$

and matrix $[L]$ is the 6×3 matrix of derivative operators.

The stress-strain relation is expressed in matrix form as:

$$\{\sigma\} = \begin{Bmatrix} \sigma_x \\ \sigma_y \\ \sigma_z \\ \tau_{xy} \\ \tau_{xz} \\ \tau_{yz} \end{Bmatrix}$$

$$= \frac{E}{(1+v)(1-2v)} \begin{bmatrix} 1-v & v & v & 0 & 0 & 0 \\ v & 1-v & v & 0 & 0 & 0 \\ v & v & 1-v & 0 & 0 & 0 \\ 0 & 0 & 0 & \frac{1-2v}{2} & 0 & 0 \\ 0 & 0 & 0 & 0 & \frac{1-2v}{2} & 0 \\ 0 & 0 & 0 & 0 & 0 & \frac{1-2v}{2} \end{bmatrix} \{\varepsilon\} \quad (3\text{–}16)$$

and for simplicity, σ, can be shown as:

$$\{\sigma\} = [D]\{\varepsilon\} \quad (3\text{–}17)$$

where $[D]$ corresponds to the material property matrix, and for the general case, it is a 6×6 matrix involving only the elastic modulus, E, and Poisson's ratio, v (Hutton, 2004).

For three-dimensional elastic element having M nodes, the displacement components discretized as:

$$u(x,y,z) = \sum_{i=1}^{M} N_i(x,y,z)u_i \quad (3\text{–}18)$$

$$v(x,y,z) = \sum_{i=1}^{M} N_i(x,y,z)v_i \quad (3\text{–}19)$$

$$w(x,y,z) = \sum_{i=1}^{M} N_i(x,y,z)w_i \quad (3\text{–}20)$$

where u_i, v_i, and w_i are the Cartesian nodal displacement, and $N_i(x,y,z)$ is the interpolation function associated with node i.

Moreover, for a general three-dimensional element with any element shape or number of nodes, the discretized displacement field can be written in matrix form as:

$$\begin{Bmatrix} u \\ v \\ w \end{Bmatrix} = \begin{bmatrix} [N] & 0 & 0 \\ 0 & [N] & 0 \\ 0 & 0 & [N] \end{bmatrix} \{\delta\} = [N_3]\{\delta\} \qquad (3\text{–}21)$$

In the last equation, each submatrix is $[N]$ is the $1 \times M$ row matrix of interpolation functions (depending on the choice of element shape and number of nodes). So, the matrix $[N_3]$ is a $3 \times 3M$ matrix composed of the interpolation functions and many zero values.

Finally, the total potential energy theorem can be utilized to construct the stress-displacement relation for any given three-dimensional element. The total potential energy of an element can be expressed as:

$$\Pi = U_e - W = \frac{1}{2} \iiint_V \{\varepsilon\}^T [D]\{\varepsilon\} dV - \{\delta\}^T \{f\} \qquad (3\text{–}22)$$

where U_e is the elastic energy (strain energy), and W is the mechanical work of a conservative force which is considered to be a loss in potential energy. The strain-displacement matrix is given by the relation below, and is observed to be a $6 \times 3M$ matrix composed of the first partial derivatives of the interpolation functions.

$$[B] = [L][N_3] = \begin{bmatrix} \frac{\partial}{\partial x} & 0 & 0 \\ 0 & \frac{\partial}{\partial y} & 0 \\ 0 & 0 & \frac{\partial}{\partial z} \\ \frac{\partial}{\partial y} & \frac{\partial}{\partial x} & 0 \\ \frac{\partial}{\partial z} & 0 & \frac{\partial}{\partial x} \\ 0 & \frac{\partial}{\partial z} & \frac{\partial}{\partial y} \end{bmatrix} \begin{bmatrix} [N] & 0 & 0 \\ 0 & [N] & 0 \\ 0 & 0 & [N] \end{bmatrix} \qquad (3\text{–}23)$$

In order to simplify the stress-displacement relation further, and after applying the principle of minimum potential energy ($\frac{\partial \Pi}{\partial U_i} = 0$), the following form is obtained:

$$\iiint_V \{B\}^T [D]\{B\} dV \{\delta\} = \{f\} \qquad (3\text{–}24)$$

From the above equation, we identify the element stiffness matrix as below

$$[k] = \iiint_V \{B\}^T [D]\{B\} dV \qquad (3\text{–}25)$$

The element stiffness matrix is defined as a $3M \times 3M$ symmetric matrix, as expected for a linear elastic element (Hutton, 2004). Moreover, the integration in these equations depend on the specific element type in question. If an eight-node brick element is to be used, the interpolation functions, mentioned earlier, are such that strains vary linearly and the integrands in the stiffness matrix are not constant. The integrands are polynomials in the spatial variables, and hence numerical integration is performed (e.g. Gaussian quadrature in three dimensions). The stress and strain components can be computed as secondary (post-processing) phase of the analysis. The calculation of these parameters becomes a simple task, once the unknown nodal displacements are determined by the stiffness method which was previously elaborated. The strain components at each node in the model are discretized in the finite element form:

$$\{\varepsilon\} = [L] \begin{Bmatrix} u \\ v \\ w \end{Bmatrix} = [L][N_3]\{\delta\} = [B]\{\delta\} \qquad (3\text{–}26)$$

It must be noted that the strain component calculated in the above equation corresponds to an individual element and must be carried out for every element on the finite element model. On the other hand, the stress components are identified in the same manner, and the matrix form is as follow:

$$\{\sigma\} = [D][B]\{\delta\} \qquad (3\text{–}27)$$

and the material property matrix $[D]$ depends on the state of the stress (i.e. plane stress, plane strain, or axisymmetric).

3.4 Finite Element Analysis Software (ABAQUS)

There are many commercially available software packages that are used for finite element analysis of reinforced concrete structures. Some of which includes: ADINA (Automatic Dynamic Incremental Nonlinear Analysis) developed by ADINA R&D Inc., and is mainly used for modelling fluid structure interactions, heat transfer and also linear and nonlinear structural analysis (ADINA R&D, 2015), DIANA (Displacement Analyzer) developed by TNO DIANA, which employs the displacement method and mainly used for structural and geotechnical analysis (TNO DIANA BV, 2015), and ANSYS developed by ANSYS Company, is used for simulation in different technologies including structural mechanics, fluid mechanics, and electromagnetic (ANSYS, 2015). However, ABAQUS is the finite element software that was selected for the simulation performed in this study (DSS, 2014).

ABAQUS was developed by Hibbitt, Karlsson and Sorensen, Inc. which was established in 1978. This company was then acquired by Dassault Systemes Simulia Corp. (DSS) located in Providence, Rhode Island USA, in 2005. ABAQUS is a very powerful finite element analysis tool due to its broad selection of materials and elements and its capacity to model one, two, and three-dimensional projects. The ABAQUS program suite includes three major products: ABAQUS/CAE, ABAQUS/Standard, and ABAQUS/Explicit. The first product refers to Complete ABAQUS Environment, and is used to create, analyze, and visualize model output all in one environment using graphical user interface (GUI). ABAQUS/CAE gives the option of creating the model geometries using the software drawing tools, or importing CAD models that have been prepared by another compatible products. Users can then submit the assembled and meshed model parts for analysis. The results are reviewed and graphed by the help of the available comprehensive visualization tools. ABAQUS/Standard is generally used for finite element simulations of structures that are subjected to static and low-speed dynamic effects. ABAQUS/Explicit on the other hand is more suitable for transient dynamic and highly nonlinear simulations. However, ABAQUS/CAE supports both Standard and Explicit version for pre-processing and post-processing simulations (DSS, 2014).

3.5 Constitutive Models of Concrete in ABAQUS

There are three concrete constitutive models supported by ABAQUS, and their application depends on the type of structural loading and cracking analysis. These models include: Smeared Crack Model (SCM), Brittle Cracking Model (BCM), and Concrete Damaged Plasticity Model (CDPM). The three models are fully capable of modelling a variety of concrete structures such as beams, trusses, shells, and solids. Although, these models can be used for plain concrete or other quasi-brittle materials, they are mainly utilized to model reinforced concrete structures (Stoner, 2015).

The Smeared Crack Model (SCM) can be employed in ABAQUS/Standard and is primarily used for concrete structures subjected to monotonic loadings at low confining pressure. Cracking of concrete is one of the most crucial aspects in any structural analysis, and thus it is imperative to implement the cracking and post-cracking behaviour of concrete in the modelling. A smeared crack approach is usually used to reflect the discontinuous brittle response of cracked concrete. However, this technique does not track the formation of macrocracks, instead it updates the stress and stiffness material properties to account for the crack effect.

The Brittle Cracking Model (BCM) is usually implemented in ABAQUS/Explicit and is intended for applications in which tensile cracking of materials is dominant. This approach is suitable for ceramics, brittle rocks, and plain concrete. In this model, the concrete compressive behaviour is assumed to be linear-elastic which is an enormous simplification of the actual response. Thus, the BCM is only practical in applications where tensile behaviour overshadows the assumption of linear-elastic compression model. The BCM only represents the brittle aspects of concrete behaviour (i.e. when micro-cracks merge to form discrete macrocracks resulting in a highly localized deformation).

On the other hand, the Concrete Damaged Plasticity Model (CDPM) can be utilized in both ABAQUS/Standard and ABAQUS/Explicit. It is usually used to analyze plain concrete and other quasi-brittle materials. The CDPM can be implemented for the analysis of concrete structures under monotonic, cyclic, and dynamic loading under low confining pressure. It is

proven that Concrete Damaged Plasticity Model is highly flexible in modelling concrete under different loading conditions. Therefore, the CDPM model was selected for the analysis of concrete materials in this study, and will be reviewed in broader details in the following section.

3.6 Concrete Damaged Plasticity Model

In most recent numerical studies of concrete materials, including this research work, plasticity and damage evolution of concrete parts are considered in the basic finite element modelling. The typical damaged plasticity model uses the concepts of isotropic tensile and compressive plasticity to represent the inelastic behaviour of concrete. These concepts are reflected by the assumption of two failure mechanisms: tensile cracking and compressive crushing of concrete composites. Hardening variables correspond to the extent of damage in concrete, and stiffness degradation parameter is used to characterize the uniaxial tensile and compressive stress-strain relationships under applied loads. The hardening variables are then used in cooperation with the yield surface to identify the failure mechanisms under tensile and compressive loading. In concrete modelling, a non-associated plastic flow potential is implemented using the Drucker-Pager hyperbolic function to represent flow potential. Furthermore, a viscoplastic regularization of the constitutive models is sometimes used to improve the convergence rate in the concrete softening and stiffness regimes. The following sections give more details on the available constitutive models which are used for the concrete plasticity concepts.

3.6.1 Concrete Compression Model

The general stress-strain response of the concrete under uniaxial compression is illustrated in Figure 3.2. It is observed that concrete behaves linearly within the elastic region until the initial yield, σ_{co}. After reaching the initial yield point, concrete starts behaving in a plastic fashion and exhibits some work-hardening up to the ultimate stress, σ_{cu}, followed by strain-softening.

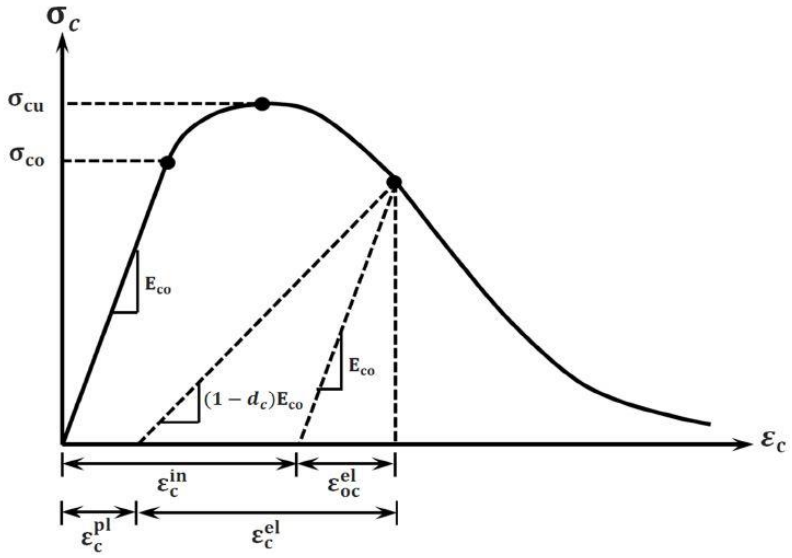

Figure 3.2: Compressive stress-strain response of concrete (DSS, 2014)

The elastic compression behaviour of concrete can be modelled by calculating the initial undamaged modulus of elasticity, E_{co}. For the inelastic response, compressive stresses are provided in a tabular form as a function of the inelastic strain, ε_c^{in} which can be calculated by the following equation:

$$\varepsilon_c^{in} = \varepsilon_c - \varepsilon_{oc}^{el} = \varepsilon_c - \frac{\sigma_c}{E_{co}} \qquad (3\text{–}28)$$

where ε_c^{in} is the inelastic strain, ε_c is the total compressive strain, ε_{oc}^{el} is the elastic compressive strain corresponding to the undamaged material, σ_c is the compressive stress, and E_{co} is the initial undamaged modulus of elasticity. The inelastic strain data are inputted in the material definition section of ABAQUS model as positive values, starting at zero value corresponding to the initial yield point.

3.6.2 Concrete Tension Model

Figure 3.3 illustrates the general stress-strain response of a concrete member under uniaxial tensile loading. It can be seen that the stress-strain response is linear elastic until the peak stress σ_{to}. The onset of micro-cracks occurs when the tensile stress reaches the peak point, which leads to strain localization. The latter impacts the crack growth and may result in the unloading

of regions beyond strain localization which in turn induces strain-softening post-peak response. In a typical reinforced concrete beam, the concrete (a quasi-brittle material) is bonded to the reinforcement. When cracking initiates in the member, concrete continues to resist some tensile stresses between the cracks. This characteristic is referred to as "tension stiffening", and it helps improve the control of the deformation of an RC member and the growth of crack widths.

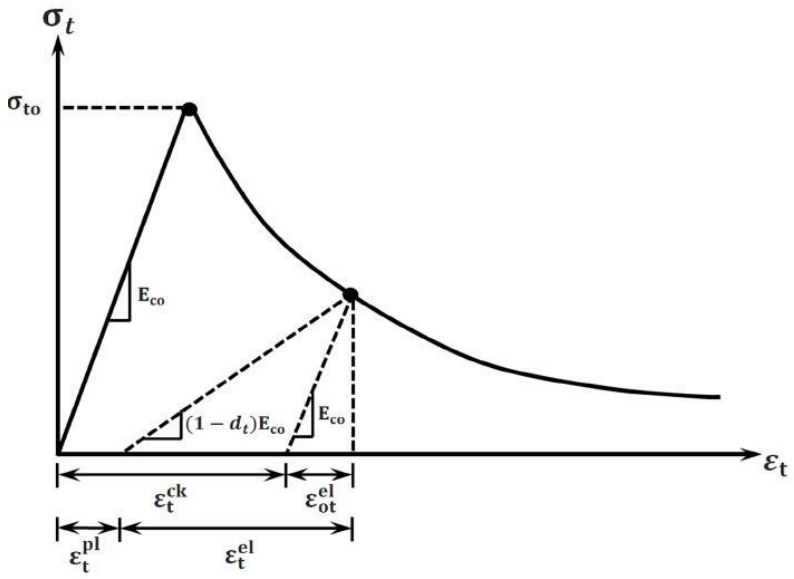

Figure 3.3: Tensile stress-strain response of concrete (DSS, 2014)

In ABAQUS, the user is required to define the post-peak tensile response of concrete in order to account for the interaction between the concrete and the reinforcing bars. The Concrete Damaged Plasticity Model in ABAQUS provides three different methods that can be used to characterize the post-peak response of concrete in tension:

1. The tensile stress in concrete can be entered in a tabular form as a function of the corresponding cracking strain, ε_t^{ck}.
2. The tensile stress can be entered in a tabular form as a function of the crack-opening-displacement, w.
3. The value of concrete fracture energy, G_f, can be simply inputted into the model.

In the first method, the user can plot a stress-strain curve similar to that illustrated in Figure 3.3. The post-peak response can be determined in a procedure similar to the one described in the

concrete compression model. The cracking "inelastic" strain, ε_t^{ck}, can be calculated using the following expression:

$$\varepsilon_t^{ck} = \varepsilon_t - \varepsilon_{ot}^{el} = \varepsilon_t - \frac{\sigma_t}{E_{co}} \qquad (3\text{–}29)$$

where ε_t^{ck} is the cracking strain, ε_t is the total tensile strain, ε_{ot}^{el} is the elastic tensile strain corresponding to the undamaged material, σ_t is the tensile stress, and E_{co} is the initial undamaged modulus of elasticity. Similarly, the cracking strain data are entered in the Concrete Damaged Plasticity Model of ABAQUS model in a positively increasing manner. The first value is set as zero corresponding to the initial yield stress.

In the second method, the post-peak tensile behaviour of concrete is defined in a way that the user has to input the tensile stress as a function of the crack-opening-displacement, w. Hillerborg et al. (1976) has proposed the concept of using fracture energy, G_f, in this method. This fracture energy of a brittle material corresponds to the energy required to open a crack of unit area. Therefore, the post-peak behaviour of concrete in idealized by a stress-displacement response rather than a stress-strain response as in the first method. The user has the liberty to modify the tension stiffening response of the concrete member by selecting one of the proposed examples of stress-displacement curves as shown in Figure 3.4.

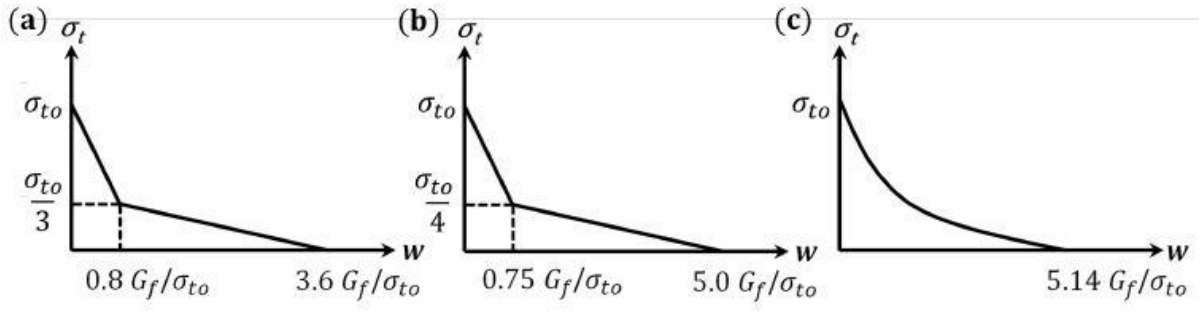

Figure 3.4: Various examples of stress-displacement curves (Stoner, 2015)

It is worth mentioning that the area under these curves represents the fracture energy of the material. Therefore, this method has the advantage of allowing the user to define the rate of strength loss after cracking and also the material's fracture energy (Stoner, 2015).

Finally, the third method allows the user to simply define the tensile peak stress, σ_{to}, and the value of the fracture energy, G_f. As it can be seen in Figure 3.5, this method assumes a linear stress-displacement post-failure response.

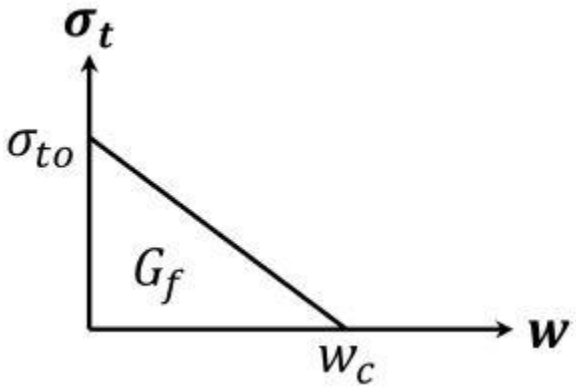

Figure 3.5: Linear stress-displacement curve (Stoner, 2015)

The user is expected to identify the value of the peak stress and the area under the linear curve (i.e. the calculated fracture energy). Then after, the maximum crack displacement corresponding to a complete loss of strength, w_c, is computed by the equation:

$$w_c = \frac{2G_f}{\sigma_{to}} \qquad (3\text{–}30)$$

3.6.3 Damage Modelling

Sometimes, unloading of the concrete member can occur within the post-peak region of the compression and tension stress-strain curves. In such case, the unloading response becomes weaker and degraded, and modulus of elasticity is utilized to account for this degradation as expressed in Figure 3.2 and Figure 3.3. This degradation during the unloading phase is identified by two damage variables, $d_c$and d_t for member subjected to compression and tension, respectively. The damage parameters are functions of the plastic strains $\varepsilon_c^{pl}$and ε_t^{pl}, temperature θ, and other predefined filed variables f_i, as can be seen in the next equations. It is noted that the values of the damage parameters ranges from zero (corresponding to the undamaged material) to one (for the material with complete loss of strength).

$$d_c = d_c\left(\varepsilon_c^{pl}, \theta, f_i\right) \quad 0 \le d_c \le 1.0 \qquad (3\text{–}31)$$

$$d_t = d_t\left(\varepsilon_t^{pl}, \theta, f_i\right) \quad 0 \le d_t \le 1.0 \qquad (3\text{–}32)$$

As it has be mentioned previously, the damage parameters are functions of plastic strains, and hence, ABAQUS will automatically generate the plastic strains from the user-defined inelastic or cracking strain. The plastic strain in compression is obtained by converting the inelastic strain ε_c^{in},and damage parameters, d_c as expressed below:

$$\varepsilon_c^{pl} = \varepsilon_c^{in} - \frac{d_c}{1 - d_c}\frac{\sigma_c}{E_{co}} \qquad (3\text{–}33)$$

where E_{co} is the initial undamaged modulus of elasticity. However, the calculation of plastic strain in tension depends on the method used to define the tensile post-peak response of concrete. If the first method was used, damage parameters are provided as functions of the cracking strains, ε_t^{ck}, which are converted to plastic strains as shown below:

$$\varepsilon_t^{pl} = \varepsilon_t^{ck} - \frac{d_t}{1 - d_t}\frac{\sigma_t}{E_{co}} \qquad (3\text{–}34)$$

However, if method two or three was used to define the tensile post-peak curve of the concrete member, damage parameter values are considered as functions of the crack-opening-displacement, u_t^{ck}(also referred to as w). The plastic displacements are then obtained by the equation:

$$u_t^{pl} = u_t^{ck} - \frac{d_t}{1 - d_t}\frac{\sigma_t l_o}{E_{co}} \qquad (3\text{–}35)$$

and the term $l_o$corresponds to the specimen length which is assumed to be equal to 1.0. Furthermore, the value of the damage parameter ought to be controlled within the range of 0-0.99 to avoid severe damage, and thus possible convergence issues (Stoner, 2015).

When the initial undamaged modulus of elasticity E_{co} is identified, the stress-strain response of the concrete under tension and compression with consideration of the degradation of the elastic stiffness can be represented by:

$$\sigma_c = (1 - d_c)E_{co}(\varepsilon_c - \varepsilon_c^{pl}) \quad (3\text{–}36)$$

$$\sigma_t = (1 - d_t)E_{co}(\varepsilon_t - \varepsilon_t^{pl}) \quad (3\text{–}37)$$

It should, however, be mentioned that a concrete structure subjected to uniaxial load will exhibit crack initiation and propagation. Therefore, a reduction in the expected load carrying area is expected which in turn increases the concrete effective stresses. ABAQUS accounts for that phenomenon by calculating these effective compressive and tensile stresses, $\bar{\sigma}_c$ and $\bar{\sigma}_t$, respectively. These terms are expressed in the following equation:

$$\bar{\sigma}_c = \frac{\sigma_c}{1 - d_c} E_{co}(\varepsilon_c - \varepsilon_c^{pl}) \quad (3\text{–}38)$$

$$\bar{\sigma}_t = \frac{\sigma_t}{1 - d_t} E_{co}(\varepsilon_t - \varepsilon_t^{pl}) \quad (3\text{–}39)$$

3.6.4 Yield Function

The Concrete Damaged Plasticity Model in ABAQUS implements a yield function proposed by Lubliner et al. (1989), and incorporates modifications presented by Lee and Fenves (1998) to account for different modes of strength evolution. The yield function can be expressed as follows:

$$F(\bar{\sigma}, \tilde{\varepsilon}^{pl}) = \frac{1}{1 - \alpha}[\bar{q} - 3\alpha\bar{p} + \beta(\tilde{\varepsilon}^{pl})\langle\hat{\bar{\sigma}}_{max}\rangle - \gamma\langle-\hat{\bar{\sigma}}_{max}\rangle] - \bar{\sigma}_c\left(\tilde{\varepsilon}_c^{pl}\right) = 0 \quad (3\text{–}40)$$

$$\alpha = \frac{(\sigma_{bo}/\sigma_{c0}) - 1}{2(\sigma_{bo}/\sigma_{c0}) - 1} \quad (3\text{–}41)$$

$$\beta = \frac{\bar{\sigma}_c\left(\tilde{\varepsilon}_c^{pl}\right)}{\bar{\sigma}_t\left(\tilde{\varepsilon}_t^{pl}\right)}(1 - \alpha) - (1 + \alpha) \quad (3\text{–}42)$$

$$\gamma = \frac{3(1 - K_c)}{2K_c - 1} \quad (3\text{–}43)$$

where:

- $\bar{\sigma}_c\left(\tilde{\varepsilon}_c^{pl}\right)$ and $\bar{\sigma}_t\left(\tilde{\varepsilon}_t^{pl}\right)$ are the effective compressive and tensile cohesion stress, respectively;
- σ_{bo} is the initial equibiaxial compressive yield stress;
- σ_{c0} is the initial uniaxial compressive yield stress;
- $\bar{q}$ is the Mises equivalent stress, where $\bar{q} = \sqrt{\frac{2}{3}\bar{S}:\bar{S}} = \sqrt{3J_2}$; and J_2 is the second deviatoric stress invariant;
- $\bar{p}$ is the effective hydrostatic pressure stress, where $\bar{p} = -I_1/3$; and I_1 is the first stress invariant;
- $\hat{\bar{\sigma}}_{max}$ is the maximum principal effective stress.

The two terms α and γ represent material constants. The term α is a function of the ratio of σ_{bo} and σ_{c0}, and experimental data put this ratio between 1.10 and 1.16, resulting in values of α between 0.09 and 0.12 (Lubliner, et al., 1989). The default value of $(\sigma_{bo}/\sigma_{c0})$ adopted by ABAQUS is 1.16 based on a parametric study performed by Kupfer et al. (1969). On the other side, the term γ corresponds to the state of triaxial compression where $\sigma_{max} < 0$, and is a function of the parameter K_c. the latter is defined as a ratio of the second stress invariant on the tensile meridian (T.M.) to the second stress invariant on the compression meridian (C.M.) at initial yield for any given pressure invariant value. The value of K_c governs the shape of the failure surface within the deviatoric plane (see Figure 3.6). In the case of $K_c = 1.0$, the failure surface within the deviatoric plane takes the shape of a circle, which sets well with the classical Drucker-Prager theory. Moreover, the original model suggested by Lubliner et al. (1989) indicates that constant values of K_c varying from 0.64 to 0.80 are acceptable. However, the Concrete Damaged Plasticity Model in ABAQUS recommends a default value of 2/3 for K_c, and limits the permissible value to $0.5 < K_c \leq 1.0$ (Stoner, 2015).

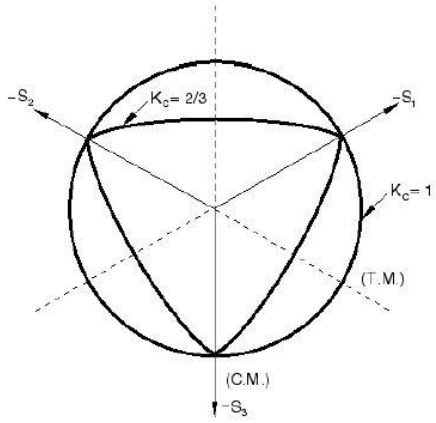

Figure 3.6: Yield surfaces in plane stress (DSS, 2014)

3.6.5 Hardening Variables

Lubliner et al. (1989) have recommended the use of isotropic hardening in their plasticity model. Though this hardening rule is effective in modelling members under monotonic loading, it has been proven inappropriate for cyclic response of concrete structures. When cyclic load is applied, the progress of one strength (compression or tension) does not affect the progress of the other strength. Consequently, in the modifications proposed by Lee and Fenves (1998) included two-variable hardening rule; one variable to control compression and the other to control tension. As discussed in section 2.14.2, this approach assumes independent hardening rule. In another word, the hardening of the material occurs in an independent manner in both compression and tension. Nonetheless, the evolution of yield and loading surface, in the Plasticity model of concrete, is governed by two hardening variables, $\tilde{\varepsilon}_c^{pl}$ and $\tilde{\varepsilon}_t^{pl}$, which refer to the tensile and compressive equivalent strains, respectively.

3.6.6 Flow Rule

Several studies have shown that the application of the associated rule for concrete is not adequate for full range of the concrete response spectrum, and thus results in large inconsistencies between the experimental and theoretical predictions (Hu & Schnobrich, 1989). Concrete is proven to be a material that undergoes large volumetric changes under loading. Therefore, a non-associated flow rule is appropriate to control the dilatancy in the

modelling (Lee & Fenves, 1998). The Concrete Damaged Plasticity Model in ABAQUS uses a non-associated plastic potential flow rule, which can be expressed in the effective stress space as follows:

$$\dot{\varepsilon}^{pl} = \dot{\lambda}\frac{\partial G(\bar{\sigma})}{\partial \bar{\sigma}} \qquad (3\text{–}44)$$

where $\dot{\varepsilon}^{pl}$ is the plastic strain rate, G is the flow potential function and $\dot{\lambda}$ is a non-negative scaler hardening parameter. The flow potential function, G, used in this study is a hyperbolic Drucker-Prager function and is expressed in the $p-q$ plane (meridional plane) using the following equation:

$$G = \sqrt{\epsilon\sigma_{to}tan\psi + \bar{q}^2} - \bar{p}tan\psi \qquad (3\text{–}45)$$

where ψ is the dilation angle, σ_{to} is the user-defined uniaxial tensile stress of concrete at failure, and ϵ is the plastic potential eccentricity.

The flow potential curve helps establish a connection between the plastic flow direction and the plastic strain rate. This curve is continuous and smooth to ensure that the flow direction is always clearly defined. Figure 3.7 defines the flow potential curve within the $p-q$ plane.

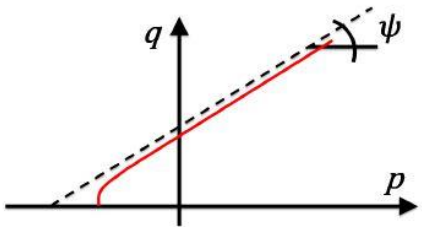

Figure 3.7: Hyperbolic Drucker-Prager flow potential function (DSS, 2014)

The function asymptotically approaches the linear Drucker—Prager flow potential as the confining pressure increases, and intersects the hydrostatic pressure axis at 90°. The shape of the hyperbola is modified by the use of the eccentricity parameter, ϵ. This parameter is taken as a small positive quantity that defines the rate in which the plastic potential function approaches the asymptote. ABAQUS recommends a default value of 0.1 for this parameter which implies that the material has a relatively constant dilation angle over a wide range of confining pressure. However, trials have shown that using an eccentricity value that is

considerably different from the default value might lead to convergence issues when modelling low confining pressure. This can be attributed to the tight curvature of the function at the intersection with the *p*- axis (Stoner, 2015).

Moreover, the flow potential function depends on the dilation angle, ψ. This angle is defined as a material property which is used to measure the inclination of the flow potential function within the meridional plane relative to the hydrostatic pressure axis at high confining pressures (see Figure 3.7). When a small value is assumed for this angle, a brittle behaviour is expected. On the contrary, higher value of eccentricity angle leads to more ductile response (Malm, 2009).

3.6.7 Viscoplastic Regularization

The softening behaviour and stiffness degradation that occur in some materials upon loading often result in severe convergence issues in the model. This problem is more profound in member loaded in tension due to the significant change in slope of the tensile stress-strain curve at peak stress. One of the common techniques used to resolve this issue is to implement viscoplastic regularization of the constitutive models. The Concrete Damaged Plasticity Model in ABAQUS uses a generalization of the Devaut-Lions approach which allows the stresses to pass the yield surface. To incorporate the viscoplastic regularization in the ABAQUS model, the user can enter a small value of viscosity parameter, μ instead of the default value of zero. When a viscosity parameter is greater than zero, the viscoplastic strain, $\dot{\varepsilon}_v^{pl}$, is defined by the following equation:

$$\dot{\varepsilon}_v^{pl} = \frac{1}{\mu}(\varepsilon^{pl} - \varepsilon_v^{pl}) \qquad (3\text{–}46)$$

where μ is the viscosity parameter which represents the relaxation time of the viscoplastic system, ε^{pl} is the plastic strain evaluated in the inviscid solution (i.e. no viscoplastic regularization is assumed), and ε_v^{pl} is the viscoplastic strain. Moreover, when the viscoplastic strain is used, the viscous stiffness damage variable, d_v' is introduced and expressed below:

$$\dot{d}_v = \frac{1}{\mu}(d - d_v) \qquad (3\text{–}47)$$

where d is the damage variable of the inviscid solution. It has to be noted that when viscoplastic regularization is used, model output will be based on plastic strain and elastic stiffness degradation values, ε_v^{pl} and d_v, respectively. In conclusion, the use of a small value for the viscosity parameter will yield a significant improvement in the solution convergence rate without affecting the accuracy of the results (Stoner, 2015). When the value of μ approaches zero, the solution becomes a plastic response. Conversely, as the μ parameter is taken significantly larger than the iteration time increment, the solution tends to be elastic solution.

3.7 Traction-Separation Model

ABAQUS provides a variety of constitutive models that are utilized to define the interactions between surfaces, and can range from mechanical to thermal contact models (DSS, 2014).
Traction-separation law is a mechanical model that is generally utilized to simulate the bond between two surfaces, and it is expressed as linear elastic relationship between traction (bond stress) and separation (slip). The damage can also be accounted for by defining the maximum allowable stress or displacement in the bond-slip response. Damage is usually observed when the interfacial materials start to behave in an inelastic manner. Once the initiation of damage is recorded, the evolution of damage can then be defined in order to model the inelastic behaviour of the interfacial bond. The method of modelling using the typical traction-separation model are thoroughly described in the next sections.

3.7.1 Linear Elastic Model

The traction-separation model in ABAQUS follows initially linear elastic behaviour followed by the initiation and evolution of damage. This elastic relation is written in the form of an elastic constitutive matrix, *K*, which relates the nominal stress to nominal strains across the interface, as seen in the next equation. The nominal stresses are defined as the force

components divided by the original area at each integration point. While the nominal strains are simply the separations divided by the original thickness at each integration point.

$$\{t\} = [K]\{\delta\} \qquad (3\text{–}48)$$

where $\{t\}$ is the traction stress vector, $[K]$ is the elastic constitutive matrix, and $\{\delta\}$ is the separation vector.

The traction stress vector consists of the normal tractions, t_n, and shear tractions, t_s for two dimensional problems. Whereas, a tangential shear tractions, t_t, is added to the traction vector in the case of three-dimensional modelling. The separation vector are made up of the corresponding contact separations. The contact separations are characterized by the relative displacements between nodes on the slave surface and their projections on the master surface. The surface under load is considered the master surface, such as steel or FRP reinforcement in pull-out specimen. While the slave surface is defined as the reacting surface such as the concrete.

The complete matrix form of the constitutive stiffness relation for the bond is expressed in the following equation:

$$\begin{Bmatrix} t_n \\ t_s \\ t_t \end{Bmatrix} = \begin{bmatrix} K_{nn} & K_{ns} & K_{nt} \\ K_{ns} & K_{ss} & K_{st} \\ K_{nt} & K_{st} & K_{tt} \end{bmatrix} \begin{Bmatrix} \delta_n \\ \delta_s \\ \delta_t \end{Bmatrix} \qquad (3\text{–}49)$$

In ABAQUS the behaviour of bond can take two main forms: uncoupled and coupled response. In the case of the uncoupled form, the stiffness matrix above is modified so the non-diagonal terms have zero values ($K_{ns} = K_{nt} = K_{st} = 0$). This implies that the separation occurring in the tangential direction has no effect on the normal traction stress. Similarly, separation normal to the bond surface does not influence the traction in the tangential shear plain. Whereas, in the second form of bond behaviour (coupled) one or more of the constant that were mentioned previously is not equal to zero. Consequently, there is some of shared effect between the tractions and the separations acting in different directions.

In order to efficiently evaluate the material parameters in the elastic constitutive matrix, a simple comparison can be made between this bond stiffness and the equation of elastic truss.

The stress- strain relationship of the liner elastic truss can be expressed by the use of Hooke's law as shown below:

$$\sigma = E\varepsilon \qquad (3\text{–}50)$$

where σ is the stress, E is Young's modulus, and ε is the strain. In the case of a beam or truss member, this strain can be defined as change in length (dl) over the original (undeformed) length (L) of the member (see Figure 3.8).

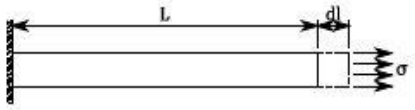

Figure 3.8: Beam under tensile load (Wenkenbach, 2011)

The original stress-strain equation can be modified by replacing the strain with the $(\frac{dl}{L})$ term, so that the stress can be defined in terms of displacement. Therefore, the uncoupled interaction behaviour in the normal direction for example can be modelled as a truss element with a length equal to the thickness of the cohesive layer (T) as shown in Figure 3.9. The value of the normal stiffness can be represented as:

$$K_{nn} = \frac{E_{nn}}{T} \qquad (3\text{–}51)$$

where E_{nn} is the Young's modulus of the bonding layer in the direction normal to the bond surface. The stiffness, *K*, in this case has a unit of [Force/Length^3], which is equivalent to the Young's modulus in homogeneous material.

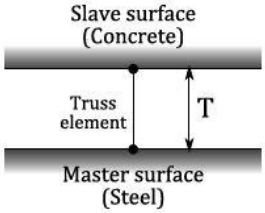

Figure 3.9: Approximation of the bond interface in the normal direction (Wenkenbach, 2011)

The constitutive stiffness matrix does not define the material properties but rather the interface behaviour. The traction corresponds to the stress between the surfaces and has a unit of [Force/Length^2]. While the separation is characterized by the change in original length and clearly has a unit of [Length]. When adopting the traction-separation model in ABAQUS, the user is required to fill the stiffness matrix with appropriate values of *K* to better reflect the interaction between contact surfaces (Wenkenbach, 2011).

3.7.2 Damage Initiation

As the name implies, the damage initiation refers to the onset of degradation of the material response after a specific point. In this stage, ABAQUS allows the user to define the maximum stresses (t_n^o, t_s^o, t_t^o) or maximum displacements $(\delta_n^o, \delta_s^o, \delta_t^o)$ that can be allowed without any damage occurring. In the case of assuming maximum stress criterion, the damage takes place when one or all of the stress exceeds a maximum allowed value. ABAQUS interprets the initiation of damage when any of the expression in the following equation is equal to one:

$$max\left\{\frac{\langle t_n \rangle}{t_n^o}, \frac{t_s}{t_s^o}, \frac{t_t}{t_t^o}\right\} = 1.0 \qquad (3\text{–}52)$$

The normal stress, t_n, in the above equation has been placed between Macaulay brackets to avoid a case where a compressive stress may result in damage initiation. Moreover, the damage initiation point can be expressed in a quadratic form using a quadratic interaction function. In a similar fashion, damage will initiate when the following criterion is met:

$$\left(\frac{\langle t_n \rangle}{t_n^o}\right)^2 + \left(\frac{t_s}{t_s^o}\right)^2 + \left(\frac{t_t}{t_t^o}\right)^2 = 1.0 \qquad (3\text{–}53)$$

The quadratic function shown that the stresses in each direction contribute to the definition of the damage initiation (Wenkenbach, 2011). The normal stress was put again in Macaulay brackets to eliminate the effect of compressive normal stresses on the damage initiation. It is important to mention that the procedure of using stresses to define the damage initiation is identical to the case where displacements are considered instead.

3.7.3 Damage Evolution

This crucial stage of describing the interfacial bond behaviour simply refers to the degradation of material stiffness beyond the point where damage has been initiated. The damage evolution can be computationally expressed by defining the separation at which the bond is fully degraded, or as the energy required to overcome the bond between surfaces. In order to describe the evolution of damage under a combination of normal and shear deformations across the interface, it is useful to introduce an effective displacement term as defined below:

$$\delta_m = \sqrt{\langle \delta_n \rangle^2 + \delta_s^2 + \delta_t^2} \qquad (3\text{–}54)$$

The full bond response of a typical interfacial material can be illustrated by Figure 3.10 and Figure 3.11 for linear and exponential damage evolution, respectively.

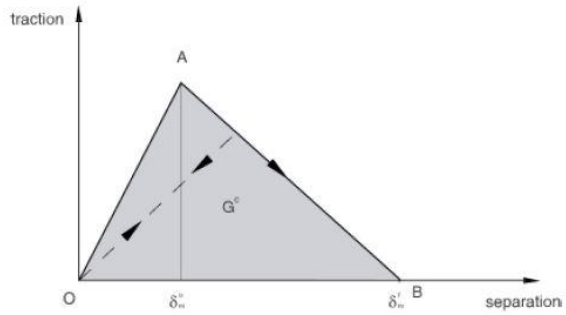

Figure 3.10: Bond traction separation relationship with linear damage evolution (DSS, 2014)

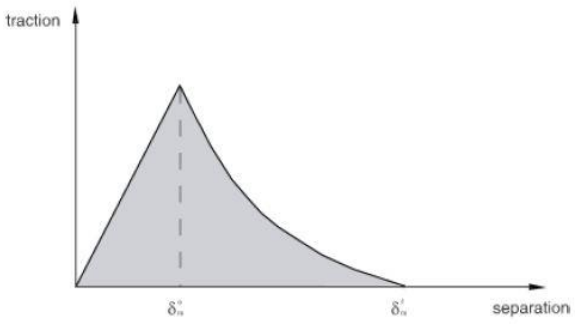

Figure 3.11: Bond traction separation relationship with exponential damage evolution (DSS, 2014)

At point (A), the effective separation at damage initiation is represented by δ_m^o. While point (B) corresponds to the effective separation, δ_m', at full degradation. The area under the (OAM) reflects the energy dissipated due to full failure. In summary, damage evolution defines the behaviour between the damage initiation (point A) and the full degradation stage (point B). ABAQUS provides a choice of linear, exponential, or user-defined response of the damage evolution.

The stress components of the traction-separation law are affected by the damage according to:

$$t_n = \begin{cases} (1-D)\bar{t}_n & \bar{t}_n \geq 0 \\ \bar{t}_n & otherwise \end{cases} \quad (3\text{–}55)$$

$$t_s = (1-D)\bar{t}_s \quad (3\text{–}56)$$

$$t_t = (1-D)\bar{t}_t \quad (3\text{–}57)$$

The damage tractions (t_n, t_s, t_t)in the previous equations is determined by the implementing a scalar damage variable (D), and the theoretical tractions $(\bar{t}_n, \bar{t}_s, \bar{t}_t)$ are calculated using equation (3–49). The value of the damage variable (D) ranges from zero at the initiation of damage (point A) to 1.0 at full degradation (point B).

For linear and exponential softening, the evolution of damage variable, (D), can be expressed in the following forms, respectively:

$$D = \frac{\delta_m^f(\delta_m^{max} - \delta_m^o)}{\delta_m^{max}(\delta_m^f - \delta_m^o)} \quad (3\text{–}58)$$

$$D = 1 - \left\{\frac{\delta_m^o}{\delta_m^{max}}\right\}\left\{1 - \frac{1 - exp\left(-\alpha\left(\frac{\delta_m^{max} - \delta_m^o}{\delta_m^f - \delta_m^o}\right)\right)}{1 - \exp(-\alpha)}\right\} \quad (3\text{–}59)$$

where δ_m^o is the effective displacement recorded at the point of damage initiation, δ_m^{max} refers to the maximum value of the effective displacement at any given point during the loading

history beyond damage initiation, δ_m^f corresponds to the effective displacement at complete bond failure, and α is a non-dimensional material parameters which defines the rate of damage evolution (DSS, 2014). Furthermore, ABAQUS allows the definition of the failure mode mix using a variety of methods including the Power Law and the Benzeggagh-Kenane form (Benzeggagh & Kenane, 1996). Both are based on the fracture energies in the normal and shear directions. In conclusion, the accuracy of the traction separation analysis is contingent on the choice of the interfacial parameters and how closely they represent the actual bond properties.

3.8 Elements in ABAQUS

The general procedure of modelling any structure in ABAQUS is to assemble meshed sets of finite elements into one global assembly, and then evaluate its overall response under loading. ABAQUS provides an extensive library of elements that can be effectively used to model a variety of materials. The geometry and the type of an element is characterized by several parameters including: family, degree of freedom, number of nodes, formulation, and integration. Each element in ABAQUS has a unique name which is derived from the five aspects mentioned previously. Figure 3.12 illustrates some of the most commonly used elements.

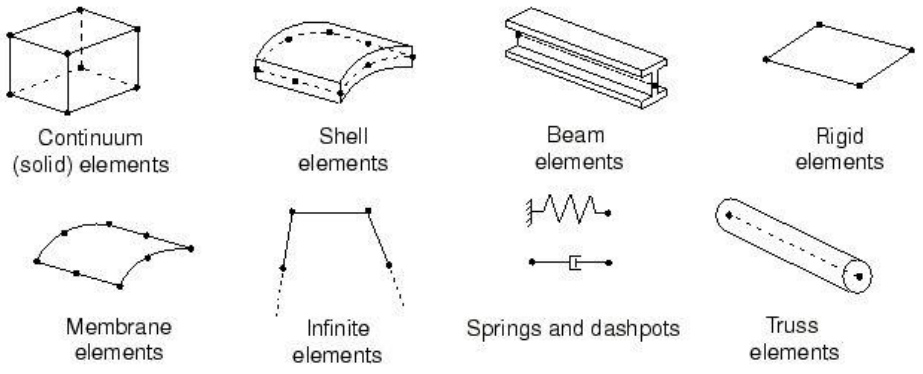

Figure 3.12: Various elements types (DSS, 2014)

In a standard stress analysis, the degrees of freedom of interest are the translations of the element nodes. In order to evaluate the field variables (usually displacements) at all nodes within the element domain, interpolation of these nodal values is performed. The number of nodes per elements determines the order of the interpolation (e.g. linear, quadratic, cubic, etc.). The 8-node continuum brick element, shown in Figure 3.12 , uses linear interpolation and is referred to as a first-order element. On the other hand, a 20-node continuum element utilizes quadratic interpolation and known as a second-order element. In theory, second-order elements provide more accurate results than first-order elements, if they were used in adequately small applications. However, the use of higher-order elements has some of drawbacks associated with convergence issues, especially when used in highly nonlinear analyses. For that reason, it is imperative to select the appropriate type of elements to achieve a sound numerical analysis. Although first-order elements are a quite practical choice for a large number of applications, they happen to exhibit a phenomenon called "shear locking". This phenomenon can be seen as a constrained distortion which may lead to drastic convergence issues. For example, when the two-dimensional block illustrated in Figure 3.13(a) is subjected to pure bending, the entire element will deform in the manner shown in Figure 3.13(b). However, if a two-dimensional, 4-noded, quadrilateral, linear element with four integration points is used to model that block, the material is expected to deform as seen in Figure 3.13(c).

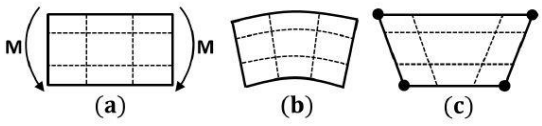

Figure 3.13: Shear locking of first-order elements (DSS, 2014)

In Figure 3.13(c), the dashed lines are no longer perpendicular at each integration point which implies that the shear is not zero at these points. This development contradicts the assumption that material under pure bending do not exhibit shear stresses. This is attributed to the inability of linear elements to have curved edges. Consequently, strain energy is generating shearing deformation as opposed to the expected bending deformation, which results in a stiffer elements. However, one of the effective resolutions to this issue is to reduce the number of integration points per element so the excessive restraint is prevented (check Figure 3.14).

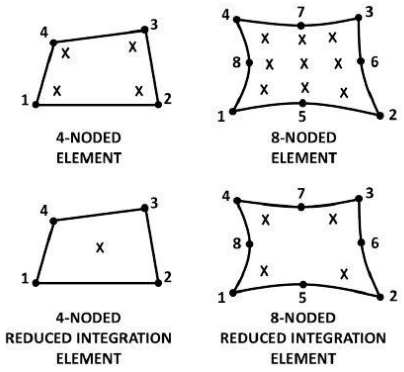

Figure 3.14: The reduction of integration points (DSS, 2014)

The reduced integration method is considered rather advantageous in modelling three-dimensional problem as it decreases the time of analysis. Within the environment of ABAQUS, the user can choose the type of integration to be performed on the elements. A solid element such C3D8 is an 8-node continuum element with 8 integration points refers to full integration option. While a C3D8R is the same element with the exception of having only one integration point (reduced integration option). Although, this practice is effective in eliminating shear locking, it may also result in a phenomenon named "hourglassing". The quadrilateral element in Figure 3.15 has only one integration point (reduced from a fully integrated element with 4 integration points). When this element is subjected to pure bending, the length of the two dashed lines and the angle between then remain unchanged. This implies that all the components of stress at the element's single point of integration is equal to zero. In another word, the strain energy in the element is assumed to be zero, and thus the element will not resist this type of deformation as it has no stiffness under this loading. As a result, the occurrence of hourglassing may cause significant uncontrolled distortions in the mesh (Stoner, 2015). However, ABAQUS offers elements with hourglass control to overcome this issue.

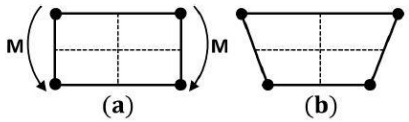

Figure 3.15: Hourglassing in reduced integration point (DSS, 2014)

Chapter Four
Beam Modelling

4.1 Introduction

Fibre reinforced polymer composites are commercially available materials that are often utilized for strengthening new or existing RC structures. Although extensive research have been dedicated to study the effect of fibre composites on the structural capacity of concrete members, numerical studies on the debonding mechanism of FRP composites in these members are still scarce. Brena et al. (2003) have conducted a comprehensive experimental program on a series of carbon reinforced polymer strengthened concrete beams. The study was designed to investigate the increase in flexural capacity and the potential failure modes that these beams might exhibit. The CFRP composites were attached to the surface of concrete beams in different configurations. Some of the laminates were placed at the bottom face of the beams, while other were placed on the sides. All of the beams were tested under four-point loading until the ultimate capacity was reached. It was observed that the dominant failure mode in this program was attributed to the crack-induced debonding at the FRP-Concrete interface.
This chapter represents the numerical analysis and the modelling techniques used to model some of those beams (namely control specimen and A4 specimen), tested by Brena et al. (2003). The modelling was perofmed using the commercial finite element program ABAQUS/CAE version 6.14-2. The constitutive models of concrete, steel reinforcement, FRP composites, and the interface elements (e.g. FRP-concrete) are discussed thoroughly in the next sections.

4.2 Concrete Compression Model

The uniaxial stress-strain behaviour of concrete in compression was modelled using the constitutive relationship proposed by Hognestad (1950). In this model, the acceding branch of the compressive stress-strain curve is modelled with a parabolic relationship. The curve inflection point resides at the peak stress of concrete, f_c'', and at which the corresponding strain is called ε_{co}. The peak compressive strength of concrete is calculated as the product of a constant *k*, which was set equal to 0.9, and the compressive stress determined from concrete cylinder tests, f_c'. This constant is identified as the ratio between the compressive strength obtained from concrete cylinders to that of the concrete in the actual tested member (Hognestad, et al., 1955). However, the concrete also exhibits an elastic phase prior to the occurrence of first cracking. Experimental evidence has shown that this linear response can be limited to the range of $(0.4f_c'')$. Beyond the peak load point, f_c'', the parabolic branch starts descending linearly with increasing strain until the maximum usable strain in the concrete is reached, ε_{cu}. The stress corresponding to the maximum concrete strain is assumed to be equal to 85% of the peak stress. Figure 4.1 depicts the governing equations and the stress-strain behaviour of concrete under compression.

The material properties of concrete, used in the finite element model, were adopted from the experimental tests of Brena et al. (2003). The peak compressive strength of concrete, f_c', was taken as 37.2MPa. For a constant value of $(k = 0.9)$, the theoretical value of the peak compressive strength in Hognestad's curve, f_c'', is set to be 33.48MPa. The modulus of elasticity of concrete (Young's modulus) was computed using the simplified relationship provided by CSA A23.3-04, which is applicable for normal density concrete with compressive strengths between 20 and 40MPa.

$$E_c = 4500\sqrt{f_c'} \qquad (4\text{–}1)$$

Therefore, the calculated value of E_c was found to be 27446.3MPa. The literature suggests a value of 0.2 to the Poisson's ratio, *v*, for concrete with normal strength.

Accordingly, the value of the shear modulus, *G*, was taken as 11435.96MPa and calculated below:

$$G = \frac{E_c}{2(1+v)} \qquad (4\text{–}2)$$

The concrete strain, ε_{co}, at the peak stress was calculated using the equation provided in Figure 4.1, and found to be 0.0024. Finally, the ultimate strain the concrete can undergo, ε_{cu}, is limited to 0.0035.

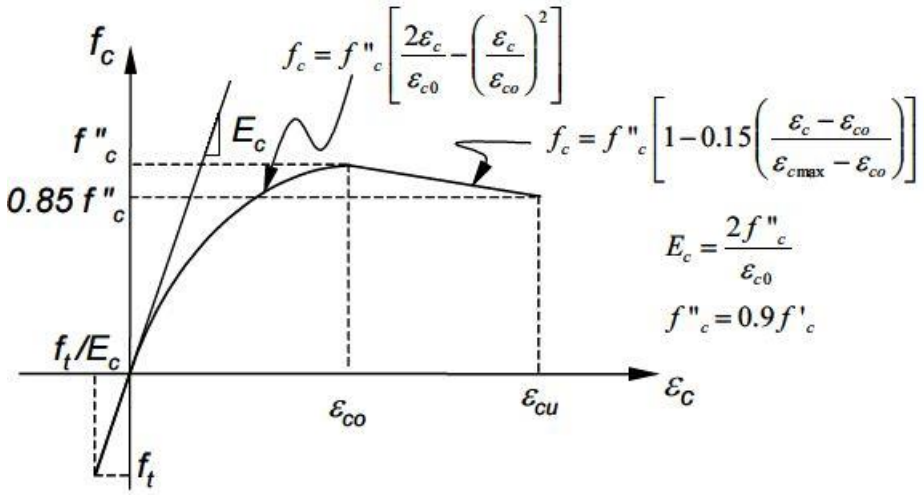

Figure 4.1: Idealized stress-strain relationship for concrete (Brena, et al., 2001)

4.3 Concrete Tension Model

Concrete in tension is usually assumed to behave linearly up to the stress corresponding to its tensile capacity f_t'. The tensile strength of concrete is governed by the type of aggregates, compressive strength of concrete, and the presence of confining stresses. This value can be determined by various test settings, including the direct tensile test, split-cylinder test, and the modulus of rapture test. The latter is commonly chosen to determine the tensile strength of concrete, because of the difficulty of applying the first two tests as well as the tensile capacity

of concrete under flexure is a primary concern. The modulus of rupture, f_r, is identified using the CSA A23.3-04 equation:

$$f_r = 0.6\lambda\sqrt{f_c'} \qquad (4\text{–}3)$$

where λ is a parameter that depends on concrete density, and is taken as 1.0 for normal concrete. Therefore, the value of the tensile strength of concrete used in the model was 3.66MPa.

As previously indicated in section 3.6.2 , there are three methods to define the uniaxial post-peak tensile behaviour of concrete in the Concrete Damaged Plasticity Model: (1) Stress-strain approach; (2) Crack-opening-displacement approach; (3) Fracture energy approach. The following subsections elaborate on the procedure of each approach

4.3.1 Stress-Strain Approach

The tensile strength of concrete beyond the cracking is often ignored in design standards. Nevertheless, in reality concrete is capable of carrying some tensile stresses between cracks when there is sufficient bond between the concrete and the internal reinforcement. This phenomenon is known as "tension stiffening', and can be modelled using a descending post-peak tensile response (see Figure 4.2).

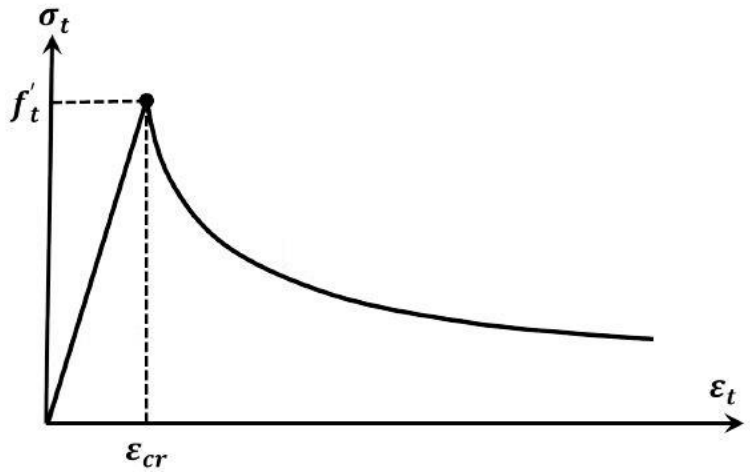

Figure 4.2: Idealized uniaxial stress-strain curve of concrete under tension (Stoner, 2015)

The following constitutive model, proposed by Tamai (1988), was used to plot the stress-strain behaviour of concrete:

$$f_t = E_c \varepsilon_t \qquad for \quad \varepsilon_t \leq \varepsilon_{cr} \tag{4–4}$$

$$f_t = f_t' \left(\frac{\varepsilon_{cr}}{\varepsilon_t}\right)^{0.4} \qquad for\ \varepsilon_t > \varepsilon_{cr} \tag{4–5}$$

$$\varepsilon_{cr} = \frac{f_t'}{E_c} \tag{4–6}$$

where E_c is the modulus of elesticty of concrete, ε_{cr} is the concrete strain at peak stress (cracking), and is found to be 0.00013.

Nevertheless, many studies have found that employing the stress-strain approach to model concrete response under tension has significant drawbacks. It was observed that the use of such model might lead to convergence issues and premature termination of the job analysis particularly in ASBAQUS software. This problem can be caused by the abrupt change in curvature of the stress-strain curve at the peak stress (Wang & Hsu, 2001). Moreover, models implementing this technique might encounter major mesh sensitivity issues, especially when large regions of concrete has little or no reinforcement (e.g. beams with no stirrups) (DSS, 2014).

4.3.2 Fracture Energy Approach

As discussed previously, the tensile behaviour of concrete can be defined by the use of fracture energy (Hillerborg, et al., 1976). This response is assumed to be linear when this method is adopted. The fracture energy parameter represents the energy required to propagate a tensile crack of unit area in concrete under tension. This parameter depends on several factors such as water-to-cement ratio, maximum aggregate size, curing condition, and age of concrete. The influence of the type and quality of aggregate become more significant in high strength concrete. Tougher aggregates are more difficult to fracture and may cause the crack orientation to change, hence more energy is needed in the fracture process (Stoner, 2015).

In the absence of experimental data, G_f may be evaluated using following expression introduced by Model Code 1990:

$$G_f = G_{Fo}\left(\frac{f_{cm}}{f_{cmo}}\right)^{0.7} \quad (4\text{–}7)$$

where f_{cmo} is equal to 10MPa. f_{cm} is the mean value of the concrete compressive strength, and can be expressed as a function of the characteristic compressive strength, f_{ck}, as shown below:

$$f_{cm} = f_{ck} + \Delta f \quad (4\text{–}8)$$

where Δf is taken as 8MPa. Reineck et al. (2003) proposed that the characteristic compressive strength, f_{ck}, can be estimated as a function of the concrete cylinder strength, f_c', as explained below:

$$f_{ck} = f_c' - 1.6MPa \quad (4\text{–}9)$$

The G_{Fo} is the base value of fracture energy, and it depends on the maximum aggregate size, d_{max}, as given in the next table.

Table 4.1: Base value of fracture energy G_{Fo} (Nmm/mm^2) (CEB-FIP, 1990)

d_{max} (mm)	G_{Fo} (Nmm/mm^2)
8	0.025
16	0.030
32	0.058

In this finite element model, the values of the base fracture energy, G_{Fo}, taken as 0.025Nmm/mm^2, corresponding to the aggregate size of 8 mm that were used in Brena et al. (2003) test. The values of f_{ck} and f_{cm} were set to 35.6MPa and 43.6MPa, respectively. Therefore, the calculated value of the fracture energy, G_f, was 0.070N/mm or 70N/m. However, when fracture energy approach is used in the Concrete Damaged Plasticity Model within ABAQUS, the user needs to select the "GFI" tension type and only enter the values of the tensile strength of concrete and the fracture energy.

4.3.3 Crack-Opening-Displacement Approach

This method allows the user to plot a custom stress-displacement relationship and implement the response into ABAQUS model. While the pre-cracking tensile response of concrete is assumed linear, the post-cracking behaviour is defined as a function of the crack-opening-displacement, w. The post-cracking tensile behaviour of concrete can be simulated in various forms, including bilinear and exponential curve. In this study, a bilinear relationship was adopted to model the post-cracking behaviour of concrete subjected to tension (see Figure 4.3).

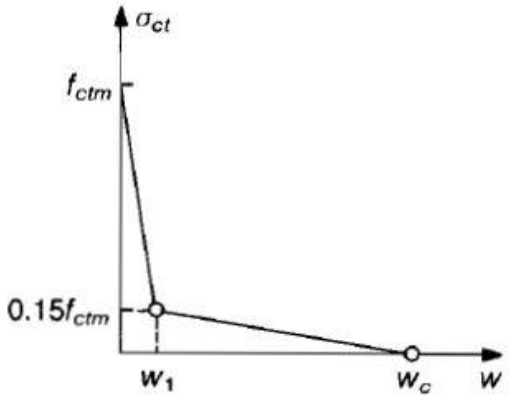

Figure 4.3: Stress-crack opening diagram for uniaxial tension (CEB-FIP, 1990)

The constitutive models introduced by the Model Code 1990 were taken for a cracked section, and presented as follow:

$$f_t = f_{ctm}\left(1 - 0.85\frac{w}{w_1}\right) \qquad for \quad 0.15f_{ctm} \le f_t \le f_{ctm} \qquad (4\text{–}10)$$

$$f_t = \frac{0.15f_{ctm}}{w_c - w_1}(w_c - w) \qquad for \quad 0 \le f_t \le 0.15f_{ctm} \qquad (4\text{–}11)$$

$$w_1 = 2\frac{G_f}{f_{ctm}} - 0.15w_c \qquad (4\text{–}12)$$

$$w_c = \alpha_F \frac{G_f}{f_{ctm}} \qquad (4\text{–}13)$$

$$f_{ctm} = f_{ctko,m}\left(\frac{f_{ck}}{f_{cko}}\right)^{2/3} \quad (4\text{–}14)$$

where the code value of $f_{ctko,m}$ is taken as 1.40MPa, and f_{cko} as 10MPa. The w represents the crack opening (mm), w_1 is the crack opening at ($f_t = 0.15f_{ctm}$), w_c is the crack opening (mm) at the complete failure point ($f_t = 0$), and G_f is the fracture energy calculated using equation (4–7). Finally, α_F is a coefficient given by the following table, and was taken as 8 for the aggregate size of 8mm:

Table 4.2: Coefficient α_F used to estimate w_c (CEB-FIP, 1990)

d_{max} (mm)	8	16	32
α_F[–]	8	7	5

This method was employed in modelling the tensile response of concrete in this study due to the impracticality of the first two techniques. As indicated before, the stress-strain approach might lead to mesh sensitivity issues, and thus produces inaccurate results. On the other hand, and despite the fact that the fracture energy method is simple and doesn't require many parameters to implement, it enforces a linear stress-displacement curve which might offset the actual tensile behaviour of cracked concrete. For those reasons, the crack-opening-displacement approach was adopted in the Concrete Damaged Plasticity Model throughout the numerical analysis segment of this research.

4.4 Concrete Damage Modelling

The loading of concrete member beyond the elastic region induces plastic strains, and hence the subsequent unloading of this member will result in a degraded modulus of elasticity. The Concrete Damaged Plasticity Model in ABAQUS allows for the consideration of this effect by implementing the damage parameters, d_c and d_t, for both compression and tension loading,

respectively. In ABAQUS model, the user needs to define these parameters in a tabulated form as a function of the inelastic strain, ε_c^{in}. As depicted previously in Figure 3.2, the compressive damage parameter, d_c, is a function of the plastic strain, ε_c^{pl}, and elastic strain, ε_c^{el}. Recalling equation (3–28), the inelastic concrete strain can be expressed as:

$$\varepsilon_c^{in} = \varepsilon_c - \varepsilon_{oc}^{el} = \varepsilon_c - \frac{\sigma_c}{E_{co}} \qquad (4\text{–}15)$$

where σ_c and ε_c are determined using the specified constitutive models. The plastic strain of concrete, ε_c^{pl}, can be approximated using a proposed model by Polling (2001):

$$\varepsilon_c^{pl} = b_c \varepsilon_c^{in} \qquad (4\text{–}16)$$

The recommend value of b_c for concrete under compression is 0.7. Thus, the elastic strain corresponding to the damaged concrete can be calculated using the following:

$$\varepsilon_c^{el} = \varepsilon_c - \varepsilon_c^{pl} = \varepsilon_c - b_c \varepsilon_c^{in} \qquad (4\text{–}17)$$

Along with the calculated elastic strain, the compression damage parameter at any given strain level can be determined by:

$$d_c = 1 - \frac{\frac{\sigma_c}{\varepsilon_c^{el}}}{E_{co}} \qquad (4\text{–}18)$$

Similarly, the damage parameter of concrete subjected to tension, d_t, can be inputted into the model in a tabulated form as a function of either the cracking strain, ε_t^{ck}, or the cracking-opening-displacement, w. When using the stress-strain approach to define the tensile response of concrete, the tensile damage parameter, d_t, is evaluated in a similar fashion to that of the compression damage parameter, d_c. However, Polling (2001) suggests a b_t value of 0.1:

$$\varepsilon_t^{ck} = \varepsilon_t - \varepsilon_{ot}^{el} = \varepsilon_t - \frac{\sigma_t}{E_{co}} \qquad (4\text{–}19)$$

$$\varepsilon_t^{pl} = b_t \varepsilon_t^{ck} \qquad (4\text{–}20)$$

$$\varepsilon_t^{el} = \varepsilon_t - \varepsilon_t^{pl} = \varepsilon_t - b_t \varepsilon_t^{ck} \quad (4\text{–}21)$$

$$d_t = 1 - \frac{\frac{\sigma_t}{\varepsilon_t^{el}}}{E_{co}} \quad (4\text{–}22)$$

In the case of implementing the crack-opening-displacement approach, d_t is entered as a function of the crack displacement, w. The latter can be estimated using the methods discussed in sections 4.3.2 and 4.3.3. However, the damage parameter varies from $(d_t = 0)$at crack opening of zero to $(d_t = 1.0)$ at the maximum crack opening, w_c. In order to avoid possible excessive damage which might lead to convergence issues in ABAQUS model, the damage parameter is usually limited to 90% reduction of the elastic modulus (Stoner, 2015).

4.5 Concrete Plasticity Modelling

The plasticity modelling within the Concrete Damaged Plasticity Model is governed by the following parameters:ψ, ϵ, σ_{bo}/σ_{c0}, K_c and μ. As mentioned before, the parameters σ_{bo}/σ_{c0} and K_c directly influence the yield function. The term σ_{bo}/σ_{c0} is defined as the ratio of the initial equibiaxial compressive yield to the initial uniaxial compressive yield stress. The default value of 1.16 was used for this ratio in all simulations. The parameter K_c represents the ratio of the second stress invariant on the tensile meridian to the second stress invariant on the compressive meridian. The default value of 2/3 was used for K_c for all beam simulations. ϵ corresponds to the potential eccentricity which influence the flow potential function, G. The default value of 0.1 was adopted through the plastic model.

The dilation angle of concrete, ψ, is a material parameter that is also used to control the plastic flow potential function, G. This angle is a measure of the inclination of the plastic flow potential function within the meridional plane relative to the hydrostatic pressure axis at high confining pressure. A numerical study, using ABAQUS, was performed by Malm (2006) to examine the effect of the dilation angle on the structural response of RC beams. The study

suggested that small dilation angles of concrete (10^o) induced very brittle beam response, while angles larger than 40^o triggered more ductile response and produced larger peak loads. The author has concluded that dilation angles between 30^o and 40^o provided the best fit to the experimental results. Lee and Fenves (1998) have recommended a dilation angle of 31^o for both uniaxial tension and compression. Therefore, typical values for the dilation angle of normal grade concrete varies from 30^o to 40^o as found in literature (Stoner, 2015). For this reason, a dilation angle of 30^o was adopted for the plastic modelling of concrete in all simulations.

As mentioned earlier, the Concrete Damaged Plasticity Model in ABAQUS allows the user to perform viscoplastic regularization of the constitutive equations to prevent convergence issue related the post-peak response of concrete. This regularization is provided through the viscosity parameter, μ (Stoner, 2015). The default value of this parameter is zero, which indicates no viscoplastic regularization is used. For the beam modeled in this study, a value of 0.0002 was used for the μ parameter in the plastic modelling of concrete. This non-zero value introduces viscoplastic regularization that overcomes the potential convergence problems, and improves computational efficiency, without affecting the accuracy of the results.

4.6 Steel Reinforcement Model

The stress-strain relationship for the reinforcing steel with a clear yield point was idealized using three linear segments as shown in Figure 4.4. The slope of the first linear segment represent the elastic modulus, E_s, and was assumed to be 200GPa associated with a yield strength of 440MPa, from Brena et al. (2003) test. Beyond the yield strain, ($\varepsilon_y = 0.0022$), the slope of the stress-strain curve was assumed equal to zero (straight line) until the point of strain hardening, ε_{sh}, is reached. The strain hardening behaviour of the steel in this study was modelled using a line with a positive slope beginning at ε_{sh}. The slope of this line, E_{sh}, was calculated from the stress at ε_{sh} to the stress at a strain equal to 0.015 (Brena, et al., 2001).

This value was calculated as 6368.58MPa. The Poisson's ratio used in the modelling of steel material was taken as 0.3, as suggested by literature.

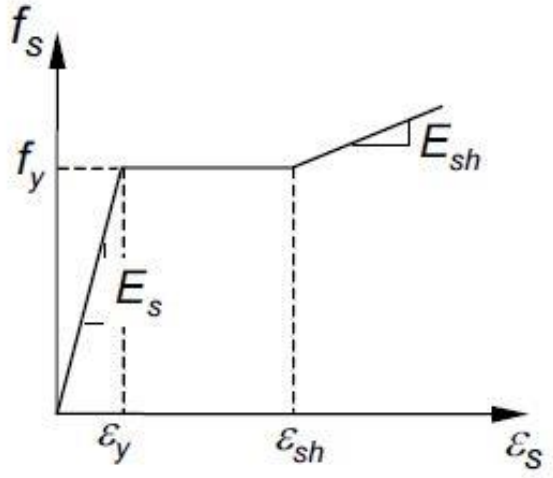

Figure 4.4: Idealized stress-strain relationship for steel (Brena, et al., 2001)

4.7 Fibre Reinforced Polymer Composites Model

The uniaxial behaviour of the carbon fibre reinforced polymer composites (CFRP) used in this research was assumed be elastic linear up to failure (see Figure 4.5). The failure in these materials normally occurs when the ultimate strain, ε_{pu}, corresponding to the rupture stress, f_{pu}, is reached. Moreover, the FRP composites in this study are primarily used to carry tensile stresses. Therefore, only longitudinal stiffness (along the fibre) was considered, and hence no shear or lateral resistance is observed. Based on the experimental data of Brena et al. (2003) test, the mechanical properties of FRP composites were recorded as follows: the ultimate strength of fibre (rupture stress), f_{pu} was taken as 3790MPa, the equivalent rupture strain was 0.015, the Young's modulus value was 230GPa, the Poisson's ratio was 0.3, and the thickness of the CFRP laminates was taken as 0.165mm (per ply).

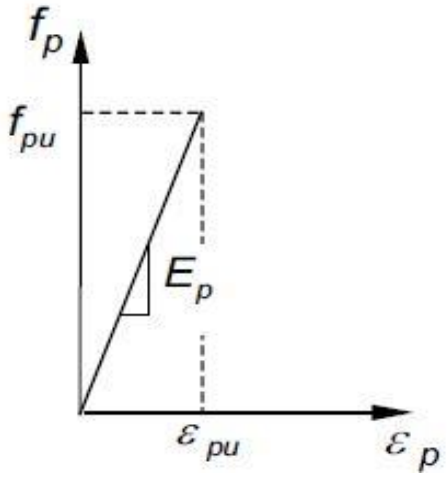

Figure 4.5: Idealized stress-strain relationship for FRP composites (Brena, et al., 2001)

4.8 FRP-Concrete Interface Model

FRP-Concrete interface was modelled first using a perfect bond assumption, and second implementing a bond-slippage relationship between the FRP and the concrete. The interface between the two materials plays a significant role in transferring the stresses from concrete to the FRP composites. In this study, the FRP-Concrete interface refers to the thin layer of adhesive and adjacent concrete. This layer is quite important to be examined as within which the relative strains between the concrete and the FRP mainly occur (Yuan, et al., 2004). Several studies have been conducted to propose rational bond stress-slippage relationships for the FRP-concrete interface. The simplified model proposed by Lu et al. (2005) was adopted to simulate the interfacial bond behaviour between the concrete and the FRP in this study. As indicated in section 2.11.3.2 this model was chosen over the precise model due to its simplicity and accuracy. When the structural members are subjected to external loading, interfacial stresses are developed along the FRP-Concrete interface. Initially, the applied load is small and the interfacial stress, τ, is less than the ultimate bond strength, τ_{max}, and hence the interface response is considered within its elastic range (see Figure 4.6). As the load increases, the initial slip at the location of flexural crack widens until it reaches s_o (the onset of micro-cracking).

Beyond this stage the micro-cracking continues to grow until the interfacial stresses reduce to zero at full debonding stage (macro-cracking).

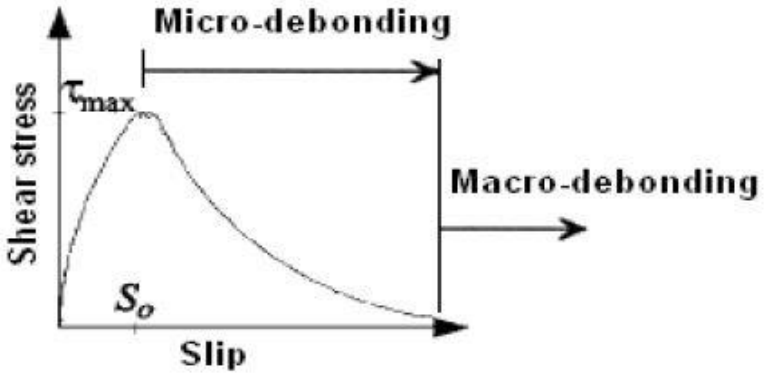

Figure 4.6: Bond stress-slip model for FRP-concrete interface (Monteleone, 2008)

Restating equations (2–22) through (2–26), equations (2–14) and (2–21), the bond stress-slip curve was expressed as follows:

$$\tau = \tau_{max}\sqrt{\frac{s}{s_o}} \qquad if\ s \le s_o \qquad (4\text{–}23)$$

$$\tau = \tau_{max} e^{-\alpha\left(\frac{s}{s_o}-1\right)} \qquad if\ s > s_o \qquad (4\text{–}24)$$

$$s_o = 0.0195\beta_w f_t \qquad (4\text{–}25)$$

$$G_f = 0.308\beta_w^2\sqrt{f_t} \qquad (4\text{–}26)$$

$$\alpha = \frac{1}{\frac{G_f}{\tau_{max}s_o} - \frac{2}{3}} \qquad (4\text{–}27)$$

$$\tau_{max} = \alpha_1\beta_w f_t \qquad (4\text{–}28)$$

$$\beta_w = \sqrt{\frac{2.25 - b_f/b_c}{1.25 + b_f/b_c}} \qquad (4\text{–}29)$$

The width factor, β_w was found to be 1.0, and consequently the ultimate bond strength, τ_{max}, was calculated as 5.49MPa for ($\alpha_1 = 1.5$). The s_o value was 0.071, the interfacial fracture energy, G_f, was 0.589N/mm, and the value of the parameter α was 1.194.

These constitutive models can be utilized in ABAQUS by the use of traction-separation law. The material properties required for modelling the interaction between the FRP and the concrete will be discussed later.

4.9 Beam Modelling

The objective of the experimental investigation conducted by Brena et al. (2003) was to examine the flexural capacity of CFRP beams, in which FRP debonding is the cause of failure. Two beams (control and A4) were selected for this numerical analysis because they provided the most rational results data. Moreover, the CFRP configuration of A4 specimen allows to study the intermediate crack-induced debonding mechanism. The beam was first modelled as a "control beam" where no CFRP was added, and second as a "CFRP beam" in which fibre laminates were attached to the bottom face of the RC beam. The CFRP beam model was created in two phases: initially a perfect bond relationship was assumed at the interface between the concrete and the CFRP laminate, and then a cohesive model was implemented for the interfacial bond. As indicated before, ABAQUS/CAE version 6.14-2 was used in the finite element modelling of all beams. This software is very powerful and offers a customizable graphical user interface (GUI), in which the user can navigate through a large library of tools that help create the model efficiently (see Figure 4.7).

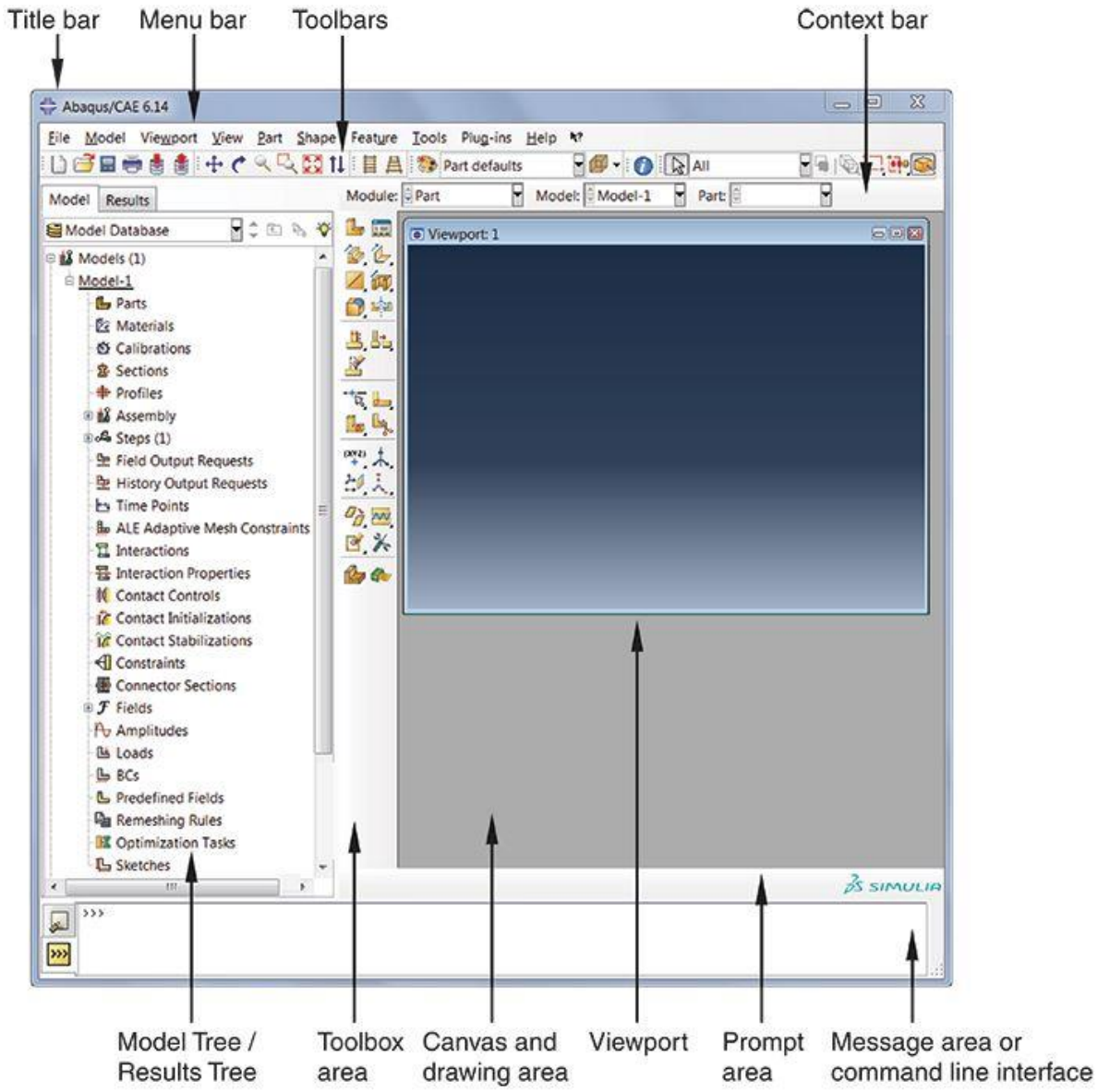

Figure 4.7: Components of main window in ABAQUS/CAE 6.14-2 (DSS, 2014)

The following sections review the geometric properties of the beams, the material definitions, model parts and sections, the finite elements used to model each material, and beam boundary conditions.

4.9.1 Beam Geometry

All the beams modelled in this numerical analysis have a rectangular cross section and tested under four-point monotonic loading as shown in Figure 4.8. The two vertical loads were applied symmetrically about the midspan of the beams to generate a 560 mm region of constant moment. The modelled beams were 200 mm wide, 350 mm deep, and 2890 mm long. The beams were supported by a pin support on one end and a roller-shaped support on the other end to allow for possible movements under loading. In order to limit stress concentration occurring in the concrete elements around the loading and supporting points, elastic steel plates of dimensions 200 x 100 x 25 mm were introduced into the numerical model. Two different steel grades were used in the longitudinal direction, 2-M10 for the compression zone and 2-M15 for the tension zone. 10M stirrups were spaced every 100mm to guarantee flexural response of the tested beams (20 stirrups were used in total). The thickness of the FRP laminates used in the model was taken as 0.165mm. Table 4.3 summarizes all the geometric properties of the modelled beams. Due to the symmetry of the beams and applied loading, only quarter of the beams were analyzed to reduce computational effort. Each beam was split at the mid-span along the *xy*- and *yz*- plane, as depicted in Figure 4.9.

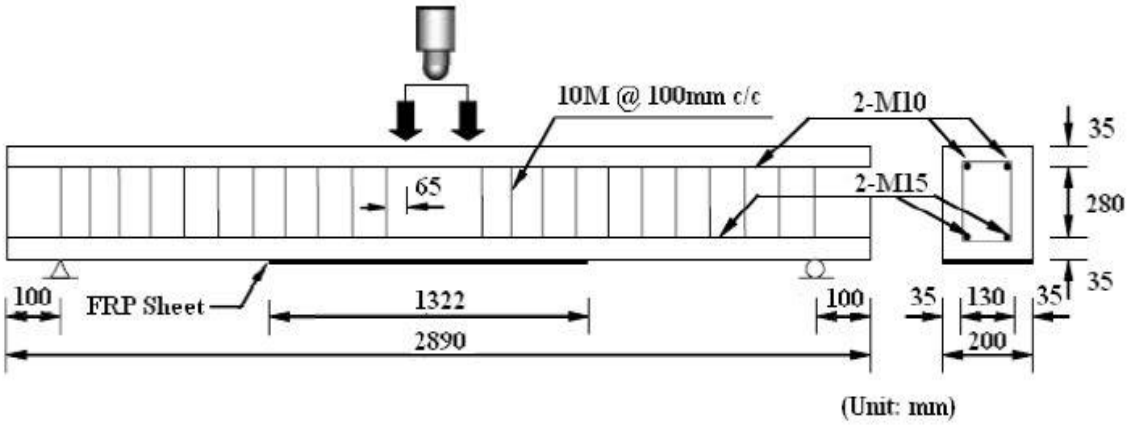

Figure 4.8: Beam dimensions and reinforcement details

Table 4.3: Beam geometric properties

Beam width, *b*	200 mm
Beam height, *h*	350 mm
Beam effective depth, *d*	315 mm
Beam total length	2890 mm
Beam clear length	2690 mm
Shear span, *a*	1065 mm
Shear span-to-effective depth, *a/d*	3.3
$A_{sb} \quad of\ (\emptyset 16\ mm)$	200 mm^2
$A_{st} \quad of\ (\emptyset 10\ mm)$	71 mm^2
$A_{stirrup} \quad of\ (\emptyset 8\ mm)$	50 mm^2
Reinforcement ratio, ρ	0.0086
FRP length	1320 mm
FRP width	200 mm
FRP thickness	0.165 mm

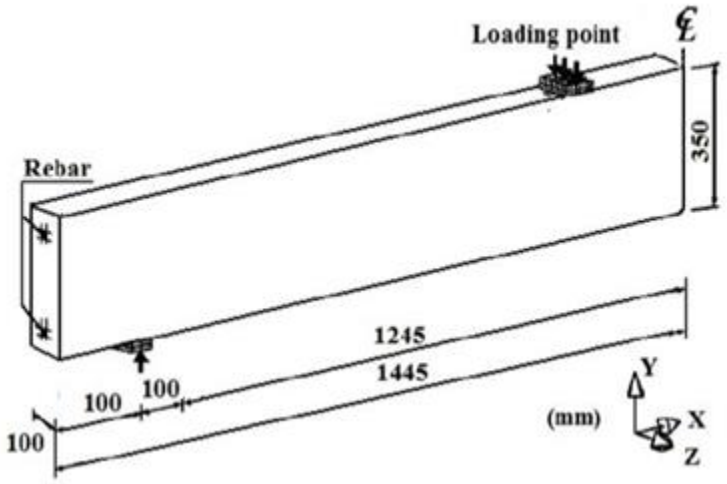

Figure 4.9: Schematic representation of the modelled beams (double symmetry)

4.9.2 Beam Parts

The finite element model in this study is characterized as a nonlinear three-dimensional model. The first step in constructing any model in ABAQUS/CAE is to create the "Parts". These parts represent the building blocks of any ABAQUS model, and are collected in an assembly to create the final model. Each part has an independent geometry in which the material is defined, and specific sections are assigned. A section contains the information about the properties of a part or region of a part. The type of parts being modelled determines the properties of the assigned sections. For a deformable wire part, the section will define the cross-sectional area of the wire. Whereas, for beam parts, the section will carry information about the profile of the part (i.e. defining the cross-sectional properties of the part in terms of moment of inertia, etc.) Moreover, the other goal of the section assignment is to relate the desired material to the part. In summary the following primary steps are required to create a complete part in ABAQUS: (1) create part; (2) define material; (3) create section; (4) assign the material to the section; and (5) assign the section to the part.

For the finite element models created in this research, six main parts were necessary to build the model. The first part was the rectangular geometry of the beam consisting of concrete elements. The second part was the bearing steel plate for both the loading point and the support point. The third and the fourth part was the longitudinal tensile and compressive steel reinforcement, respectively. The fifth part was related to the steel stirrups. Finally, the sixth part was the CFRP composites and it was only added to the second beam model (CFRP Beam). Each of these parts was created independently, assigned material and section properties, and then assembled to form the final model as illustrated in Figure 4.10.

The concrete part was created as a three-dimensional "Deformable" body, which means it can take any arbitrary shape and can deform under mechanical, thermal, or electrical loading (as opposed to a "Discrete Rigid" body which is assumed to remain rigid under loading). The section assigned to the concrete part was a "Solid Homogeneous" section. This type of section allows to define a single material for solid regions (as opposed to "Composite Solid" and "Generalized Plane Strain").

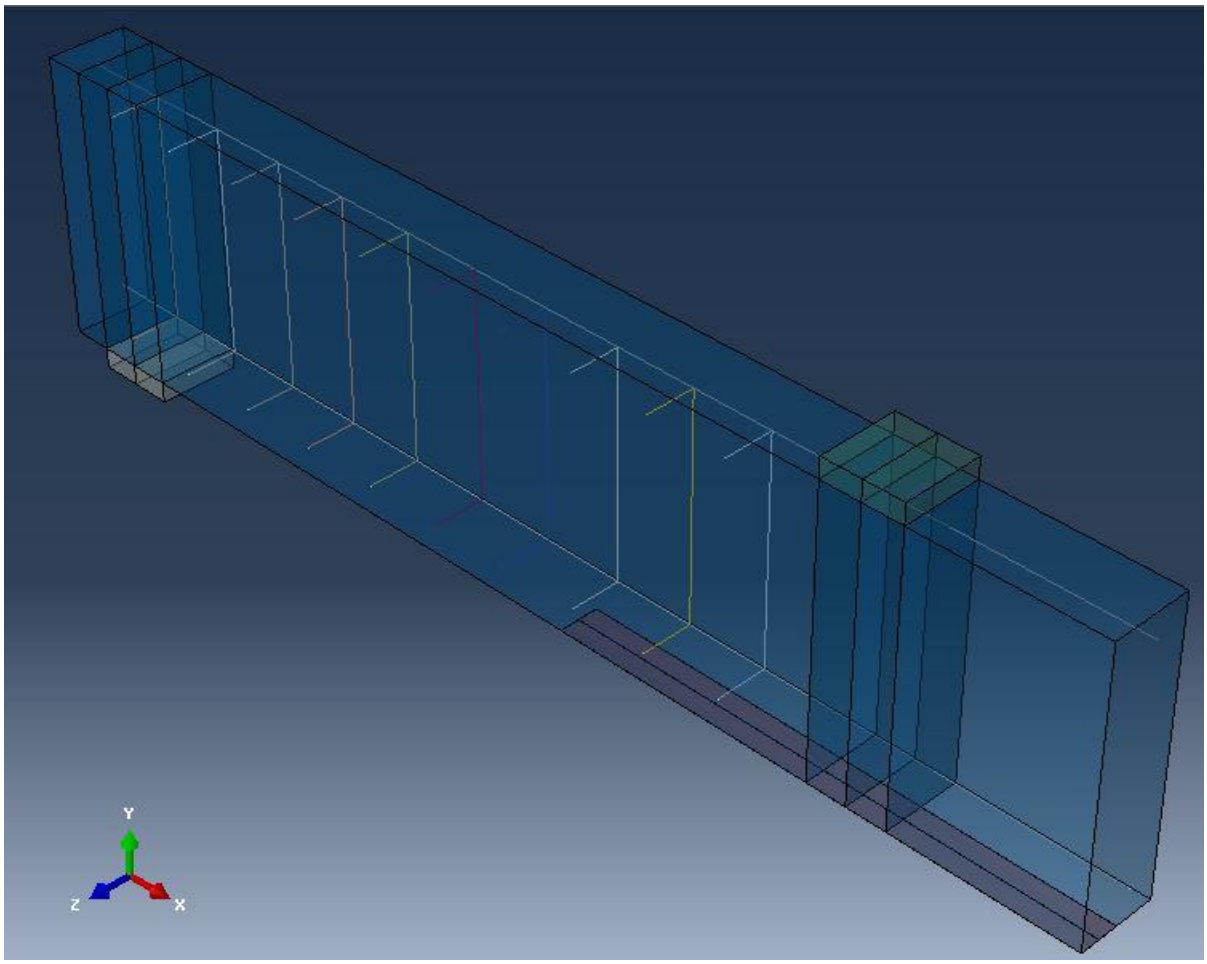

Figure 4.10: CFRP Beam Model parts

The parts of the tensile and compressive steel reinforcement were created in ABAQUS using embedded region technique. In this technique the interaction between the steel and the surrounding concrete was assumed to be a perfect bond, and the steel rebars were defined as deformable "Wire" parts. This type of part is created in ABAQUS as a line and used to model a solid that has a very small thickness and depth when compared to its length. The "Truss" section was assigned to the wire parts, and in which the cross-sectional area of each bar was provided as shown in Table 4.3.

For the shear reinforcement in all models, each stirrup was formed using three discrete rods to create an opened-channel stirrup due to symmetry cut, as shown in Figure 4.10. The stirrups parts were then assigned material and cross-sectional properties through the use of "Truss"

section. Furthermore, the CFRP laminate in the CFRP beam model was created using a three-dimensional "Deformable "part. Afterward, the CFRP composite was assigned the appropriate material and section properties. Finally, Table 4.4 through Table 4.6 summarize the material properties for the concrete, steel, and FRP composites, which were calculated using the corresponding constitutive models explained in previous sections. These parameters were used in defining the sections of all parts of the models.

Table 4.4: Concrete parameters used in the beam models

Compressive strength, f_c'	37.2 MPa
Peak strain, ε_{co}	0.0024
Ultimate strain, ε_u	0.0035
Tensile strength, f_t'	3.66 MPa
Cracking strain, ε_{cr}	0.00013
Young's modulus, E_c	27446.31 MPa
Shear modulus, G	11435.96 MPa
Poison's ratio, v	0.2
Fracture energy, G_f	70 N/m
Dilation angle, ψ	30^o
σ_{bo}/σ_{c0}	1.16
Eccentricity, ψ	0.1
K_c	2/3
Viscosity parameter, μ	0.0002

Table 4.5: Steel reinforcement parameters used in the model

Yield strength, f_y	440 MPa
Yield strain, ε_y	0.0022
Strain hardening, ε_{sh}	0.0076
Young's modulus, E_s	200000 MPa
Strain hardening modulus, E_{sh}	6368.58 MPa
Shear modulus, G	76923.08 MPa
Poison's ratio, v	0.3

Table 4.6: FRP composite parameters used in the model

Ultimate strength, f_{pu}	3790 MPa
Rapture strain, ε_{pu}	0.015
Young's modulus, E_p	230000 MPa
Thickness, t	0.165 mm
Poison's ratio, v	0.3

4.9.3 Elements Selection

In this numerical analysis the composite beam in consideration is broken down into finite elements. Since more than one type of material and interfaces are considered in the analysis, various types of finite elements are required to discretize the structure. Every individual part of the model is assigned a specific element and meshed in a certain way to produce the final form of the finite element model (i.e. mesh). The analysis is then run in a static form and the output data are plotted at the post-processing stage. The following sections review the selection of elements for all the material used in the models.

4.9.3.1 Concrete Elements

The concrete is modelled using "Continuum" elements (see Figure 3.12) as they are more suitable for three dimensional nonlinear materials. In addition, this type of elements is typically used when plasticity and large deformations are expected, such as in the case of concrete beams. Linear reduced-integration option was used throughout the analysis of concrete parts for their ability to withstand severe distortions, as previously mentioned in section 3.8. In summary, C3D8R elements were employed to model all concrete region. These elements are hexahedral continuum elements (C) three dimensional (3D), 8-noded linear brick (8), and reduced integration (R) with hourglass control.

4.9.3.2 Reinforcing Steel Elements

The main steel reinforcements were modelled using "Truss" elements in all beam models. Truss elements are slender structural elements that can only transmit axial force and do not transmit moments or transverse loads. These elements are available in either 2-noded form or 3-noded form in ABAQUS (see Figure 3.12). The former implements linear interpolation of the nodal displacement values and carry constant strains. While the latter perform a quadratic interpolation, and hence allowing for curved elements and linear, non-constant, strain distribution within the element (Stoner, 2015). The T3D2 elements were chosen to model the truss sections, as (T) refers to truss elements, (3D) refers to three-dimensional, and (2) corresponds to 2-nodes per linear element.

Each reinforcing steel bar is then embedded into the concrete body through the "Embedded Region" constraint that is available in ABAQUS tools. This type of constraint defines the truss elements as the "embedded region" and the solid continuum concrete as the "host region". The nodes of the embedded region become tied to the nodes of the host region, and thus the translational degrees of freedom of the rebars are constrained to that of the concrete. Therefore, in the proposed models, the influence of the interaction between the concrete and steel bars are not considered.

The transverse steel reinforcement (stirrups) were modelled using truss elements as in the main rebars of the proposed model. They were embedded individually into the concrete region through the embedded region tool, as mentioned earlier.

4.9.3.3 FRP Elements

The FRP laminate is modelled as a three-dimensional solid element (C3D8R), similar to that of concrete region "continuum" element. In the CFRP Beam model, where perfect bond is assumed, The FRP element is tied to the bottom surface of concrete through tie constraints. However, in the CFRP beam model where a cohesive zone technique is used, the top surface of the laminate is connected to the cohesive surface, and the latter is attached to the concrete substrate through the use of "surface-to-surface contact" tool available in ABAQUS. This CFRP-Concrete cohesive surface allows for differential movement between the two materials, and hence simulates any possible slippage that might occur within that vicinity.

4.9.3.4 Cohesive Elements

These elements were essentially used in the beam models where interfacial bond between adjacent materials was considered. As mentioned previously, cohesive elements enable the modelling of fracture initiation and development in finite element analysis. The constitutive response of cohesive element in ABAQUS may be based on a continuum description of the material or a traction-separation description of the interface. The first approach is more convenient when the actual thickness of the interface is considered. Whereas the second approach is suitable when the thickness of the interface is negligible and considered to be zero. The constitutive behaviour of cohesive elements with a continuum description is defined by any of the general material models offered by ABAQUS, with the relative material properties obtained from physical testing of the bulk material constituting the cohesive layer. On the other hand, the parameters of the cohesive elements with traction-separation behaviour are determined beforehand, including the initial stiffness, damage initiation, and damage evolution properties (DSS, 2014). For this purpose, the traction-separation modelling technique described in section 3.7 is followed so that these parameters can be implemented in ABAQUS. Nevertheless, the initial stiffness parameter defined in terms of traction-separation laws does

not represent a physically measurable quantity and is treated as a "penalty" parameter. Ideally, the stiffness value of the cohesive element should be infinite (for layer's thickness of zero) so that it does not affect the overall response of the model prior to damage initiation point. However, a finite value of the penalty stiffness, K, must be entered in ABAQUS model, and it can be expressed using an equation proposed by Turon et al. (2007):

$$K = \alpha \frac{E}{t} \qquad (4\text{–}30)$$

where E is the Young's modulus of the adjacent member, t is the thickness of the cohesive layer which was considered 1.0mm, and the parameter α has to be much larger than 1.0, and was recommended to be 50 by Turon et al. (2007). The damage initiation point corresponds to the peak value of the traction-separation relationship (i.e. the strength of the interfacial layer). However, the damage evolution can be represented in ABAQUS model by defining the effective displacement at the point of complete debonding of FRP laminate, the fracture energy dissipated as a result of the damage process, or in a tabulated form as a function of the damage parameter and the relative displacement.

As stated earlier, cohesive elements were utilized to model the FRP-concrete interface in this thesis. The constitutive simplified model proposed by Lu et al. (2005) was used to create the necessary parameters of the cohesive elements. Based on equation (4–30) the initial stiffness was found to be 1.37×10^6MPa/mm for normal stresses and 0.57×10^6MPa/mm for shear and traction stresses. While the damage was assumed to initiate when the traction stress reached a value of 5.49MPa, which was calculated by equation (2–14). The damage evolution was accounted for by using the effective displacement parameter at complete bond failure. This effective displacement, δ_m^f, was expressed by equation (2–30) and found to be 0.214mm. The exponential nature of the softening branch, in the used bond-slip curve, was accounted for by the use of parameter α, which was evaluated as 1.194.

4.9.4 Beam Boundary Conditions

Only quarter of the beam was modelled due to its symmetry in the *xy*- and *yz*- plane. The beams were supported by two types of supports: one that constraints the vertical and longitudinal

displacements (pin support), and other provided restraint to only vertical displacements (roller support). To simulate these conditions, a displacement of zero was prescribed in the 1 and 2-axes which corresponds to the *x* and *y*-axes in ABAQUS ($U1 = 0, U2 = 0$). Moreover, as only quarter of the beam was modelled, additional boundary conditions were applied at the cut faces of the specimen to provide continuity of the beam (see Figure 4.11).

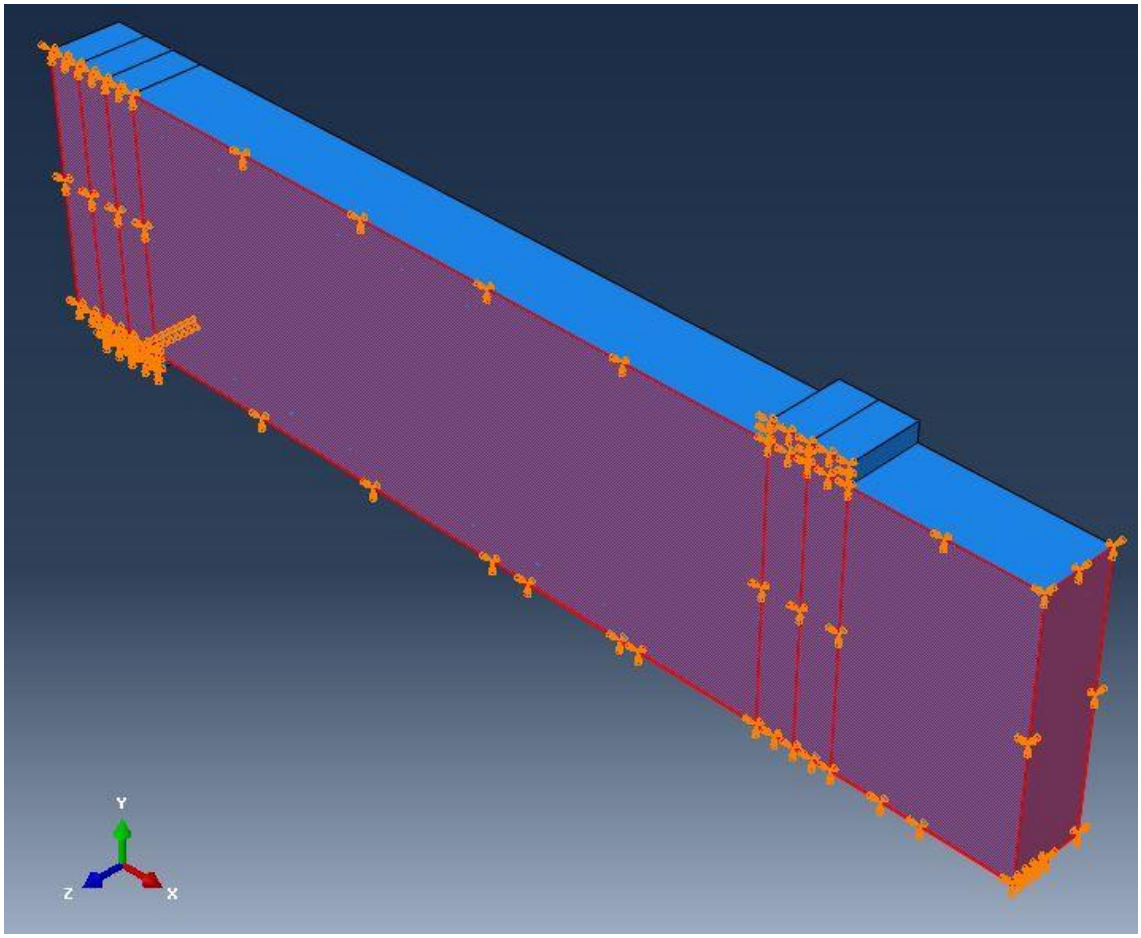

Figure 4.11: Boundary conditions used in the beam models

Load was applied in the form of an imposed displacement at the top face of the loading plate. A displacement-controlled loading was selected for this model to capture the post-peak response of the load-displacement behaviour of each beam. A downward vertical displacement boundary condition was applied at the point load. This displacement was large enough to ensure the failure of each specimen. Furthermore, the value of the output load (reaction force)

was quadrupled in order to represent the real applied load, given that only quarter of the beam was modelled. The reaction forces were distributed on a series of nodes at the bottom face of the support plate (see Figure 4.12). Therefore, the output data at each support were summed and multiply by 4 to represent the real applied load. The midspan deflection was plotted by extracting the values of vertical displacement at the inner corner of the beam as shown in Figure 4.12. This corner point was predefined before running the analysis, so that a complete output history is recoded. The load versus midspan deflection curve is then plotted using those points, as will be illustrated in next chapter.

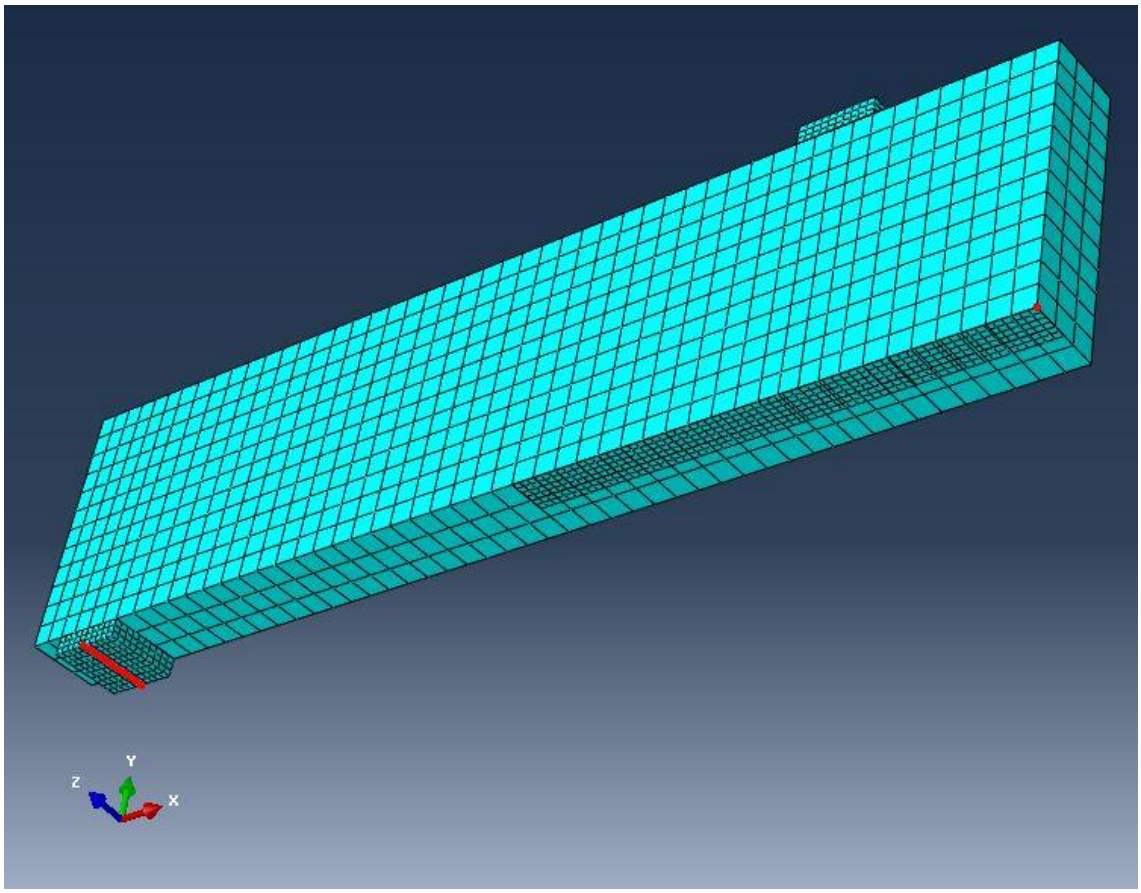

Figure 4.12: Predefined reaction forces and midspan nodes

4.9.5 Time Step Configuration

One of the important features in any ABAQUS model is the analysis step, in which the user controls the sequence of essential modelling operations. The size and sequence of the steps help capture changes in the loading and boundary conditions, and changes to the interaction between parts in the model. Moreover, the type of analysis procedure (i.e. static, dynamic, quasi static, etc.) can be specified in the step tool as well (DSS, 2014). Only one step was needed to capture the static loading conditions of the proposed model in this thesis. ABAQUS/Standard was used for modelling all the specimens, in which Newton's method is incorporated to solve nonlinear equilibrium equations within each step. This method basically runs a series of iterations to acquire equilibrium within each step increments. The user can use "Automatic Incrementation" option, in which the software will determine increment size automatically based on computational efficiency. However, it is necessary to define the maximum number of increments, the initial size of increment, and the minimum and maximum increment size. If ABAQUS needs a larger number of increments than the specified value to reach convergence, the analysis will be prematurely terminated. Therefore, a value of 10000 increments was inputted to ensure the continuity of the analysis. Similarly, when ABAQUS requires a smaller increment time than the predefined value, the analysis will also be terminated. Consequently, a very small increment size is recommended for highly nonlinear analysis such as the one in this study, and hence a value of $1x10^{-15}$ was used for all proposed models. The Automatic Incrementation option in ABAQUS allow the analysis to use the largest increment size possible to increase time efficiency. However, the software will not exceed the user-defined value of the maximum increment size. This value was set as 0.01 for control beam and CFRP beam (with perfect bond assumption) models. While, a larger value of maximum increment size was used in the CFRP beam (with cohesive zone model). A value of 0.1 was used in the CZM analysis as it was found to achieve a good correlation between the numerical and experimental data.

Chapter Five

Model Results Analysis

5.1 Introduction

As stated before, Brena et al. (2003) have conducted a four-point flexural testing on a series of CFRP-strengthened RC beams. The aim was to evaluate the flexural capacity of these beams in the presence of intermediate crack-induced debonding of the CFRP plates. Two of the tested beams were chosen for this numerical study. A control beam where no external FRP reinforcement was present, and CFRP Beam in which the cause of failure was the debonding of CFRP plate due to intermediate flexural cracking. A three-dimensional nonlinear FE model was initially created using ABAQUS/CAE, and then expanded to account for different interactions and mesh analyses. The ABAQUS models were created in the manner described before, and the material definitions were adopted from the experimental results.

This chapter focuses on the collection and the calibration of the modelling results, on both local (material) and global (composite beam) levels. The results obtained from the numerical study were validated against the experimental data collected from the tested beams. This validation of numerical data was performed by correlating the overall flexural response of the proposed beams, recording the strain development in the internal and external reinforcements, and observing crack patterns throughout the analysis process. In order to ensure the reliability and effectiveness of the proposed models, the mechanical properties and the simulation techniques used to model the constitutive materials were also calibrated.

5.2 Constitutive Material Calibration

The material properties were numerically tested in accordance with CSA testing procedures to further validate the proposed models. The mechanical properties of the concrete under compression were calibrated using the standard cylinder test. While, the performance of main steel reinforcement were evaluated by the use of coupon test. Finally, the interfacial mechanisms between the concrete and the externally bonded FRP laminate were validated by simulating a pull-out test on a numerical specimen created for that purpose. The testing procedures and analysis results are elaborated in the next sections.

5.2.1 Concrete

The uniaxial concrete compressive response for all beams was simulated using the Hognestad Parabola constitutive equations. For the purpose of ensuring the validity of this simulation, a compressive concrete cylinder was created using ABAQUS, and tested according to the CSA standard. The recorded stress-strain relationship was then compared to data reported by Brena et al. (2003).

5.2.1.1 Model Prepartion

The finite elemnet model was contsructed using the same numrical steps described in Chapter four. The cylinder was 100mm in diamter and 200mm in height, and contstructed using concrete matreial only. The mechanical properties of the used concrete were identical to those used in all models, with compressive strength, f_c', equals to 37.2MPa, Young's modulus value, E_c, of 27446.3MPa, and the Poisson's ratio, v, of 0.2. Moreover, concrete plasticity was also accounted for in this test by using Concrete Damage Plasticity Model with the same parameters as described in the main models.

The concrete is modelled using continuum elements (C3D8R), because they are more suitable for this type of material as mentioned previously. The model is then meshed using a relatively small mesh size (5mm) to enhance analysis convergence and accuracy. Two bearing plates, with negligible properties, were placed on both ends of the cylinder to evenly distribute the load on the concrete specimen. The cylinder is then loaded monotonically on both ends by

using displacement-controlled loading approach. A vertical displacement of 0.35mm was imposed on the specimen to ensure total failure of the concrete. Figure 5.1 depicts the boundary conditions used in this model, and the stresses at the final stage of the simulation process.

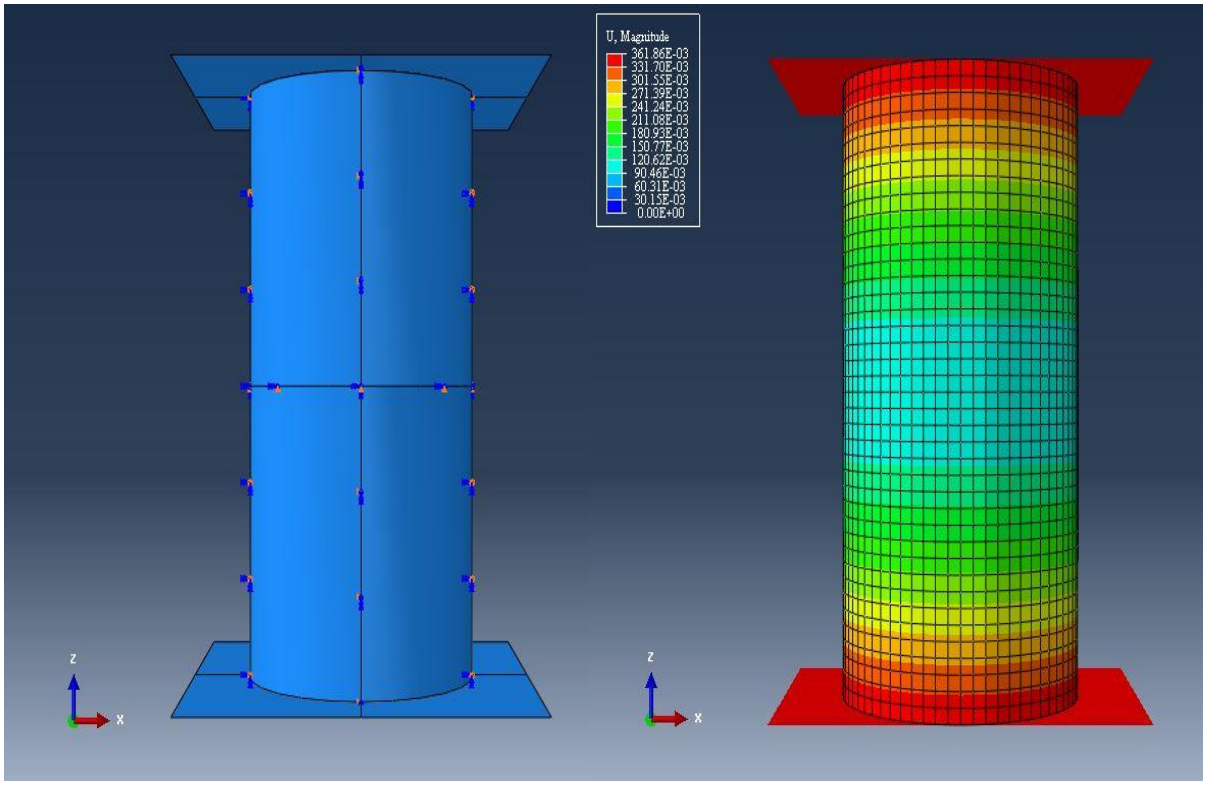

(a) Boundary conditions of tested concrete cylinder

(b) Stresses at ultimate stage of tested concrete cylinder

Figure 5.1: Concrete cylinder model: (a) boundary conditions; (b) stresses at complete failure

5.2.1.2 Results Calibration

The post-processing stage of this numerical simulation involved recording the compressive stress-strain response of the concrete cylinder. The plotted curve was then validated against the actual data reported by Brena et al. (2003), as seen in Figure 5.2. The three distinct regions of the stress-strain cuve can be obsereved in the numrical results. The model behaved in a linear elastic manner up to the initial cracking point at a stress of 13.46MPa and a corresponding strain of 0.00049. The ascendinng branch of the curve was modelled with a

parabolic relatioship, as indicated before. This segment of the stress-strain curve follows the experimental response very closy, and the recoded concrete strength, f_c'', was 33.55MPa, which corresponds to peak strain, ε_{co}, of 0.0024. Therefore, there is only 1.04% difference between the numerical value and the experimental peak strength of 33.90MPa. There was also an agreement between the descending linear branch of the finite element model and the real data. Finally, the good correlation between the numerical material model and the experimental data implies that the concrete material properties and constitutive equations were properly used.

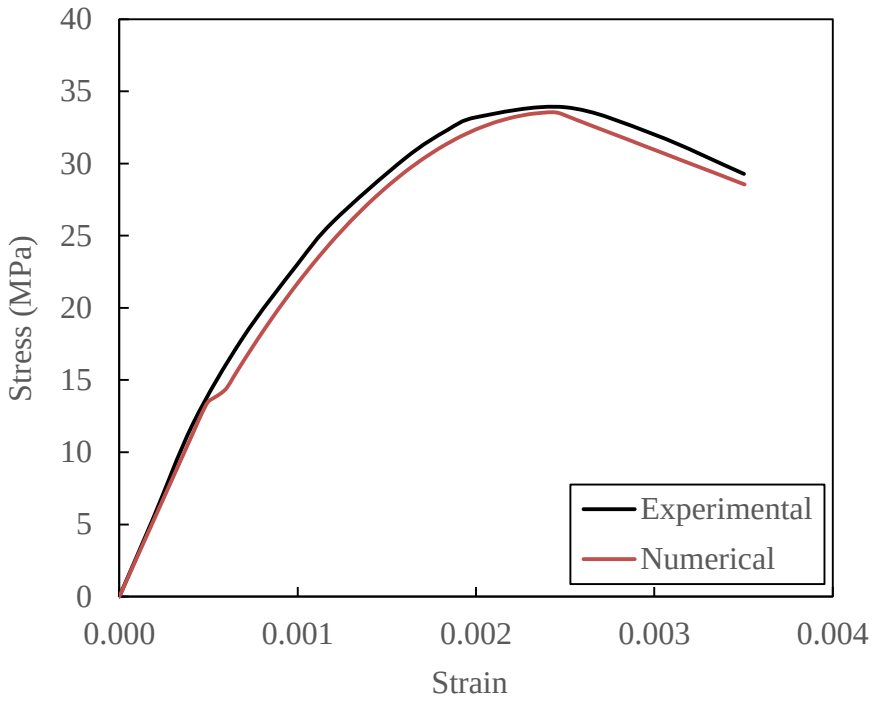

Figure 5.2: Compressive stress-strain relationship for concrete cylinder

5.2.2 Main Steel Reinforcement

The reinforcing steel rebars were also modelled using ABAQUS, to simulate and validate the mechanical properties and the modelling techniques used in the global models. It is essential to define the flexural response of the steel reinforcement properly to ensure that the beam has sufficient ductility and avoid shear failure. Moreover, the appropriate modelling of steel rebars

limit mesh sensitivity issues that can be exhibited with tensile cracking of concrete as the load develops.

5.2.2.1 Model Preparation

A finite element model was designed to simulate the steel rebar performance under tension. The model's geometry and boundary conditions were based on the CSA provisions, namely the coupon testing of steel rebars. The outputted stress-strain response was then compared to that reported by Brena et al. (2003). The mechanical properties of this modelled rebar are based on the ones used in all poposed models of this research. The model included a value of yield strength, f_y, equals to 440MPa, elastic modulus value, E_s, of 200000MPa, and the Poisson's ratio, v, of 0.3. With the exception of Poison's ratio, the remaining properties match those of the rebars used in the experimental study.

A single steel rebar was modelled as a "deformable wire", with a length of 600mm and a diameter of 16mm. the model was then meshed using a 2-node truss elements (T3D2), with a small size of 5mm to ensure convergence and accuracy. All degrees of freedom (movements) of the steel rebar was constrained at the bottom end. While, the tensile loading was applied on the upper free end of the rod, in the form of displacement-controlled loading to help capture the ductile response of the specimen. This value of this imposed vertical displacement was calculated based on the recorded rupture strain of this steel grade, and was found to be approximately 22mm. Figure 5.3 illustrates the boundary and loading conditions used in this model, as well as the state of tensile deformations at the final stage of the analysis.

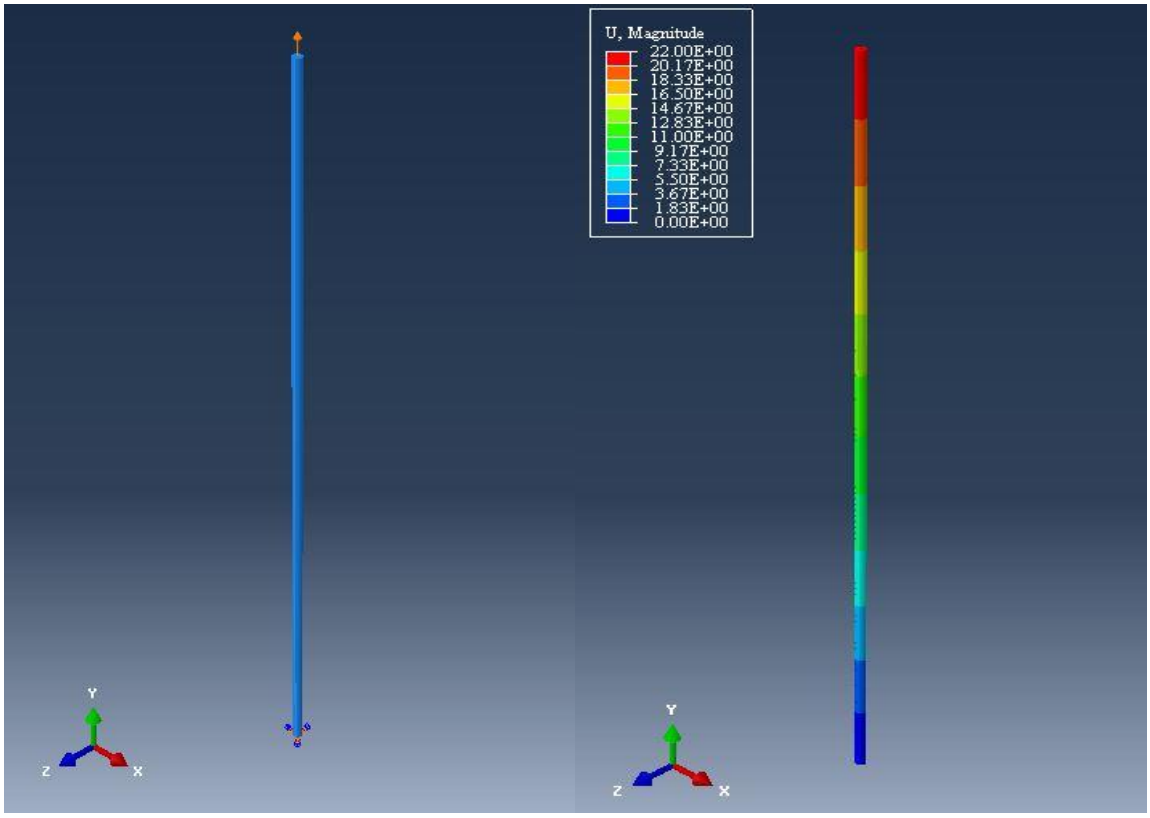

(a) Boundary conditions of tested steel rebar

(b) Stresses at ultimate stage of tested steel rebar

Figure 5.3: Reinforcing steel rebar: (a) boundary conditions; (b) stresses at complete failure

5.2.2.2 Results Calibration

The results of this numerical analysis were plotted in the form of stress-strain relationship, and then calibrated with the real response recorded in the experimental program. Figure 5.4 depicts the elastic-plastic relationship, which is typical of conventional steel reinforcement. There are three linear segment of that response that are identified by: a linear elastic region, then a yield constant region which ends with an ascending branch of strain hardening response. It is noted that the elastic behaviour of the numerical model is almost identical to the actual response of the tested rebar. The predicted yielding stress was 440.04MPa, with a yielding strain of 0.0022. Thus, there is only 0.04MPa difference between the numerical and the experimental value. The

yielding plateau region continues as a horizontal line, which represents unchanged stresses with growing strains. Similar to the elastic response, this region follows the experimental plot very closely. The modelled steel rebar does not exhibit strain hardening until the stress reached 443.86MPa, with a corresponding strain of 0.008. While, the actual steel rebar started experiencing strain hardening at a stress of 440.40MPa and a strain equals to 0.0075. It can be observed that the overall strain hardening response for the numerical model was slightly overshadowed by the experimental plot. However, the ultimate strength of the numerical specimen was 615.57MPa, with a maximum strain of 0.036. Consequently, the model ultimate strength is only 1.7% lower than the 626.56MPa which is recorded in the experiment. Nevertheless, the observed ultimate strains remain the same for both the numerical and the experimental program. Finally, the results obtained from this ABAQUS model indicate that the mechanical and constitutive properties of main steel rebars are reliable, and can properly simulate the real specimens.

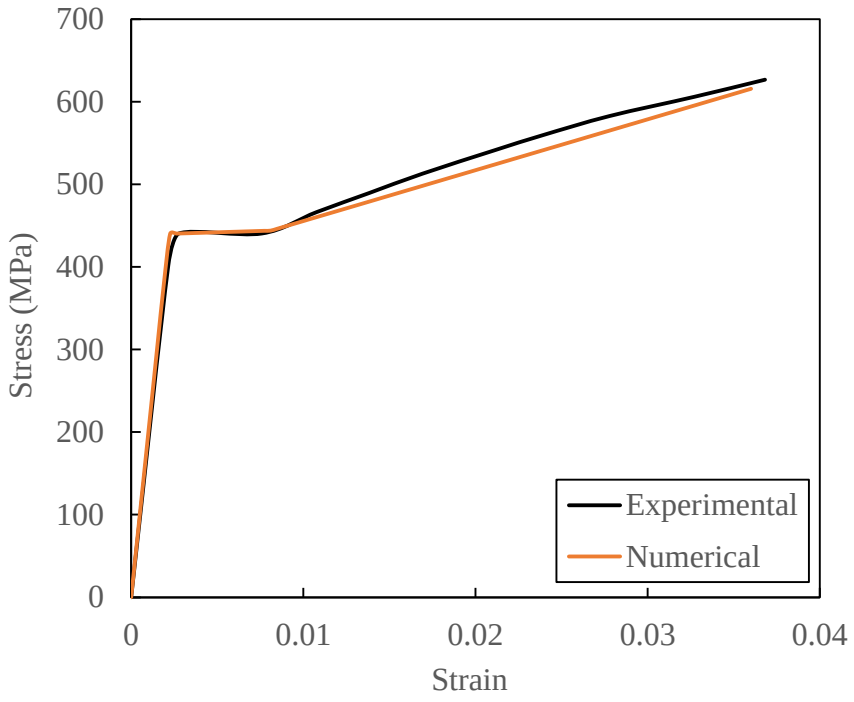

Figure 5.4: Tensile stress-strain relationship for steel rebar ($\emptyset = 16mm$)

5.2.3 CFRP-Concrete Interface

It has been proven that when using FRP laminates or sheets to enhance flexural capacity of RC beams, FRP-concrete interface plays a significant role in maintaining ductility and reaching beam's ultimate capacity. The possible delamination of FRP composite is very brittle in nature, and thus must be avoided in practical applications. As indicated in Chapter two, mode II cracking and load discrepancies along beam length can lead to the debonding of FRP's. As a result, a sound interface law is critical to account for these scenarios and effectively predict the debonding response of FRP laminate. In this study, the interfacial region between the bottom face of the concrete beam and the top surface of the CFRP reinforcement was modelled by cohesive elements. The governing interfacial equations and the inputted parameters were tested and calibrated against an experimental study conducted by Mazzotti et al. (2008), as will be explained more in the following sections.

5.2.3.1 Experimental Specimen

Mazzotti et al. (2008) investigated the debonding of CFRP plates bonded to concrete surface by performing a "single shear pull-out" test. The tested concrete specimen was 600mm long, 150mm wide, and 200mm deep. This prism was fabricated by using normal strength concrete, with mean compressive strength, f_c', equals to 52.6MPa, Young's modulus value, E_c, of 30700MPa, and a Poisson's ratio, v, of 0.227. A CFRP plate, of 200mm length and 50mm width, was then attached to the top surface of the concrete specimen. The bonded plate was extended a certain distance away from the block front face to avoid generating stress concentrations at the contact corner. Moreover, the plate bonded length starts 100mm far from the front corner of specimen. This was done to ensure that debonding behaviour of CFRP plates is not affected by the boundary effects of the specimen. The concrete block was mechanically clamped with steel plates to prevent horizontal and vertical movements (see Figure 5.5). A series of 10 strain gauges were placed along the centerline of the CFRP plate, to measure axial strains. The test was carried out by applying an initial pullout load of 4kN on the free edge of the CFRP plate. The loading was then increased monotonically at a rate of about 0.1kN/s.

However, during the final stages of testing (i.e. during plate delamination) the loading was conducted under controlled-displacement mode (Mazzotti, et al., 2008).

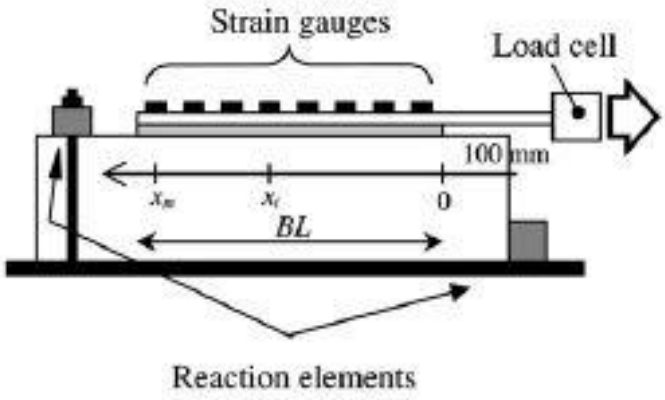

Figure 5.5: Experimental specimen test setup (Mazzotti, et al., 2008)

5.2.3.2 Model Preparation

The experimental specimen, described in previous section, was numerically tested using ABAQUS/CAE software. A three-dimensional finite element model was created based on the mechanical and physical properties of the tested specimen. Similar to the actual tested block, the FE model is comprised of two main parts: concrete and CFRP laminate. The concrete prism was created as 3D deformable solid entity, and the appropriate material definitions were assigned to it. This part was modelled with continuum elements (C3D8R), and given a (20x20mm) mesh size. Although the modelling process of the CFRP composite was similar to that of concrete, a smaller mesh size of (10x10mm) was used for this part due its relatively small geometry.

The debonding response of the CFRP plate was simulated by the use of Cohesive Zone Modelling technique (CZM). The CFRP-Concrete interface was modelled as an interaction surface, and a nonlinear traction-separation law was adopted for that purpose. The constitutive model proposed by Lu et al. (2005) was utilized once again to define the deboding response of the said interface. The initial stiffness parameter of this formula was calculated by equation (4–30) and found to be 1.53×10^6MPa/mm for normal stresses and 0.62×10^6MPa/mm for shear and traction stresses. The micro-debonding of CFRP plate was estimated to start when the

interfacial shear stresses reach 6.29MPa, based on equation (2–14). Moreover, the damage evolution parameter was set based on the effective displacement, δ_m^f, at point of failure. Equation (2–30) predicted a value of 0.23 mm for, δ_m^f, and the exponential rate parameter, α, was evaluated as 1.33. Finally, the composite system was constrained from all movements in the *x* and *y* directions, by identifying boundary conditions on the front and bottom faces of the block (see Figure 5.6). These constrains simulate the supporting configuration of the actual tested specimen. The model was then tested under monotonic loading until significant delamination of CFRP plate was observed.

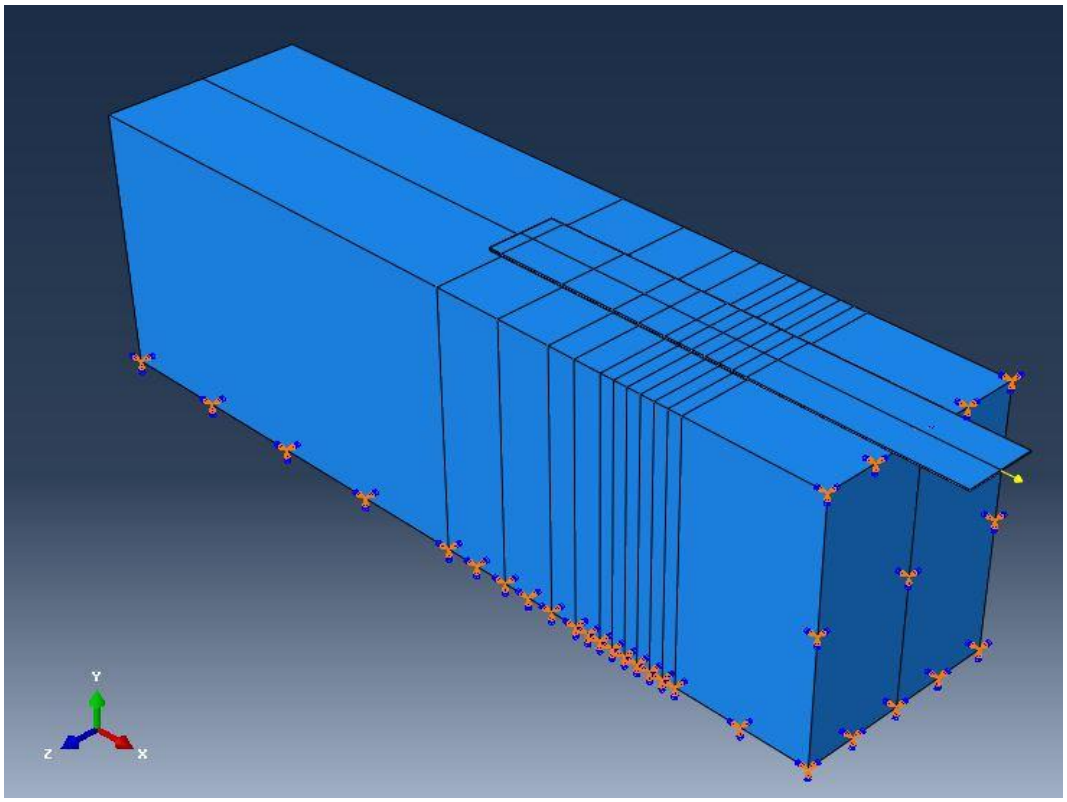

Figure 5.6: Boundary and loading conditions of the pullout-test model

5.2.3.3 Results Calibration

As indicated previously, the sole purpose of this numerical modelling is to validate the effectiveness and reliability of CZM technique used in this research. In addition, the nonlinear interaction laws used in creating the cohesive elements were also verified. The experimental

results presented by Mazzotti et al. (2008) plot the axial strains exhibited by the CFRP plate along the concrete block. These data were recorded by a series of strain gauges, glued to the surface of CFRP plate on certain intervals. Nonetheless, this response was plotted under six different loading stages (4, 8, 12, 16, 18, and 19.8kN), as can be seen in Figure 5.7. The results obtained from the finite elmenet model were compared to the expiremental data, and a good correlation was found between them. Despite the minor differeneces within the strain softening stages at higher loads, the ultimate strain points seem to be aligned very well.

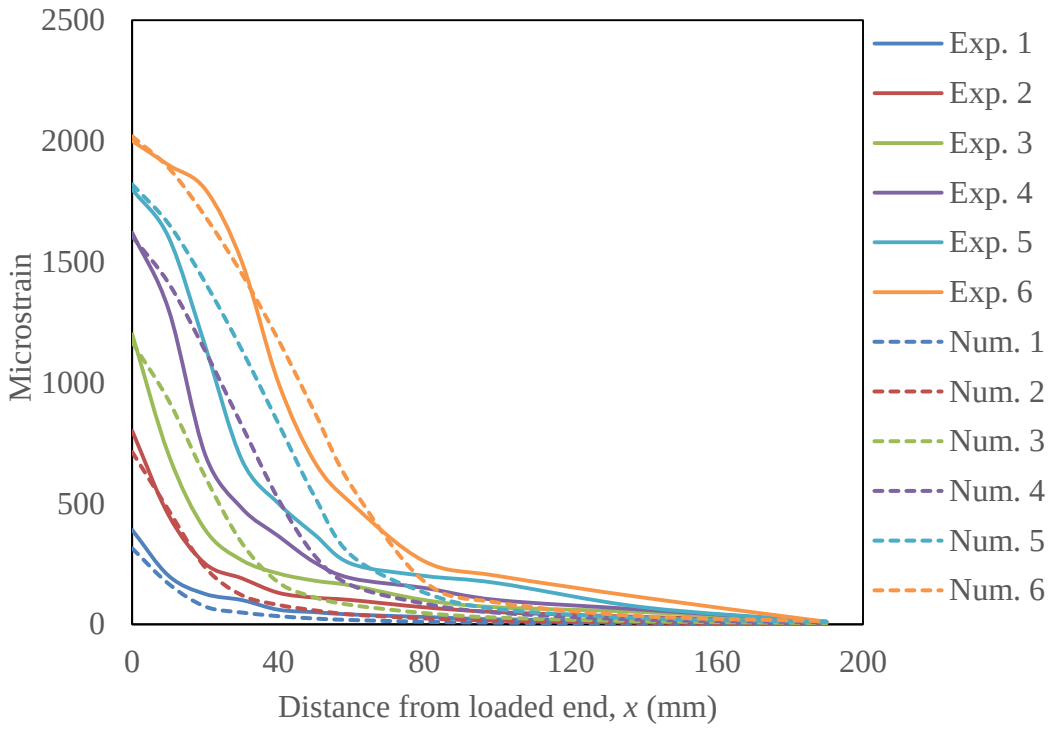

Figure 5.7: Comparison between the numerical and experimental axial strains along the bonded length

Furthermore, the development of interfacial shear stresses along the cohesive surface was graphed for the six loading stages. Figure 5.8 demonstrates a typical debonding response of CFRP-Concrete interface as the load progresses. The plots also show a clear resemblance to the constitutive traction-separation equation, predicted by Lu et al. (2005), and used in fabricating this model.

When the pullout load was applied on the CFRP plate, the shear stresses were concrnetrated at the loaded end of the plate near the front face of the block. The shear stresses become neglible as the load moves further into the plate, as can be noticed in Figure 5.8. More visible debonding of CFRP plate started to appear when the applied load reached 12kN. The debonding evolution of CFRP plate can be schematically expressed by the moving peaks of the curves away from the loaded end. As indicated before, each peak represents the ultimate bond stresses that can be resisted by the cohesive surface. Once the system sustains such stresses, micro-debonding take place between the concrete surface and the attached CFRP plate. The stresses then start to diminish until they become zero at the point of failure (macro-debonding stage). In summary, the interfacial stress profiles under the last three loading stages indicate significant delamination of CFRP plate, which was also experimentally detected.

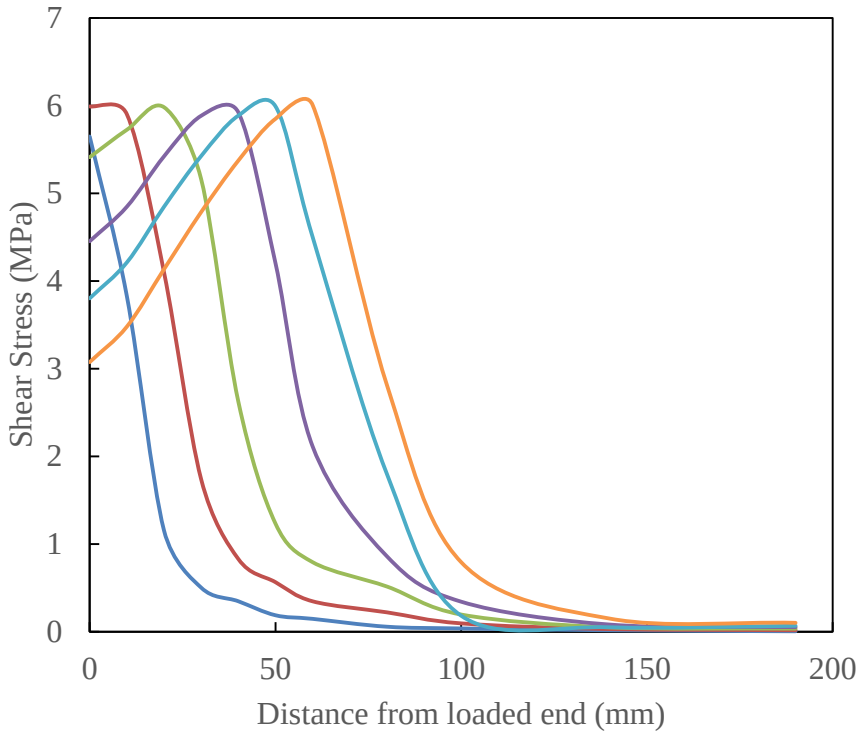

Figure 5.8: Shear stresses along the concrete-CFRP Interface for different loading stages

At the end of the analysis, it was observed that approximately 1/3 of the CFRP plate has experienced complete debonding from the concrete block, as can in Figure 5.9. Finally, the

numerical results obtained from the finite element model show a good agreement with the experimental data. Moreover, the nonlinear formula, which was used to formulate the cohesive surface, allowed for an accurate prediction of the potential debonding mechanism. Therefore, this comprehensive numerical analysis confirms that the Cohesive Zone Model method, used in simulating some of the CFRP-Concrete interfaces in this thesis, is valid. It also supports the ability of such technique to predict the debonding of CFRP laminate under Mode II loading.

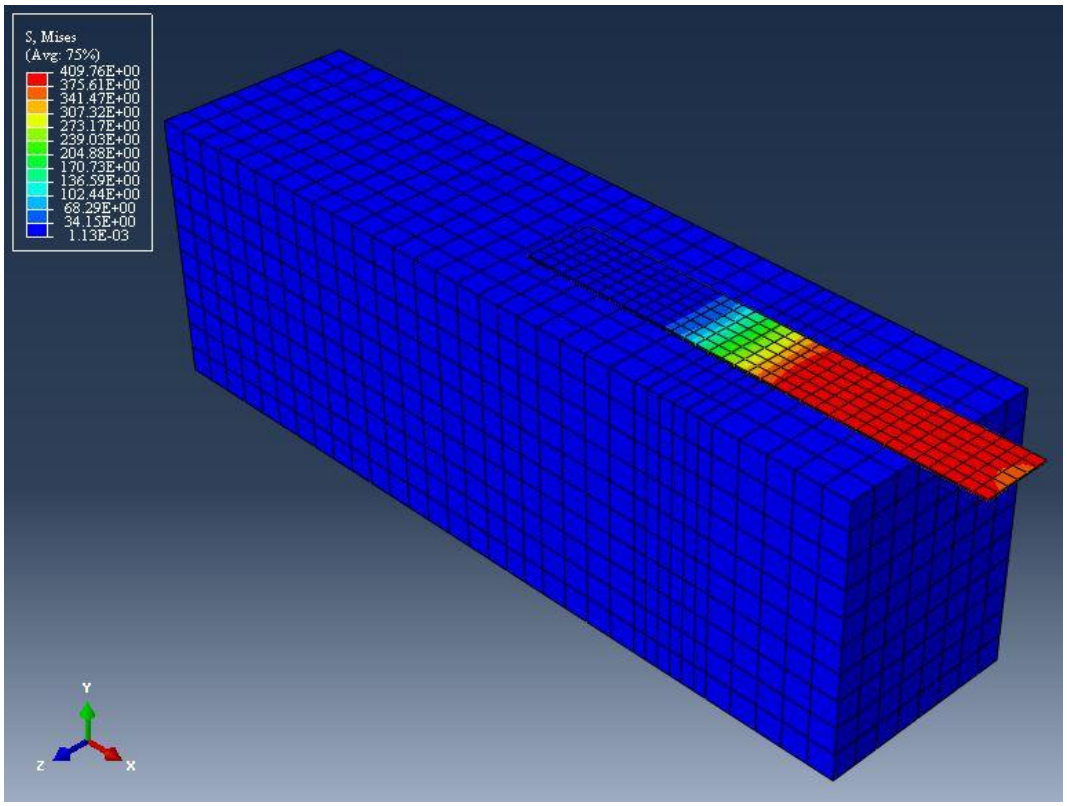

Figure 5.9: Final stage of tested pull-out specimen

5.3 Beam Models Verification

This section reviews the distinctions between the main beam models that are proposed in this thesis. A brief description of the modelling procedures and mesh analysis is also presented herein. Moreover, a thorough evaluation of the current numerical predictions against the

experimental data is made in the following sections. The aim of such numerical analysis is to determine the efficiency of each model against selected beams tested by Brena et al. (2003). The modelling approach used in Chapter four has produced three different beam models, which were fabricated based on actual beam specimens. The database consists of Control Beam, CFRP Beam (with perfect bond assumption), and finally CFRP Beam (with Cohesive Zone Model). As mentioned in previous chapter, the tested beams were subjected to four-point loading conditon. The control concrete beam was construted without any FRP reinforcemenmt, while externally bonded CFRP laminate was added to the substrate of the CFRP beams.

In addition to the mesh analysis conducted on each model, the flexural capacity of each model was evaluated by measuring its "load-deflection' response. A comparative analysis was made between the numerical and experimental load-deflection profiles. Furthermore, the typical load-deflection plot of the studied specimens can be described by Figure 5.10.

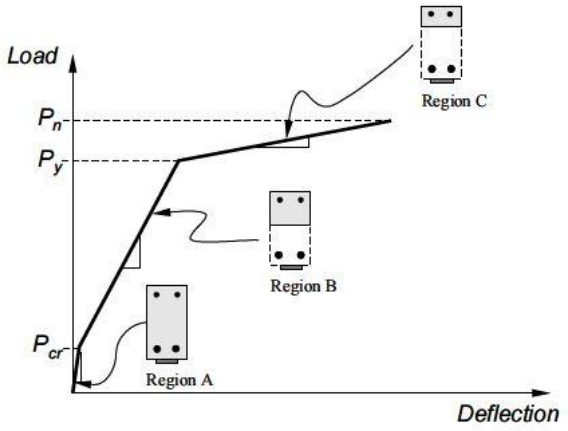

Region	Material Behavior		
	Concrete	Reinforcement	CFRP
A	Uncracked	Elastic	Elastic
B	Cracked	Elastic	Elastic
C	Cracked	Yielding	Elastic

Figure 5.10: Schematic representation of the typical load vs deflection response of the CFRP beams (Brena, et al., 2001)

In this figure, three distinct regions are observed. Each region is represented schematically by a line with a slope that depends on the flexural stiffness of the composite beam. The first region reflects the elasticity of the beam, and ends when first cracks start to form. The second region is bounded by the cracking load and the load at which steel reinforcements yield. Finally, region three represents the remaining stiffness of the beam to the point of ultimate capacity.
As stated before, the slope of the load-deflection curve in each region is governed by the stiffness of the composite beams. The flexural stiffness of region A can be calculated by using gross cross-sectional properties of the beam, because the specimen remains uncracked at this stage. In region B, the flexural stiffness of the beams corresponds to cracked concrete and elastic behaviour of both internal (steel) and external (CFRP) reinforcements. Therefore, the slope of curve in this region is governed by the amount of steel and CFRP composites used in beams. On the other hand, the stiffness of region C is controlled by the stiffness of the CFRP laminate and the strain hardening stiffness of steel rebars.

5.3.1 Control Beam Model

The beam analyzed in this section was modelled by ABAQUS using the calibrated Concrete Damage Plasticity (CDP) model. The geometry and material definitions used in this model, inspired by the control beam in Brena et al. (2003) report, are extensively described in Chapter four. To reiterate, this beam model consists of concrete, main steel reinforcement, and steel stirrups. To simulate the experimental testing configuration, a static load was assigned to this analysis with a small time step of 0.01. However, four different meshing criteria were followed in manufacturing each control beam model. Mesh size was changed in order to examine the effect of smaller elements on the convergence and the overall performance of the proposed models. The selected mesh sizes for this analysis vary from coarse (size 30x30) mm and (25x25) mm to finer mesh (size 20x20) mm and (15x15) mm. The model with the largest mesh consists of 2720 elements and 3952 nodes, while the one with finest mesh have 16054 elements and 19540 nodes. The breakdown of each model, in terms of element types and numbers is summarized in Table A-1 of Appendix A. However, it must be noted that the global mesh size of the model was determined by the element size of the largest component in the specimen (i.e.

concrete). While an element size of (10x10) mm was set for the steel reinforcements and the two bearing plates in all control beam models. During the postprocessing stage of the finite element modelling, the response of the proposed models was recorded and compared to the experimental data, as shown in Table 5.1.

Table 5.1: Critical loading points (Control Beam Model)

Specimen	Cracking		Yielding		Capacity	
	Load (kN)	L.R.*	Load (kN)	L.R.	Load (kN)	L.R.
Experimental	29.40	1.00	100.50	1.00	130.80	1.00
Mesh 30x30	41.20	0.71	100.80	1.00	119.23	1.10
Mesh 25x25	42.38	0.69	100.90	1.00	120.04	1.09
Mesh 20x20	46.27	0.63	102.79	0.98	120.43	1.09
Mesh 15x15	52.45	0.56	102.15	0.98	120.16	1.09

* L.R.: load ratio calculated as the experimental load divided by the predicted numerical load

The resisted load for each model was recorded at three critical points: cracking, yielding of main steel rebars, and finally when the beam reached its ultimate capacity. The predicted values were then compared to the experimental data to evaluate the accuracy of the FE models. The load ratio (L.R.) in Table 5.1 can be used to indicate how the numerical model performed. For a given load response, if this ratio was greater than 1.0 that means the proposed model underpredicted the load relative to the experimental specimen. On the other hand, if the ratio was less than 1.0 then the numerical model overpredicted the loading response. Moreover, the load versus midspan deflection response was plotted for each individual model, as seen in Figure 5.11(a) through (d). It can be observed that the strength and deformation capacity of the numerical models varied depending on the element size used in each model. However, it must be noted that all four beam models overpredicted the cracking and yielding loading compared

to the experiment. This can be attributed to two reasons: possible irregularities in the actual test, or convergence instability of FE model due to lack of sufficient restraints in the plain beam which allows for more cracking to occur in concrete. More details about this justification will be made in section 5.4. Control beam model with mesh size (30 x 30) mm overestimated the cracking and yielding loads by 40.34% and 0.27%, respectively. Whereas, the largest difference was observed in the model with finest mesh size (15 x 15) mm. the cracking and yielding loads were overpredicted by 78.66% and 1.61%, respectively in the fine mesh model. Nonetheless, the finite element model underestimated the ultimate capacity of the control specimen by as low as 8.82% for model with coarse mesh size (30 x 30) mm. The closet estimation of the ultimate strength load was recorded in the beam model with mesh size (20 x 20) mm. This model predicted the beam to fail at 120.43kN, compared to 130.8kN of the actual control beam.

The axial strains were also studied for the bottom steel rebar, and calibrated against the corresponding data from the tested specimen. In the actual experiment, the strains of embedded steel rebars were recorded by strain gauges placed on the steel surface. These strain gauges were located at a position that is aligned with the point of applied load. Similarly, the axial strains of the steel rebars in the numerical models were recorded at the same location (loading point), as can be seen in Figure 5.12. It is noted that strain profiles in the FE models match closely the response of steel reinforcement in the actual beam. It is worth mentioning that possible dissimilarities can been observed in strain plots between numerical and experimental data, due to testing environments which might impact the strain gauges reading and performance.

Finally, the crack pattern of each model at final stage of loading was depicted in Figure 5.13. Although Brena et al. (2003) did not report the experimental crack patterns of the beams, the authors indicated that debonding initiated at a main flexural crack located near the loading point and then propagated toward the plate ends. This phenomenon was also observed in this proposed model. The crack patterns at different loading stages was captured in Figure A-1 through Figure A-4 in Appendix A. The loading stages, at which the observations were made,

included: the cracking of concrete, at a midspan deflection of 5mm, the yielding of steel rebar, and finally at a midspan deflections of 20mm and 47.2mm, respectively.

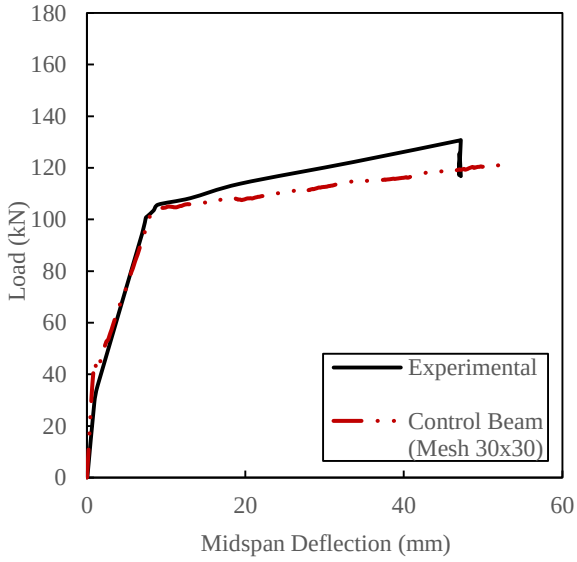

(a) Mesh (30 x 30) mm

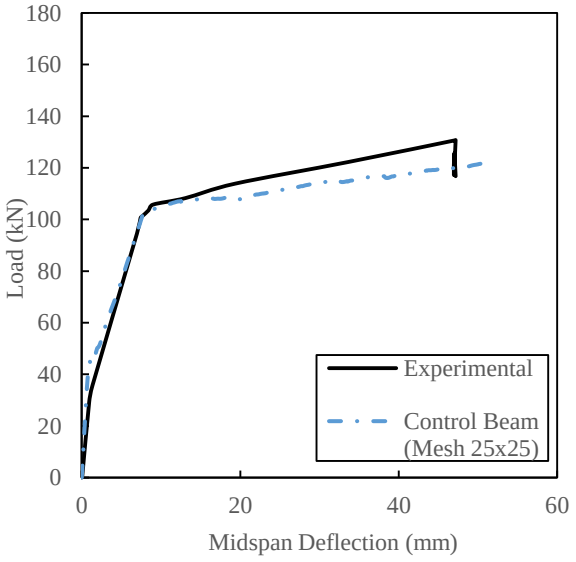

(b) Mesh (25 x 25) mm

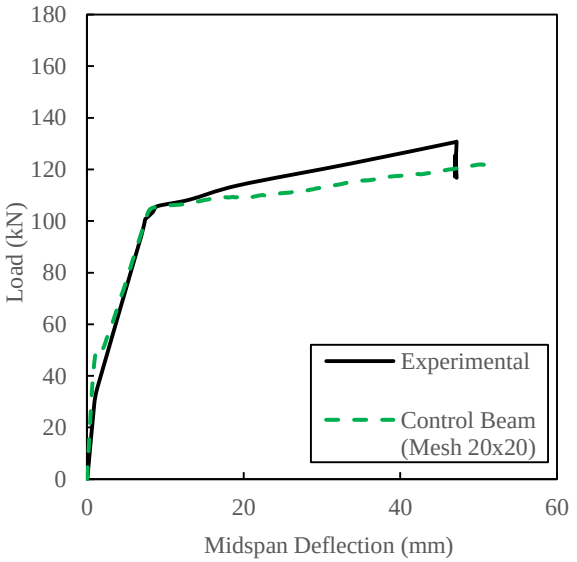

(c) Mesh (20 x 20) mm

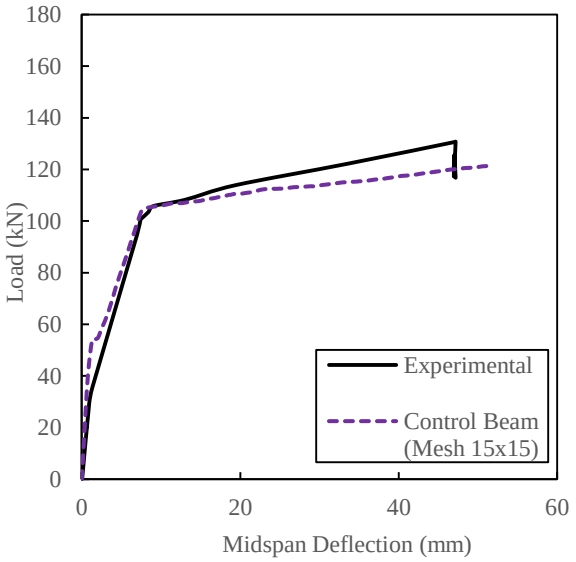

(d) Mesh (15 x 15) mm

Figure 5.11: Load vs midspan deflection response (Control Beam Model)

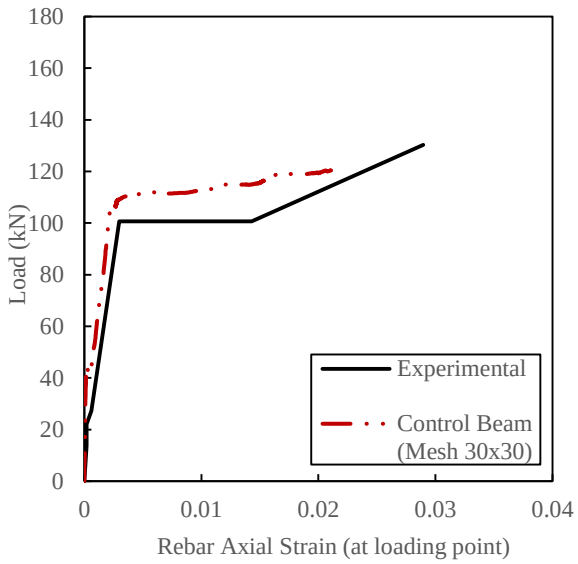

(a) Mesh (30 x 30) mm

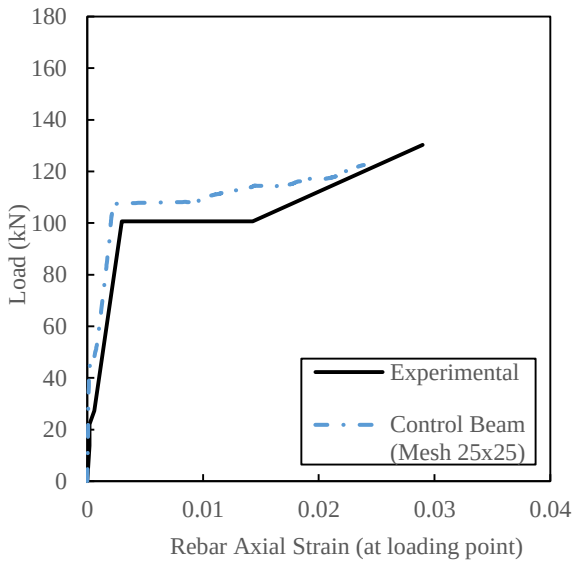

(b) Mesh (25 x 25) mm

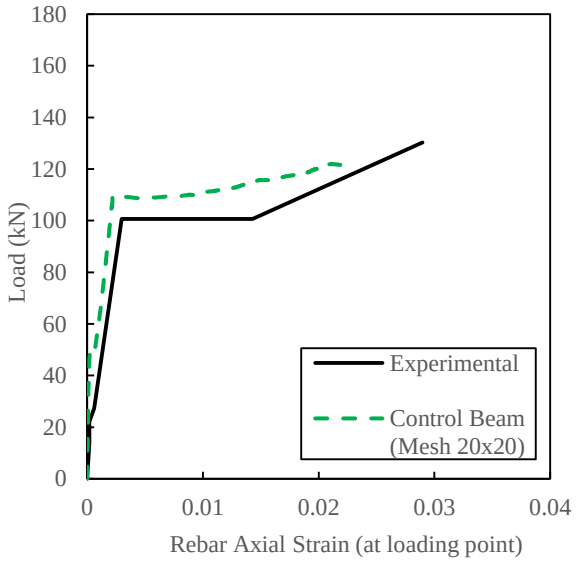

(c) Mesh (20 x 20) mm

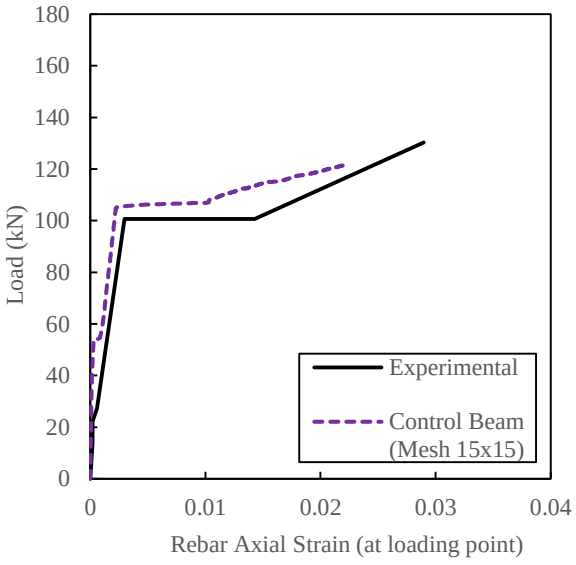

(d) Mesh (15 x 15) mm

Figure 5.12: Axial strain in steel rebar (Control Beam Model)

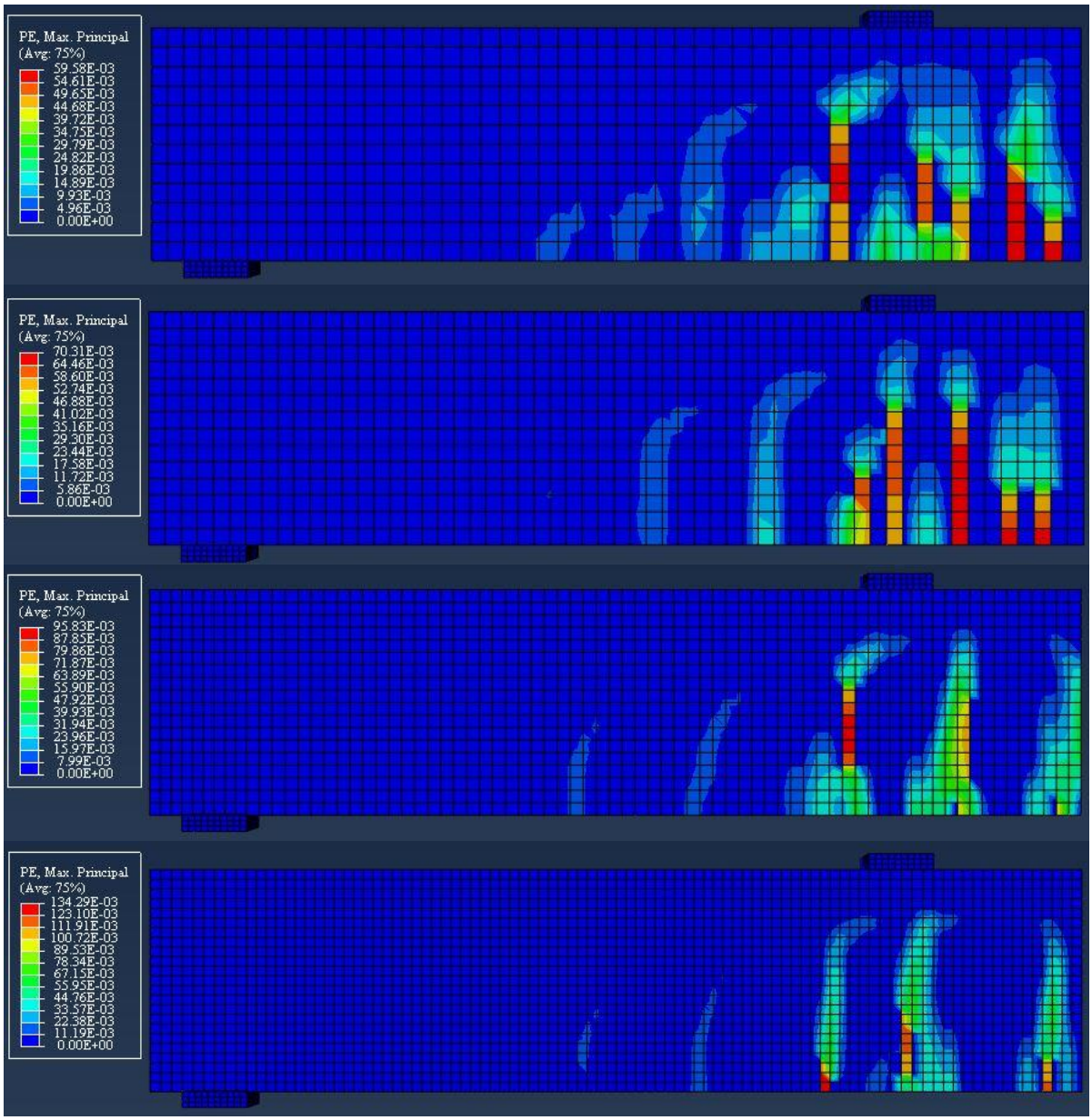

Figure 5.13: Comparison of crack patterns at final stage (Control Beam Model)

5.3.2 CFRP Beam Model (Perfect Bond Assumption)

This finite element model was created identical to the control beam described in previous section, with the exception of adding CFRP external reinforcement. The geometry and mechanical properties of the CFRP laminate are based on specimen A4 from the experiment. As in the Control Beam Model, a static loading condition and a time step of 0.01 were used in this model. The distinct characteristic of the current proposed model is the assumption of perfect bond between the bottom surface of concrete and the attached CFRP laminate. As mentioned before, this sort of mechanism can be incorporated into the ABAQUS model by using the "tie constraints" tool. This type of constraint basically links two regions with different geometry and /or meshes so that there is no relative motion between them. The mesh analysis conducted on this specimen incorporated the same meshing criteria as in the last model. The coarse mesh size (30 x 30) mm was built by 3116 elements, while the finest mesh of size (15 x 15) mm used 16450 elements. The complete description of element types and numbers used in each mesh density is provided in Table A-2. On the other hand, the flexural response of proposed model was analyzed and calibrated with the experimental response (see Table 5.2).

Table 5.2: Critical loading points (CFRP Beam Model, Perfect Bond Assumption)

Specimen	Cracking		Yielding		Capacity	
	Load (kN)	L.R.*	Load (kN)	L.R.	Load (kN)	L.R.
Experimental	37.4	1.00	110.8	1.00	129.0	1.00
Mesh 30x30	38.22	0.98	105.92	1.05	124.37	1.04
Mesh 25x25	39.09	0.96	105.36	1.05	125.58	1.03
Mesh 20x20	42.21	0.89	107.14	1.03	124.04	1.04
Mesh 15x15	47.44	0.79	110.29	1.00	124.37	1.04

L.R.: load ratio calculated as the experimental load divided by the predicted numerical load

The loads at the three critical points (cracking, yield, and ultimate) were recorded and normalized with the experimental data. It can be seen that the current model overpredicted the cracking loads as compared to the experiment as high as 26.97% for the fine mesh of (15 x 15) mm. However, the yielding of steel occurred at an earlier stage than the actual beam, as can be seen in Table 5.2. Mesh (15 x 15) mm matched the yielding response of the experiment very closely. In terms of the ultimate load of the beam, the coarsest and finest mesh predicted similar beam capacity, which was 3.5% lower than the actual test. While, the closest representation of the failure load was produced by model (mesh 25 x 25 mm), with only 2.64% underestimation. The longitudinal strains in streel rebars at the loading location were plotted in Figure 5.14(a) through (d). Beam model with mesh size (30 x 30) mm provided the best presentation of the actual strain in streel reinforcements, followed by beam with mesh (15 x 15) mm. The strains in the other two models can be characterized by the lack of strain hardening response, immediately after the yielding of rebar. This behaviour can be justified by the additional capacity of perfectly-attached CFRP laminate to carry the load, which it turn might idle the steel performance.

A new strain profile was added in this model, which captures the axial deformation endured by CFRP laminate. The plot was again drawn to each individual mesh density, and the readings were taken at a point underneath the loading location to simulate the actual strain gauges positions. From Figure 5.15(a) through (d), the best prediction of strain activities in CFRP plate is given by the models with mesh size (30 x 30) mm and (15 x 15) mm. Moreover, the lack of close representation of steel axial strain in mesh size (25 x 25) mm and (20 x 20) mm is compensated by their close predication of strains in CFRP laminate.

Figure 5.17 illustrates a comparison between the crack patterns for the various mesh densities in the proposed CFRP beam model. It can be seen that the cracks captured in this model are smaller in size as compared to those in the Control Beam Mode. This is however expected when adding external reinforcement such as CFRP laminate, as they tend to bridge the cracks and prevent them from widening. Finally, Figure A-5 through Figure A-8 show more details about cracking patterns that were captured at different loading stages (e.g. cracking, midspan

deflection of 5mm, steel rebar yielding, midspan deflections of 12mm and 19mm, respectively).

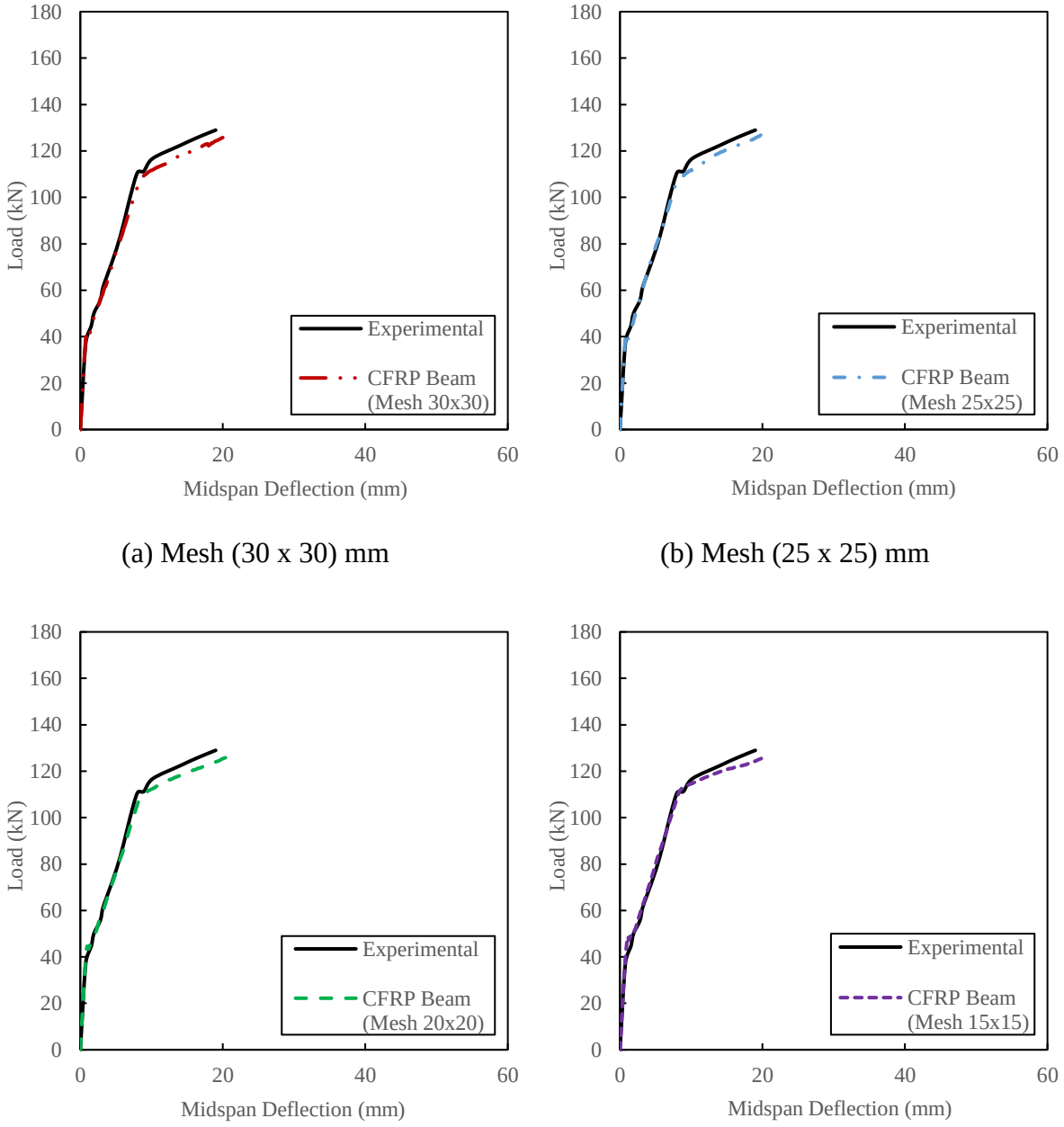

(a) Mesh (30 x 30) mm

(b) Mesh (25 x 25) mm

(c) Mesh (20 x 20) mm

(d) Mesh (15 x 15) mm

Figure 5.14: Load vs midspan deflection response (CFRP Beam Model, Perfect Bond)

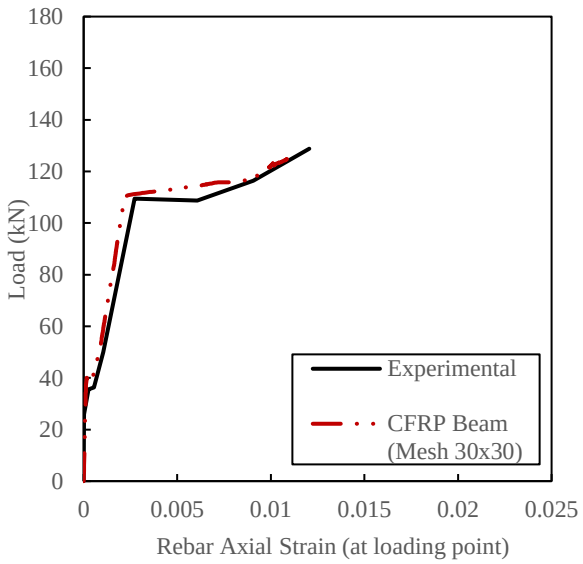

(a) Mesh (30 x 30) mm

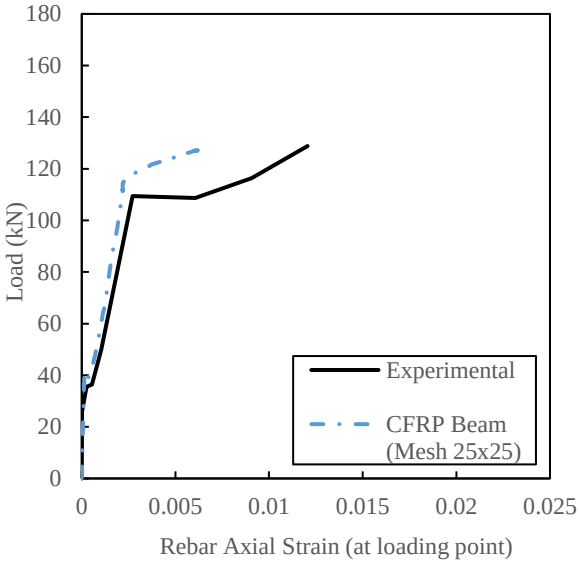

(b) Mesh (25 x 25) mm

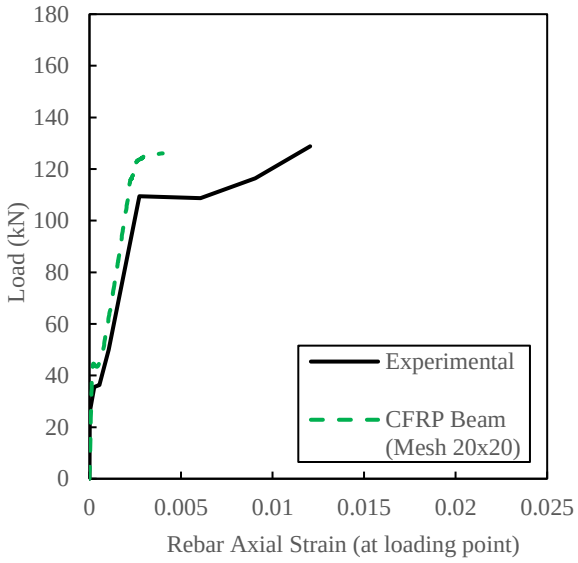

(c) Mesh (20 x 20) mm

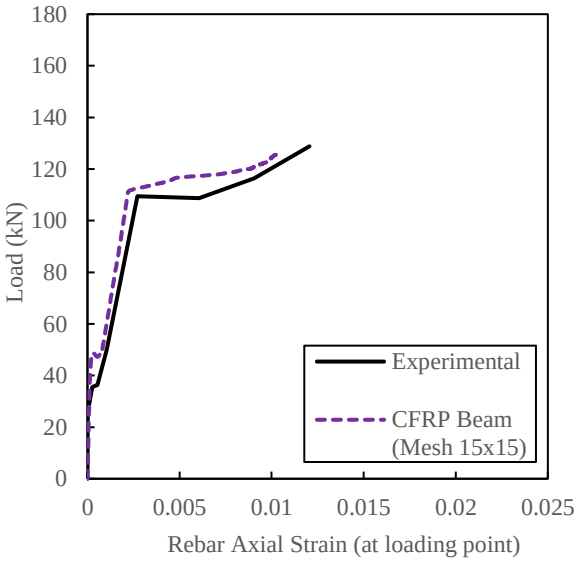

(d) Mesh (15 x 15) mm

Figure 5.15: Axial strain in steel rebar (CFRP Beam Model, Perfect Bond)

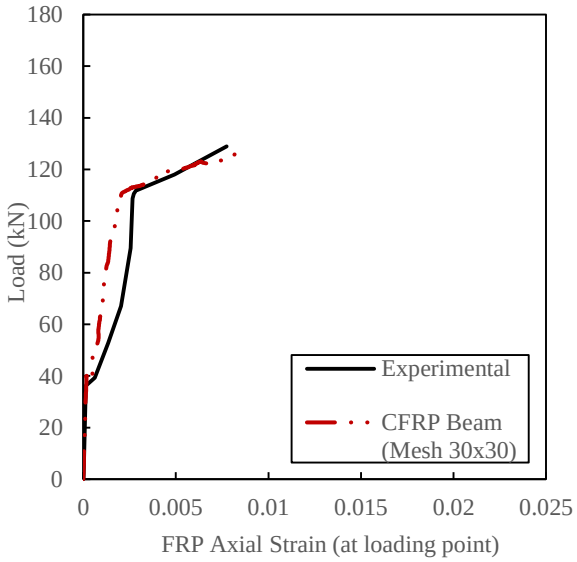

(a) Mesh (30 x 30) mm

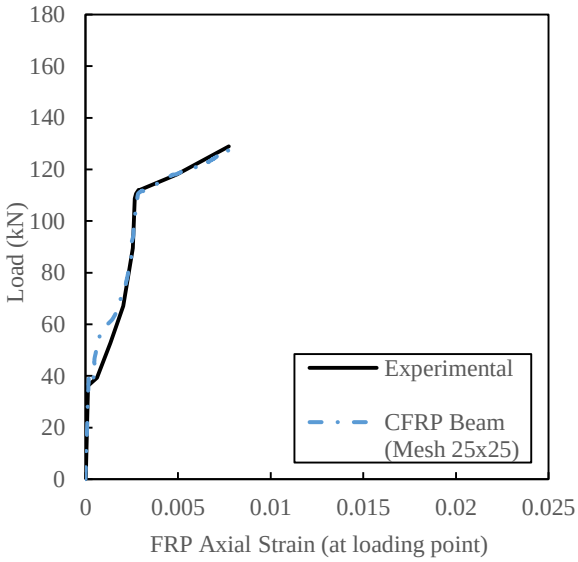

(b) Mesh (25 x 25) mm

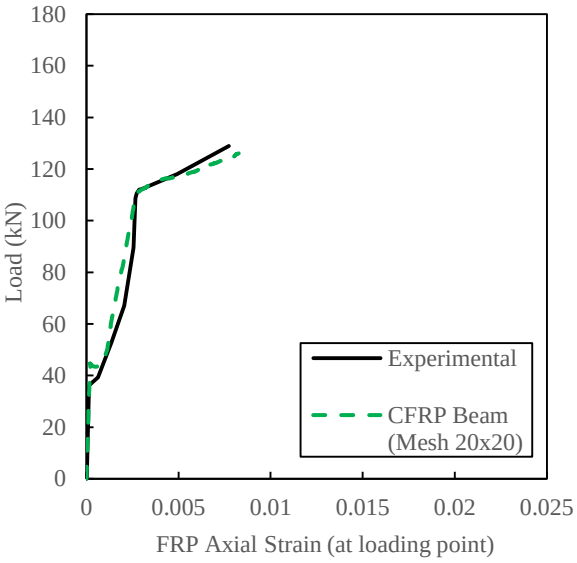

(c) Mesh (20 x 20) mm

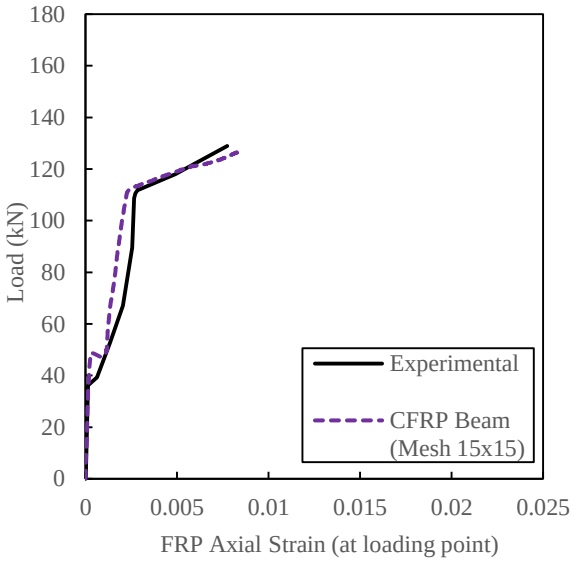

(d) Mesh (15 x 15) mm

Figure 5.16: Axial strain in CFRP laminate (CFRP Beam Model, Perfect Bond)

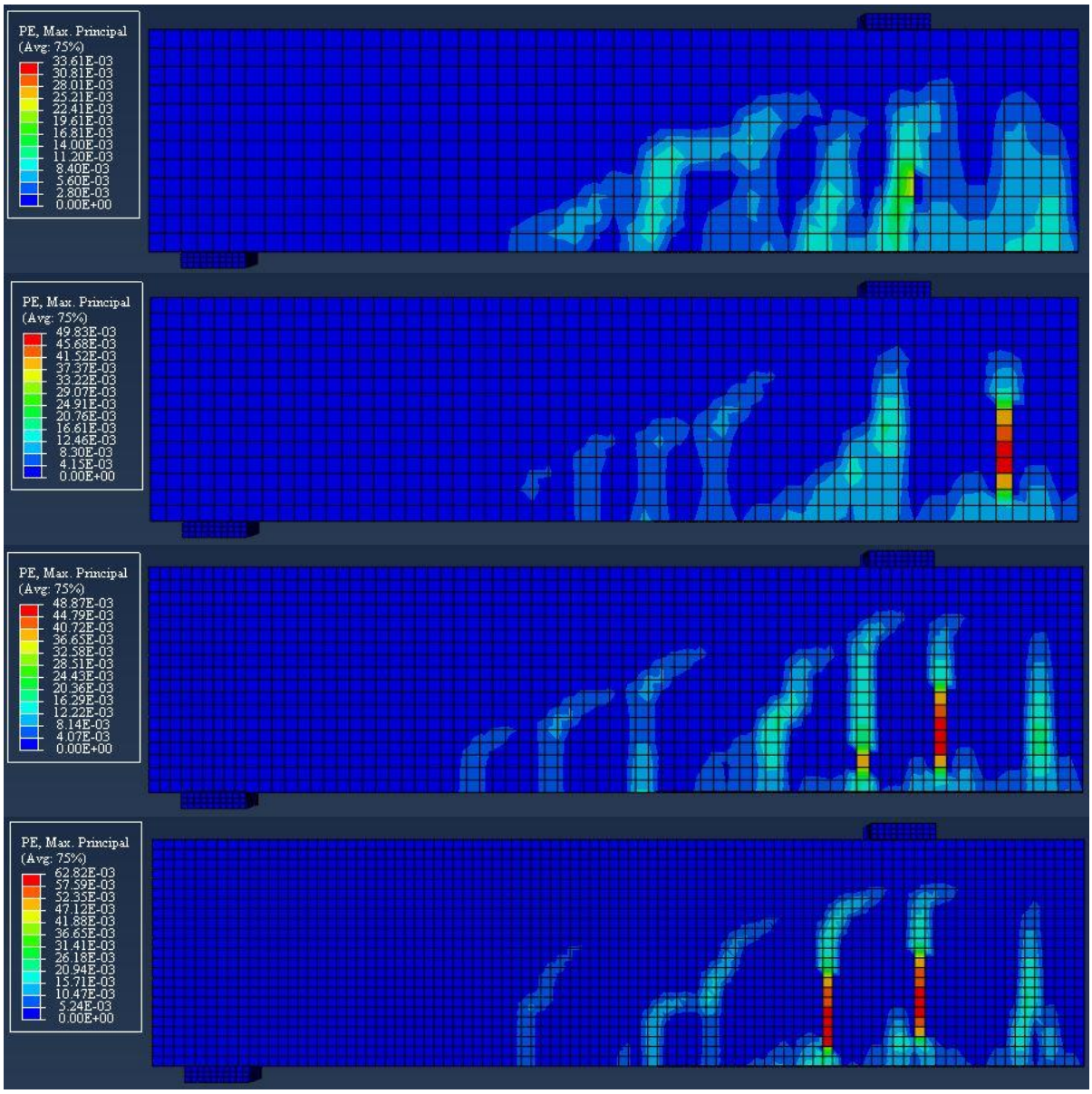

Figure 5.17: Comparison of crack patterns at final stage (CFRP Beam Model, Perfect Bond)

5.3.3 CFRP Beam Model (Cohesive Zone Model)

This model is the final one in this series, and it was constructed in a similar fashion to the specimen in the pervious section. Similarly, the physical properties of this model and the mechanical parameters of the constitutive materials are those of beam A4 in Brena et al. (2003) experimental program. A static loading was applied to this model , and the size of step time was increased to 0.1 to enhance convergence and reduce computational time. On the other hand, the CFRP-Concrete interface was simulated by using the Cohesive Zone Model approach, to simulate any potential slippage between the concrete and the CFRP laminate.The mechanism and the governing equations of this technique was explained comprehensively in Chapter four. It must be noted that a different procedure was followed to mesh this model as compared to the last two beams. The region of concrete confined by the perimeter of CFRP plate was meshed using a smaller sized elements. This was done to improve convergence quality in highly small parts such as the thin CFRP laminate. The description of element types and numbers used in this mesh study are shown in Table A-3. Moreover, the flexural response was recorded during the postprocessing stage of the FE analysis, as summarized in Table 5.3.

Table 5.3: Critical loading points (CFRP Beam Model, Cohesive Zone Model)

Specimen	Cracking		Yielding		Capacity	
	Load (kN)	L.R.*	Load (kN)	L.R.	Load (kN)	L.R.
Experimental	37.4	1.00	110.8	1.00	129.0	1.00
Mesh 30x30	44.32	0.84	109.78	1.01	127.38	1.01
Mesh 25x25	44.18	0.85	112.13	0.99	127.78	1.01
Mesh 20x20	46.67	0.80	113	0.98	127.04	1.02
Mesh 15x15	49.05	0.76	111.37	0.99	126.56	1.02

L.R.: load ratio calculated as the experimental load divided by the predicted numerical load

It is worth mentioning that a significant improvement in simulation capability was shown by this model, in comparison to the Control Beam and CFRP Beam (Perfect Bond) Models. The closest prediction of cracking load was shown by mesh size (25 x 25) mm, with only 18.24% difference to the experimental value. However, the finest mesh of size (15 x 15) mm overestimated the cracking load by the highest margin (31.27%), similar to the response of the same mesh size in last two models. Nonetheless, with the exception of mesh size (30 x 30) mm, this model slightly overpredicted the yielding response of steel reinforcements in test with only 2.2kN difference seen in mesh size (20 x 20) mm. Most importantly, the ultimate load prediction of the current model was the most accurate between the three proposed beam models. Mesh size (25 x 25) mm predicted the failure of beam at 127.38kN, with only 0.93% difference to the actual beam.

The axial strains in steel rebars, at the loading location, were drawn in Figure 5.19(a) through (d). In this model, the closest prediction was provided by mesh size (25 x 25) mm and (20 x 20) mm, respectively. While, the strain response of the remaining two models were brittle in nature and did not exhibit strain hardening. This incomplete strain response of steel can be attributed to the delayed debonding of CFRP laminate in these meshes, which means additional loads are being mostly carried by the CFRP system instead of steel rebars.

The strain response of CFRP laminate at loading positions are plotted in Figure 5.20(a) through (b). In general, the CFRP strain predictions in this model are more representative of the actual material. This enhancement was expected when the interfacial region between concrete and external CFRP plate was modelled using CZM technique. In another word, accounting for possible slippage between the two adjacent materials provides a more realistic performance as compared to the use of perfect bond assumption in section 5.3.2. Beam model with mesh size (20 x 20) mm and (25 x 25) mm presented the best simulation to CFRP strains.

The crack patterns were compared at the final loading stage between the four mesh densities, as can be shown in Figure 5.21. There are minor dissimilarities in crack presentation within the beam region bounded by CFRP plate, as mesh size was reduced in this area to improve convergence. The more detailed crack patterns for each mesh size are illustrated in Appendix A (see Figure A-9 through Figure A-12). The same loading stages, as in previous model, were

used to plot these crack patterns. Moreover, Figure A-13 depicts the debonding evolution of CFRP plate, which was allowed by the use of CZM technique in this model.

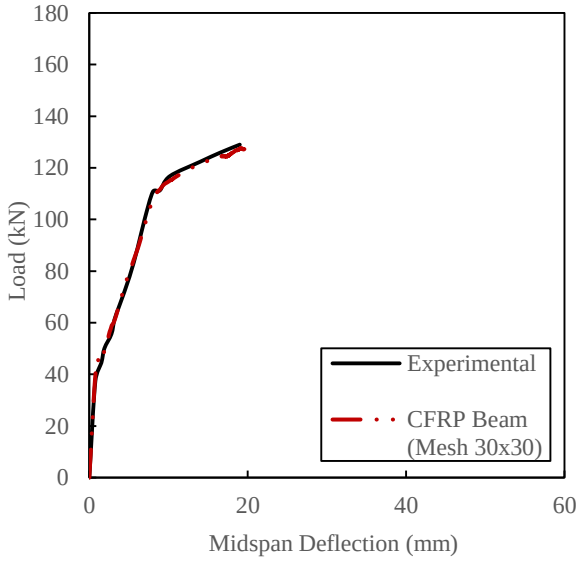

(a) Mesh (30 x 30) mm

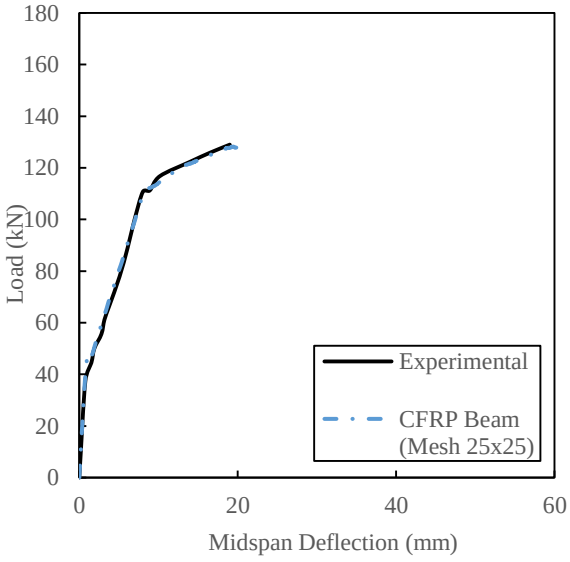

(b) Mesh (25 x 25) mm

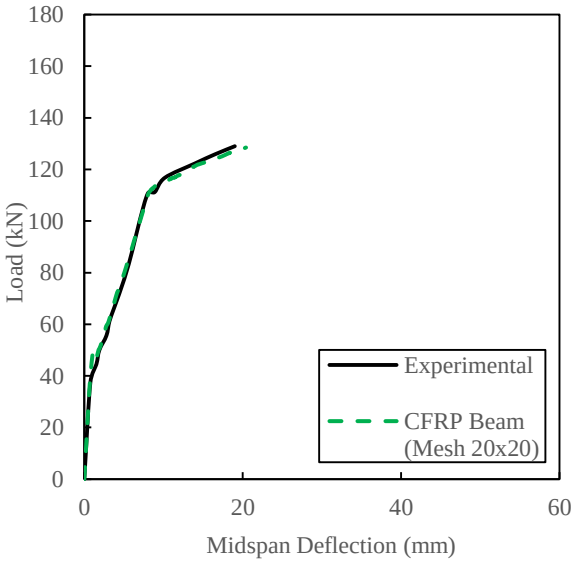

(c) Mesh (20 x 20) mm

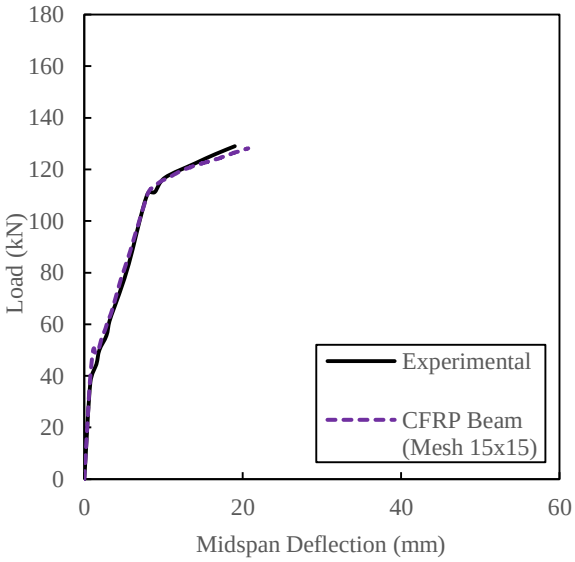

(d) Mesh (15 x 15) mm

Figure 5.18: Load vs midspan deflection response (CFRP Beam Model, CZM)

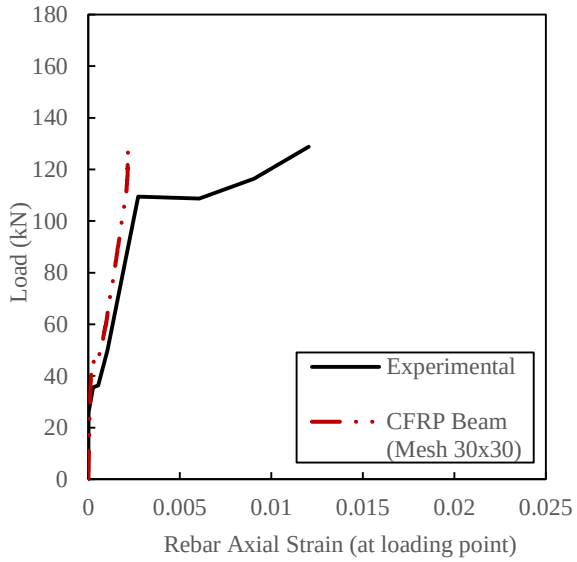

(a) Mesh (30 x 30) mm

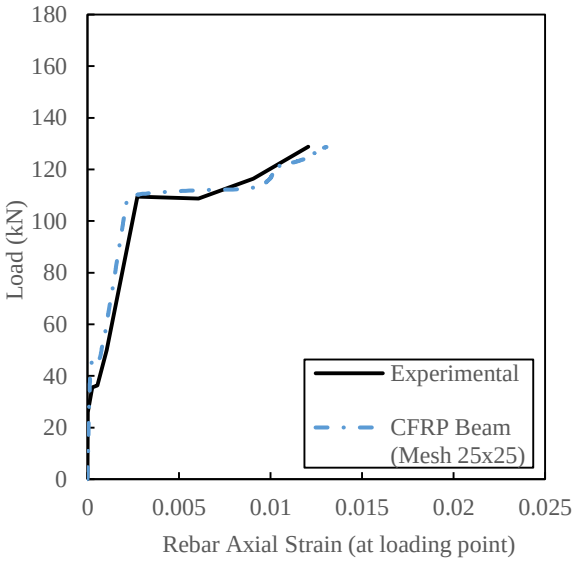

(b) Mesh (25 x 25) mm

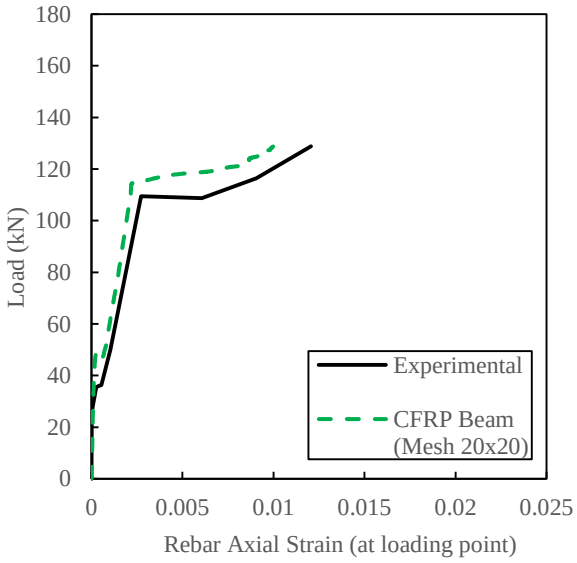

(c) Mesh (20 x 20) mm

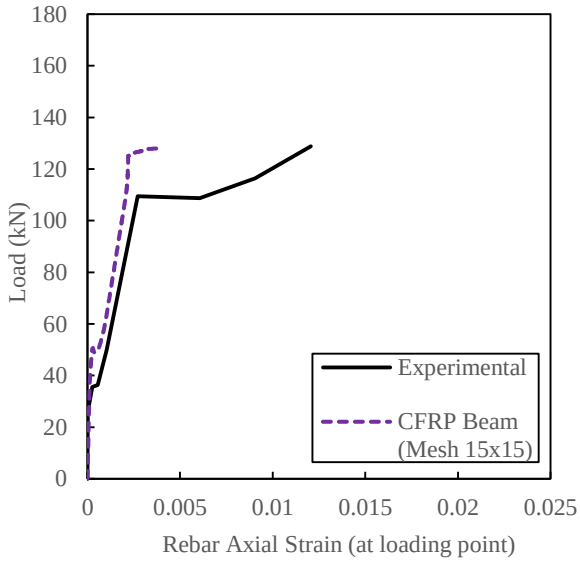

(d) Mesh (15 x 15) mm

Figure 5.19: Axial strain in steel rebar (CFRP Beam Model, CZM)

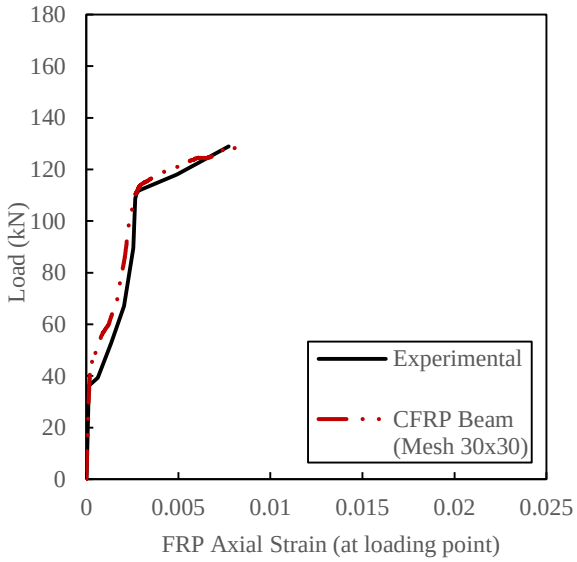

(a) Mesh (30 x 30) mm

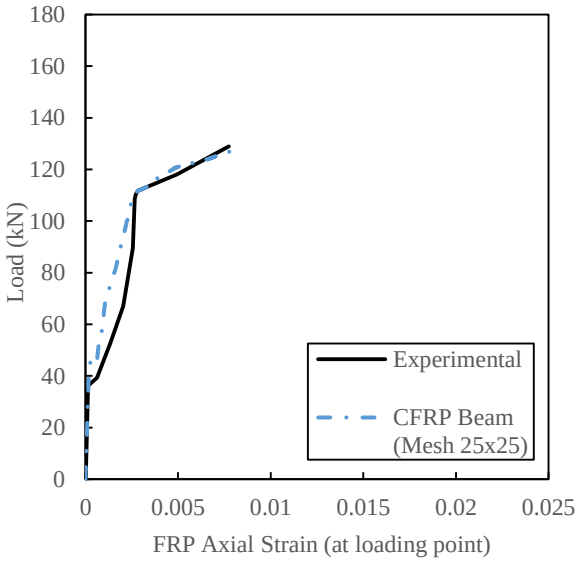

(b) Mesh (25 x 25) mm

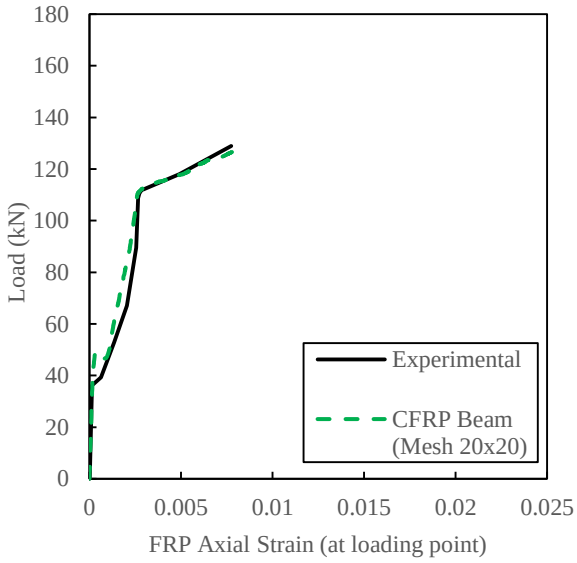

(c) Mesh (20 x 20) mm

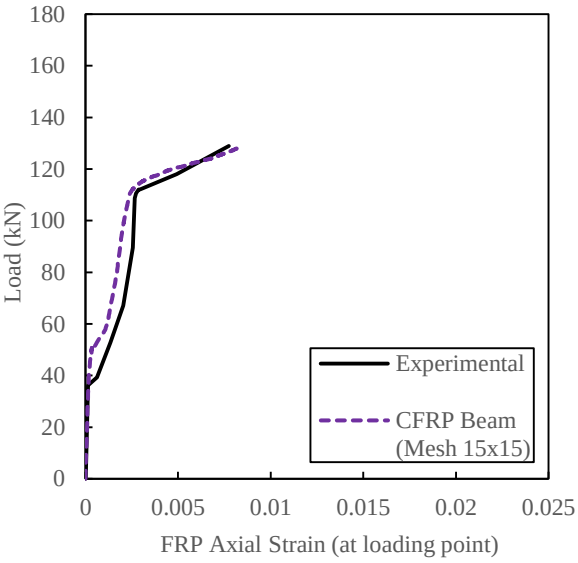

(d) Mesh (15 x 15) mm

Figure 5.20: Axial strain in CFRP laminate (CFRP Beam Model, CZM)

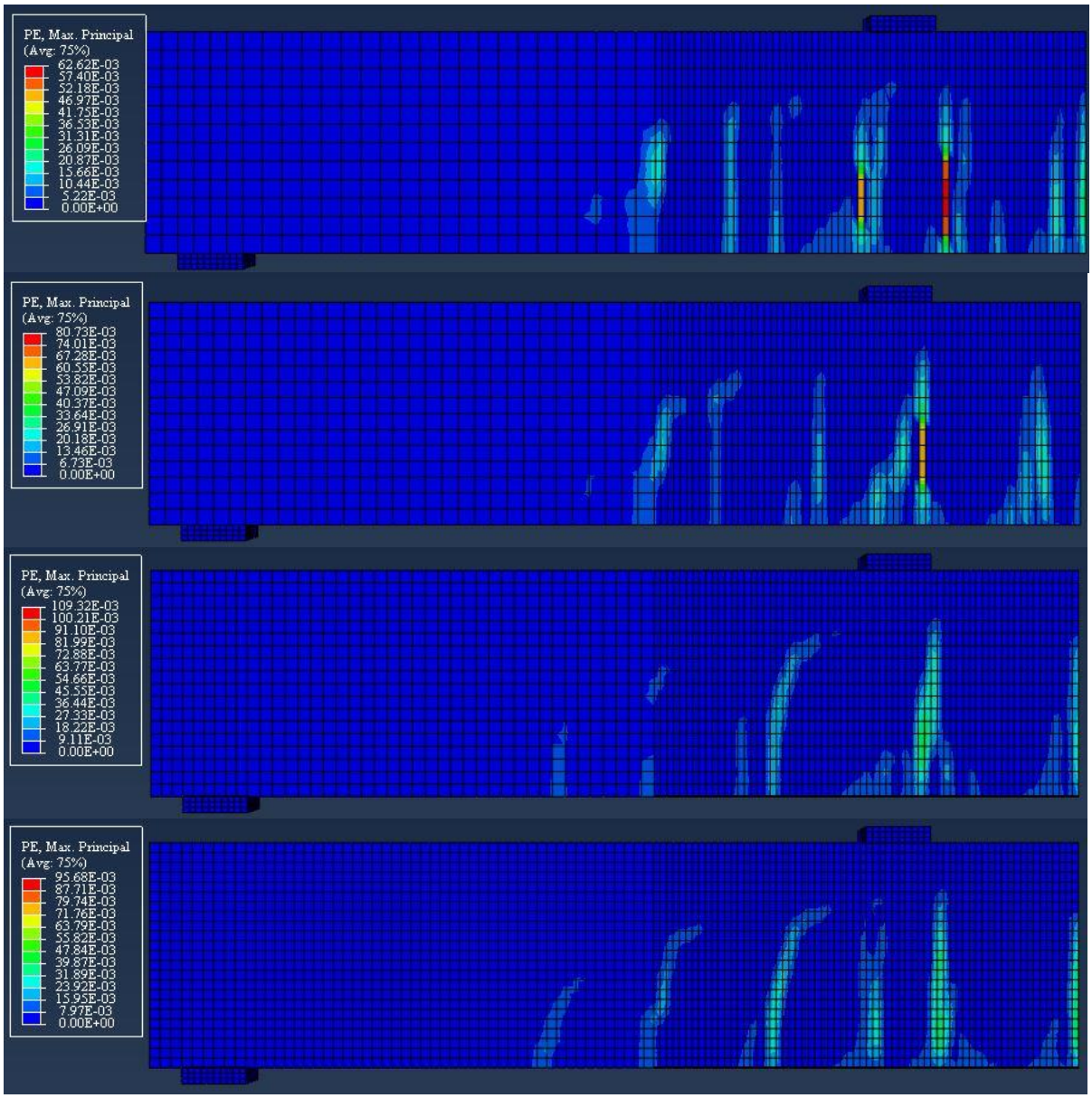

Figure 5.21: Comparison of crack patterns at final stage (CFRP Beam Model, CZM)

5.4 Summary

It has been observed that cracking and yielding loads for all three proposed models were either overpredicted or underpredicted, depending on mesh size and procedure followed to model CFRP-Concrete interface. However, the ultimate load capacity of the experimental control and CFRP beams was underestimated by the proposed ABAQUS models in this chapter. As seen in the Control Beam Model, all mesh sizes provided ultimate load predictions that were within 9% of the experimental results. However, the difference between the simulation and the actual ultimate capacity was narrower for the CFRP Beam Models. The specimen with perfect bond assumption predicted the failure load within 4% range. Whereas, the model with CZM provided the closest estimate, and the kept the estimate at 2% range.

It must be said that the flexural response of different mesh densities presents a consistent trend for all proposed beams in this section. When finer mesh is utilized, the pre-peak response of the proposed beam model becomes stiffer. This trend contradicts the expected outcome of mesh refinement where smaller mesh size yields less restraint to nodal displacements, and hence less stiff response. However, this observation was made by other researchers such Malm (2006) and Stoner (2015). In addition to these studies, ABAQUS manual suggets that such mesh sensitivities can be expected in regions of concrete with little or no reinforcemnet. The absence of reinforcemnet can lead to uneven distribution of cracking failure which in turn leads to possible localization of craking. This narrow and localized crack bands can prevent the model from converging to a unique solution as the mesh size is decreased. Moreover ABAQUS manual stated that three-dimensional models are more vulnerable to experience mesh sensitivity, due to out-of-plane cracking (Stoner, 2015).

Nevertheless, it is noted that the prediction of the FE model has improved by the addition of CFRP laminate, when compared to the Control Beam Model. Furthermore, the mesh sensitivity issues, which led to stiffer beams with the refinement of mesh, are avoided in this model. The localization of cracking in concrete due to the absence of constraints are dampened or eliminated by the presence of CFRP system. However, this enhancement in the predicted flexural response was more superior in CFRP Beam Models with CZM, as relative to the beam

with perfect bond assumption. On the other hand, the strain deformations in both steel rebars and CFRP laminates were captured in this analysis, and calibrated with their corresponding data in the experimental program. Although some of the predicted strain profiles of steel rebars were more sensitive to mesh size and cohesive surface design, a close prediction can still be reached by changing elements size and using CZM method. Nonetheless, the simulation of strain response in CFRP plates for most of the FE models was found in a good agreement with the actual tested CFRP composite.

The final stage of this numerical analysis was designated to review the crack patterns observed in each model. The cracking of concrete for each mesh density was illustrated at five stages as the load increases. Moreover, it can also be seen in Figure A-1 through Figure A-12 in Appendix A that all mesh densities accurately capture the presence of diagonal shear cracks in beams. These cracks were represented by large plastic strains, extending from the load point to the support. In addition, with the refinement of the mesh, the crack pattern remains the same, but the crack bands become narrower and better defined.

Finally, the outcome of this modelling analysis and the calibration of the numerical results have confirmed the validity of the proposed models in this thesis. It further reflects the effectiveness of the adopted modelling parameters and techniques in simulating the debonding response of externally-attached CFRP in concrete beams.

Chapter Six

Parametric Study

6.1 Introduction

The analysis in this chapter is an extension to the numerical program described in Chapter five. In the last two chapters a comprehensive finite element study, of concrete beams strengthened with external FRP reinforcements, was presented. Initial recommendations were made concerning the effect of some of the beam parameters on the prediction's accuracy of the ABAQUS models. In another word, the advantage of considering concrete plasticity, the appropriate tension and compression constitutive equations, and the damage behaviour, was previously introduced during the modelling process. Moreover, the effect of accounting for the interfacial behaviour between concrete and CFRP plates was also observed. Extensive mesh analysis was also conducted on each models, to acquire the best simulation of the relative experimental program. Therefore, it can be safely presumed that the failure mode, ductility, and flexural capacity of FRP-strengthened RC beams are sensitive to changes in geometric and material parameters.

This chapter mainly examines the effect of common physical and mechanical parameters on the flexural and debonding response of CFRP-strengthened RC beams. Based on the demonstrated accuracy of the proposed FE models, a numerical parametric study was performed in the following sections. The findings of this analysis will add to the contributory nature of the developed ABAQUS models, and may provide some implications for future design codes.

6.2 Scope and Objective of Study

Three models were initially proposed in previous chapters, but the main focus was given to the CFRP Beam Model with CFRP-Concrete cohesive surface. This particular model was chosen to further investigate the effect of local (constitutive material) and global (geometric) parameters on the CFRP beam behaviour. The numerical and mesh analysis conducted in section 5.3.3 has led to the conclusion that the beam model with mesh size (25 x 25) mm produced the most accurate replication of the experimental specimen. Therefore, this model was selected for this parametric study and referred to as "Reference Model". The initial material and geometric properties were unchanged, in order to have a base model for comparison. Similar to the approach followed in previous chapters, the analysis represented herein is that of only one quarter of the beam due to symmetry. The loading criteria and the step time size were kept the same (i.e. static load with step size = 0.1).

The primary objective of this parametric study was to investigate the effect of changing some of the parameters related to the concrete material, such as: concrete compressive strength, f_c', concrete dilation angle, ψ, and viscosity parameter, μ. The impact of excluding one or both damage parameters (e.g. compression and tension damage) is also examined. The ratio of main steel reinforcement, ρ, was part of the current analysis. On the other hand, some of the constitutive (e.g. interfacial shear strength, τ_f) and geometric (e.g. L_f, B_f) properties of the external CFRP reinforcing laminate was also investigated. Furthermore, the effect of removing shear steel reinforcement (stirrups) was reviewed, to pave the way for part of the modifications that will be applied to the CFRP Beam model next chapter. The developed stages of this parametric study are summarized in Table 6.1. Finally, the overall outcome of this parametric study will be summarized at the end of this chapter.

Table 6.1: Summary of concrete parameters used in this study

Study Mode	f_c' (MPa)	ρ (%)	Concrete Plasticity	Damage Parameter	τ_f (MPa)	B_f (mm)	L_f (mm)	Stirrups
I	20 30 50 70	0.86	$\psi = 30^o$ $\mu = 0.0002$	Compression & Tension	5.49	100	661	✓
II	37.2	0.45 0.63 1.27 1.54	$\psi = 30^o$ $\mu = 0.0002$	Compression & Tension	5.49	100	661	✓
III	37.2	0.86	$\psi = 20^o$ $\psi = 50^o$ $\mu = 0.00001$ $\mu = 0.001$	Compression & Tension	5.49	100	661	✓
			$\psi = 30^o$ $\mu = 0.0002$	No damage Compression Tension				
IV	37.2	0.86	$\psi = 30^o$ $\mu = 0.0002$	Compression & Tension	1.5 3 7 10	100	661	✓
V	37.2	0.86	$\psi = 30^o$ $\mu = 0.0002$	Compression & Tension	5.49	60 80 140 180	661	✓
VI	37.2	0.86	$\psi = 30^o$ $\mu = 0.0002$	Compression & Tension	5.49	100	400 500 800 1000	✓
VII	37.2	0.86	$\psi = 30^o$ $\mu = 0.0002$	Compression & Tension	5.49	100	661	×

6.3 Results Analysis

The effect of each parameter was demonstrated by comparing the load-midspan deflection response of each model to the reference beam. In addition, the tensile strains along the steel rebar and the CFRP laminate was also illustrated for each model. These axial strain deformations were plotted with the aid of "path" tool in ABAQUS. This feature allows to specify the points/nodes on which the strains are extracted. Finally, similar to the analysis procedure in last chapter, the crack pattern and evolution was captured and compared in each beam. The following sections provide an analytical review on the results of this parametric investigation.

6.3.1 Effect of Concrete Compressive Strength

There is a clear need in the current literature to develop a comparative study about the impact of concrete compressive strength on CFRP beam response. The influence of this parameter was studied by changing the value of f_c', while maintaining all the other mechanical and physical properties constant. Four values were utilized in defining the compressive strength of concrete in this parametric study: 20, 30, 50, and 70MPa. Consequently, the material definition of concrete in ABAQUS has to be modified to include the new compressive and tensile behaviour, as well as the damage evolution parameters. Furthermore, the load versus midspan deflection output of each model was compared to the corresponding response of the reference model, as shown in Figure 6.1.

It is evident from this analysis that the compressive strength of concrete has a profound impact on the flexural performance of the CFRP beam. This influence can be translated into significant increase or decrease in service and ultimate loads of the beam, depending on the used value of f_c'. As expected, the lowest response was observed in the model where $f_c' = 20MPa$ is used. The cracking, yielding, and ultimate loads resisted by this model was decreased by 19.3%, 5.07%, and 7.63%, respectively. On the other hand, the use of $f_c' = 70MPa$ has shown an increase of 34.2%, 3.97%, and 5.04% in recorded cracking, yielding, and ultimate loads, respectively. It must be noted that the effect of changing concrete compressive strength was

more prominent on cracking loads of the CFRP beams. This can be attributed to the improved concrete capacity under tension, which is proportionately related to the value of f_c'. However, once the concrete reaches its tensile strength and cracks take place, the internal (steel) and external (CFRP) reinforcements carry most of the load.

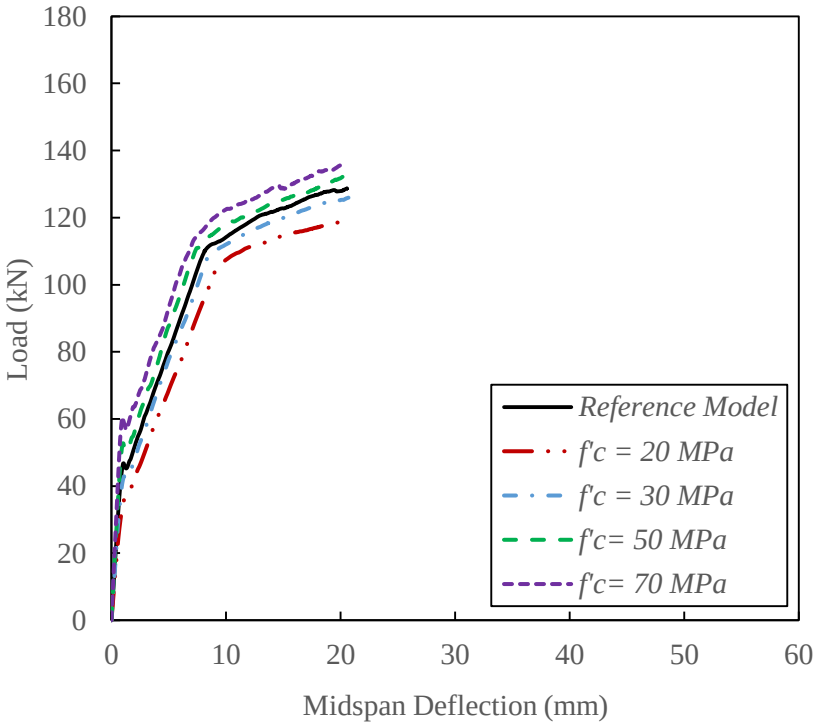

Figure 6.1: Load vs midspan deflection curve (effect of concrete compressive strength, f_c')

On the other hand, the tensile strains in steel rebar were recorded along the bottom surface of the rebar (to simulate the standard location of strain gauges). The plots introduced in Figure 6.2(a) through (b) compare the strain deformations, at the beam ultimate capacity stage, between the models with different f_c' and the reference CFRP beam. It is shown that the steel rebar in the original model exhibited the highest strains at a location that is approximately underneath the loading point. However, the strains in the first two models were relatively close to the original data. Whereas, increasing the concrete compressive strength beyond 50 MPa has shifted the strains in steel rebar toward the beam midspan.

Similar strain response was detected in CFRP laminate, as depicted in Figure 6.3(a) through (b), with higher strains recorded near the beam centre for models with f_c' larger than 50MPa.

Finally, Figure 6.4 presents the crack pattern shown in each model at the final loading stage, with more detailed illustration introduced in Appendix B (see Figure B-1 through Figure B-4).

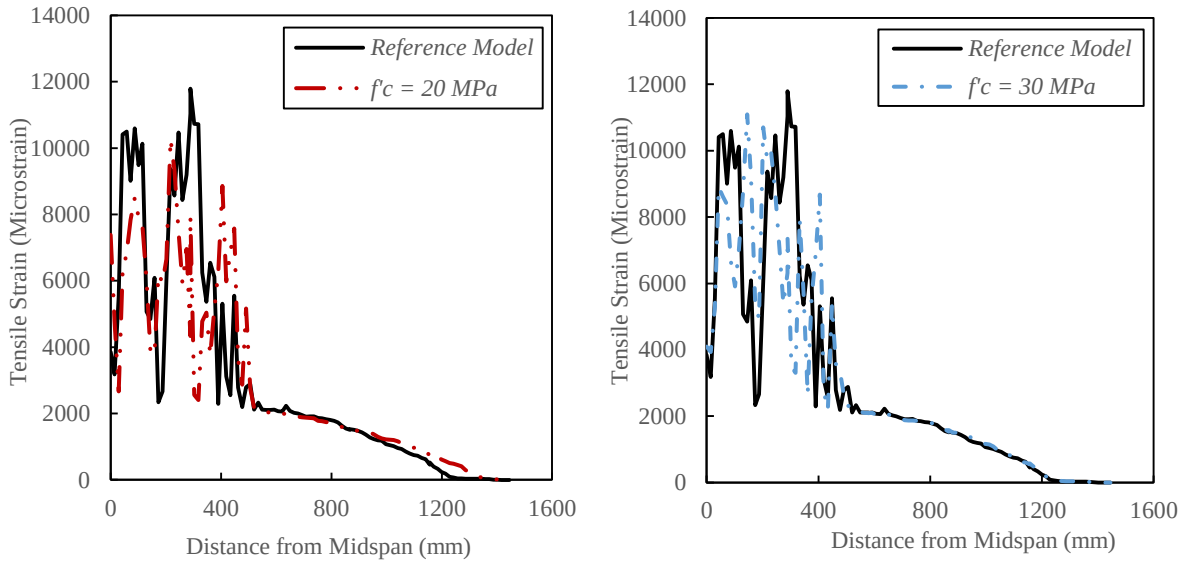

(a) $f_c' = 20\ MPa$

(b) $f_c' = 30\ MPa$

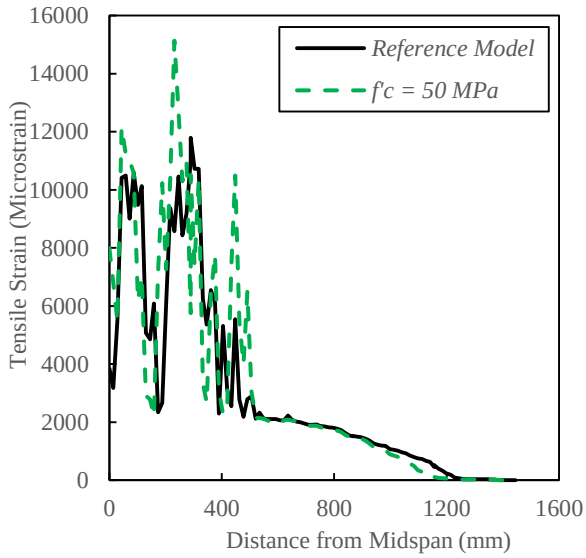

(c) $f_c' = 50\ MPa$

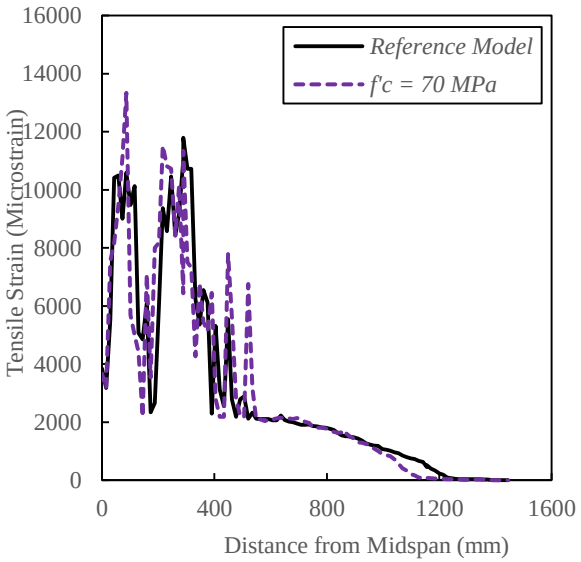

(d) $f_c' = 70\ MPa$

Figure 6.2: Axial strain in steel rebar (effect of concrete compressive strength, f_c')

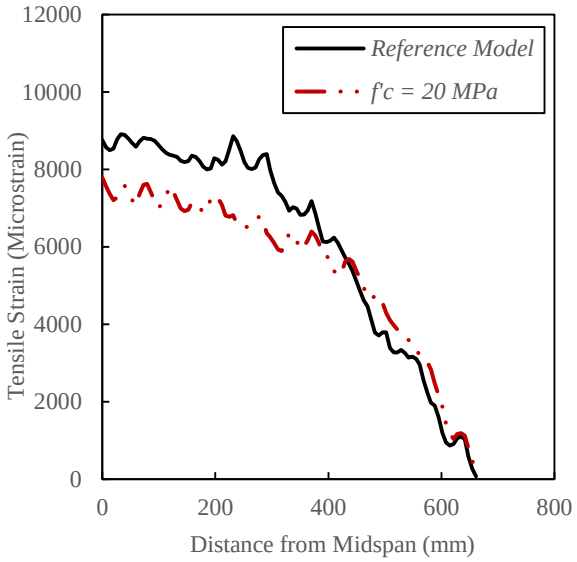

(a) $f_c' = 20\ MPa$

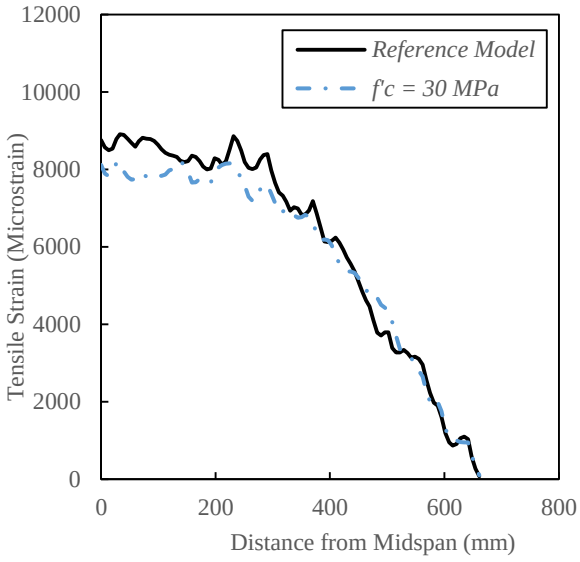

(b) $f_c' = 30\ MPa$

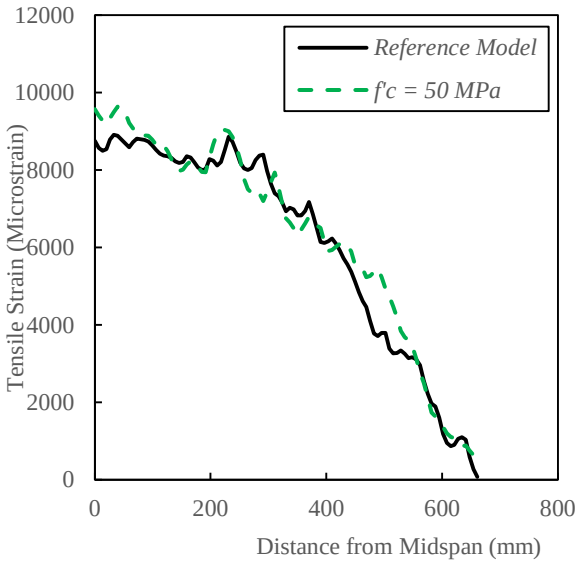

(c) $f_c' = 50\ MPa$

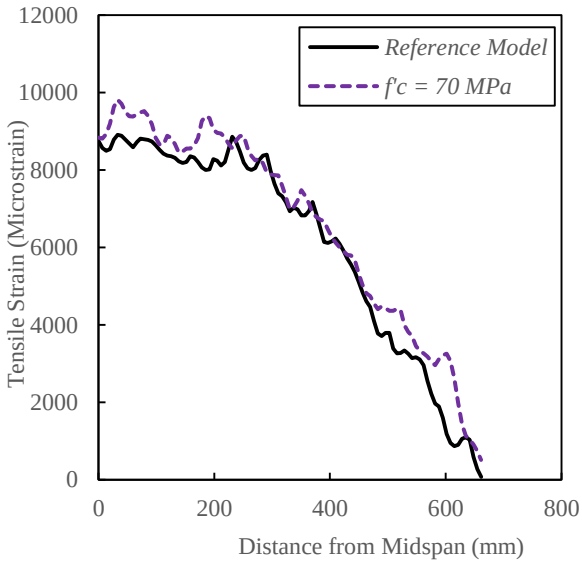

(d) $f_c' = 70\ MPa$

Figure 6.3: Axial strain in CFRP laminate (effect of concrete compressive strength, f_c')

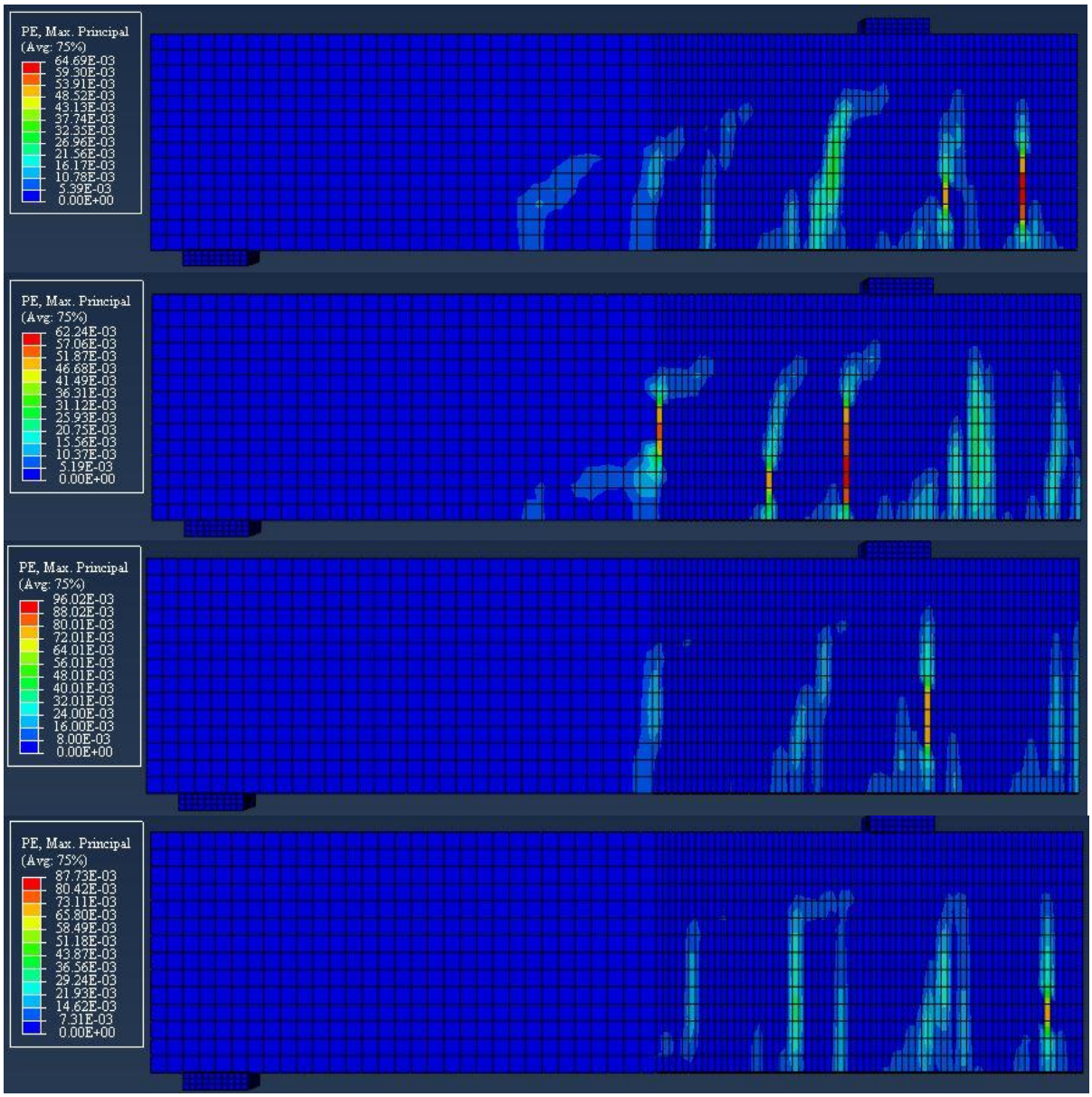

Figure 6.4: Comparison of crack patterns at final stage (effect of concrete compressive strength, f_c')

6.3.2 Effect of Steel Reinforcement Ratio

The effect of longitudinal steel reinforcement ratio, ρ, on CFRP beam response has been ignored in most research. However, it is believed that the composite action of internal and external reinforcements in concrete beam is largely affected by the quantity and configuration

in which steel rebars are implemented. Therefore, the effect of changing ρ ratio on the flexural and debonding response of CFRP-strengthened beams has been introduced in this section. As indicated before, the reference model ($\rho = 0.0086$) was constructed with 2Ø10mm and 2Ø16mm as compression and tension steel reinforcement, respectively. To conduct this parametric study, new sizes of steel rebars were used as follows: (*i*) 2Ø10mm for both top and bottom steel reinforcement ($\rho = 0.0045$); (*ii*) 2Ø10mm for top and 2Ø12.7 mm for bottom reinforcement ($\rho = 0.0063$); (*iii*) 2Ø16mm for the top and bottom reinforcement ($\rho = 0.0127$); and finally (*iv*) 2Ø16mm for top and 2Ø19mm for bottom reinforcement ($\rho = 0.0154$). Every configuration was inputted into the steel material definition in ABAQUS models, while keeping other parameters constant. The postprocessing stage involved producing the load-midspan deflection curves and compared them with the reference model (see Figure 6.5).

It can be noticed that the influence of ρ ratio on the overall capacity of the CFRP beams is tremendous. The model with the lowest steel reinforcement ratio has shown the poorest response in terms of cracking, yielding, and ultimate load. As expected, once the cracking in concrete occurred in this model at 40.86kN load, the yielding of steel rebars and the eventual collapse of the beam soon followed at 54.34kN and 66.25kN, respectively. In another word, reducing the size of the bottom steel rebars from 16mm to 10mm has dropped the overall capacity of the CFRP beam by 48.15%. This type of response is anticipated since the flexural strength (moment resistance) of RC beam is largely affected by the amount of used tensile steel reinforcement. On the contrary, increasing the ρ ratio to 0.0154, by using larger steel bars in compression and tension regions, allowed the CFRP beam to sustain higher loading and increased the ultimate capacity by 29.52%. However, in the model where the top steel rebar was replaced by bar size 16mm while the tensile rebars were kept the same ($\rho = 0.0127$), a very close response to the reference model was observed. This shows that the tensile steel reinforcement has a dominant effect on beam flexural behaviour as compared to steel rebar in compression region.

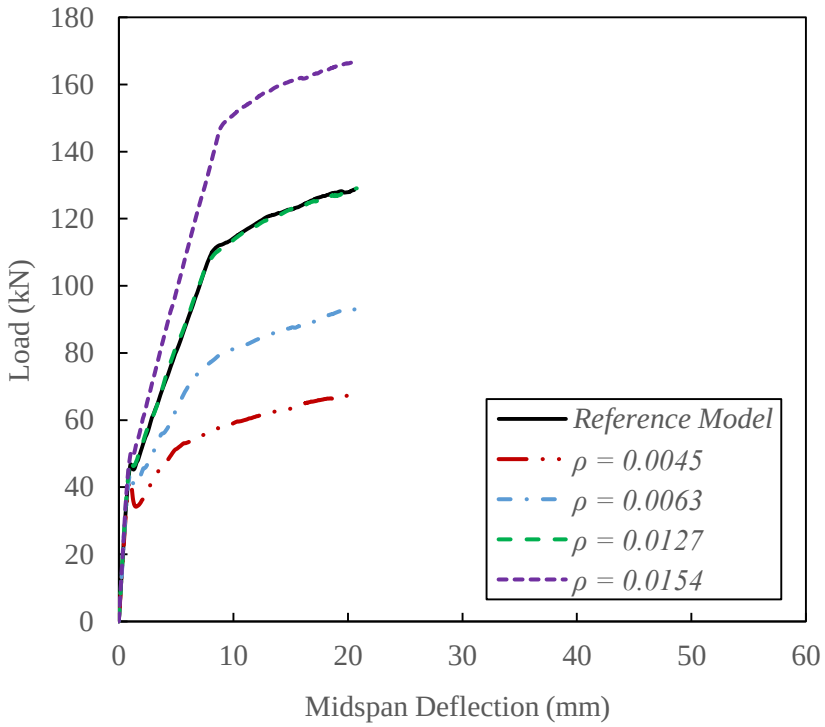

Figure 6.5: Load vs midspan deflection curve (effect of main reinforcement ratio, ρ)

Furthermore, the axial tensile strain in steel rebars was graphed at the location of loading point. The data in Figure 6.6(a) through (b) plot these deformations at the final stage of loading. It can be seen that the steel rebars in models with low steel ratio, ρ, exhibited higher strains in comparison to the original beam. This is a typical response in such beams as the internal stresses, resisted by steel rebar, increase with decreasing the cross sectional area of the rebar.

Figure 6.7(a) through (b) illustrates the tensile strains resisted by CFRP laminate at the final loading stage. The strain response of the four models seems to be close to that of the reference beam. However, a slight increase in strain is observed in the first two models ($\rho = 0.0045$, and $\rho = 0.0063$) within the far half section of the laminate. This increase took place to compensate for the sudden drop in tensile strain of steel rebar around the same region.

In every model, concrete cracking at the final stage was captured and shown in Figure 6.8. Larger cracks are seen in models with low steel ratio, while more diagonal cracks initiate in beams with larger tensile steel rebars. More detailed images are available in Appendix B (see Figure B-5 through Figure B-8).

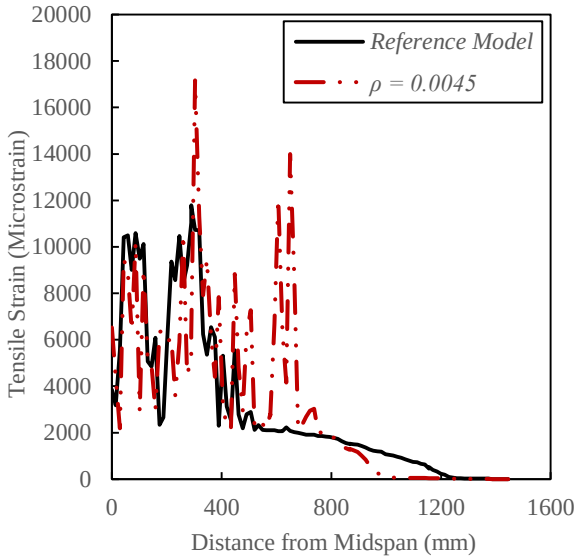

(a) $\rho = 0.0045$

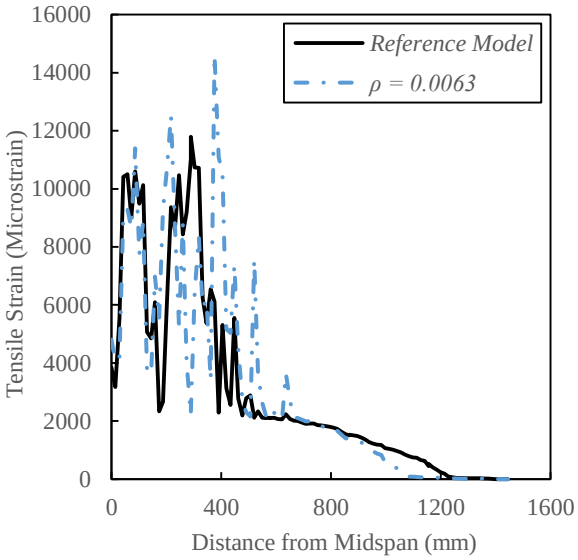

(b) $\rho = 0.0063$

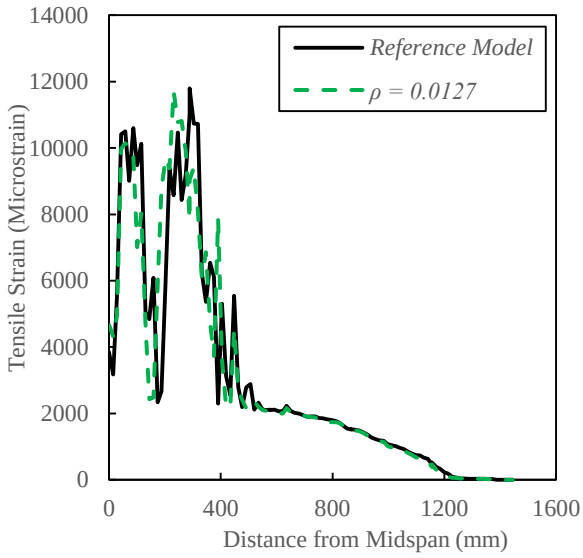

(c) $\rho = 0.0127$

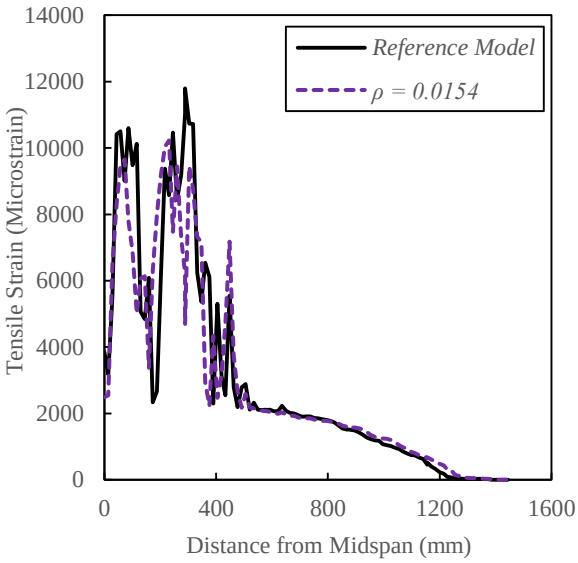

(d) $\rho = 0.0154$

Figure 6.6: Axial strain in steel rebar (effect of main reinforcement ratio, ρ)

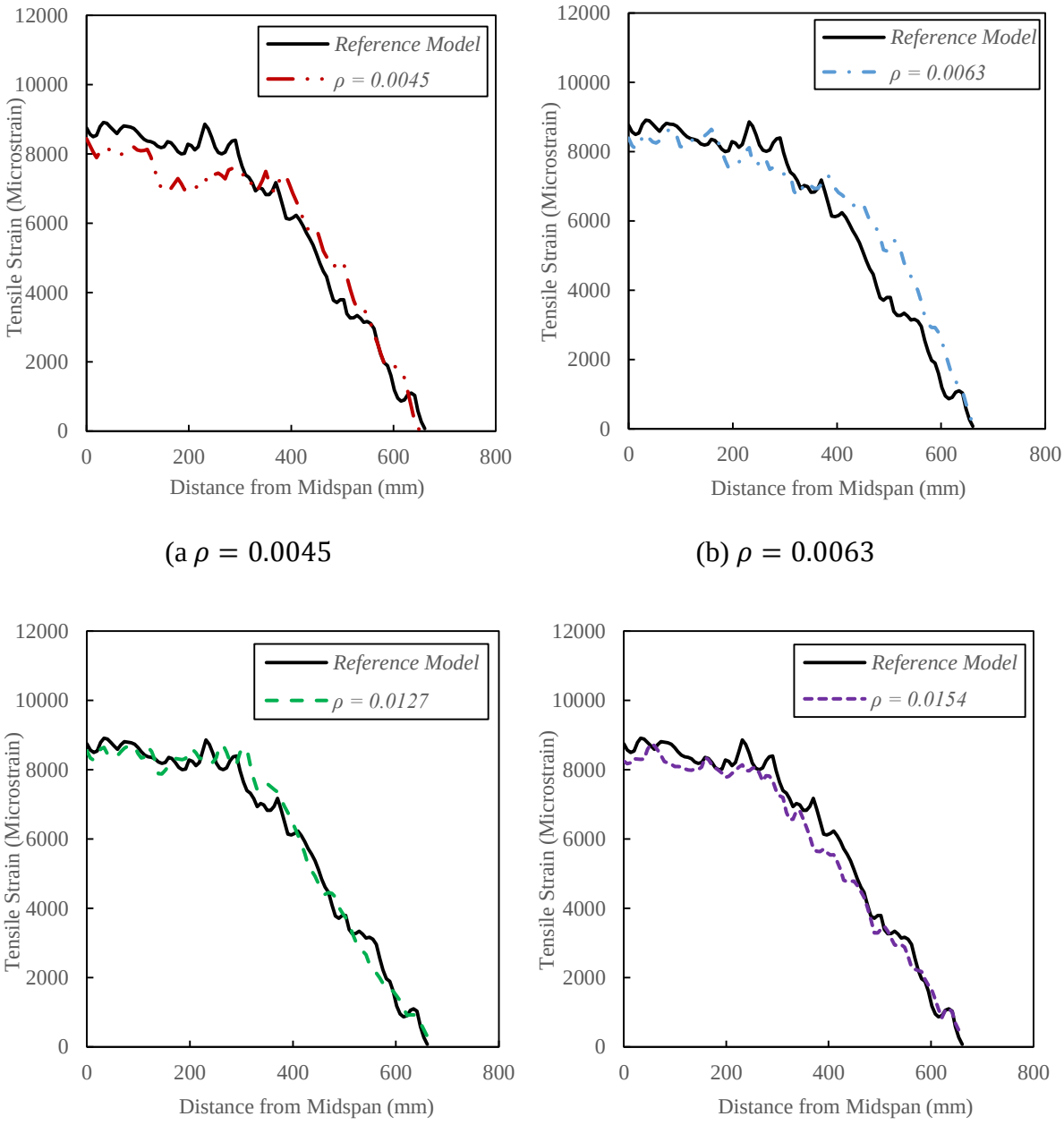

(a $\rho = 0.0045$

(b) $\rho = 0.0063$

(c) $\rho = 0.0127$

(d) $\rho = 0.0154$

Figure 6.7: Axial strain in CFRP laminate (effect of main reinforcement ratio, ρ)

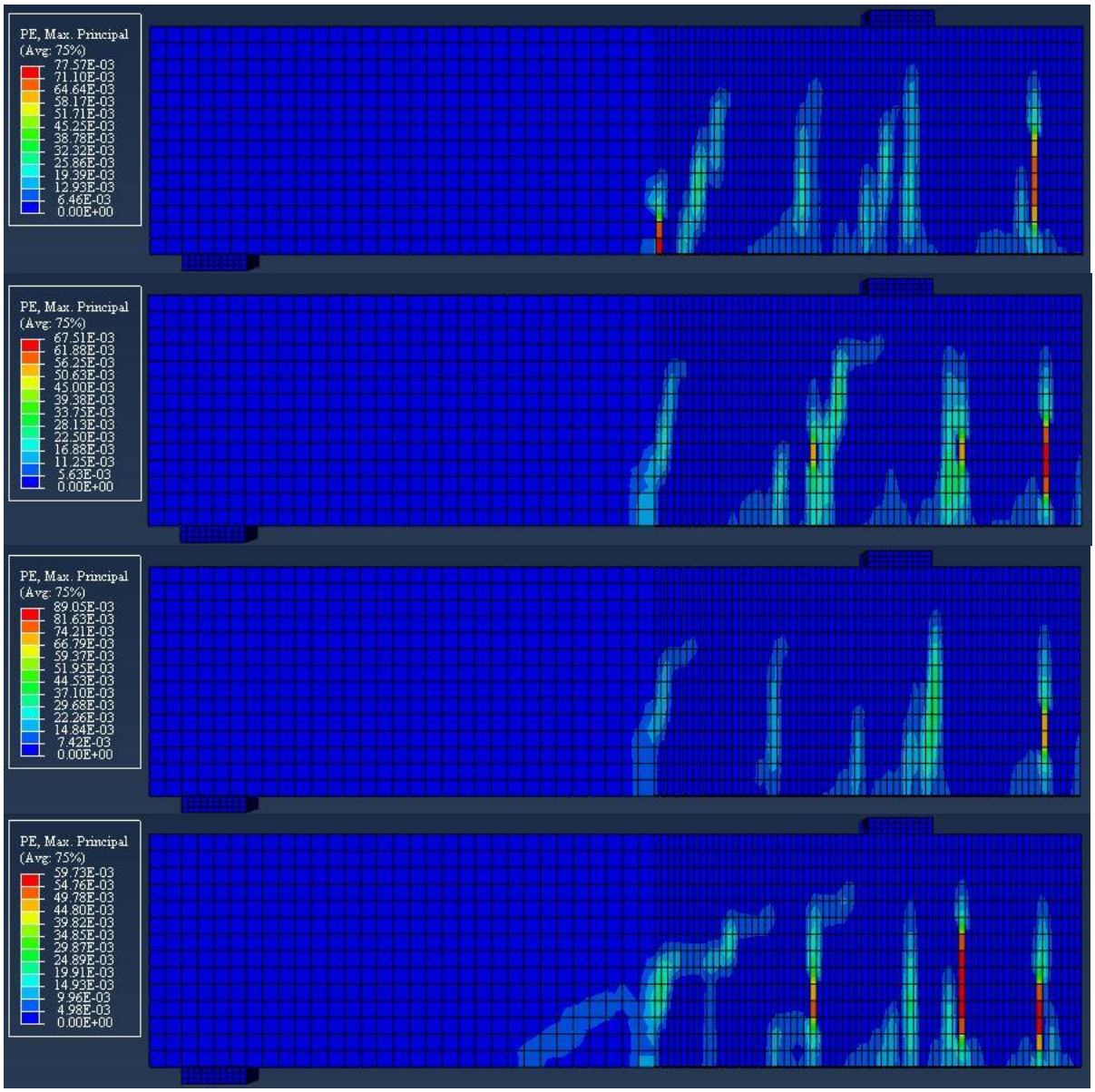

Figure 6.8: Comparison of crack patterns at final stage (effect of main reinforcement ratio, ρ)

6.3.3 Effect of Concrete Plasticity Parameters

As indicated in section 4.4 and section 4.5, the damage evolution and plasticity of concrete were incorporated in the proposed ABAQUS models by including the Concrete Damaged Plasticity Model (CDPM). This model is defined by parameters directly related to plasticity such as: ϵ, σ_{bo}/σ_{c0}, K_c, ψ and μ, and others representing the damage growth in concrete such

as: compression and tension damage parameters, d_c and d_t, respectively. It was noted in Chapter four that using the default values of the first three plasticity parameters provided relatively close predictions in the FE modelling. However, the simulation was more sensitive to the last two parameters (e.g. dilation angle, ψ, and viscosity parameter, μ), and hence their effect will be investigated further in the first segment of this section. The current parametric analysis was carried out by introducing new plastic parameters for concrete elements in the developed models, and keeping other properties constant. The following values were implemented in the initial analysis: $\psi = 20^o, 50^o$ and $\mu = 0.00001, 0.001$. The models were then compared to the reference beam in terms of their flexural response as shown in Figure 6.9.

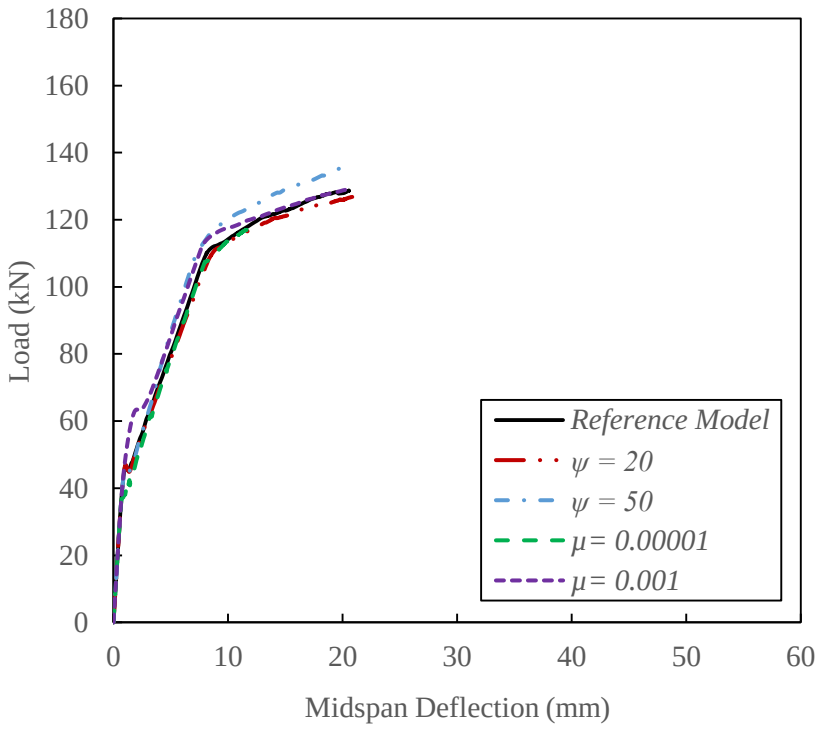

Figure 6.9: Load vs midspan deflection curve (effect of concrete plasticity parameters (I))

The definition and method of calculating the dilation angle were thoroughly covered in previous chapters. However, the effect of changing ψ on the ductility and debonding mechanism of CFRP-strengthened beams was the main focus of this analysis. The comparison seen in Figure 6.9 demonstrates that when the dilation angle was increased to 50^o, the tested

model failed a peak load of 134.27kN, which represents a 5.08% increase in the ultimate capacity of reference beam. In addition, higher dilation angle has produced a slightly stiffer post-cracking response in the FE model. On the other hand, the model with dilation angle equal to 20^oshowed an improved post-cracking behaviour, and followed the original model's response closely. However, the ultimate capacity of the beam was dropped by 2.1% when this low dilation angle is used.

As stated in section 4.5, the use of non-zero value of viscosity parameter, μ, in the CDPM provides some control over the convergence and computational time of ABAQUS model. Beside the control value of $\mu = 0.0002$, used in all previous FE models of this study, the effect of a lower and higher value was reviewed. As seen in Figure 6.9, the use of significantly small μ has led a slight decrease in beam stiffness and capacity. The ultimate load recorded in this model was 1.7% lower than that in the reference beam. Moreover, the computational time of the model with small μ was approximately 50% higher as compared to the original beam. On other hand, increasing the μ value to 0.001 has improved the analysis running time significantly, however, the stiffness of the beam was increased tremendously. The cracking and the ultimate load of reference model was increased by 42.91% and 0.16%, respectively.

The effect of dilation angle on the tensile strains exhibited by both steel rebar and CFRP laminate was more prominent as compared to the impact of changing the viscosity parameter (see Figure 6.10 and Figure 6.11). As the beam's stiffness and ultimate capacity increased by using higher ψ, so did the axial strains in steel and CFRP reinforcements. The highest strain recorded in steel rebar and CFRP sheet was 0.012 and 0.010, respectively. However, the significant portion of these deformations remained within the constant moment region of the beam. Nevertheless, the strain profiles of models with different viscosity parameters did not deviate very much from the response of reference beam.

Finally, the crack pattern at the final loading stage was captures and compared for each model, as illustrated in Figure 6.12. It can be seen from the second and fourth image that models with higher ψ and μ show less visible cracks to the other two models, due to the increased stiffness as mentioned previously.

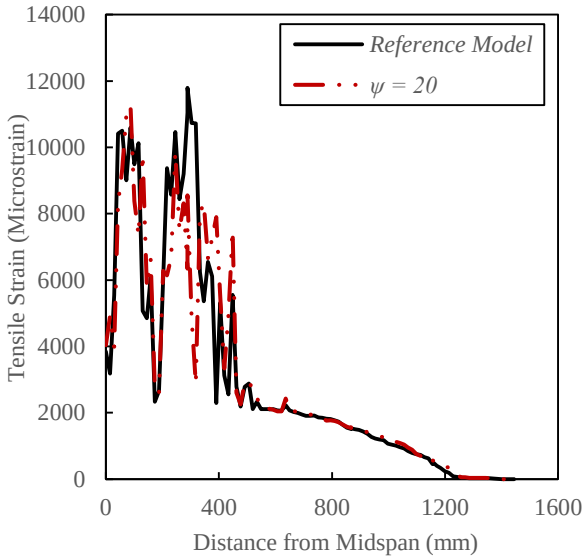

(a) $\psi = 20$

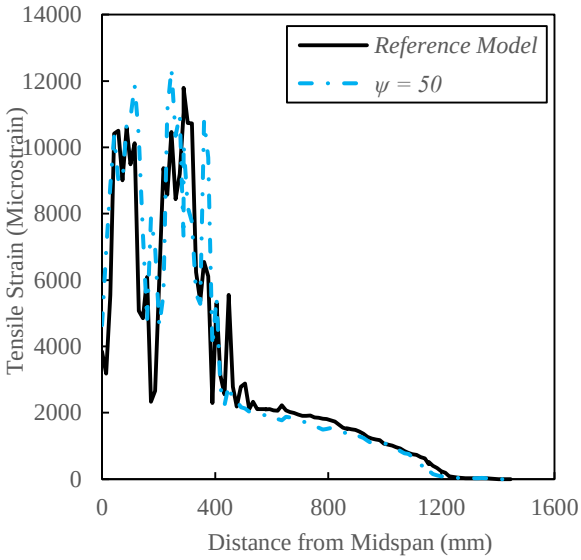

(b) $\psi = 50$

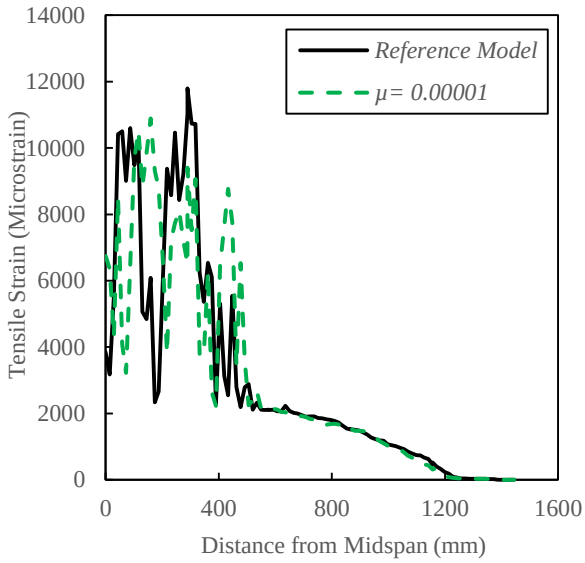

(c) $\mu = 0.00001$

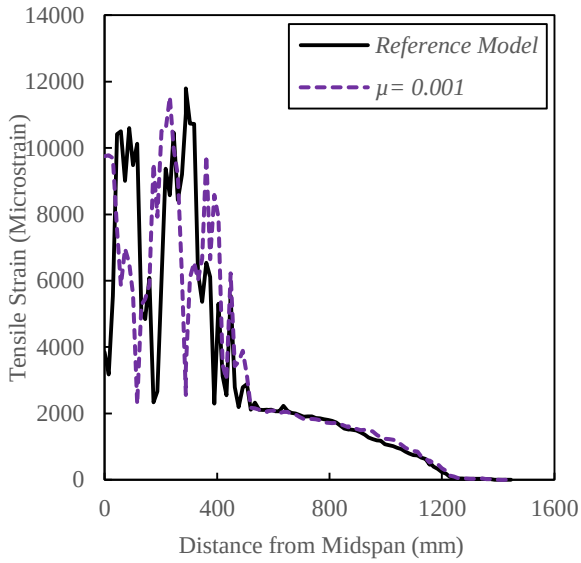

(d) c) $\mu = 0.001$

Figure 6.10: Axial strain in steel rebar (effect of concrete plasticity parameters (I))

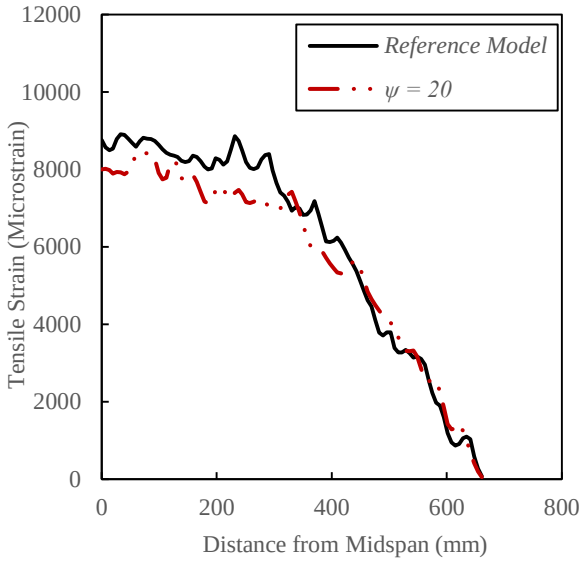

(a) $\psi = 20$

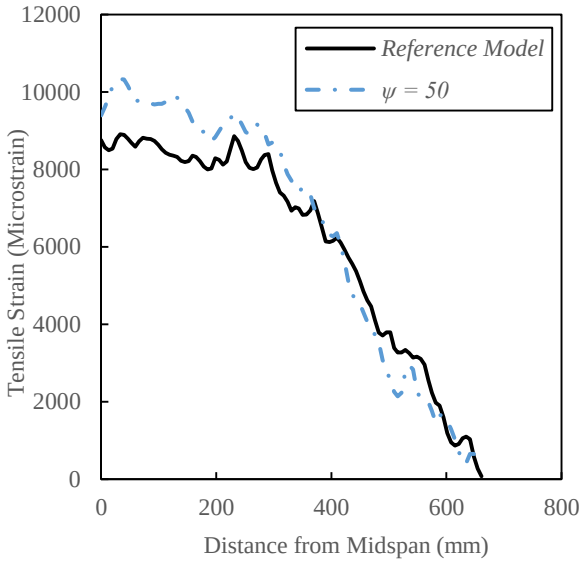

(b) $\psi = 50$

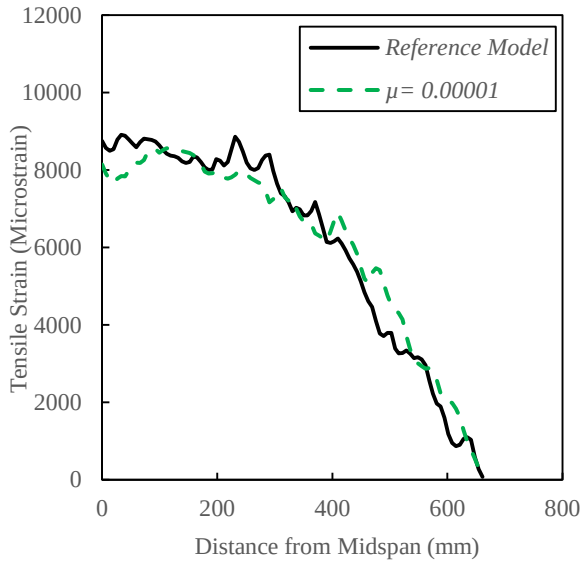

(c) $\mu = 0.00001$

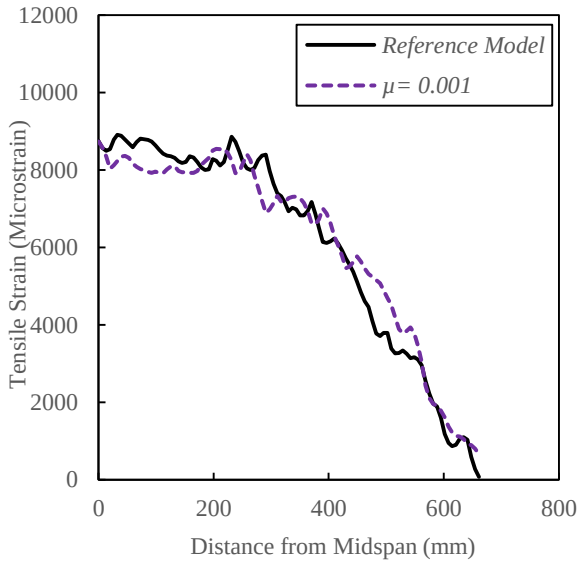

(d) $\mu = 0.001$

Figure 6.11: Axial strain in CFRP laminate (effect of concrete plasticity parameters (I))

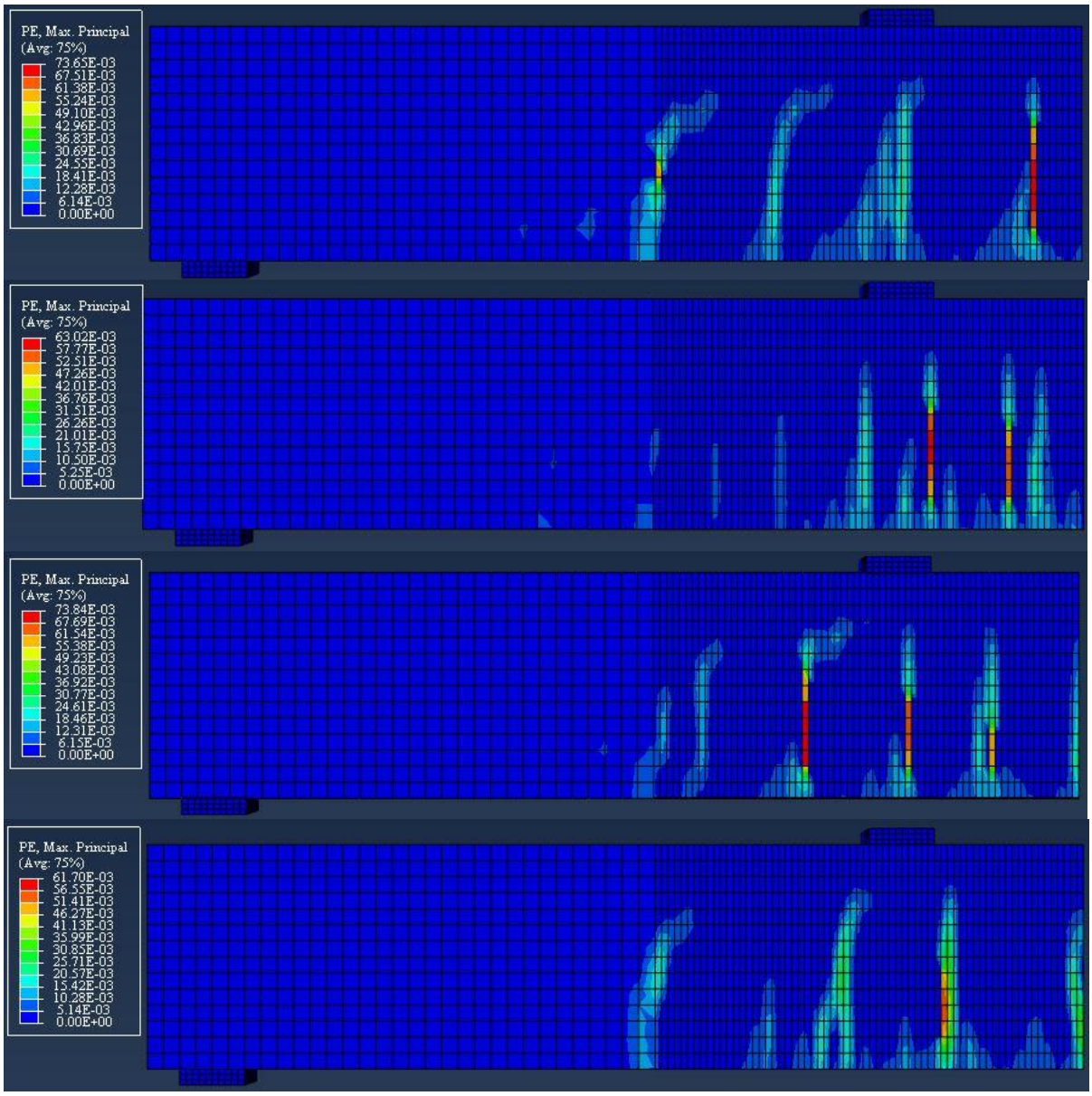

Figure 6.12: Comparison of crack patterns at final stage (effect of concrete plasticity parameters (I))

The second segment of this section involves studying the effect of the concrete damage parameters, within the CDPM, on the flexural and debonding behaviour of CFRP-strengthened concrete beam. The definition and calculation of the tensile and compressive damage parameters were extensively covered in section 4.4. However, the following cases were examined in this parametric study: (*i*) no damage parameters were included; (*ii*) only

compression damage parameters were included; (*iii*) only tension damage parameters were included. The results of the developed beam models were then compared to the reference beam in which both damage parameters were considered. The flexural response of each CFRP beam model was evaluated in the form of load-midspan deflection relationship, as shown in Figure 6.13.

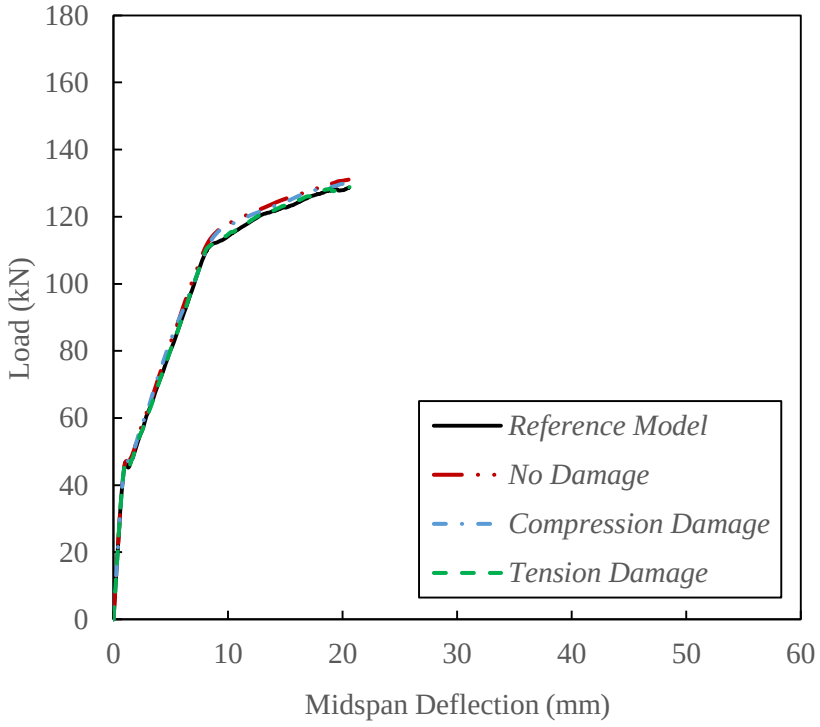

Figure 6.13: Load vs midspan deflection curve (effect of concrete plasticity parameters (II))

It can be observed from this plot that the effect of removing either or both damage parameters was minimal in the service loading region, when compared to the original specimen. In another word, the cracking loads in the three previously listed cases was increased by only 6.72%, 5.27%, and 3.48%, respectively. Moreover, the steel reinforcement in these specimens yielded at loads that are 2.03%, 3.28%, and 0.05%, respectively. It was also noted that the beam models with compression damage and tension damage parameters failed at approximately similar loads (128.86kN and 128,21kN, respectively). However, the beam where both damage parameters were omitted exhibited an ultimate load that is 1.61% higher than that of the reference model. Furthermore, it can be established that including only the tension damage

parameter in the FE models yielded the closest response to the reference beams (with both damage parameters). Therefore, including only the compression damage parameter has a higher effect on the overall response of the CFRP beam model.

The strain distributions under tension was graphed for the lower steel rebar of each model, and compared to the corresponding response of the original beam (see Figure 6.14(a) through (c)). The rebar strain profile of the models with no damage and only compression damage parameter can be categorized as more uniform and lower than the response of steel reinforcement in reference beam. The abrupt changes seen in the rebar strain plot of the original model can be the result of growing cracks at certain locations. Such growth is made possible with the inclusion of both concrete damage parameters, as mentioned in previous chapters. Moreover, to emphasize the point made earlier, the axial strain response of the model with only tension damage parameter was almost identical to that of the reference model.

Similarly, the tensile strains in CFRP laminates were plotted for the three models and compared to the original beam as shown in Figure 6.15(a) through (c). The models with no damage and compression damage parameter experienced lower strain deformations near the midspan region of the beam, as compared to the beam with both damage parameters. However, the strains started to match those of the reference beam near half the length of the CFRP laminate. Similar to the case of the rebar strains, the inclusion of only tension damage parameter inflicted the minimal effect on the strain response of the CFRP reinforcement in the reference model.

The status of concrete cracks in FE models was observed and compared for the three cases, at the final loading stage, as can be seen in Figure 6.16. It is noticed that the cracks are closer to each other in the model with no damage parameter. This is expected as more minor crack are allowed to initiate in the absence of growing major cracks (i.e. no damage parameter exist to localize the growth of damage within few major cracks). The model with only compression damage parameter exhibited more diagonal cracks, far away from the midspan region of the bam. However, the tension damage parameter eliminated the visible shear cracks seen in the third section of the beams in the last two models. In general, more detailed illustration of cracks evolution, at different loading stages, are presented in Appendix B for both segments of the analysis made in this section (see Figure B-9 through Figure B-15).

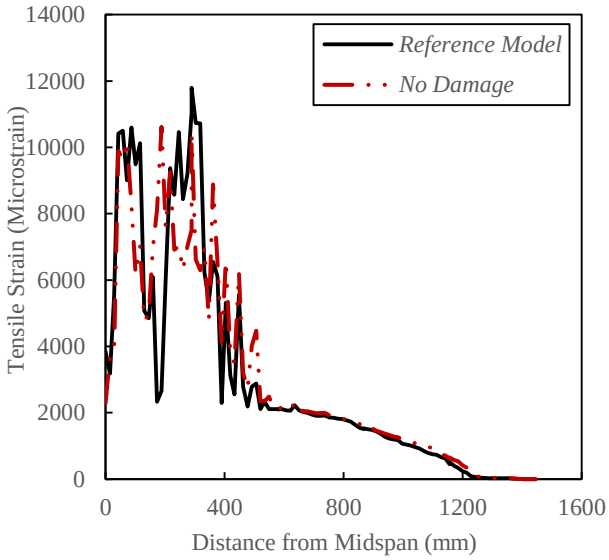

(a) No Damage

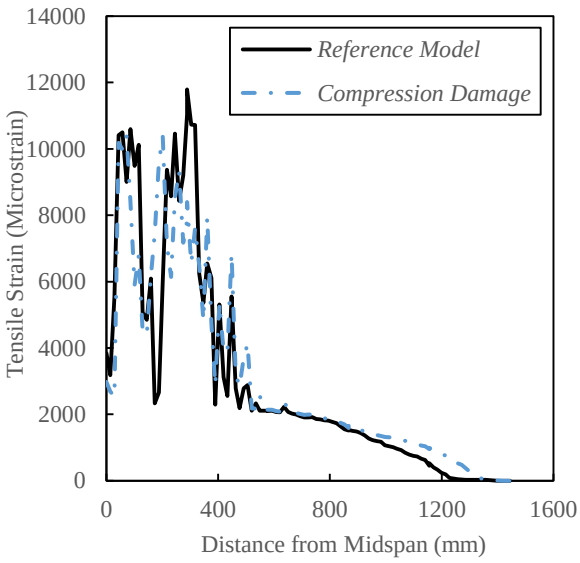

(b) Compression Damage

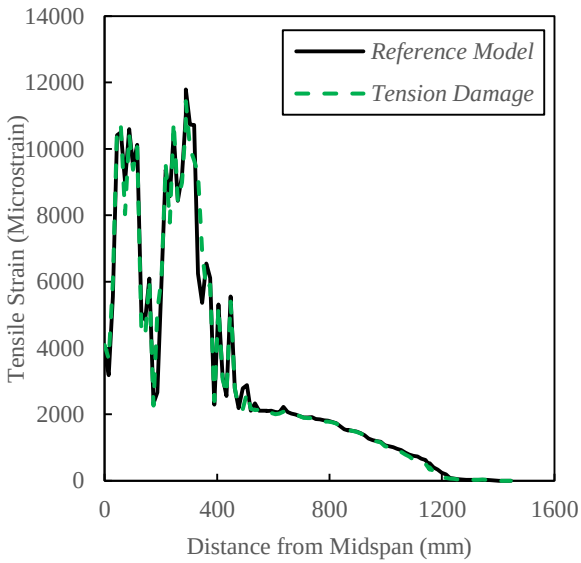

(c) Tension Damage

Figure 6.14: Axial strain in steel rebar (effect of concrete plasticity parameters (II))

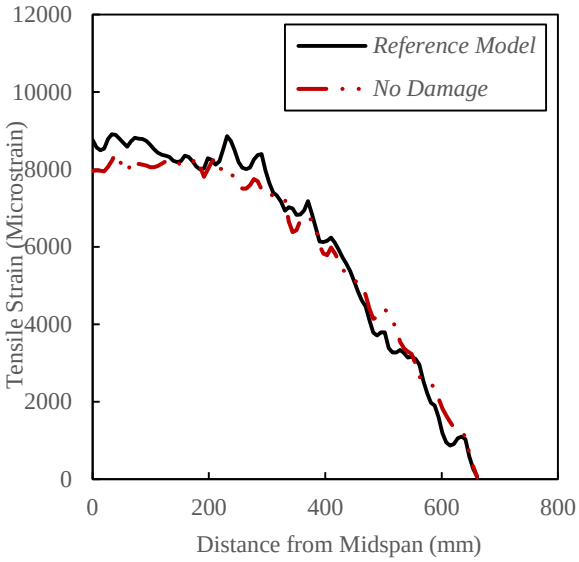

(a) No Damage

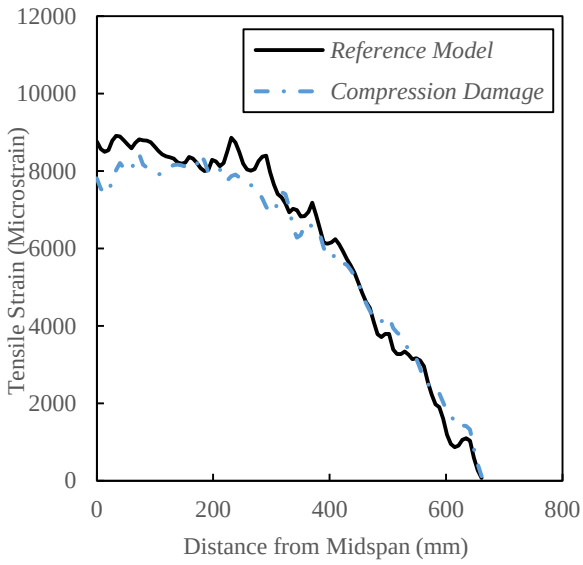

(b) Compression Damage

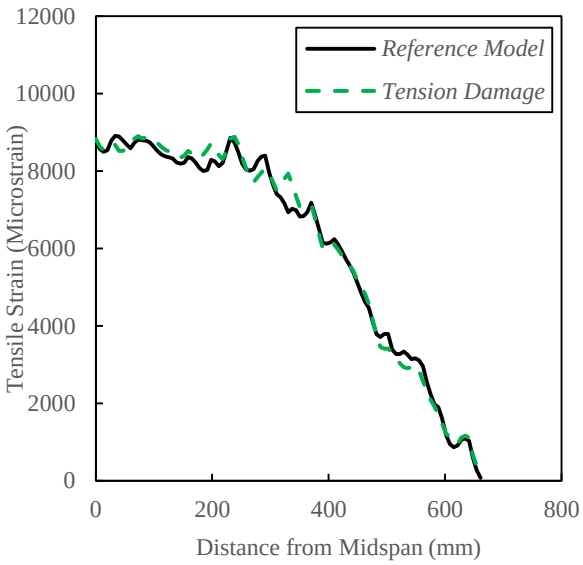

(c) Tension Damage

Figure 6.15: Axial strain in CFRP laminate (effect of concrete plasticity parameters (II))

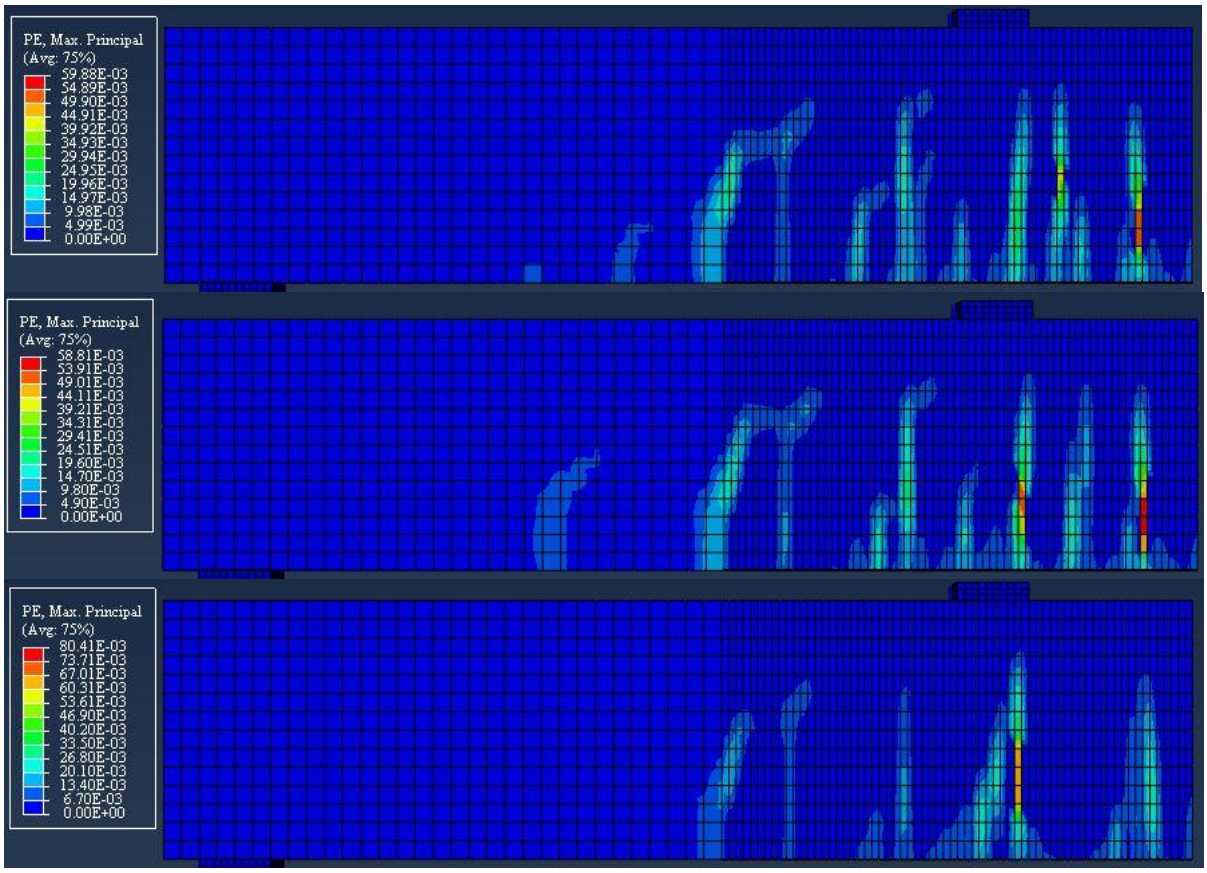

Figure 6.16: Comparison of crack patterns at final stage (effect of concrete plasticity parameters (II))

6.3.4 Effect of CFRP-Concrete Interfacial Bond Strength

It has been proven that the effectiveness of CFRP external reinforcement in RC beams is contingent on the bond stresses between the CFRP and the concrete surfaces. These stresses are produced along the CFRP-Concrete interface due to changes of internal moments within that vicinity. Moreover, differential forces, at CFRP plate-ends and across intermediate cracks in the concrete beams, contribute to the interfacial bond stresses at the interface. However, to ensure adequate bond between concrete surface and the attached CFRP laminate, interfacial stresses must not exceed the ultimate bond strength of the cohesive. Due to the importance of this parameter on the debonding mechanism and the strengthening capacity of CFRP plates, this section was dedicated to investigating the effect of varying the CFRP-Concrete interfacial

bond strength parameter, τ_{max}. As explained in Chapter four, the simulation of this interface was achieved by implementing the cohesive element in the ABAQUS models. The constitutive equations that govern the mechanism of this cohesive element are defined in section 4.8. In this parametric study, four different values of CFRP-Concrete Interfacial bond strength, τ_{max} were used: 1.5MPa, 3MPa, 7MPa, and 10MPa. All other parameters in the FE models were kept the same. The postprocessing of data obtained from this parametric study included generating a load versus midspan deflection curve for each model, and compare these curves to the reference model, as shown in

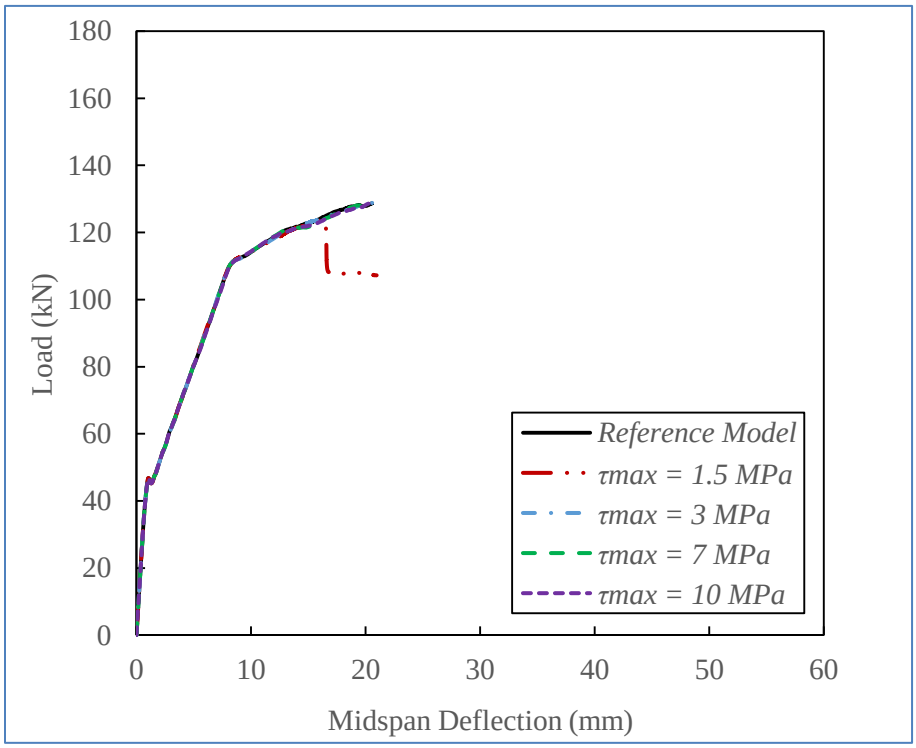

Figure 6.17: Load vs midspan deflection curve (effect of CFRP-Concrete bond strength, τ_{max})

As can be seen from the plot, the most effect on the flexural response of reference beam was induced by the model with the lowest bond strength ($\tau_{max} = 1.5MPa$). The beam in this case has abruptly failed at load of 107.84kN, which represents a decrease of 15.6% in the ultimate load capacity of the original specimen. The sudden failure of this beam indicates that the full

capacity of CFRP reinforcement was not fully achieved, due to the insufficient bond between the CFRP laminate and the concrete substrate. As a result, premature debonding of the plate took place before the beam reached its capacity. On the other hand, increasing the value of τ_{max} to 7MPa did not have any effect on the peak load of the reference beam. The response of the other two values of bond strength was very close to the original data. It was also noticed that the yielding load of steel rebar occurred at similar rate in all studied cases. With the exception of the first case ($\tau_{max} = 1.5MPa$), complete debonding of CFRP sheet was not expected in the proposed models. This is attributed to the CFRP bond length used in all models being sufficient to transfer and sustain shear stresses along the CFRP-Concrete interface. Consequently, the interfacial bond strength has more impact on the rate in which micro and macro-debonding of CFRP laminate occurred than the flexural capacity of the beam. It has been observed in this study that macro-debonding (visible debonding) of CFRP reinforcement usually takes place after the main steel rebars have yielded. Thus, the response of the last three cases converges at the ultimate loads, due to the yielding of steel rebars in these models at similar loading stages.

The tensile strain distribution along the main steel reinforcement and the CFRP laminate is depicted in Figure 6.18 and Figure 6.19. The largest axial strains in steel rebars were recorded in the model with the lowest bond strength, as shown in Figure 6.18(a). This behaviour is expected since bond deficiencies between concrete and CFRP sheet trigger steel reinforcement to contribute more to the load-carrying capacity of the CFRP-strengthened beam. On the contrary, the low bond strength in first model has led to less stresses being transferred from concrete to the adjacent CFRP laminate, and hence less axial strains were experienced by the CFRP system in this case (see Figure 6.19(a)). Nonetheless, the strain profiles of the steel and CFRP reinforcement in the remaining three models seem to match that of the reference model, due to the reasons mentioned in last paragraph.

Finally, the crack pattern in concrete in each model was captured at the ultimate load stage, and a comparison was made between the four cases (check Figure 6.20). It can be seen that larger cracks were allowed to form in the models where high bond strength was used. This can be explained by the fact that stronger bond between concrete and CFRP sheet permits the

former to experience more cracking prior to failure. Figure B-16 through Figure B-19 in appendix B provides more detailed images of crack propagation in each model.

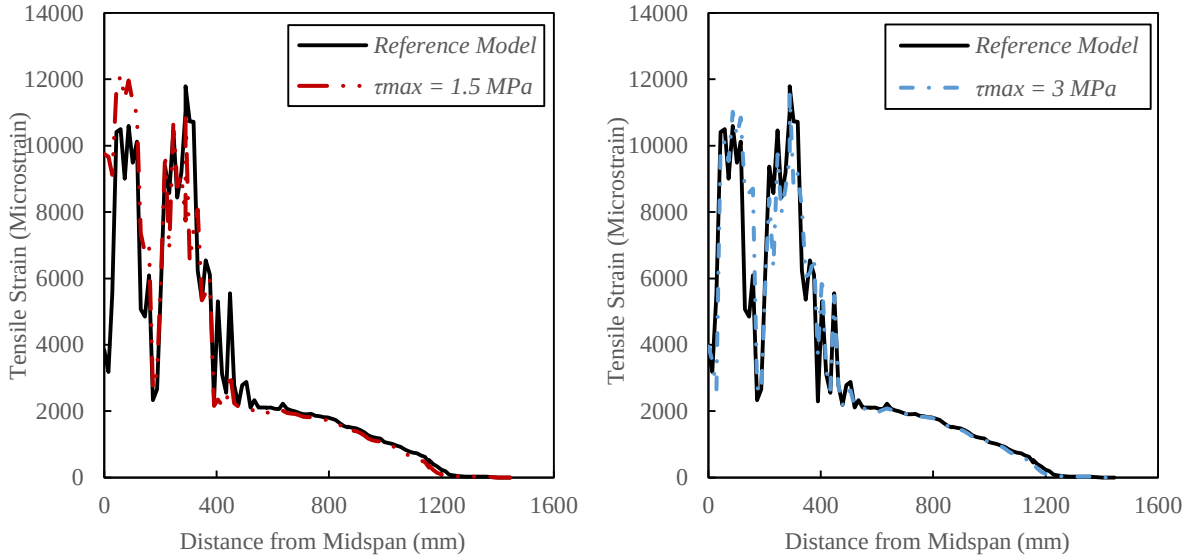

(a) $\tau_{max} = 1.5\ MPa$

(b) $\tau_{max} = 3\ MPa$

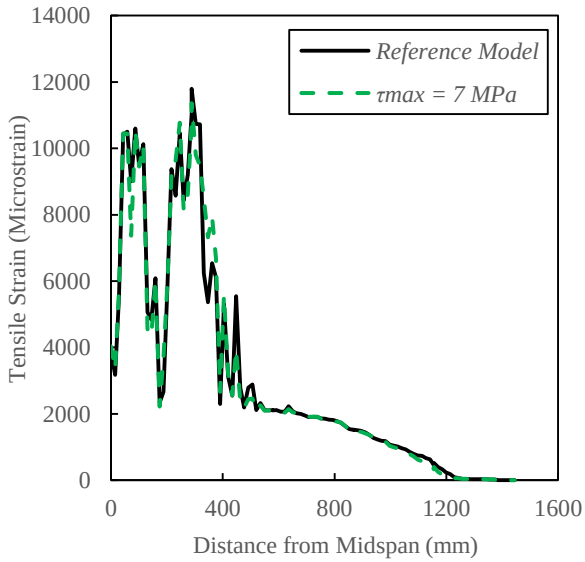

(c) $\tau_{max} = 7\ MPa$

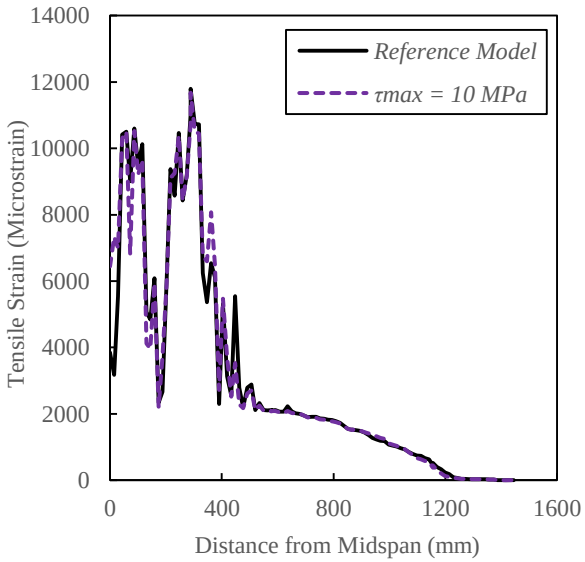

(d) $\tau_{max} = 10\ MPa$

Figure 6.18: Axial strain in steel rebar (effect of CFRP-Concrete bond strength, τ_{max})

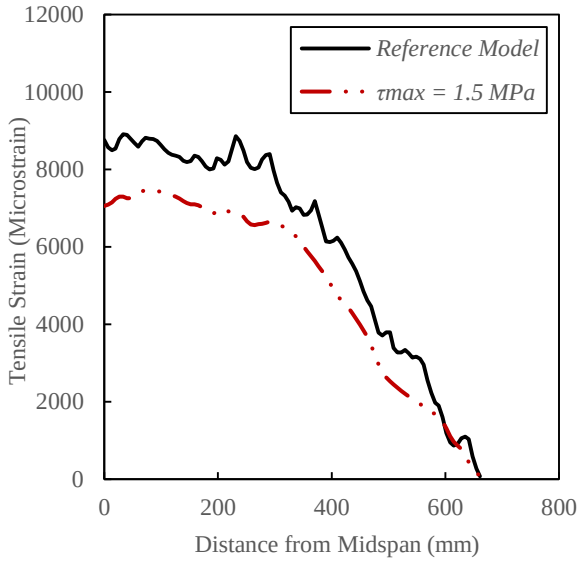

(a) $\tau_{max} = 1.5\ MPa$

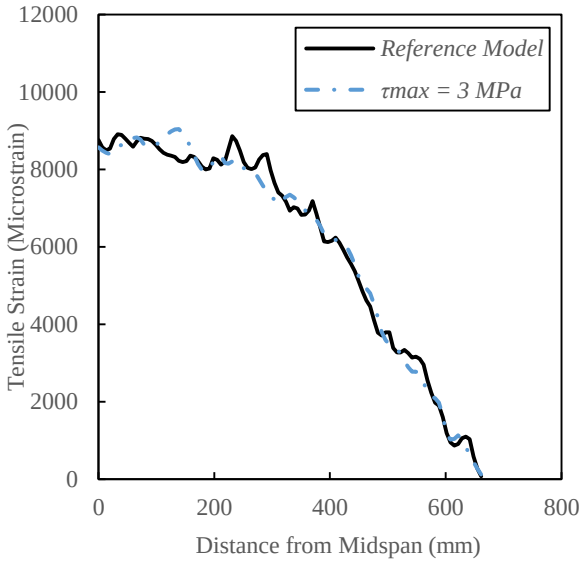

(b) $\tau_{max} = 3\ MPa$

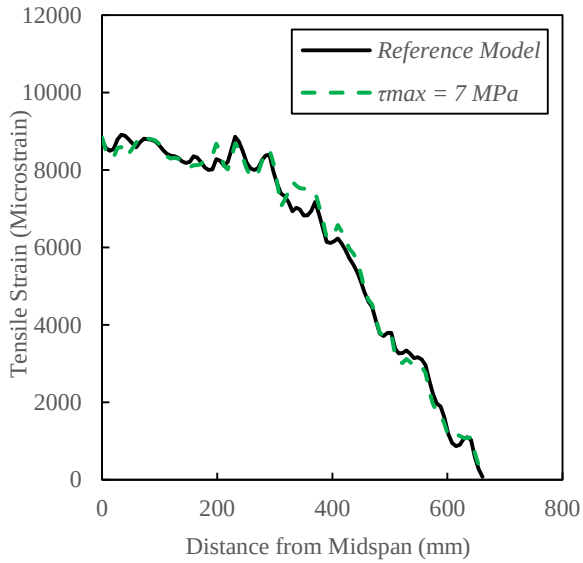

(c) $\tau_{max} = 7\ MPa$

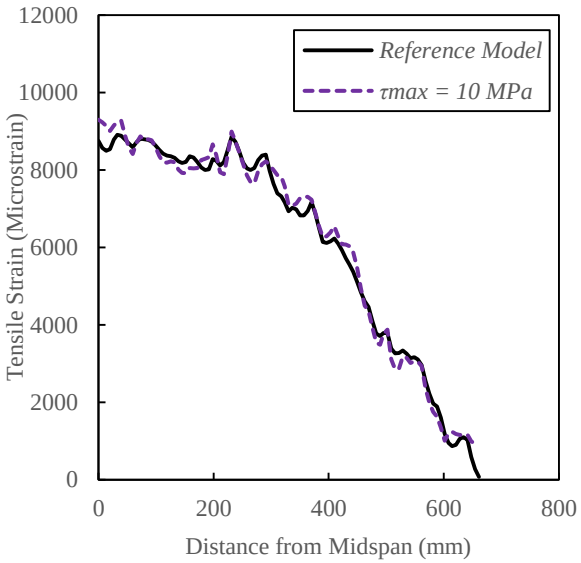

(d) $\tau_{max} = 10\ MPa$

Figure 6.19: Axial strain in CFRP laminate (effect of CFRP-Concrete bond strength, τ_{max})

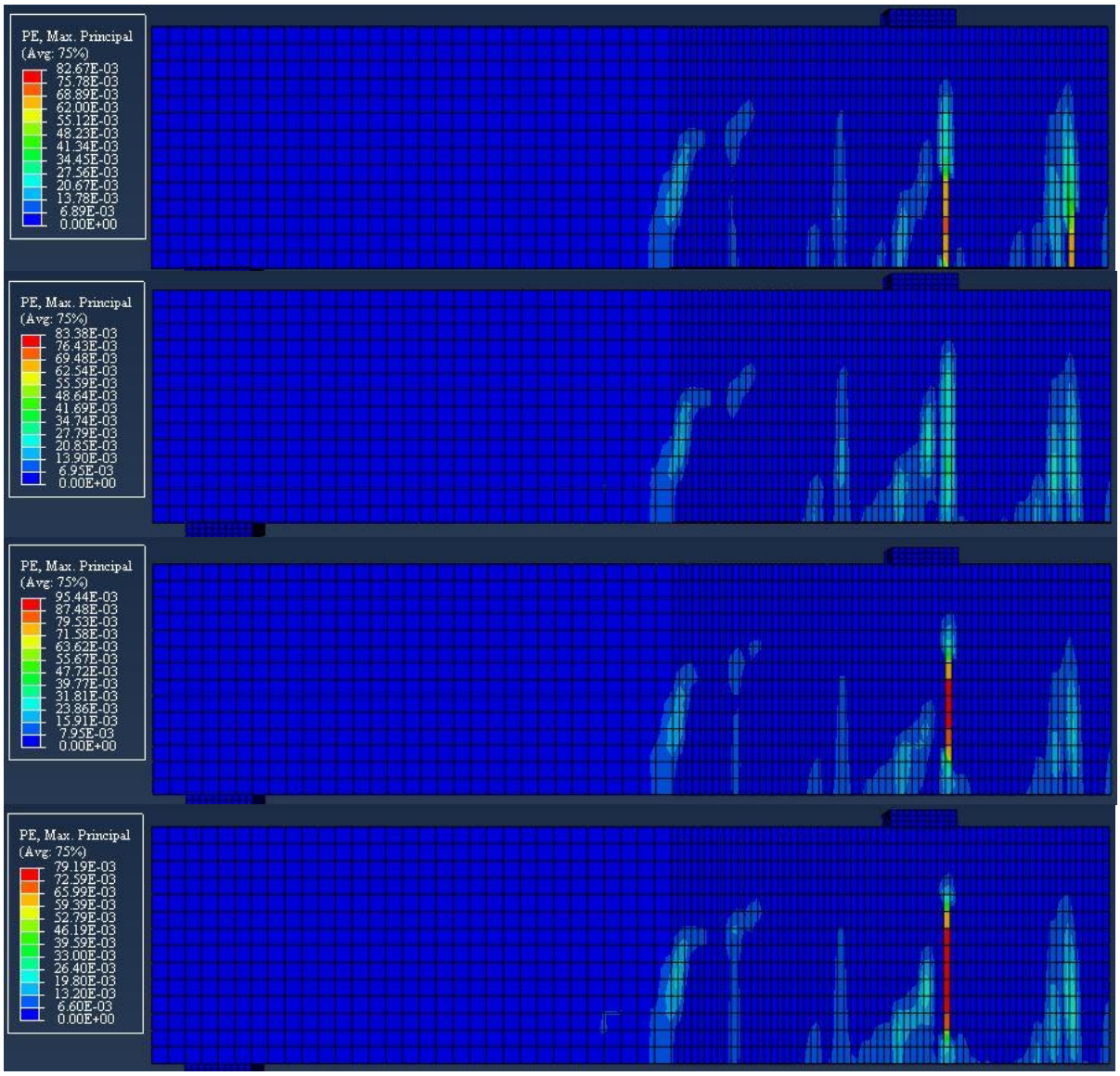

Figure 6.20: Comparison of crack patterns at final stage (effect of CFRP-Concrete bond strength, τ_{max})

6.3.5 Effect of CFRP Bond Length

Several studies have concluded that adequate bond between concrete surface and externally-attached CFRP reinforcement can be achieved when sufficient CFRP bond length, L_f, is provided. In such case, interfacial bond stresses can be efficiently transferred from concrete layer to the adjacent CFRP laminate, and complete debonding of CFRP reinforcement can be

prevented. The importance of CFRP bond length has prompted this parametric analysis, and the purpose of the study was to examine the effect of different CFRP bond lengths on the flexural response of CFRP-strengthened beams. Similar to the other ABAQUS models proposed in this study, only one quarter of the beam was analyzed (due to symmetry), and thus CFRP bond lengths presented in this section represents only half of the actual length. Four values of L_f were used as follows: 400mm, 500mm, 800mm, and 1000mm to model each specimen, while all other mechanical and geometric properties remained unchanged. The four cases were then compared to the reference model in terms of load versus midspan deflection response, as depicted in Figure 6.21.

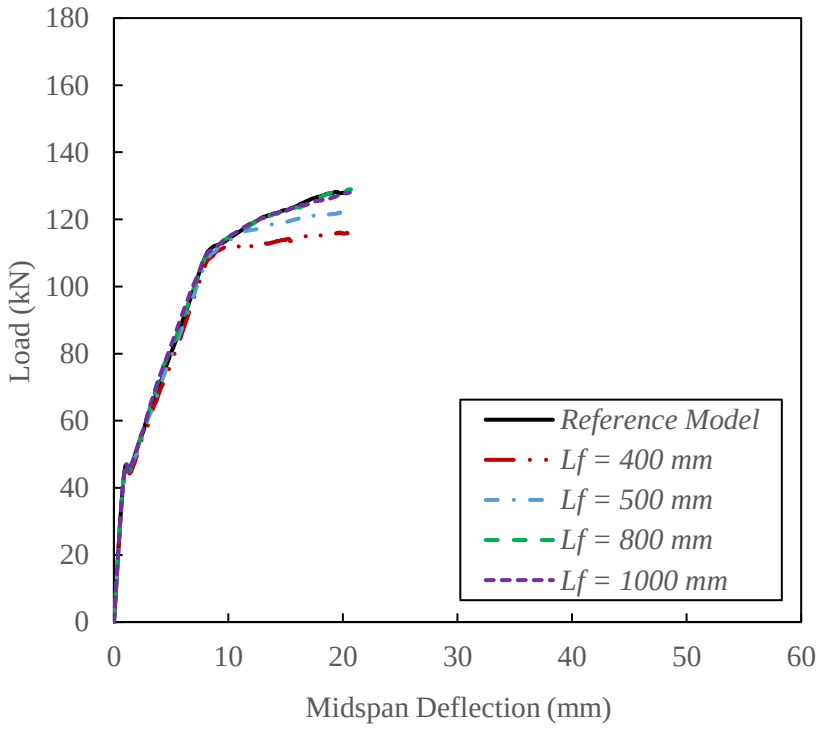

Figure 6.21: Load vs midspan deflection curve (effect of CFRP bond length, L_f)

As could have been expected, the beam models that utilized short lengths of CFRP composites were not able to withstand high loads, as compared to the reference specimen. Macro-debonding of the CFRP plates from the bottom surface of the concrete in these specimens happened shortly after yielding of steel reinforcement. The model with the shortest CFRP bond

length ($L_f = 400mm$) experienced the lowest service loads, relative to the other three models. The concrete started cracking at 43.87kN and the longitudinal steel rebar yielded at 109.02kN. In addition, the use of this bond length has resulted in a drop of 9.37% in the ultimate capacity of the reference beam. Although increasing the bond length to 500mm improved the service load capability in the second case, the beam still failed at 4.85% less capacity than the reference specimen. However, it is worth mentioning that increasing the CFRP bond length beyond the original length (661mm) did not necessarily increase the flexural capacity of the reference beam, as can be seen in Figure 6.21. This phenomenon has been reported by many previous studies (Chajes & Finch Jr., 1996) and (Taljsten, 1994), which concluded that there is an effective bond length for a CFRP composite system beyond which no further increase in load capacity can be achieved.

The steel reinforcement was subjected to different strains under tension, and the profiles of which was plotted for each model as shown in Figure 6.22(a) through (d). The highest axial strains, resisted by steel rebar, was recorded in the model with the smallest L_f value. A sudden increase of the rebar's tensile strain can be seen near a point where the CFRP laminate ended. This abrupt change in steel strain response can be indicative of a plat-end failure mode of the CFRP system. Although, the second model exhibited lower strains than the first model, more activities were observed near the middle region of the beam. Lastly, the remaining two cases did not show significant changes in the strain profiles, and followed the response of the reference beam closely.

In Figure 6.23(a) through (d), the tensile strain response of each model was plotted and compared to the reference beam. As expected, short CFRP bond lengths did not provide sufficient support to the composite beam. Therefore, low strains experienced by the CFRP plates in the first two models had to be compensated by additional strains resisted by the steel rebars, as discussed earlier. Larger bond lengths allowed the CFRP plate to sustain peak strains that are close to the original model, however, these strains extended along the plate length.

The concrete cracking at failure was captured in Figure 6.24, and a comparison was made between each model. Large cracks can be seen near the pate end in the first two models with short L_f. This can be attributed to the high stress concentration at that point, which might have

triggered plate-end debonding of CFRP sheet, as stated before. More detailed images are provided in Appendix B, as seen in Figure B-20 through Figure B-23.

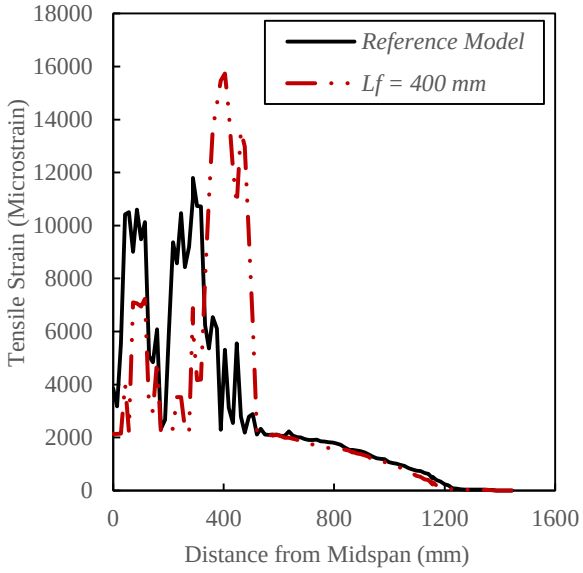

(a) $L_f = 400\ mm$

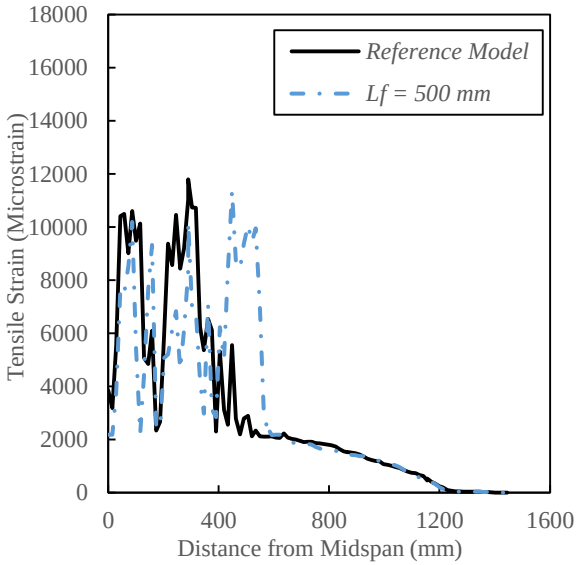

(b) $L_f = 500\ mm$

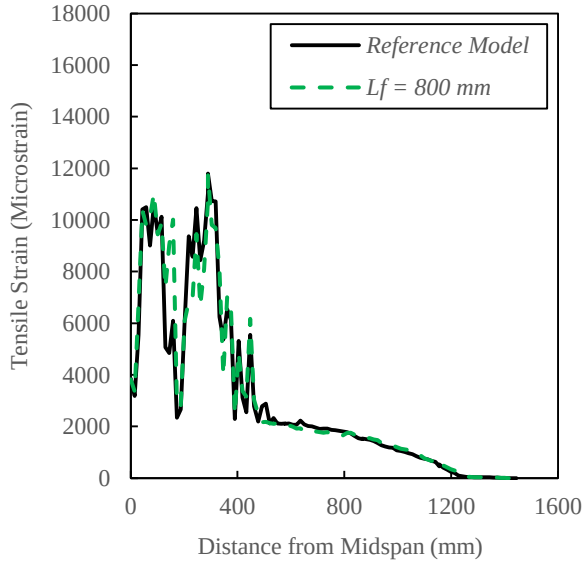

(c) $L_f = 800\ mm$

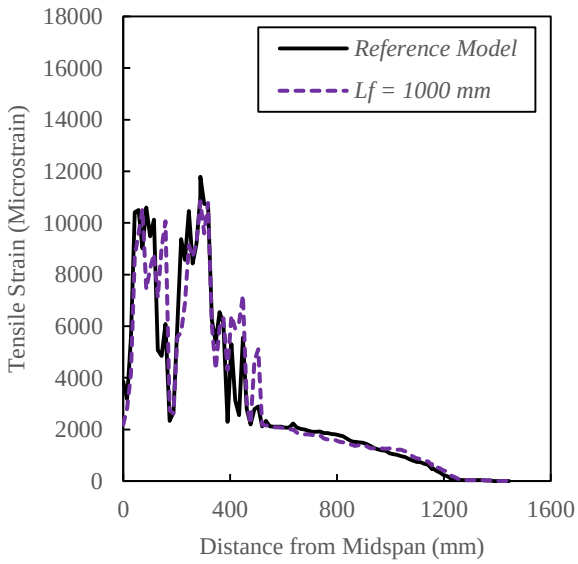

(d) $L_f = 1000\ mm$

Figure 6.22: Axial strain in steel rebar (effect of CFRP bond length, L_f)

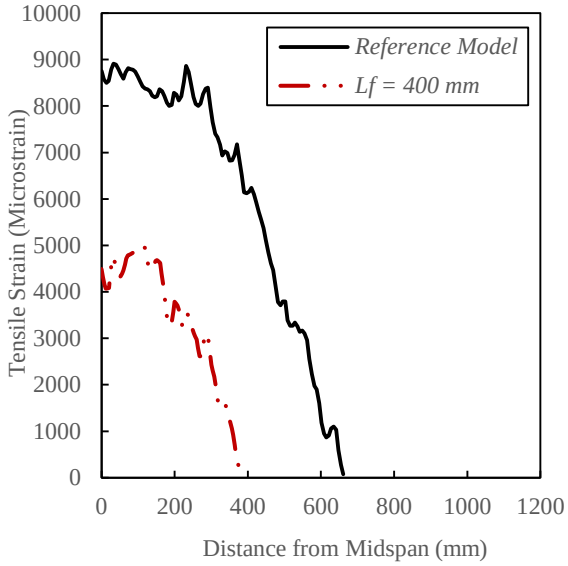

(a) $L_f = 400\ mm$

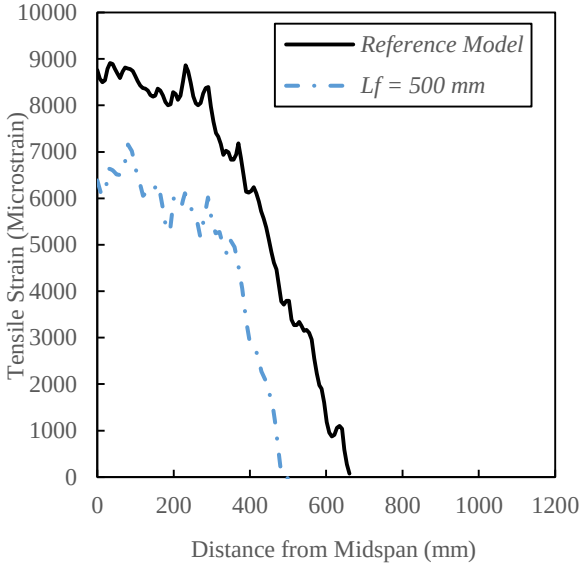

(b) $L_f = 500\ mm$

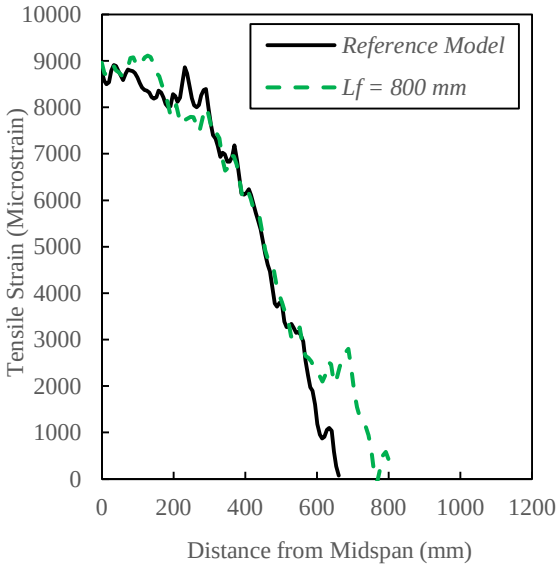

(c) $L_f = 800\ mm$

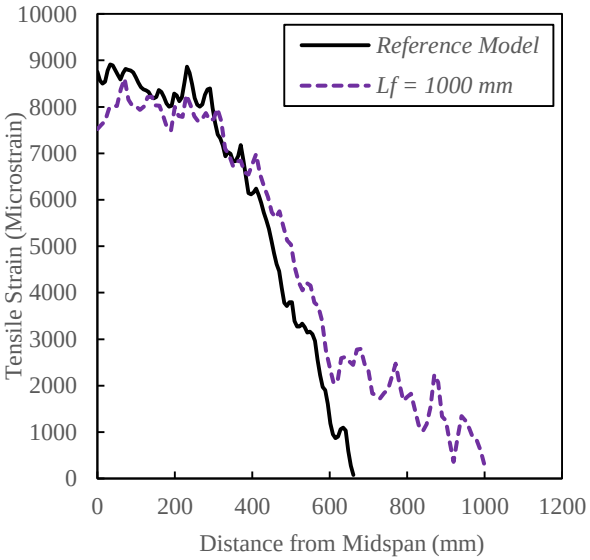

(d) $L_f = 1000\ mm$

Figure 6.23: Axial strain in CFRP laminate (effect of CFRP bond length, L_f)

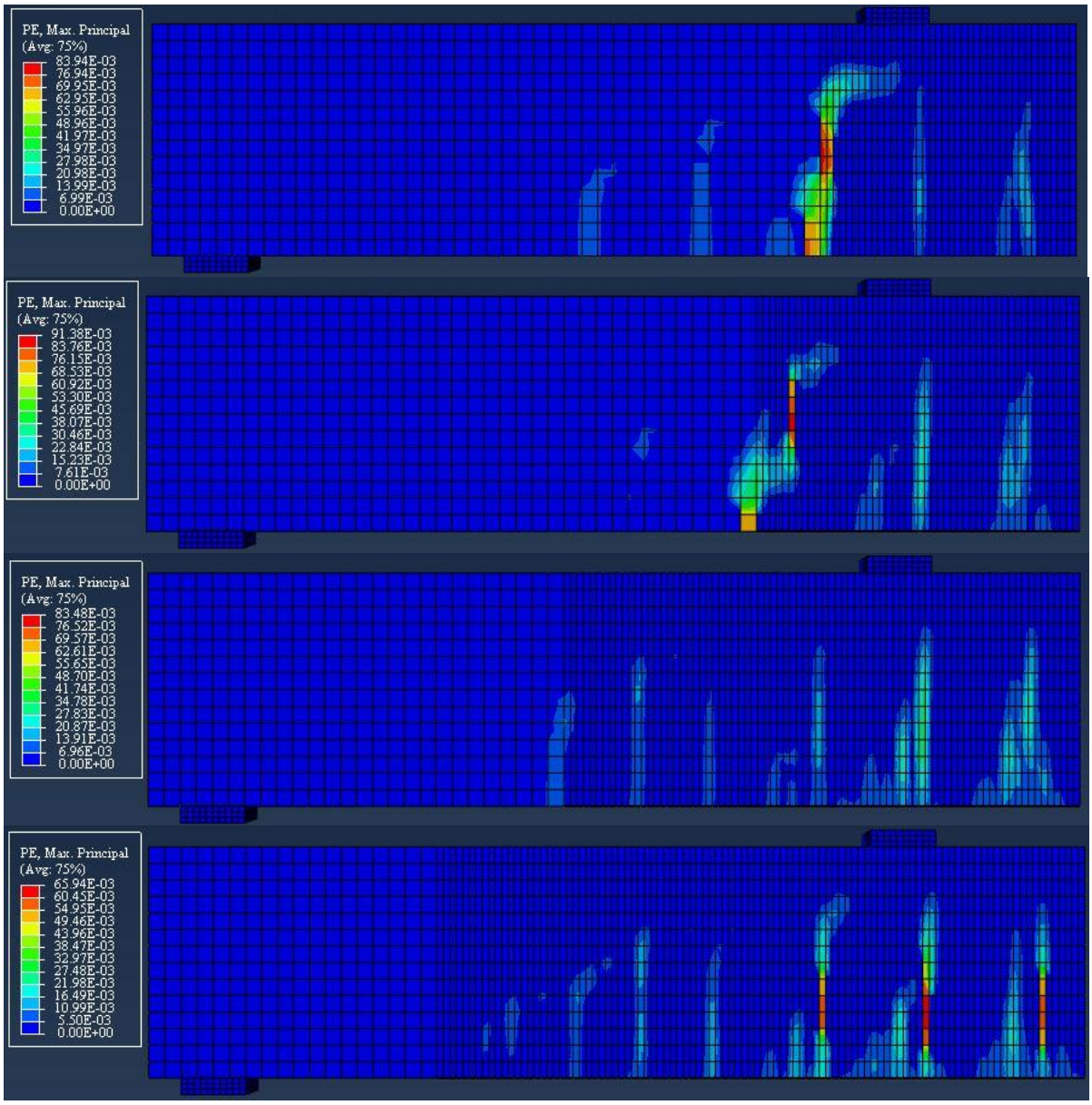

Figure 6.24: Comparison of crack patterns at final stage (effect of CFRP bond length, L_f)

6.3.6 Effect of CFRP Bond Width

It is evident that the contact area between the CFRP and the concrete surfaces in CFRP beams plays an important role in controlling the debonding effect of CFRP reinforcement. In another word, if sufficient surface/contact area exist between the concrete and the externally-bonded CFRP laminate, composite action can be achieved and beam ultimate capacity can be

improved. In addition to the CFRP bond length covered in previous section, this current analysis is dedicated to examining the other dimension of the CFRP laminate (i.e. CFRP bond width, B_f). This parametric study was conducted by utilizing four different values of B_f, while maintaining all other beam and material parameters constant. The used CFRP bond widths were: 60mm, 80mm, 140mm, and 180mm. Similar to the case in last section, these values represent only half of the actual CFRP bond width, as only one quarter of the beam is simulated because of symmetry. The effect of this parameter, B_f, on the flexural performance of CFRP beam model was illustrated by the load-midspan deflection relationship. This response was calibrated with its corresponding in the reference beam, as graphed in Figure 6.25.

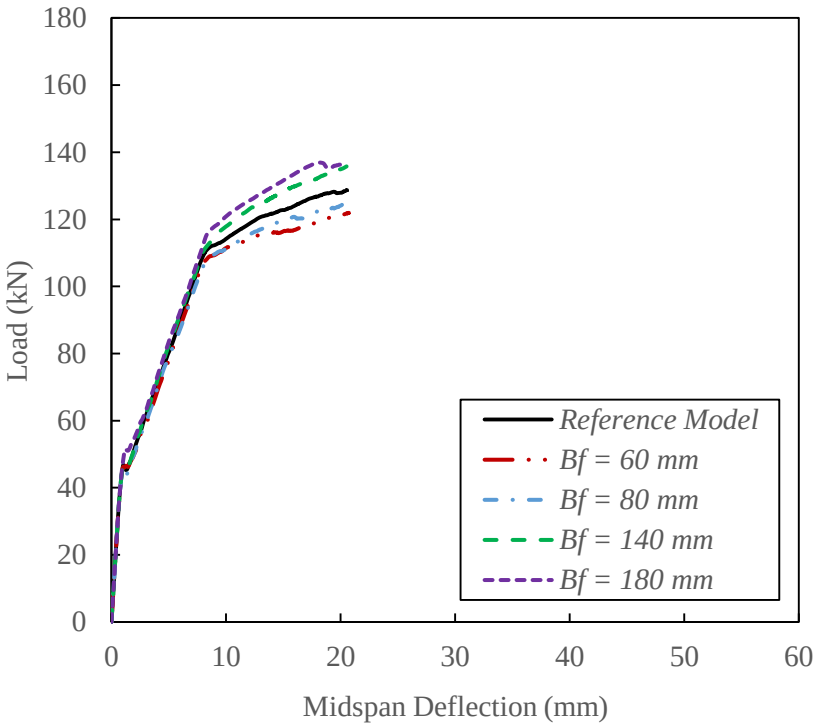

Figure 6.25: Load vs midspan deflection curve (effect of CFRP bond width, B_f)

A clear trend can be seen from the response of each model as shown in the above figure. When wider CFRP laminates are used, the service and the ultimate loading capacity of the CFRP beam increases. The cracking loads of the first three model was close to that of the reference beam. However, the model with the largest bond width ($B_f = 180mm$) was able to withstand

a load of 51.25kN before cracking in concrete initiated, which corresponds to over 16% increase in the cracking load of reference beam. The steel reinforcement yielded at loads which were as low as 108.28kN for the model with ($B_f = 60mm$), and as high as 116.28kN for the model with ($B_f = 180mm$). On the other hand, a range of -5.74% to +5.7% in ultimate load capacity of the reference beam was observed in the first and forth models, respectively. This enhancement in serviceability and capacity of the CFRP beam models, where large values of B_f were used, can be justified by the increase in contact area of the CFRP-Concrete interface. Such increase can lead to more efficient bond and transfer of stresses between the adjacent materials, and hence delayed debonding of CFRP laminate is expected.

Figure 6.26(a) through (d) shows the axial tensile strains along the steel rebar in each model of this study. It can be noted that relatively higher strains were observed in the first two cases where small values of CFRP bond width were used, in comparison to the original model. This can be the result of more stresses being transferred from concrete to the embedded steel rebars, due to the incapability of narrow CFRP laminates to withstand high stresses. However, wider CFRP sheets helped dampened the strain deformations in the steel reinforcement of the last two models, as seen in Figure 6.26(c) and (d). Moreover, some residual axial strains near the quarter of the beam can be noticed in last model. This indicates more improvement in the composite action between internal and external reinforcement is achieved, as a result of using wider CFRP laminate.

The tensile strain response of the CFRP reinforcement displayed similar trend to that of steel rebar mentioned above (see Figure 6.27(a) through (d)). Higher strain records were seen in the first two model with small CFRP bond width. While the strain values seemed to have dropped slightly when winder CFRP composite was used in the other two models. It can be concluded that when wider CFRP bond width is used, less axial strain is recorded, due to the increase in cross-sectional area of the CFRP plate. While using a CFRP laminate with a smaller bond width lead to an increase in tensile strains across the cross section of the composite.

Finally, Figure 6.28 provides a comparison of crack patterns at final loading stage in all proposed models. Moreover, Figure B-24 through Figure B-27 in Appendix B show more details on crack patterns of the studied cases in this section.

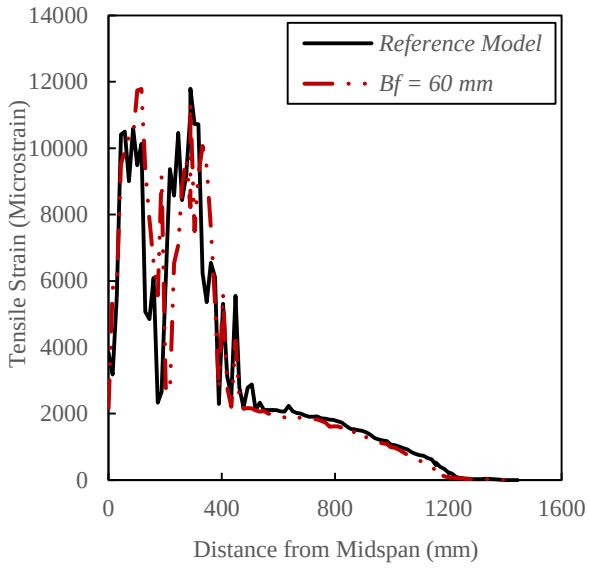

(a) $B_f = 60\ mm$

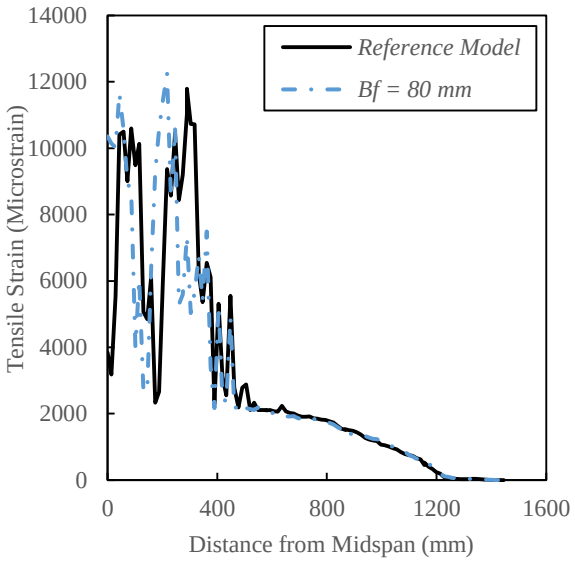

(b) $B_f = 80\ mm$

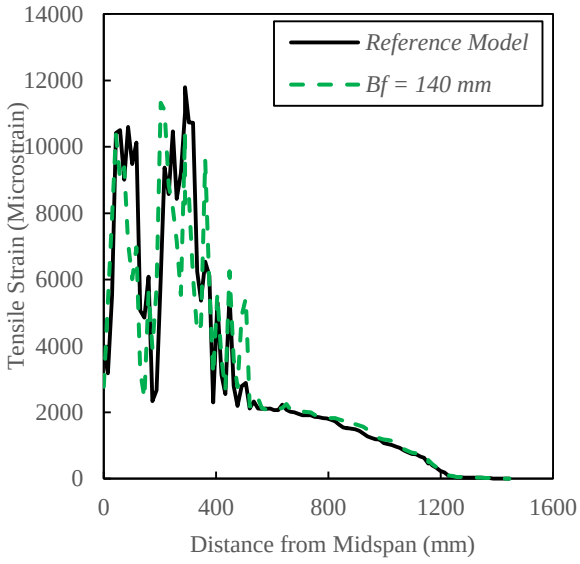

(c) $B_f = 140\ mm$

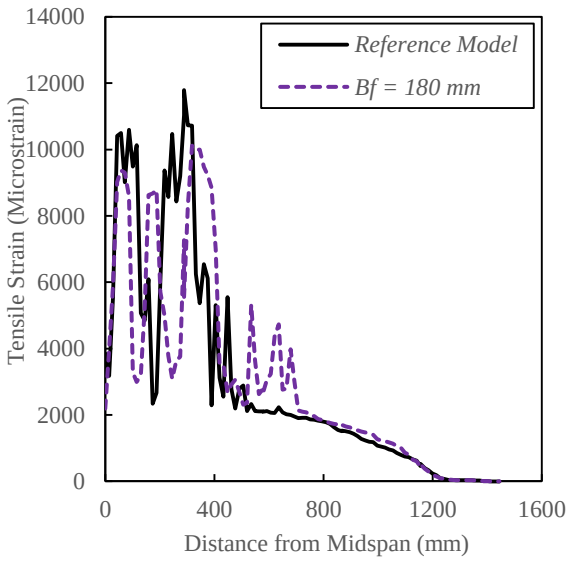

(d) $B_f = 180\ mm$

Figure 6.26: Axial strain in steel rebar (effect of CFRP bond width, B_f)

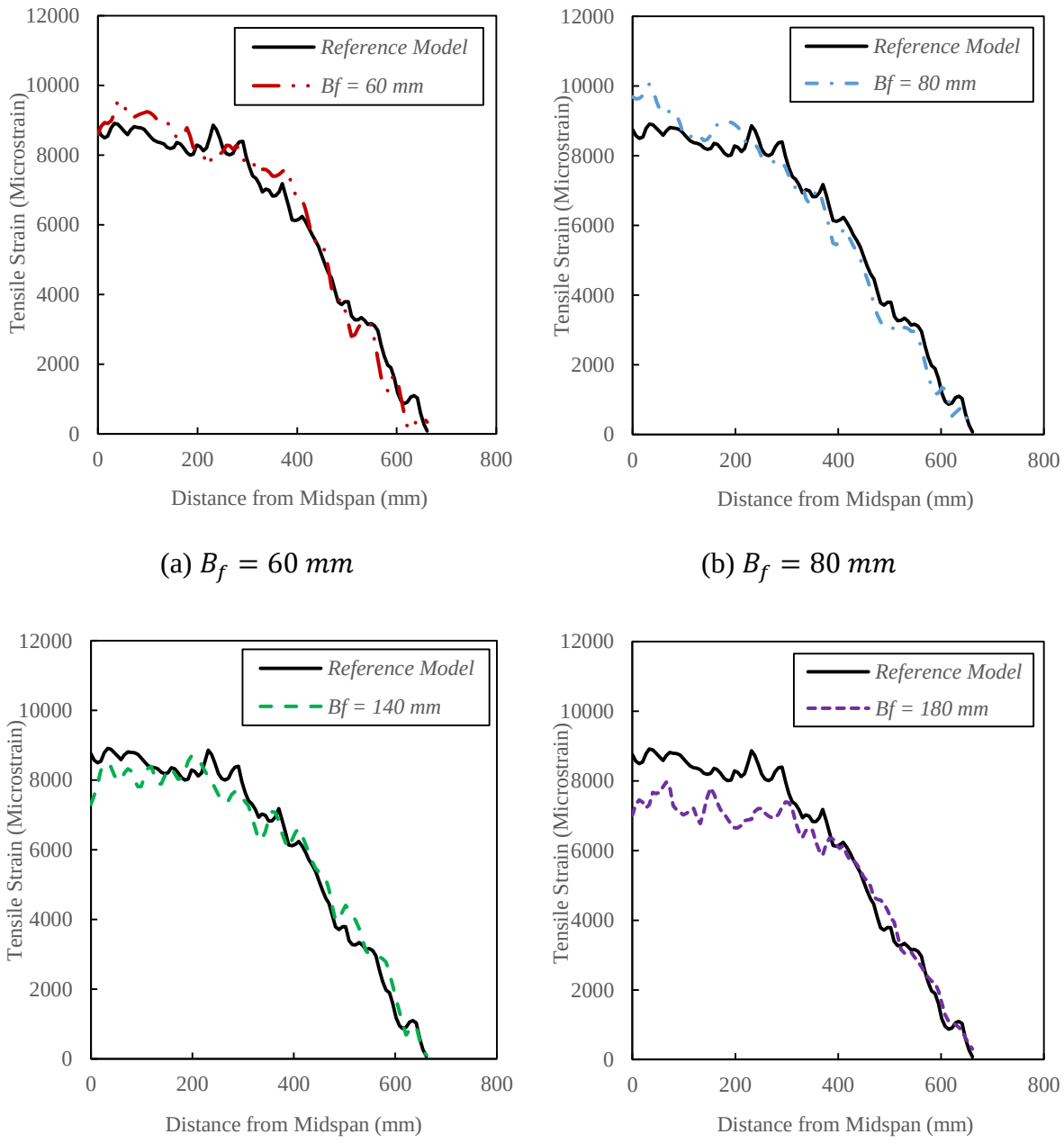

(a) $B_f = 60\ mm$

(b) $B_f = 80\ mm$

(c) $B_f = 140\ mm$

(d) $B_f = 180\ mm$

Figure 6.27: Axial strain in CFRP laminate (effect of CFRP bond width, B_f)

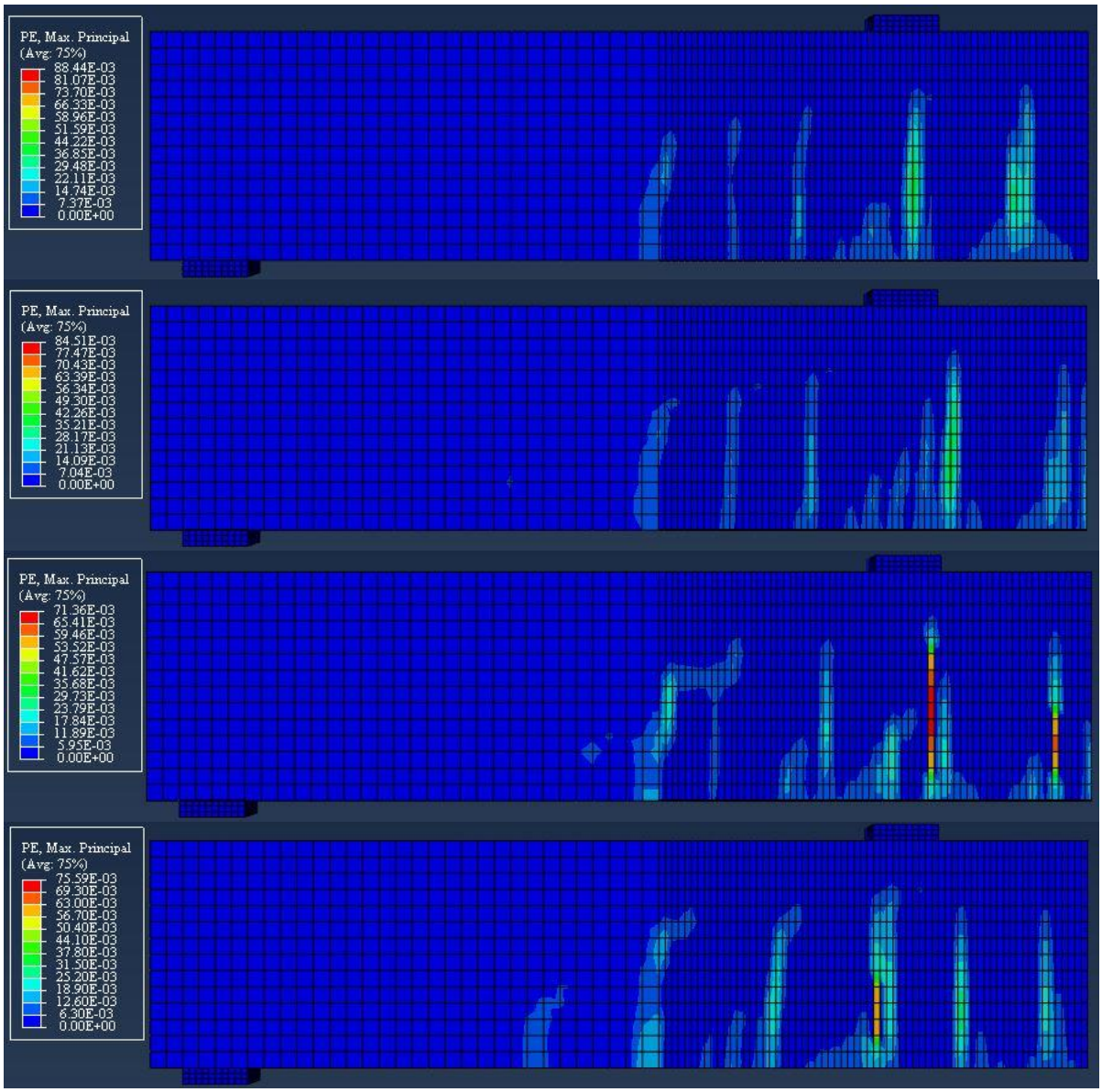

Figure 6.28: Comparison of crack patterns at final stage (effect of CFRP bond width, B_f)

6.3.7 Effect of Steel Stirrups Removal

The final segment of the parametric analysis, conducted in this chapter, involves studying the potential effect of removing steel stirrups from the proposed CFRP-strengthened beams. Steel stirrups (also called shear reinforcement) are usually added to concrete beams to provide sufficient shear resistance, and enhance flexural capacity and ductility of the reinforced member. As indicated in Chapter four, 10 stirrups were used in each model to ensure that the

beam does not fail in shear. However, it was suggested by several experimental and numerical studies that the employment of external CFRP reinforcement in concrete beams can allow for higher ductility. Consequently, the elimination of some or all shear stirrups might be feasible in CFRP-strengthened beams, while maintaining the integrity of the system. In this section, the proposed ABAQUS model was fabricated with the same original parts and materials of the original model in Chapter four, however, no steel stirrups were added to the model. During the postprocessing stage of the finite element analysis, the flexural response of the developed model was compared to the corresponding behaviour of the reference beam. Load versus midspan deflection curve was created, as depicted in Figure 6.29.

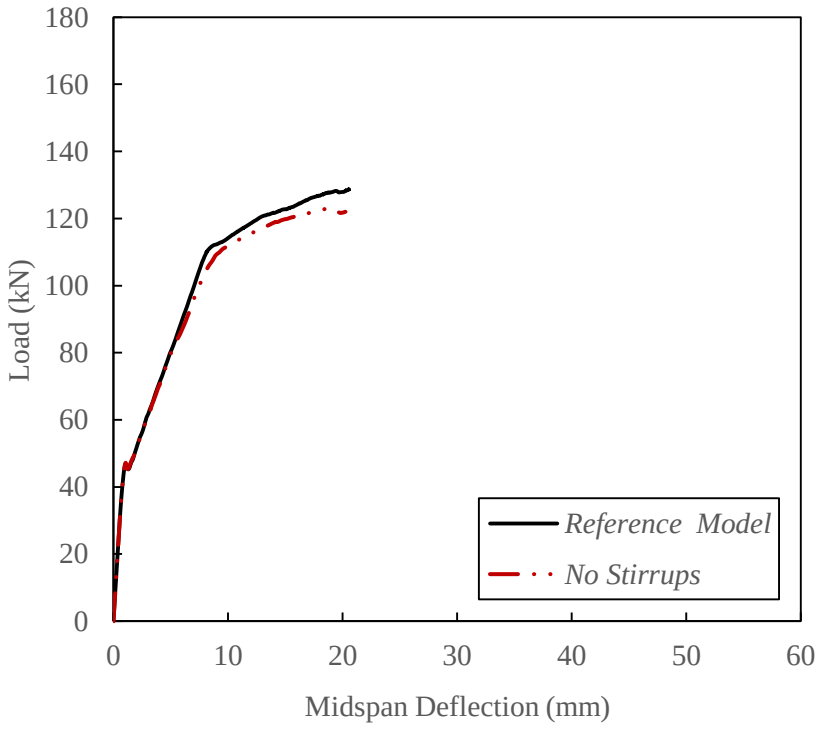

Figure 6.29: Load vs midspan deflection curve (effect of stirrups removal)

The plot indicates that the service load of reference specimen did not changed dramatically with the removal of stirrups. The cracking and yielding load reported in this model were 46.33kN and 111.52kN, respectively. On the other hand, the numerical model failed at a lower load in comparison to the original beam, with approximately 3.83% difference. The tensile strain along the steel rebar and the CFRP laminate is reported in Figure 6.30. Furthermore, the

longitudinal strain of steel reinforcement appears to be lower than the original model. However, a small increase is observed within the shear span region of the beam, due to the absence of stirrups. Moreover, the strain deformations along the CFRP sheet seem to have dropped as well near the beam's midspan, but soon after the strain profile started converging with the original data. Finally, Figure 6.31 presents the cark pattern in the current model, and large diagonal crack can be seen close to the shear span section. Figure B-28 in appendix B shows the development of concrete cracking in this model, at various loading stages.

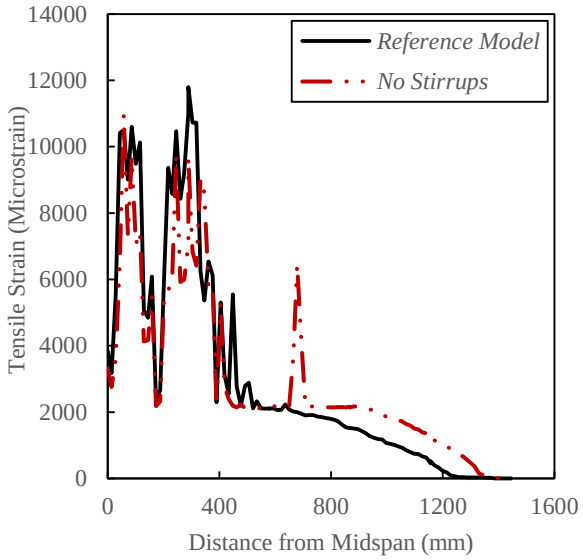

(a) Rebar tensile strain along the beam

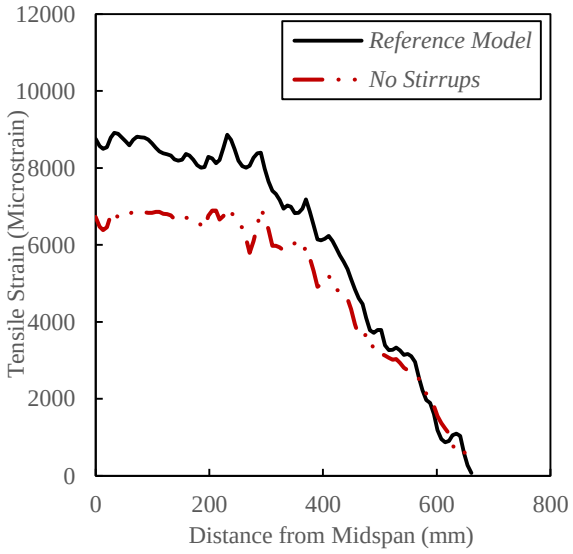

(b) CFRP tensile strain along the beam

Figure 6.30: Axial strain in: (a) steel rebar; (b) CFRP laminate (effect of stirrups removal)

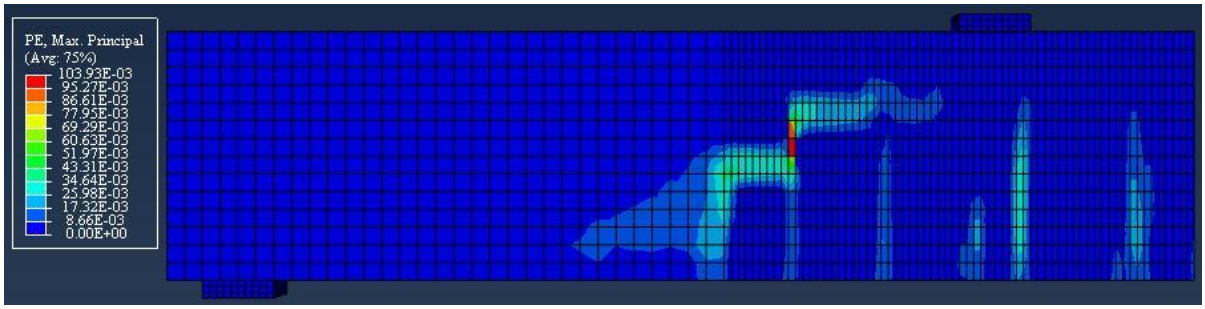

Figure 6.31: Crack patterns at final stage (effect of stirrups removal)

6.4 Summary

In this chapter, a comprehensive parametric study was carried out to investigate the effectiveness of the proposed CFRP Beam Model (CZM) in this thesis. The main focus of this analysis was to assess the influence of various critical parameters on the finite element simulation. These selected physical and mechanical parameters are believed to influence the efficiency and the load-carrying capacity of the CFRP-strengthened concrete beams. In order to characterize the impact of each parameter, a new FE model was created for each case individually. The structural response of these numerical models was then compared to the performance of the original model. This comparison was made in the form of load-midspan deflection response, the tensile strain along the internally-embedded steel rebar, the tensile strain along the externally-attached CFRP laminate, and the crack evolution of concrete in each model. The following summarizes some of the findings of this parametric study:

- The concrete compressive strength, f_c', was found to significantly affect the structural stiffness of the CFRP beam. The ultimate load capacity of the original member was found to increase with the use of higher f_c'. However, the influence of this parameter was more evident on the cracking load of the CFRP specimen, as higher compressive strength of concrete leads to an improved resistance to tensile stresses. The tensile strain deformations along the steel rebar and the CFRP laminate were very close to the original model when low f_c' is used. However, higher strains were recorded within the beam midspan region when the compressive strength exceeded 50MPa. Furthermore, the size of flexural and diagonal cracks in the concrete increases with the value of f_c' .
- The ratio of longitudinal steel reinforcement, ρ, had a significant impact on the flexural and debonding behaviour of CFRP-strengthened concrete beam. It was concluded that the cracking, yielding, and failure loads of the original beam experience large increase when larger steel rebars were used. This behaviour is expected as larger ρ values results in higher stiffness in reinforced concrete beams. However, as the cross section area of the steel rebar decreased, higher axial strains developed along the rebar's surface. This in turn resulted in smaller strain deformations along the CFRP sheet of the same

models. On the other hand, larger shear cracks were allowed to develop in the beam where high value of ρ is used.

- It was found that introducing higher dilation angle, ψ, in the Concrete Damaged Plasticity Model (CDPM) of the numerical specimen has led to a stiffer post-cracking response and higher load capacity, when compared to the reference beam. On the other hand, the effect of viscosity parameter, μ, in the CDPM is not limited to the stiffness and the ultimate capacity of the CFRP beam, it also controls the analysis running time and convergence rate. Although using small value of μ has a little effect on beam stiffness, the computational time becomes very expensive. Conversely, larger viscosity parameter increased the cracking load of the beam dramatically, which affect the accuracy of the simulation. However, the analysis running time was reduced by 50%. Moreover, the tensile strains in steel rebars and CFRP composites were more affected by the change of dilation angle than the viscosity parameters. In addition, larger cracks occurred in concrete beams when larger ψ and μ were used.

  The inclusion of only concrete tension damage parameter has a minimal effect on the beam flexural response and the reinforcement tensile strains, as compared to including only the compression damage parameter. However, the inclusion of damage parameters simulates the degradation in concrete modulus of elasticity that generates from potential unloading of beams, as elaborated in previous sections. Therefore, the difference between damaged and undamaged response, observed in this study, implies that unloading can take place within the cracked region of concrete due to the joining of localized cracks, though a monotonic load was applied to the beam.
- The effectiveness of the CFRP external reinforcement bonded to the tension surface of a flexural member is contingent on the bond strength between the Concrete and the CFRP system. However, it was found in this parametric study that CFRP-Concrete interfacial bond strength, τ_{max}, has minimal effect on the ultimate capacity of the CFRP beams, with the exception of the first model with very low bond strength. The impact of τ_{max} was more local, as it controls the initiation and development of micro and macro-debonding of CFRP plates. Moreover, higher tensile strains were seen along

the steel rebar of the first model, due to the weak bond in the CFRP-Concrete interface which in turn led to a premature debonding of the CFRP composite. Nevertheless, the strain response of the other cases followed the original data closely. Finally, larger cracks were allowed to grow in models with higher bond strength, as more efficient reinforcing system existed in these beams.

- Although increasing CFRP bond length, L_f, in CFRP beams was expected to improve the bond efficiency between the concrete and the CFRP reinforcement, the effect on the flexural capacity of the beam was found to diminish beyond certain CFRP bond length. Several studies, including this one, have concluded that there exist an effective bond length for the CFRP reinforcing composite, and any increase to that length will not necessarily enhance the global load-carrying capacity of the structural member. Furthermore, similar trends were plotted in tensile strains along the steel and CFRP reinforcements. However, large cracks evolved near the CFRP plate end in the models with short CFRP bond lengths. These cracks implies that the CFRP plate-end debonding can be the ultimate cause of failure in these CFRP beams.
- The use of larger CFRP bond width, B_f, has shown improvement in load serviceability and capacity of the CFRP beam model, when compared to the original specimen. This improvement is attributed to the increase in contact area of the CFRP-Concrete interface, and thus more efficient bond between the adjacent materials is achieved. Nonetheless, wider CFRP bond width meant larger cross section, and hence less strains were distributed across the CFRP laminate. Consequently, strains transferred from concrete to steel rebars were less in models with larger values of B_f. It was also noticed that Smaller cracks are captured in models with small B_f, while more scattered larger cracks are seen when wider CFRP bond width is used. This can be linked to the improvement in load-carrying capacity of beams reinforced with larger CFRP laminate.
- The removal of stirrups has led to a slight drop in the ultimate load of the CFRP beam in comparison to the reference specimen. This can be explained by inspecting the crack growth in the proposed model. It seems that larger dominant cracks are allowed to develop in the shear span of the model without stirrups, as compared to the pattern in

the original model with stirrups. It can be concluded that steel stirrups might help restricting the formation of such cracks and preventing them from migrating towards the load point. Therefore, a slight difference in the failure load is noticed between the two beams. Moreover, the tensile strains in the steel rebar and the CFRP composite seem to be decreased in this model with the removal of the steel stirrups. However, a light increase in rebar strain was seen near the shear span region of the beam.

In summary, the ratio of steel reinforcement, ρ, has shown the most influence on the service and ultimate load capacity of the CFRP-strengthened beam. However, increasing the CFRP-Concrete interfacial bond strength, τ_{max}, over 3MPa seem to have an insignificant effect on the ultimate load capacity of the CFRP member. Moreover, increasing the CFRP bond length beyond a specific point did not enhance the flexural and debonding performance of CFRP-strengthened beams largely. Such point can be referred to as the effective bond length. Most importantly, the tensile strains seen in all beam models, developed in this parametric study, were lower than the rupture point of CFRP composite reported by the manufacture ($\varepsilon_{pu} = 0.015$). This indicates that all beams failed due to either plate-end or midspan debonding of CFRP reinforcement.

Chapter Seven

Effect of Multiple Cracks on CFRP Debonding

7.1 Introduction

Several research programs have shown that when loading a conventional CFRP-RC beam, a number of flexural or flexural/shear cracks develop along the beam span. Some of the empirical studies, mentioned in Chapter two, stated that CFRP debonding can be triggered by intermediate cracks that are formed near the beam midspan, where high bending moment and forces are expected. However, as the applied load increases, the debonded zone of CFRP grows and spreads towards the plate end, which ultimately results in the failure of the structural member. Nonetheless, the study of CFRP debonding mechanisms associated with multiple cracks have been the focus of many scholars in the civil engineering community. Moreover, the FRP debonding failure resulting from multiple cracks has already been introduced in design provisions, such as CEB-FIB (2001). However, the proposed model has not yet been verified experimentally (Monteleone, 2008).

As indicated before, the use of finite element analysis allows to capture properties and responses that are challenging to obtain experimentally, such as interfacial stresses and potential slippage between the concrete and the externally-attached CFRP laminate. Moreover, strain deformations can be measured to a certain degree of accuracy, as opposed to conventional methods such as strain gauges. Most of the experimentally recorded CFRP strains were measured by "electrical resistance" strain gauges glued to the outside surface of the CFRP

sheet. The accuracy of strain data acquired by such method can be questionable, due to effect of several factors such as: the environment in which the test was conducted, possible vibration, and gauge malfunction. Therefore, more reliable modelling practices are needed to investigate the intermediate crack-induced debonding of CFRP reinforcement in RC beams. This chapter concentrates on the debonding behaviour and the failure mechanisms produced by flexural and flexural/shear cracks in CFRP-reinforced beams. Various crack spacings will be examined in terms of their effect on the structural performance of the CFRP beam, as will be seen in the following sections.

7.2 Modelling Approach

As mentioned earlier, the objective of this study was to assess the CFRP debonding and failure mechanisms, induced by intermediate cracks in CFRP-RC beams. There are two common approaches to simulate fracture process in finite element modelling: a continuum approach and a discrete approach. It has been reported that the first approach simulates fracture as the end process of localization and accumulation of damage in continuum, without creating real discontinuity in the material (Monteleone, 2008). On the other hand, the discrete approach allows to simulate crack as geometrical entities. However, the continuum approach, also referred to as "smeared crack approach", has been used commonly in finite element applications. It has also been utilized to model concrete elements in the proposed models of this study, due to its simple and fairly accurate representation of overall cracking in RC beams. Although the continuum approach is capable of simulating initial micro-cracking in localized regions such as pre-defined notches, it fails to capture individual macro-cracks as the load and damage progresses. As the name suggests, smeared crack approach tends to spread the cracks growth and movement over a region of a structure rather than localizing them at specific points. However, this drawback can be overcome by significantly reducing the size of elements used in the FE model. Such technique was explored in a study by Lu et al. (2005), as explained in section 2.11.3. The authors of this study proposed a meso-scale finite element model in which

smeared crack approach was used to simulate the damage in concrete. Nevertheless, the use of very small elements, to overcome the shortcoming of continuum approach, is not very efficient in full-scale structures in terms of analysis time and accuracy. Therefore, the discrete approach was selected to model individual cracks within the proposed models in this chapter. This method was adopted for its ability to measure the crack initiation and evolution in the numerical model.

7.3 Model Preparation

One of the main advantages of the discrete crack approach is its efficiency in simulating geometrical discontinuities resulting from crack opening, slipping of rebar, and debonding of FRP laminate. This method was utilized by implementing the so-called "Cohesive Zone Model" approach in the ABAQUS model. The fracture in concrete member, presented in this study, was simulated by creating two zones: traction-free and cohesive crack, as shown in Figure 7.1. The traction free region is physically fabricated by creating pre-defined small cracks (notches). The size of these notches was adopted from the main experimental study performed by Brena et al. (2003). Each tested experimental specimen was fabricated using a "crack initiator", which was 0.4mm thick, 6mm deep, and extended the entire width of the beam. It must be noted that there are no forces transferred along the traction-free zone and crack surfaces are completely separated. In the contrary, stresses are expected to intitaite within the cohesive crack zone, to simulate crack onset and development. These stresses are governed by a predefined bilinear relationship to model mode I (opening) fracture resposne in concrete. the cohesive cracks in this approach is triggered when the tensile stresses exceed the tensile capacity of concrete, f_t'. Thereafter, real cracks are assumed to take place when the frcature energy, G_c, to create a unit crack is reached. Based on the calculations pefomed in Chapter four, the tensile strength and the modulus of elasticity of concrete were taken as 3.66MPa and 27446.31MPa, respectively. However, the fracture energy of concrete was inputted as 100N/m (i.e. the average between the two values predicted by Model Code 1990 and Model Code 2010).

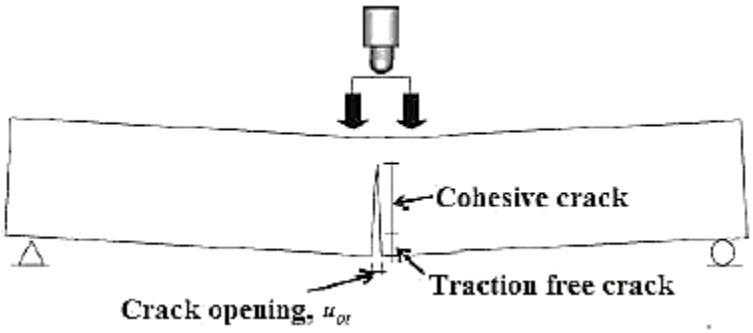

Figure 7.1: Fracture zones in concrete member (Monteleone, 2008)

Moreover, in order to constrain crack growth within the predefined cohesive zone, the compressive and tensile response of concrete were modified as shown in Figure 7.2, where strain limitations were omitted. As indicated before, the plasticity of concrete was accounted for in the FE model of this study by implementing the Concrete Damaged Plasticity Model, available in ABAQUS. The CDPM uses the smeared crack appraoch such that macro-cracks are not physically created in the model. However, the presence of these cracks is indirectly simulated by their potential effect on stress and material stifness. In another word, the cocncrete damage parameters, associated with the CDPM, control the degradation of elastic stifness and yield surface growth in material. These damage parameters generally embodies the dissipated fracture energy needed to generate cracking. Consequently, the presnsce of cracking in concrete can be associated with the softening behaviour of the material. Therefore, in order to remove the effect of crack damage and evolution, the compressive hardening and tensile softeining of concrete are removed. This parcatice will allow for cracks to grow only within the predefined locations. While hairline cracks are still premitted between these location whenever stresses exceed the specified tensile strength of concrete.

The geometry, material parameters (other than the modifications mentioned earlier), mesh size, and analysis type were adopted from the original CFRP Beam Model with CZM, introduced in Chapter four. In particular, the model with mesh size (25 x 25) mm was selected to be modified for this study, due to its superiority to other models as explained before. Moreover, the same methodology, described in Chapter four to model steel and CFRP-Concrete interfaces, were followed in this analysis. However, the CFRP bond length was increased to

1000mm to allow for more intermediate cracks to initiate and develop, and hence more induced CFRP debonding can be observed. Moreover, the steel stirrups were removed for simplicity and to reduce the analysis computational time. As indicated in previous chapter, the removal of stirrups in this model did not result in shear failure, because other reinforcement material such steel and CFRP laminate provided sufficient support and ductility to the beam to behave in a flexural manner. It should also be noted that there has been no previous numerical attempts to investigate the effect of multiple existing cracks on the debonding behaviour of CFRP in RC beams (Niu, et al., 2006) and (Monteleone, 2008). Therefore, the model proposed in this chapter and the findings of this analysis could not be compared to a reference study. However, the numerical results and observations made in this study were thoroughly verified with the available constitutive properties and mechanisms.

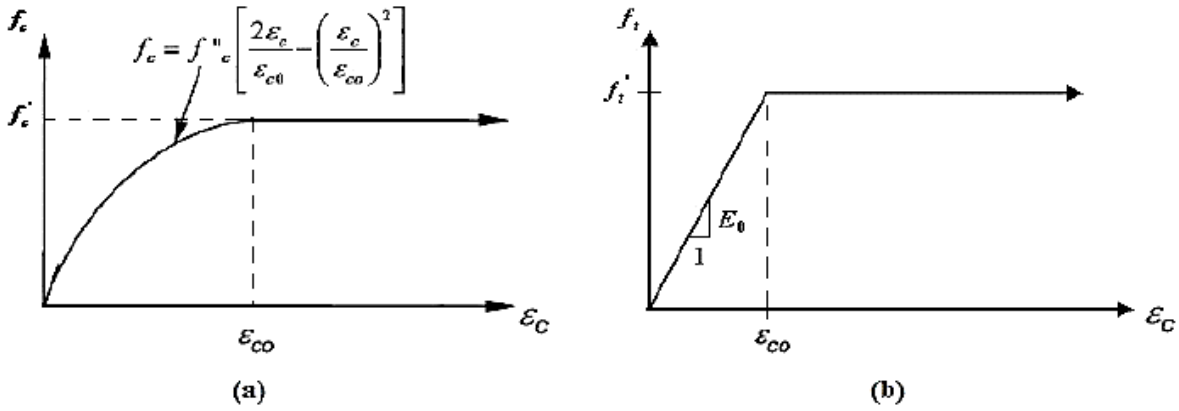

Figure 7.2: Modified stress-strain relation of concrete in: (a) compression; (b) tension

7.4 Results Analysis

The effect of intermediate cracks on the debonding response of CFRP composite in concrete beam was examined. This was achieved by creating five ABAQUS models, in which the predefined cracks varied in their number and spacing. First model included a single crack placed at the tension face of the beam, at a location that is aligned with the loading point.

However, the cracks in the other four models were spaced at 250mm, 200mm, 150mm, and 100mm, respectively. The multiple cracks were located at the bottom face of the concrete beam as well, while maintaining the location of one of the cracks under the loading. As will be presented in the following sections, the postprocessing stage of the finite element analysis included the investigation of CFRP debonding initiation and evolution, the interfacial shear stresses, and the development of tensile strains in steel and CFRP reinforcements.

7.4.1 Model with Single Crack

As indicated in previous section, a single flexural crack was introduced in this model and positioned immediately under the applied load. It is clear that prior to the crack initiation and growth at the cohesive zone, adequate bond is maintained between the concrete substrate and the CFRP laminate. Therefore, no relative slip between the two materials is observed, and hence micro-debonding does not occur. However, as the external loading increases the interfacial stresses at the CFRP-Concrete interface increase as well. Nonetheless, it was noted that micro-debonding of CFRP laminate initiated when the applied load reached 61.73kN, which corresponds to a midspan deflection of 1.54mm. As expected, this initial micro-debonding of the laminate occurred at the predefined crack location (also referred to as C1), as depicted in Figure 7.3. As mentioned in earlier chapters, micro-debonding of CFRP reinforcement is usually triggered by small cracks occurring at the weaker layer, which is the concrete in this case. This will result in a region of stress concentration at the crack toe, which in turn creates sliding between the concrete and the CFRP laminate. In another word, this leads to a differential strains between the concrete and the adjacent CFRP composite, which ultimately results in the debonding of the latter. As shown in Figure 7.3, the initial micro-debonding took place when the stress concentration at the crack tip reached the maximum bond strength of the CFRP-Concrete interface. This value was calculated in section 4.8 and found to be 5.49MPa. However, high interfacial stresses have not yet reached the ultimate bond strength in locations further away from the crack. This indicates that stresses within the CFRP-Concrete interface in these locations are still within the elastic range (i.e. no micro-debonding).

Furthermore, as the crack widens with increasing the load, the tips of bond stresses shift from the point load location in two opposite directions: toward to the plate end and beam midspan, as seen in Figure 7.3. This shift started when the steel rebar yielded at a load of 152.69kN (midspan deflection of 7.66mm). At this point the stress concentration at crack 1 started to decrease, which indicates some softening in the interface close to the crack. This debonding mechanism continued until the complete failure of the beam.

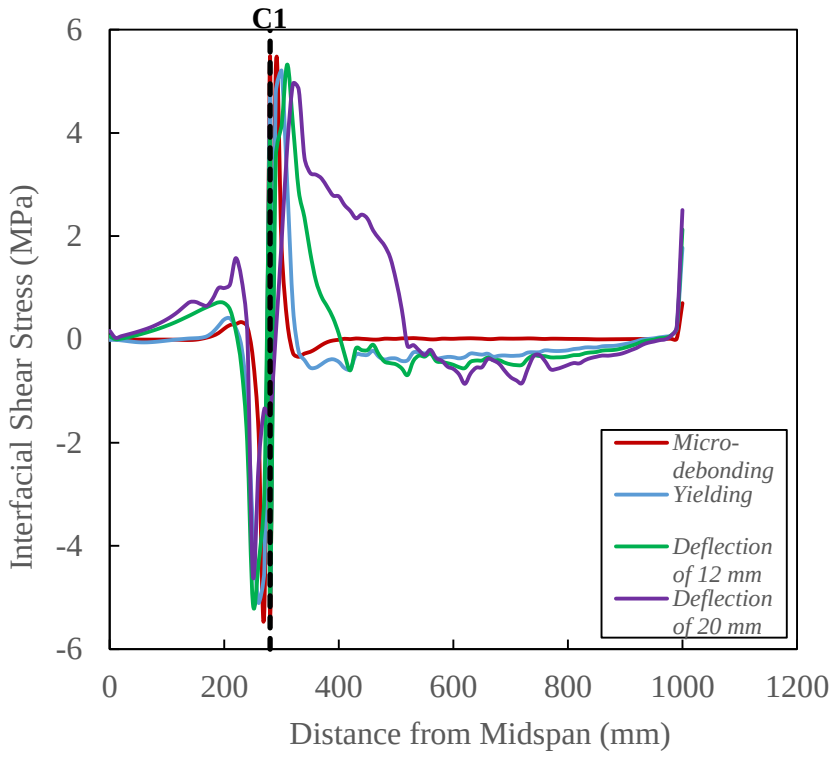

Figure 7.3: Interfacial shear stress distribution along the beam (single crack)

The tensile strain deformation along the steel rebar and the CFRP laminate are graphed in Figure 7.4 and Figure 7.5, respectively. It can be seen that strains in steel and CFRP materials started to increase at higher rates once the steel yielding occurred. This refers to the fact that the reinforcing materials are now required to restrain the opening of the flexural crack as the load progresses. Moreover, the crack pattern in the proposed beam and the interfacial stress distribution along the CFRP-Concrete interface, at the micro-debonding stage, are illustrated in Figure 7.6.

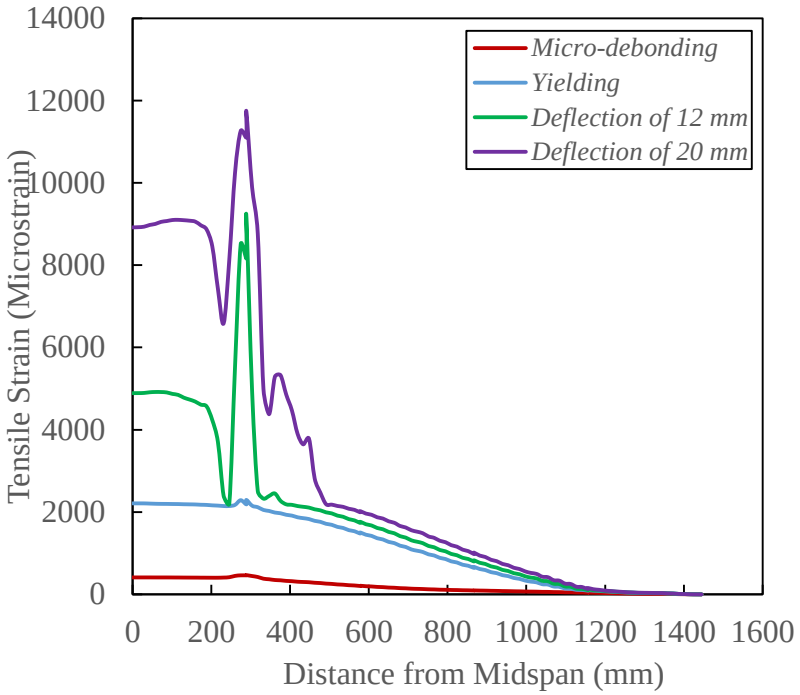

Figure 7.4: Rebar tensile strain along the beam (single crack)

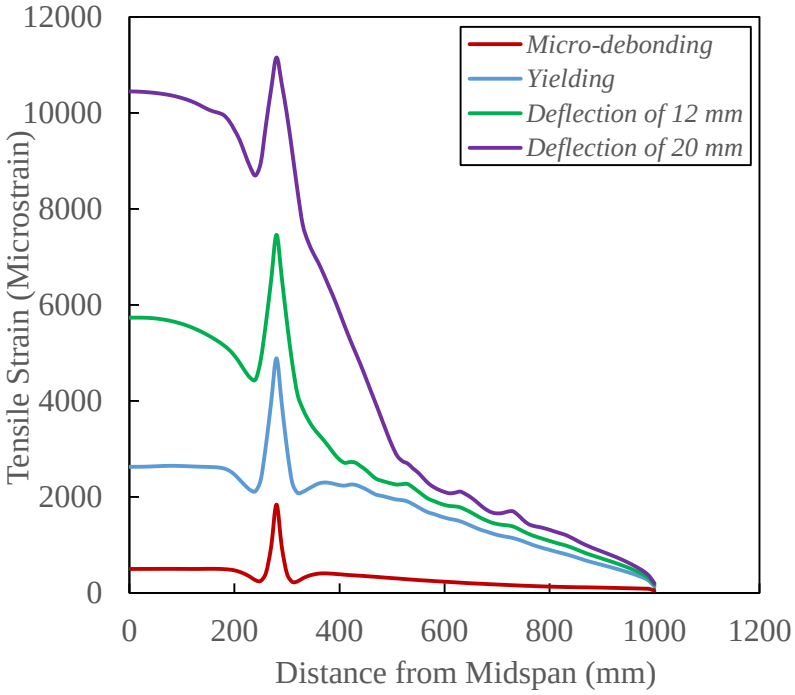

Figure 7.5: CFRP tensile strain along the beam (single crack)

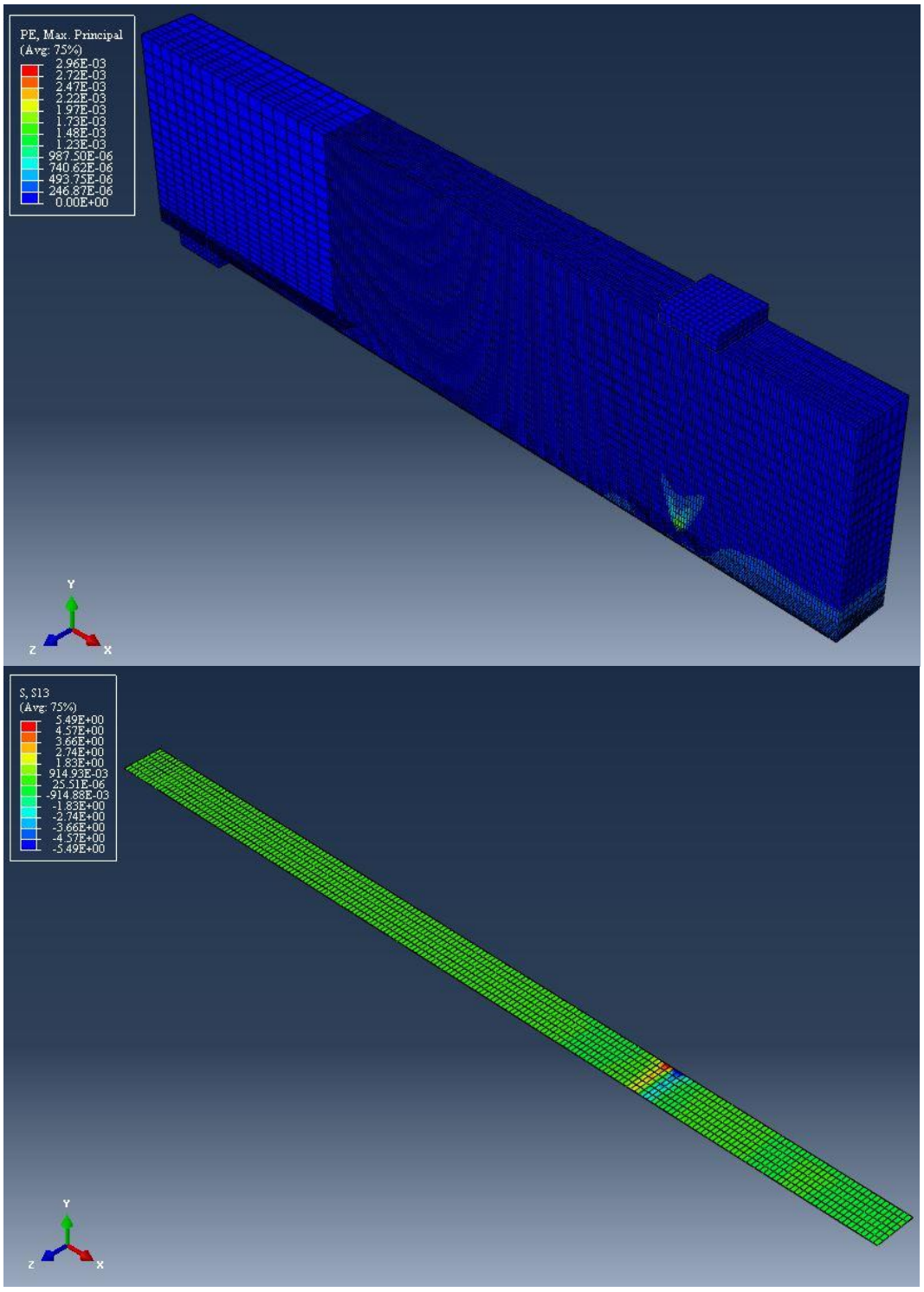

Figure 7.6: Crack pattern and interfacial stress distribution at micro-debonding (single crack)

7.4.2 Model with Crack Spacing of 250mm

The model in this case consisted of four flexural cracks along the tension face of the concrete beam. The first predefined notch was placed at 30mm from the specimen midspan. While the second crack was located 250mm from the first crack, which makes it situated under the loading point. The remaining two cracks were spaced at 250mm and 500mm from the second crack, respectively. The same loading and boundary conditions of the previous model were applied to this beam. However, no slip was observed between the concrete and the attached CFRP plate at early loading stages. Micro-debonding of CFRP system initiated when the loading reached to 104.72kN, corresponding to a midspan deflection of 4.03mm. The initial CFRP micro-debonding occurred simultaneously at crack 1, and 2, (see Figure 7.7).

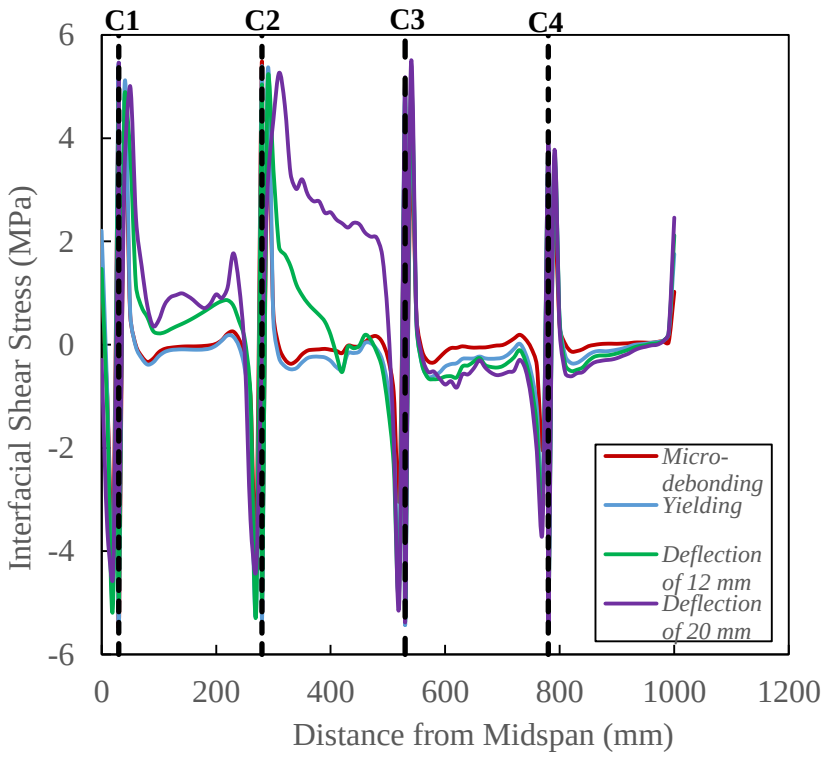

Figure 7.7: Interfacial shear stress distribution along the beam (crack spacing of 250mm)

The occurrence of micro-debonding at these cracks is expected since they are located in the maximum moment region of the beam, and hence higher interfacial stresses can be experienced at the cracks toes. Similar to the situation mentioned in previous section, the micro-cracking

initiated at the concrete layer close to the CFRP composite and progressed laterally. This crack movement has cause some relative sliding between the concrete and the CFRP plate, which caused the interfacial stresses at the crack toe to exceed the interfacial bond strength of 5.49MPa. Moreover, it has been noticed that there was a negative slip between adjacent cracks in the case of beam with multiple flexural cracking. In another word, there exists an infliction point in the interfacial stress curve between subsequent cracks in order to maintain equilibrium, as shown in Figure 7.7. However, it is observed that this zero-slip point, between crack 2 and 3, moves toward the subsequent crack as the load increases. These cracks are located in high moment region, and thus CFRP slip can be seen shifting from one side to the other. This movement may indicate that crack 2 is rapidly opening, and thus the associated slip is reduced at the left face of crack 3. Nonetheless, the inflection point between crack 3 and 4 maintained its middle position throughout the loading process. It must be mentioned that, although, micro-debonding was initiated between crack 3 and 4, the slip did not evolve to a full macro-debonding. This can be attributed to lower stresses being transferred to the CFRP plate in the varying moment region. In fact, the bond stresses at crack 4 never exceeded the ultimate stress capacity of 5.49MPa and remained in their elastic stage, due to its far location from the load point.

On the other hand, the steel rebar experienced its highest tensile strains at crack 1 and 2, due the presence of high stresses in that region as mentioned earlier (see Figure 7.8). As the yielding occurred at 151.60kN loading and midspan deflection of 7.55mm, the axial strain in the CFRP plate increased at a much higher rate as depicted in Figure 7.9. This increase can be justified by the fact that, once the steel yielded, the CFRP laminate were required to restrain the cracks in that region. The concentration of tensile strains in steel and CFRP reinforcements, within crack 1 to 2 region, implies that major debonding of CFRP plate has occurred in that location, which in turn led to the ultimate failure of the beam. Concrete crack pattern was captured at the points where the CFRP laminate started to micro-debond, and presented in Figure 7.10. It can also be seen from the bottom figure that micro-debonding has occurred at crack 1 and 2, where the interfacial stresses exceeded the bond strength of the laminate.

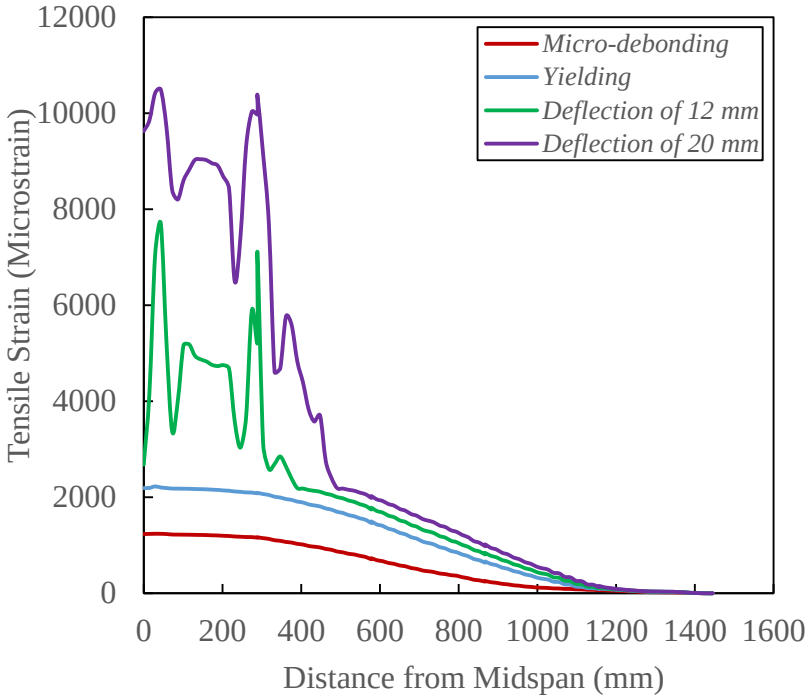

Figure 7.8: Rebar tensile strain along the beam (crack spacing of 250mm)

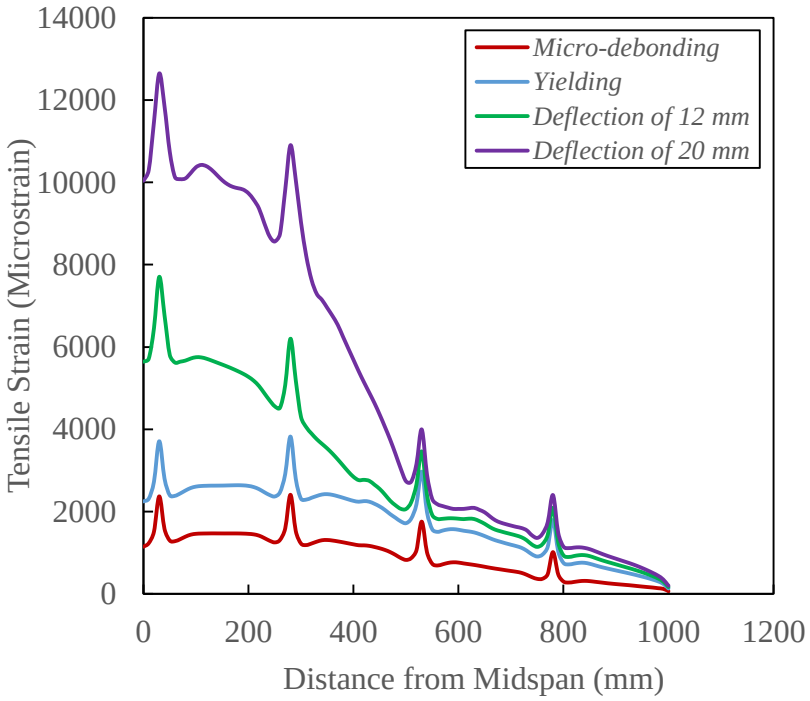

Figure 7.9: CFRP tensile strain along the beam (crack spacing of 250mm)

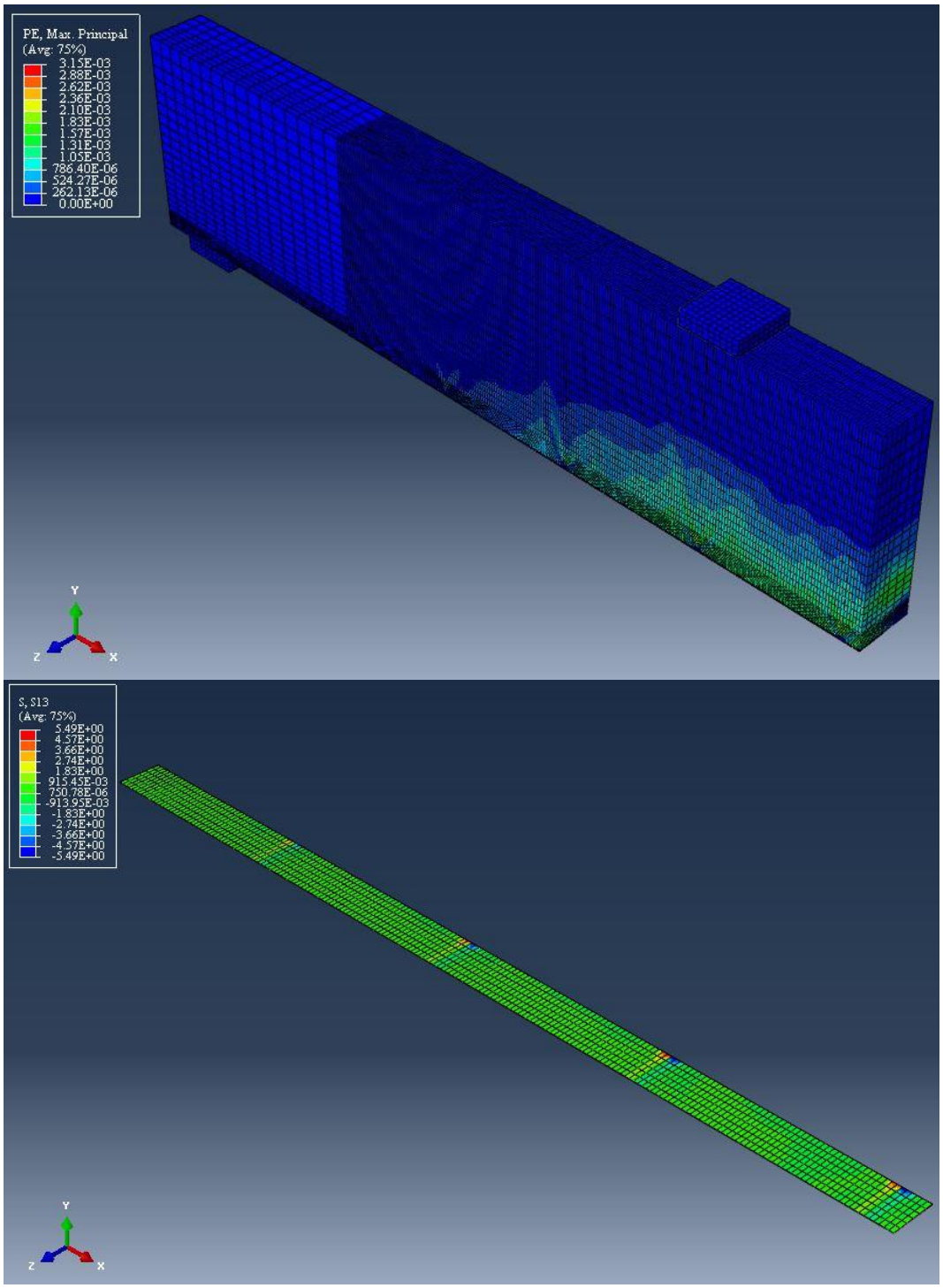

Figure 7.10: Crack pattern and interfacial stress distribution at micro-debonding (250 mm)

7.4.3 Model with Crack Spacing of 200mm

The flexural cracks were predefined at five locations in this beam model. The first crack was created at 80mm from the midspan of the beam, and the following four cracks were spaced at 200mm. Similar to the last two cases, the second cracks lies directly under the loading point. The finite element analysis was then run under the same monotonic loading, and as expected, no significant slip was observed when the load was still low. The first micro-debonding of CFRP laminate was recorded at crack 1 and 2 when the beam was loaded to 105.18kN, which corresponds to a midspan deflection of 4.08mm. Figure 7.11 provides the interfacial shear stresses between the concrete and the CFRP composite at various loading stages.

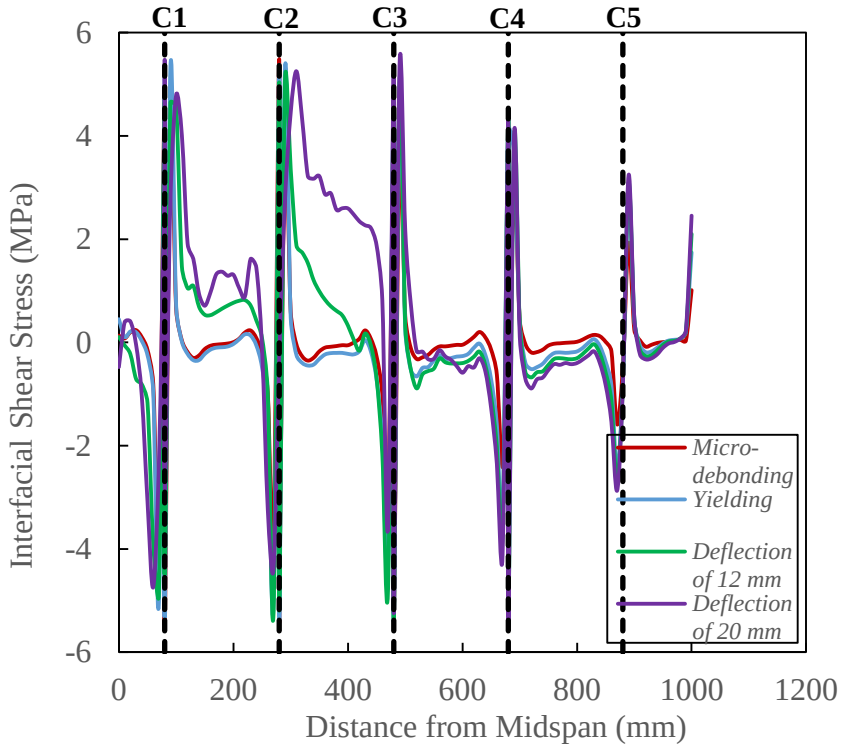

Figure 7.11: Interfacial shear stress distribution along the beam (crack spacing of 200mm)

The crack initiation and development in this model was similar to that seen in previous cases, where micro-cracking propagated horizontally across the concrete layer adjacent to the CFRP plate. These cracks generated a region of bond stress concentration at the crack toe, which caused the strain in the concrete to be different than the strain in the attached CFRP laminate.

This discrepancy led to a relative slip between the two surfaces at crack 1 and 2, as mentioned before. Moreover, the initial micro-debonding took place at these two cracks given their location within the maximum moment region. These high moments translated to high shearing stresses at the CFRP-Concrete interface, which in turn caused the micro-debonding once they exceeded the interfacial bond strength of 5.49MPa. As seen in the beam with crack spacing of 250mm, there were zero-slip points between subsequent flexural cracks in the interfacial stress curve. These inflection points were necessary to maintain equilibrium at the CFRP-Concrete interface. Moreover, this change in curve's slope was observed at the middle point between two cracks through different loading stages. However, the region between crack 2 and 3 was an exception, where the slip was recorded moving toward the left face of crack 3, similar to the case in previous model. This shift in slip can be a sign that crack 2 was widening at a higher rate as the loading increases. Nonetheless, no micro-debonding or slip were shown by the region from crack 4 to the CFRP plate end, as lower stresses are expected in regions far away from the load point. On the other hand, once the steel rebar has yielded at 150.02kN (midspan deflection of 7.44mm), the interfacial stresses at crack 1 started to soften. This can be indicative of complete CFRP debonding at that region, and consequently higher stresses were shifted to the next crack (crack 2).

The tensile strains along the steel rebar and the CFRP plate are illustrated in Figure 7.12 and Figure 7.13, respectively. The strain deformation recorded in this model was higher compared to the model described in previous section. This can be explained by the presence of larger cracks in the current beam, which caused the internal and external reinforcement to sustain larger strains as they attempt to bridge those cracks. The strains measured in steel rebar and CFRP plate of this specimen were 7.84% and 1.54% higher than their corresponding in previous model, respectively. The other observation that can be made that, similar to the previous models, the strain in steel and CFRP reinforcement experienced strains at much higher rate once the yielding of steel took place. Finally, crack development in concrete was depicted in Figure 7.14, at the load which caused the CFRP plate to start debonding. The second image of this figure supports the assumption that initial micro-debonding of CFRP composite was seen at crack 1 and 2.

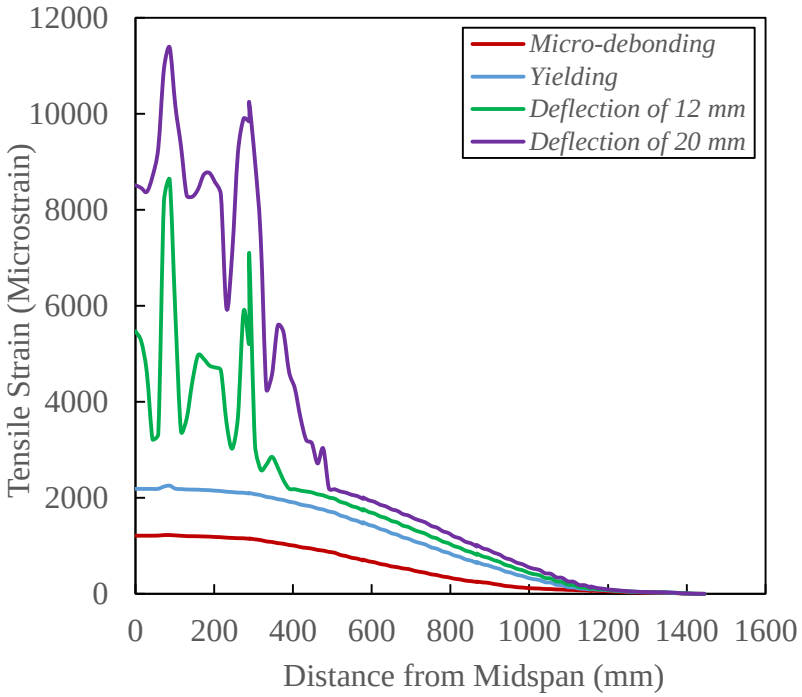

Figure 7.12: Rebar tensile strain along the beam (crack spacing of 200mm)

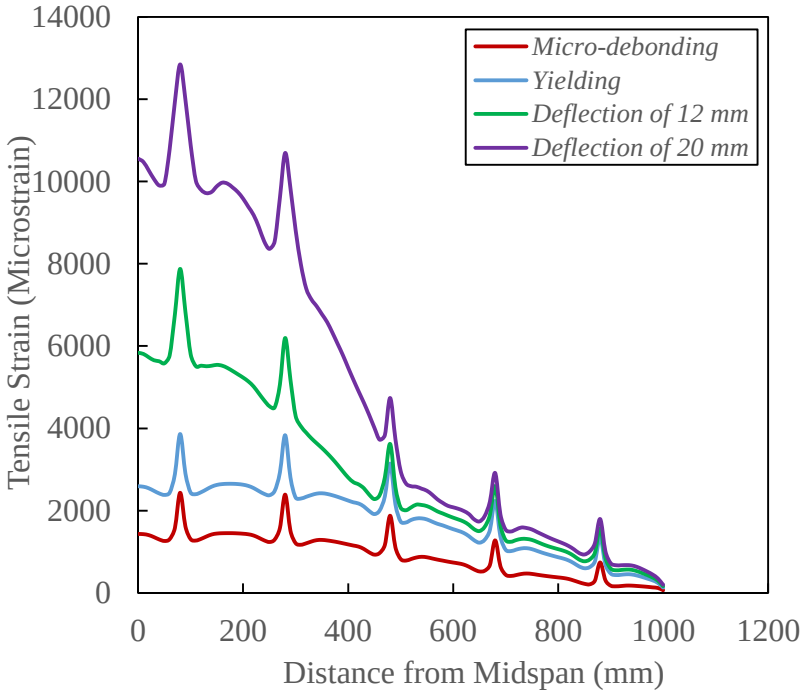

Figure 7.13: CFRP tensile strain along the beam (crack spacing of 200mm)

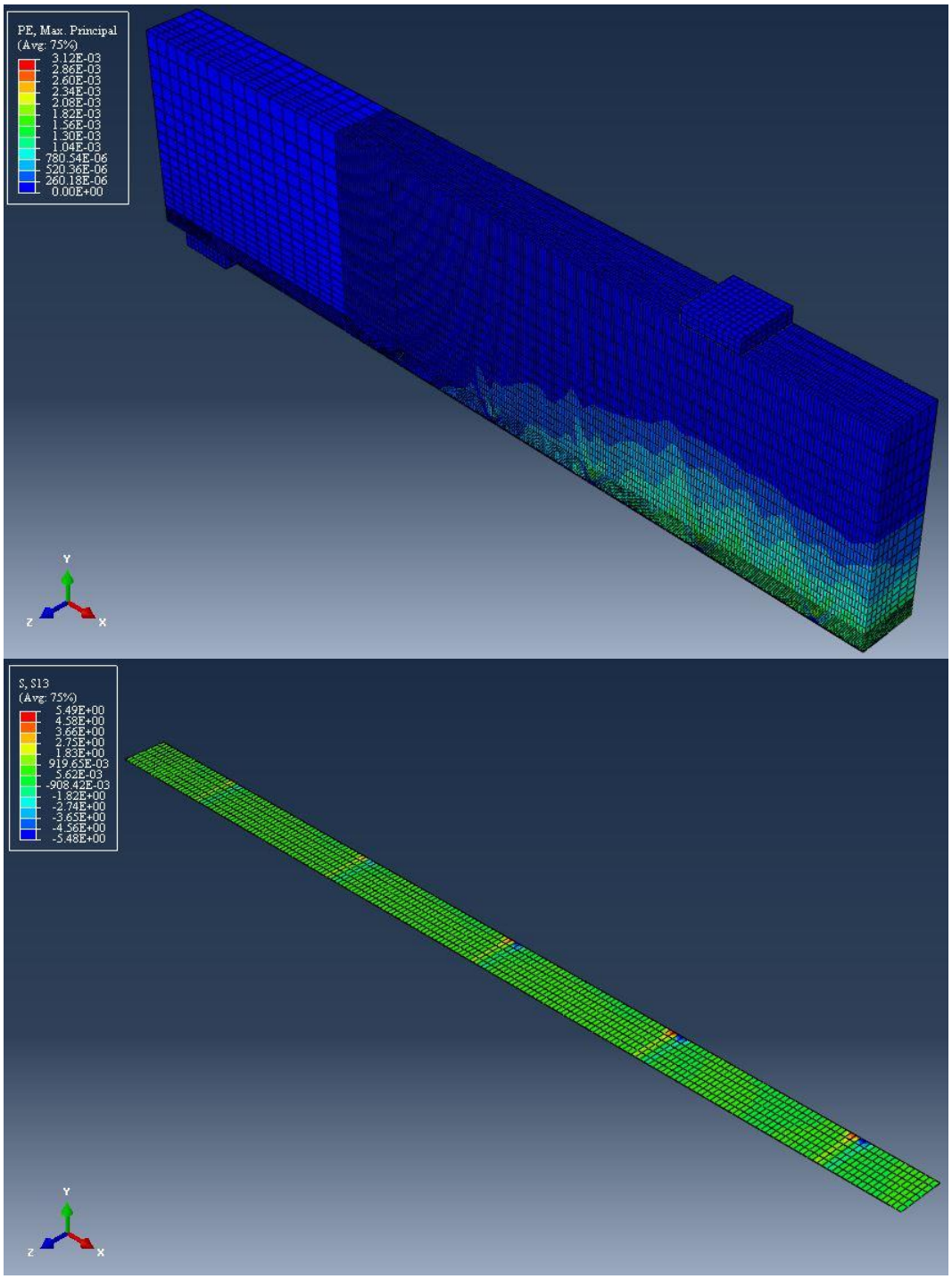

Figure 7.14: Crack pattern and interfacial stress distribution at micro-debonding (200 mm)

7.4.4 Model with Crack Spacing of 150mm

The finite element model in this analysis was constructed with six pre-existing flexural cracks at the tension face of the concrete beam. The first notch was created 130mm away from the middle of the beam. Then the second crack was spaced at 150m from the first crack, which makes it aligned with the loading point, similar to the case in the previous models. The beam was loaded monotonically until failure, and postprocessing of data was performed at the end of the analysis. No measurable slip of CFRP plate was observed prior to the initiation of flexural cracks in the cohesive zone of the notch. First sign of micro-debonding was seen at crack 1, 2, and 3, when the loading reached 105.37kN and the beam deflected to 4.08mm at midspan. Figure 7.15 represents the bond stresses between the concrete and the CFRP plate.

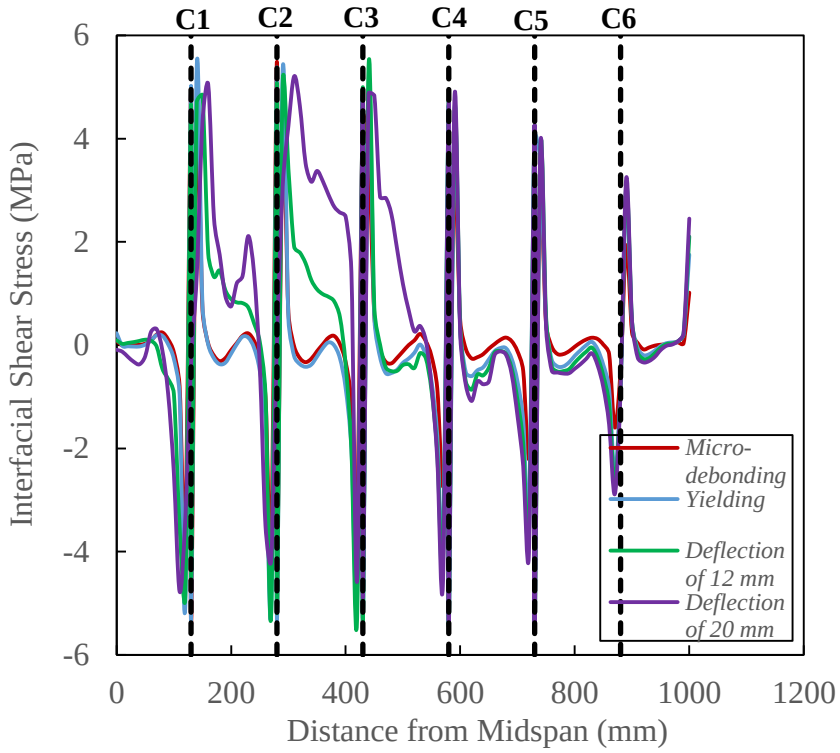

Figure 7.15: Interfacial shear stress distribution along the beam (crack spacing of 150mm)

The first micro-debonding was induced by the lateral cracking in concrete near the CFRP laminate. This led to a sudden increase in transferred bond stresses at crack tips, which generated a relative slip between the concrete and the CFRP plate at the location of the first

three cracks. The presence of first slips at these locations is the result of crack 1, 2, and 3 being within or very close to the maximum moment region. As mentioned before, high moments are translated to high shearing stresses at the CFRP-Concrete interface. Once these interfacial stresses reached the ultimate bond strength of the cohesive (e.g. 5.49MPa), micro-debonding was initiated. Moreover, the direction of slip was found to interchange between adjacent cracks in order to achieve equilibrium. The inflection points of bond curve was seen to be in the middle point of two adjacent cracks, and this was not affected by load changing. However, the zero-slip point was found to shift from crack 2 toward 3 and from crack 3 toward 4, once the steel reinforcement yielded at 151.20kN (midspan deflection of 7.52mm). As explained before, this shift can be the result of larger crack opening at location 2 and 3, which pushes the slip to the left face of crack 3 and 4. Furthermore, gradual decrease in interfacial stresses were measured as we move away from beam midspan. No actual debonding was recorded in the region restrained by crack 5 and CFRP plate end. In another word, interfacial shear stresses never reached the ultimate bond capacity of the cohesive element.

The axial strains were plotted in Figure 7.16 and Figure 7.17 for steel rebar and CFRP laminate, respectively. It is worth mentioning that strains records in this model has slightly dropped when compared to those in the beam with crack spacing of 200mm. the highest tensile strains in this beam were 0.2% and 1.63% lower than their equivalent in the previous study, for steel rebar and CFRP plate, respectively. This can be attributed to smaller crack openings relative to the previous model, as more closely-spaced cracks can limit the evolution of a single crack. Moreover, high strains in both reinforcements were limited to the region between crack 1 and 4. This is associated with the high moments in that region, and hence more strains were being carried by the steel and CFRP reinforcement to restrain the debonding-induced cracking. However, similar to the trend seen in previous models, strain values were increasing at a much higher level after the yielding of steel rebar. Finally, Figure 7.18 provides a representation of crack pattern in this model, at micro-debonding loading stage. This initial debonding can be seen to initiate once the ultimate bond strength was reached at crack 1, 2 and 3.

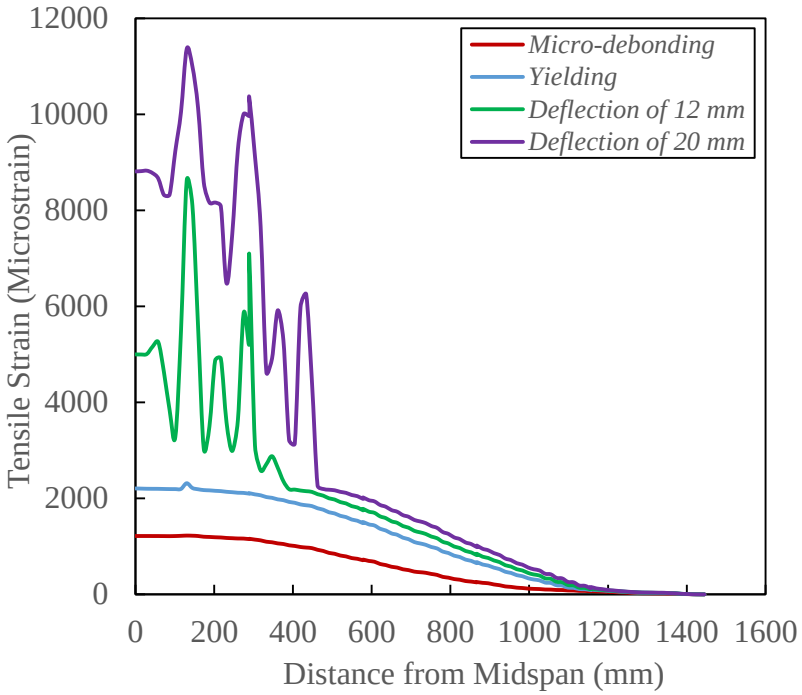

Figure 7.16: Rebar tensile strain along the beam (crack spacing of 150mm)

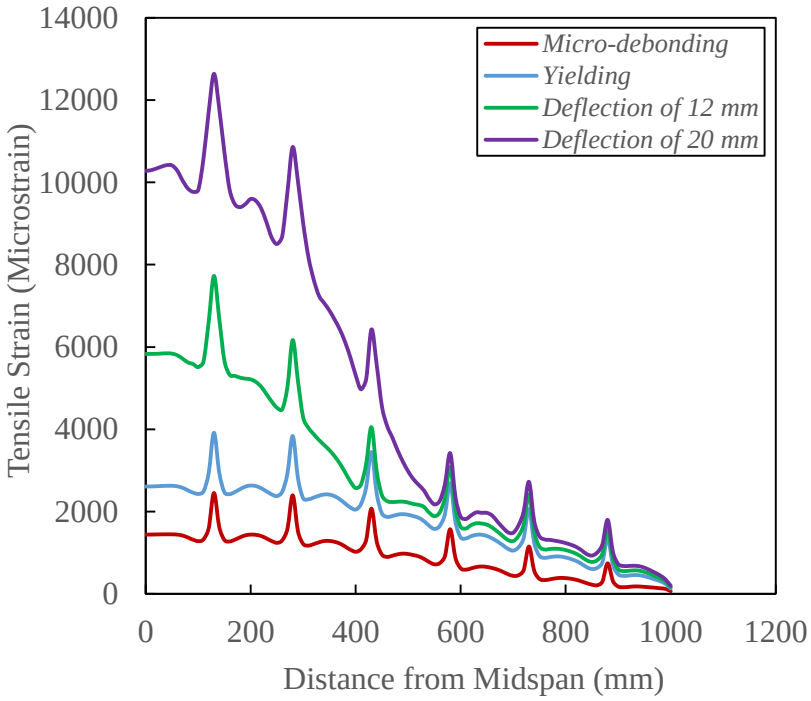

Figure 7.17: CFRP tensile strain along the beam (crack spacing of 150mm)

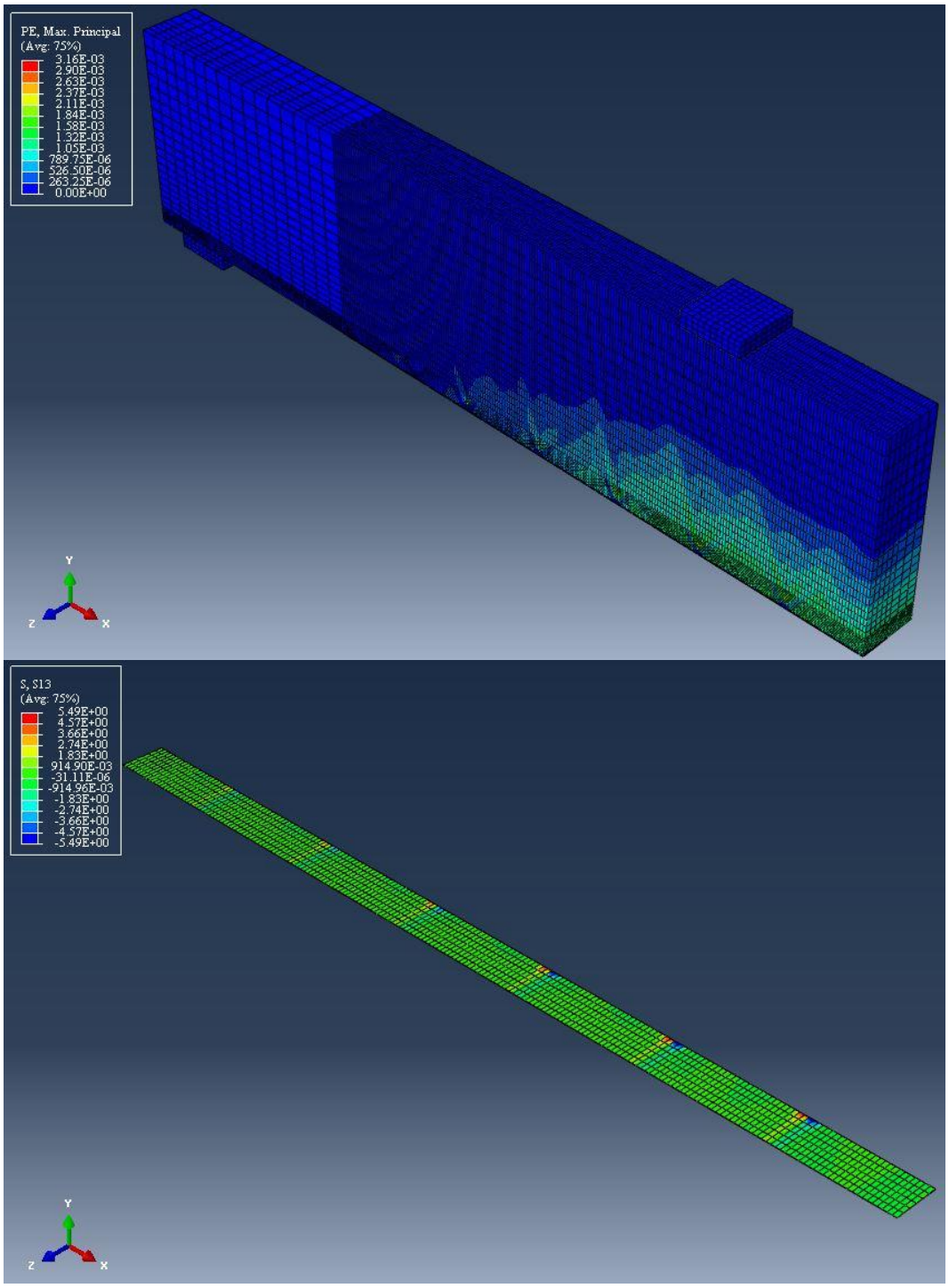

Figure 7.18: Crack pattern and interfacial stress distribution at micro-debonding (150 mm)

7.4.5 Model with Crack Spacing of 100mm

The model in this section represents the last case studied in this chapter, where the smallest possible crack spacing was chosen without jeopardizing the accuracy of the simulation. The ABAQUS model in this section was fabricated with ten flexural cracks spread along the bottom face of the concrete beam. It is found that this is relatively the largest number of cracks which can be predefined in this model while convergence can still be achieved. The first crack was placed at 80mm away from the centre of the beam. The subsequent cracks were spaced at 100mm from each other, with the third crack being positioned immediately under the load point. The same loading and supporting conditions of previous model were applied to this numerical beam. Prior to the initiation of flexural cracks, neither micro-debonding nor slip was observed in the adhesive layer. However, the onset of micro-cracking in the concrete substrate has generated the first micro-debonding in the location of crack 1, 2, 3, and 4 (see Figure 7.19).

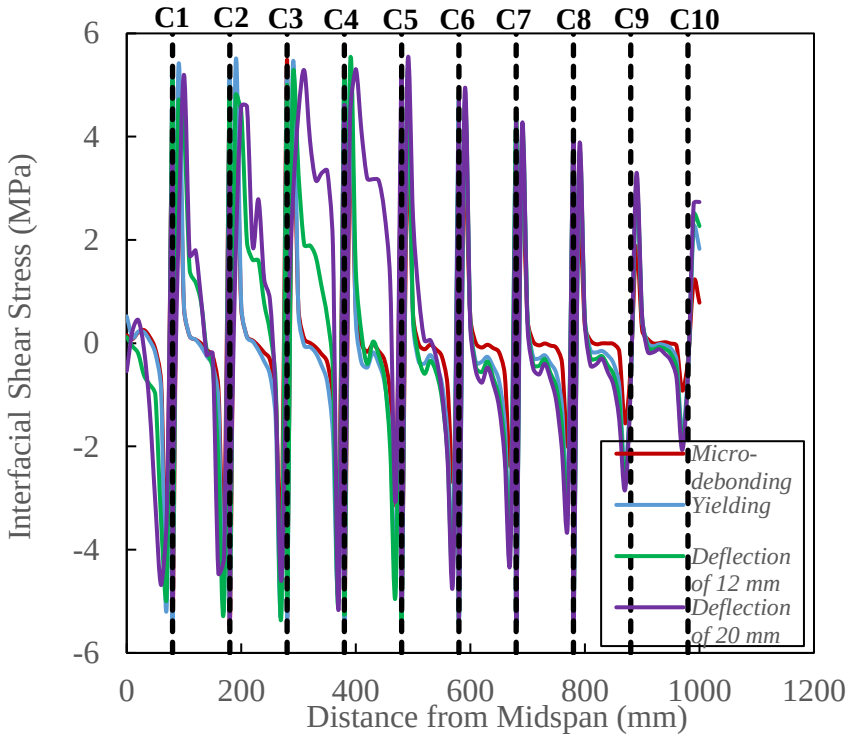

Figure 7.19: Interfacial shear stress distribution along the beam (crack spacing of 100mm)

Similar to the dynamic seen in previous model, the micro-cracking of concrete layer has produced a region high stress concentration at the cracks' toes. Therefore, the strains in the concrete substrate and the attached CFRP laminate are no longer equal, and hence slip has occurred. For the same reason mentioned in previous section, the cracking and the relative slip of CFRP plate within that particular region is the result of high stresses in that vicinity. The micro-debonding of CFRP composite was initiated when the shearing stress exceeded the ultimate bond strength value of 5.49MPa. Once again, the point of inflection in the stress distribution curve is seen in this model, where potential slips change their direction to maintain equilibrium throughout the cohesive surface. The zero-slip point was situated in the centre of two adjacent cracks within the region of crack 5 to the end of the CFRP plate. Nevertheless, the region restrained between crack 1 and 5 experienced a different trend, where the infliction points were moving away from one crack to the left face of the next crack. As explained before, this phenomenon can be used an indication of large crack openings being introduced in that region, and thus more visible debonding of CFRP plate is expected. While cracks close to the beam support remain small, due to the low shear stresses being transferred from the applied load to the CFRP-Concrete interface. it was noticed in this model that none of crack 7, 8, 9, and 10 experienced real micro-debonding as the interfacial stresses remained in their elastic range in that region (check Figure 7.19).

The longitudinal tensile strains along the steel rebar and the CFRP surface were graphed in Figure 7.20 and Figure 7.21. The strains in steel reinforcement have decreased by 2.03% when compared to the beam with 150mm crack spacing. However, the strain profile in the CFRP system did not change significantly in this model, with only -0.01% difference to previous beam model. Nonetheless, the strain deformations in steel and CFRP reinforcement started to increase dramatically after the steel rebar has yielding. This stage was recorded at an applied load of 152.08kN and midspan deflection of 7.61mm. As mentioned in previous sections, this sudden increase in strain response is justified by the fact that both reinforcing materials are now required to restrain the widening crack openings as the load progresses. On the other hand, the tensile crack pattern is depicted in Figure 7.22, where the evolution of flexural cracks and the initiation micro-debonding at crack 1, 2, 3, and 4 can be seen.

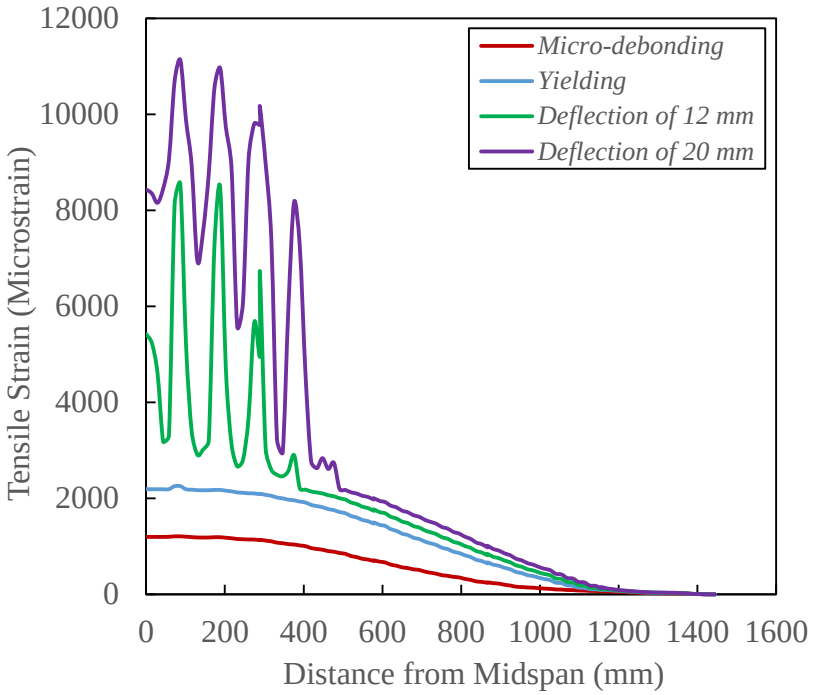

Figure 7.20: Rebar tensile strain along the beam (crack spacing of 100mm)

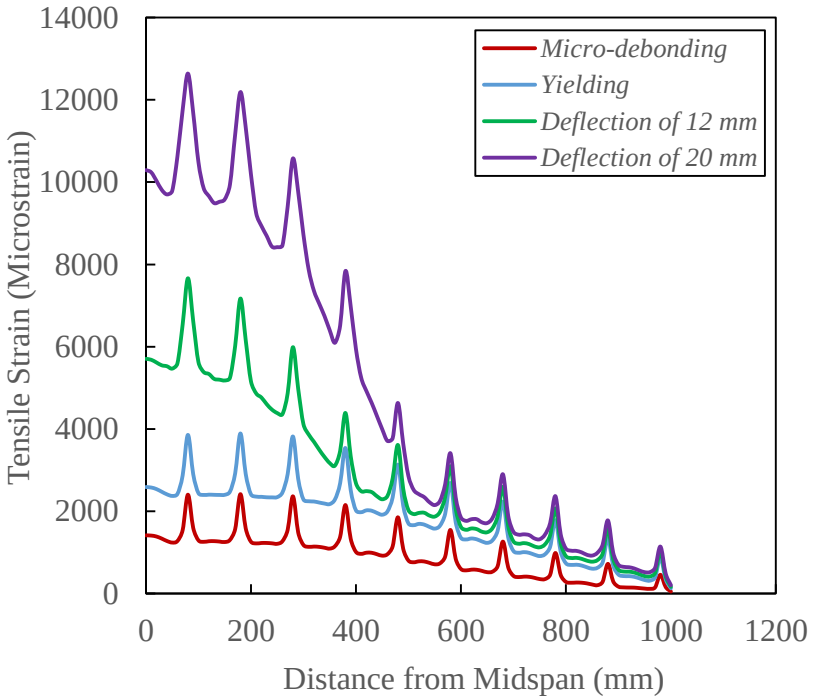

Figure 7.21: CFRP tensile strain along the beam (crack spacing of 100mm)

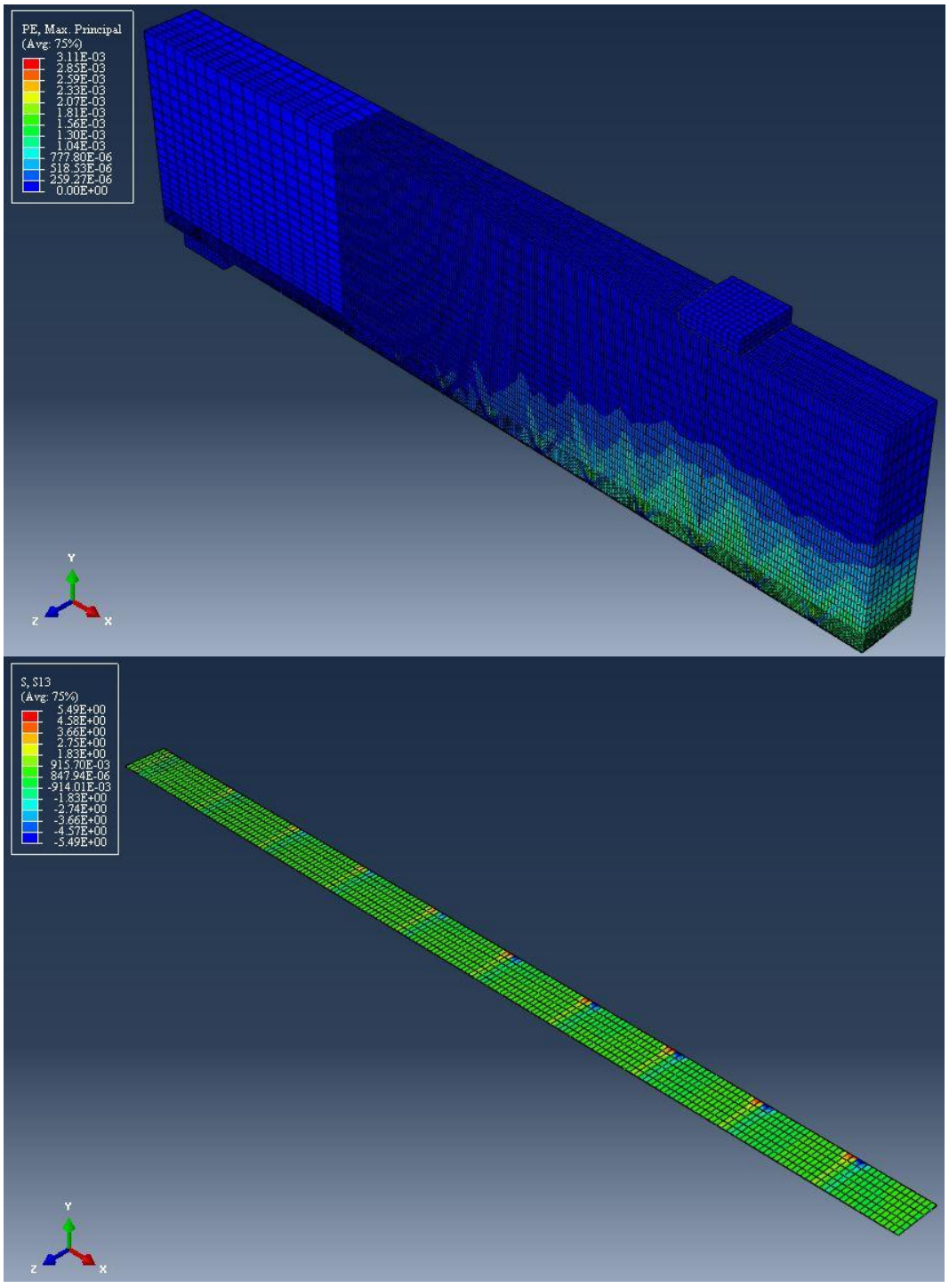

Figure 7.22: Crack pattern and interfacial stress distribution at micro-debonding (100 mm)

7.5 Summary

A finite element model was introduced in this chapter to examine the influence of multiple flexural cracks on the structural and debonding mechanisms in CFRP-strengthened RC beams. Studying these characteristics is crucial to develop an effective reinforcing and rehabilitating CFRP system in engineering applications. In order to clarify how cracking can affect the debonding initiation and evolution, a series of various crack spacings were implemented into the numerical model. The discrete crack approach was adopted to simulate concrete cracking in predefined locations. However, the presence of minor cracks was still permitted between the major flexural cracks by using smeared crack technique. Furthermore, the postprocessing analysis of the results obtained from the ABAQUS model has led to some distinct observations and trends, some of which can be summarized as follows:

- Introducing different crack spacings into the FE model did not have a significant effect on the flexural capacity of the concrete beam. The recorded failure load in all cases was between 182kN to 183kN, with midspan deflection that did not exceed 22.6mm.
- No sign of complete debonding of the CFRP laminate was observed until steel reinforcement has yielded.
- As macro-debonding occurs, the micro-cracks would propagate towards the end of the CFRP plate with few changes to the applied load, until the ultimate failure of the beam.
- The widening of flexural cracks would generate a region of stress concentration at the crack toes. This increase in interfacial stresses causes the strains in concrete and the adjacent CFRP sheet to be different, and hence relative slip would occur.
- High interfacial bond stresses were found in cracks that are located within the vicinity of beam maximum moment region. This is attributed to higher internal stresses being transferred to the cohesive layer in that part of the beam.
- There exists a zero-slip point between subsequent cracks in order to maintain equilibrium along the interface. However, these points were observed to move away from cracks close to the loading point towards the left face of adjacent cracks. This

shift can be an indication of CFRP debonding moving from the middle of the beam to the support side.

- The tensile strains in steel rebar and CFRP sheet was found to increase in a higher rate once the yielding of steel took place. Moreover, strain concentrations were observed in the maximum moment region, as reinforcing materials were expected to restrain the opening of flexural cracks in that location.

In conclusion, the flexural crack spacing was found to influence the debonding mechanisms of CFRP laminate in RC beams. In another word, the initiation of CFRP micro and macro-debonding was significantly influenced by crack spacing. Minor slip (micro-debonding) was observed in the model with single crack at a load that is approximately 40kN less than that in multiple –crack models. With the exception of the model with crack spacing of 100mm, the initiation of micro-debonding was seen to be slightly delayed as cracks were closely spaced. This might be justified by the so-called "abrasion effect" along the CFRP-Concrete interface, where additional work is needed for debonding to develop beyond secondary cracks. This phenomenon can be explained as follows: shearing stresses acting along the interface between the concrete and the adjacent CFRP plate will generate lateral micro-cracks. As the load increases, these cracks will interact and merge to produce macro-cracks that propagates horizontally inside the concrete substrate. However, the surfaces within this zone are certainly not smooth, and "interlocking effects" will increase the residual shear resistance in the interface (Leung & Yang, 2006). Therefore, the presence of multiple cracks was found to delay the initiation of CFRP micro-debonding and interfacial stress softening rate.

Chapter Eight

Conclusions and Recommendations

8.1 Overview

It is evident that the utilization of external CFRP reinforcement in RC beams is widely considered as an efficient method of retrofitting and rehabilitation. The practical advantages of CFRP composites make them an attractive alternative to conventional reinforcing materials such as steel. The structural performance and the durability of CFRP-strengthened concrete members were found to be considerably superior to their counterpart without CFRP materials. Nevertheless, there is still a need to develop reliable analytical and numerical equations that are capable of predicting the behaviour of such structures. Although there is a large database of experimental studies for concrete beams reinforced with CFRP materials, a review of the available literature concludes that further investigations of the debonding mechanisms of CFRP reinforcement in such beams is required. In particular, there is a lack of complete understanding of CFRP debonding induced by intermediate flexural or flexural/shear cracks. Moreover, additional attention must be given to how interfacial properties within the CFRP-Concrete interface influence the debonding mechanisms of CFRP laminate and load-carrying capacity of CFRP-strengthened beams.

Therefore, a comprehensive review of previous studies, concerning the performance of CFRP-strengthened RC beams, was conducted. This review has paved the way to the development of a sound nonlinear finite element model in this thesis, which can efficiently measure the structural and debonding response of CFRP-RC beams. The proposed model was tested and validated with reliable experimental specimens in order to ensure the accuracy of the numerical

simulations. This model was then utilized in an extensive parametric analysis, the aim of which was to examine the effect of various constitutive and physical parameters on the overall response of the structure. Some of the parameters were related to concrete mechanical and plastic properties, while others involved the internal and external reinforcements in the CFRP-strengthened RC beams. The influence of each parameter was then expressed by comparing the modified beam with a reference specimen which was introduced in previous sections. This comparative analysis included examining the change in ultimate strength of the original beam, and the development of tensile strains in both steel and CFRP reinforcements. Finally, the proposed finite element model was further modified to incorporate a series of predefined flexural cracks in the tension face of the concrete beam. This was done in order to investigate the impact of various crack distributions on the debonding and failure response of CFRP system, as well as the interfacial behaviour that is governed by crack growth. Nonetheless, the following sections provide a summary of the findings and remarks obtained from this numerical research.

8.1.1 Beam Modelling

This thesis presents a nonlinear finite element model produced by ABAQUS software package. This numerical model was fabricated and validated based on an experimental study conducted by Brena et al. (2003). The concrete plasticity was acounted for by the use of Concrete Damaged Plasticty Model availabe in ABAQUS. In addition to the initial Control Beam Model, the interface between the concrete and the extrenal CFRP laminate was simulated using: (*i*) a "prefect bond" assumption; and (*ii*) a "Cohesive Zone Model" technique. The postprocesing of the modelling results suggests that use of cohesive elements to replicate the CFRP-Conctrete inteface provided the most accurate prediction of the actual test data. This particular model has exhibited about 5.8% increase in overall accuracy when compared to the corresponding model without (CZM). However, the prediction effectiveness of this model was more expressed in its closseness in simulating the ultimate load of the real structure, with merely 2kN difference. Moreover, the best fitting of the experimental load-midspan deflection and tensile strain profiles was produced by the CFRP Beam Model with mesh size (25 x 25) mm. Therefore, this

particular model was then chosen to be expanded for the subsequent steps of this numerical study.

It should be noted that mesh sensitivity analysis was conducted on each beam model in order to test the convergence of the numerical solution. Mesh sizes of the tested models varied from coarse meshes (30 x 30) mm to finer ones (15 x 15) mm. This analysis has shown a particular trend that can be expressed in a noticeable increase in the stiffness of the pre-peak response in all beam models as finer meshes were used. Although this trend does not agree with the common outcome of mesh refinement (i.e. smaller mesh size produces less restraint to nodal displacement and thus less stiff response), similar outcome was reached by other researchers. Moreover, ABAQUS manual states that mesh sensitivities can be seen in regions with no sufficient reinforcement. This lack of reinforcing elements can trigger potential localization of cracking within the unreinforced areas of concrete, which can in turn affect the convergence of the numerical model as the elements size decreases.

8.1.2 Parametric study

This analysis was performed on the CFRP Beam Model (CZM), in order to test the influence of different essential parameters on the structural behaviour of the beam. Some of the studied parameters were related to the concrete material, such as f_c', ψ, μ, and concrete damage parameters. While others were associated with steel and CFRP reinforcements, like ρ, τ_f, L_f, B_f, and the removal of steel stirrups. It was found that the concrete compressive strength, f_c', has a bigger impact on the cracking load than the ultimate load of the beam. The cracking of concrete was delayed noticeably when higher value of f_c' was used, as this parameter is indirectly connected to the tensile strength of concrete. However, the most effect on the ultimate beam capacity was observed in model where steel reinforcement ratio, ρ, was varied. The cracking, yielding, and failure loads of the beam were increased significantly as larger quantities of steel were used. Moreover, using higher dilation angle of concrete, ψ, has resulted in a stiffer post-cracking response and larger load-carrying capacity. While increasing the value of viscosity parameter, μ, reduced the analysis running time by over 50%, the stiffness and the overall capacity of the beam increased. In addition, the tension damage parameter of concrete

was concluded to produce a very similar structural response to the beam with both damage parameters, relative to the effect of including only compression damage parameter.

On the other hand, the efficiency of the interaction between the concrete substrate and the attached CFRP sheet was examined. This step of the analysis was performed by examining the effect of interfacial bond strength, τ_{max}, laminate bond length, L_f, and bond width, B_f. It was found that, although the change in the ultimate beam capacity was insignificant when using τ_{max} higher than 3MPa, this parameter has more prominent effect on the initiation and growth of micro- and macro-debonding of CFRP laminate. Moreover, increasing the plate bond length beyond a certain point (e.g. effective bond length) did not lead to a noticeable improvement in the load-carrying capacity of the beam. However, the use of wider CFRP sheet has shown some enhancement in service load, as well as the ultimate load of the concrete structure.

8.1.3 Effect of Multiple Cracks on CFRP Debonding

The proposed finite element model in this study was modified to include five sets of flexural cracks, located at the bottom face of the concrete beam. The purpose of this alteration was investigating the effect of different crack spacing and configuration on the debonding mechanisms in CFRP-strengthened beams. Each pre-defined crack was created using the discrete crack approach, while minor cracks between existing flexural cracks were simulated by smeared crack approach. A cohesive zone was incorporated in every major notch, in which the crack initiation and growth are governed by the tensile strength and the fracture energy of concrete, respectively. The prediction capability of this model to simulate the cracking load of the structure was improved by about 30% in comparison to a similar specimen where damage in concrete was smeared on the entire body of the beam. Furthermore, the analysis of the numerical results has shown the ultimate load capacity of the tested beam did not change very much by changing crack spacings. However, crack distribution was found to have a tremendous impact on the rate at which micro-debonding occurred and developed in the CFRP-RC beams. It was also noticed that no complete debonding of CFRP plate was observed prior to the yielding of steel rebars. Moreover, there was a region of zero-slip between adjacent cracks, in order to maintain equilibrium of interfacial stresses at the CFRP-Concrete interface.

These points of zero-slip were seen shifting from cracks close to the load point towards cracks far away from the constant moment region. This can be a sign of the debonding moving from the middle of the beam to the end of the CFRP plate. In summary, the closer flexural cracks were introduced, the higher the load at which CFRP micro-debonding occurred. This can be justified by the "abrasion effect" between the concrete and the attached CFRP sheet. Finally, no rupture of CFRP reinforcing plate was observed in any of the studied models, as the tensile strain measured in the laminates was always below the ultimate strain value of 0.015, reported by the experimental program. This observation, in addition to the fact that major debonding of CFRP plate was seen moving from the beam midspan to the support, indicates that the dominate mode of failure in such beams was the CFRP debonding induced by intermediate flexural cracks.

8.2 Contributions

The main theme of this research concentred on investigating the debonding mechanisms of external FRP reinforcement in concrete beams. The flexural behaviour of such structures and the interfacial characteristics between the concrete and the bonded FRP laminates were numerically analyzed. The novelty and main contributions of this investigation to the civil engineering field can be demonstrated as follows:

- A sound 3D finite element model was created, using ABAQUS, which has the capacity to accurately simulate the flexural response of CFRP-strengthened RC beams. As mentioned in Chapter two, and based on the information available in literature, there is a lack of numerical understanding of the flexural capacity and debonding mechanisms in CFRP beams, where the intermediate delamination of the CFRP plate is the main cause of failure. Therefore, this pioneer numerical model can be seen as one of the first attempts to simulate the mechanical performance of such concrete structures, with a great deal of accuracy.

- This proposed model also takes into account the plasticity of concrete materials and incorporates the principles of fracture mechanics. The nonlinearity nature of this model is directly reflected by the nonlinear behaviour of concrete which is often neglected in such simulation. Parameters such as dilation angle of concrete, viscosity, and damage evolution parameters were considered in this study for the purpose of replicating the actual behaviour of concrete materials under compressive and tensile stresses.
- Furthermore, a more realistic representation of the CFRP-Concrete interface was provided by the use of the "Cohesive Zone Model". This technique allows for better simulations of the possible interfacial debonding with the interfaces. The CZM was implemented by using the traction-separation law available in ABAQUS, and each of the parameters of this mechanical model was calculated and calibrated extensively with some experimental data to ensure their validity.
- A detailed explanation into how load-carrying capacity, CFRP debonding response, and strain developments in internal and external reinforcements are affected by different constitutive and geometric parameters. The effect of some of these parameters on the debonding behaviour of CFRP laminates was often overlooked in previous studies, because of their indirect influence on externally-bonded CFRP reinforcement. Such an example involves studying the effect of main steel reinforcement ratio, and the removal of steel stirrups on the debonding response of CFRP laminates. However, the findings of this particular study presents a sufficient guideline on how to improve the structural capacity of CFRP-concrete beams by constraining/preventing premature debonding of CFRP laminates.
- The proposed model incorporates the "discrete crack" approach to simulate the effect of multiple flexural cracks on debonding of CFRP sheet from the substrate of the concrete beam. This model was able to capture the initiation and the evolution of micro-debonding at the CFRP-Concrete interface, and compare that response for various crack distributions. This particular technique replaces the smeared crack approach commonly used to simulate fracture in concrete. The outcome of this study can be

utilized to improve and control crack spacing in the main body of concrete beam, which can prolong the initiation of micro-debonding within the CFRP-Concrete interface.

- This numerical study provides an efficient alternative to large-scale experiments on the same topic, which can be very costly and time consuming. Moreover, the proposed model was capable of simulating and recording some of the parameters which could be unfeasible to capture in real settings, such as the initiation of CFRP micro-debonding and the strain development within the interfacial region.

8.3 Recommendations for Future Work

The numerical study performed in this thesis can be the base for further investigation of modelling strategies of CFRP debonding mechanisms in reinforced concrete beams. Some aspects of this research might need further examination to improve the reliability of the presented findings and conclusions. Nevertheless, the following recommendations are made for future research of this type:

- The effect of combining other FRP reinforcement, such steel fibre and/or internal FRP rebars, with the existing externally-bonded laminate on the debonding mechanisms in CFRP-strengthened RC beams.
- The expansion of this model to include the effect of cyclic and reversed-cyclic loading conditions on the overall response of the beam.
- Applying different configurations of CFRP materials in RC beams, where the laminate can be placed along the beam side, wrapped around it, or a combination of those configurations. The effect of such fabrications on the flexural and shear capacity of the CFRP beams can then be numerically investigated.
- Experimental and numerical investigations can be conducted to review the influence of aggressive environments on the bond between concrete and external FRP composite.
- Thermal and long term effects on the interfacial properties of FRP-concrete layer can be considered in future research.

References

ACI Committe 440. (2007). *"Report on fibre-reinforced polymer (FRP) reinforcement for concrete structures"*. Farmington Hills, MI: American Concrete Institute.

ACI Committee 440. (1996). *"State of the art report on fibre reinforced plastic (FRP) reinforcement for concrete structures (ACI 440-96, reapproved 2002)"*. Farmington Hills, MI: American Concrete Institute.

ADINA R&D. (2015). *"ADINA"*. Watertown, MA, USA.

ANSYS. (2015). *"ANSYS"*. Pittsburgh, PA, USA.

Arduini, M., & Di Leo, A. (1996). "Composite behaviour of partially plated beams in the linear range". *American Concrete Institute*, 43-53.

Arduini, M., & Nanni, A. (1997). "Parametric study of beams with externally bonded FRP reinforcement". *ACI Structural Journal , 94*(5), 493-501.

Ashour, A. F., El-Refaie, S. A., & Garrity, S. W. (2004). "Flexural strengthening of RC continuous beams using CFRP laminates". *Cement & Concrete Composites, 26*(7), 765-775.

Bai, J. (2013). *"Advanced Fibre-Reinfoced Polymer Composites For Structural Applications"*. Oxford: Woodhead Publishing.

Bank, L. C. (2006). *"Composites For Construction: Structural Design With FRP Materials"*. John Wiley & Sons, Inc.

Benzeggagh, M. L., & Kenane, M. (1996). "Measurement of mixed-mode delamination fracture toughness of unidirectional glass/epoxy composites with mixed-mode bending apparatus". *Composites Science and Technology, 56*(4), 439-449.

Bizindavyi, L., & Neale, K. W. (1999). "Transfer lengths and bond strengths for composites bonded to concrete". *Journal of Composites for Construction, 3*(4), 153-160.

Bocciarelli, M., & Pisani, M. (2017). "Survey on the interface behaviour in reinforced concrete beams strengthened with externally bonded FRP reinforcement". *Composites Part B: Engineering, 118*, 169-176.

Brena, S. F., Bramblett, R. M., Benouaich, M. A., Wood, S. L., & Kreger, M. E. (2001). *"Use of carbon fiber reinforced polymer composites to increase the flexural capacity of reinforced concrete beams"*. University of Texas. Austin, USA: Center for Transportation Research.

Brena, S. F., Bramblett, R. M., Wood, S. L., & Kreger, M. E. (2003). "Increasing flexural capacity of reinforced concrete beam using carbon fiber-reinforced polymer composites". *ACI Structural Journal, 100*(1), 36-46.

Canadian Standards Association. (2004). *"Design of concrete structures, (CAN/CSA A23.3-04)"*. Mississauga, Ontario, Canada.

CEB-FIP. (1990). *"CEB-FIP Model Code 1990"*. London, UK: Comite Euro-International du Beton, Thomas Telford.

CEB-FIP. (1993). *"CEB-FIP Model Code 1990"*. Lausanne, Switzerland: Comite Euro-International du Beton, Thomas Telford.

CEN. (1999). *"Products and systems for protection and repair of concrete structures: Definitions -Requirements - Quality control and evaluation of conformity, Part 4: Structural bonding"*. Brussels, Belgium: prEN 1504-4, Comite Europeen de Normalisation (CEN).

Chajes, M. J., & Finch Jr., W. W. (1996). "Bond and force transfer of composite material plates bonded to concrete". *ACI Structural Journal , 93*(2), 208-217.

Chen, G. (2010). *"Behaviour and strength of RC beams shear-strengthened with externally bonded FRP reinforcement"*. Hong Kong, China: The Hong Kong Polytechnic University.

Chen, J. F., & Teng, J. G. (2001). "Anchorage strength models for FRP and steel plates bonded to concrete". *Journal of Structural Engineering, ASCE, 127*(7), 784-791.

Chen, W. F. (1982). *"Plasticity in Reinforced Concrete"*. New York, USA: McGraw-Hill.

Chen, W. F., & Han, D. J. (1988). *"Plasticity for Structural Engineers"*. New York, USA: Springer-Verlag.

Chicoine, T. (1997). *"Conception et analyse des ancrages sur les pouters renforcees en flexion a l'aide des materiaux composites"*. Sherbrooke, Canada: University of Sherbrooke.

Cohen, M. (2012). *Structural Behaviour of Self Consolidating Steel Fiber Reinforced Concrete Beams.* Civil Engineering Department. Ottawa, Canada: University of Ottawa.

Coronado , C. A., & Lopez, M. M. (2006). "Sensitivity analysis of reinforced concrete beams strengthened with FRP laminates". *Journal of Cement and Concrete Composites, 28*(1), 102-114.

Coronado, C. A., & Lopez, M. M. (2009). "Numerical modeling of concrete-FRP debonding using a crack band approach". *Journal of Composites for Construction, 14*(1), 11-21.

Cosenza, E., Manferedi, G., & Realfonzo, R. (1997). "Behavior and modeling of bond of FRP rebars to concrete". *Journal of Composites for Construction, 1*(2), 40-51.

De Lorenzis, L., Miller, B., & Nanni, A. (2001). "Bond of FRP laminates to concrete". *ACI Materials Journal, 98*(3), 256-264.

De Rose, D., & Sheikh, S. A. (1997). *"Rehabilitation of a concrete structure using fiber reinforced plastics"*. University of Toronto.

DSS, D. S. (2014). *"ABAQUS (6.14-2)"*. Providence, RI, USA.

Esfahani, M., Kianoush, M., & Tajari, A. (2007). "Flexural behaviour of reinforced concrete beams strengthened by CFRP sheets". *Engineering Structures, 29*(10), 2428-2444.

Evan, R., & Marathe, M. (1968). "Microcracking and stress-strain curves for concrete in tension". *Materials and Structures, 1*(1), 61-64.

Ferreira, A. J., Camanho, P. P., Marques, A. T., & Fernandes, A. A. (2001). "Modelling of concrete beams reinforced with FRP re-bars". *Composite Structures, 53*(1), 107-116.

Galvez, J., Cervenka, J., Cendon, D., & Saouma, V. (2002). "A discrete crack approach to normal/shear cracking of concrete". *Cemenet and Concrete Research , 32*(10), 1567-1585.

Garden, H. N., & Hallaway, L. C. (1998). "An experimental study of the influence of plate end anchorage of carbon fiber composite plates used to strengthen reinforced concrete beams". *Composite Structures, 42*(2), 175-188.

GB 50010. (2002). *"Code for design of concrete structures" [in Chinese]*. Beijing: China Building Industry Press.

Goldston, M., Remennikov, A., & Sheikh, M. (2017). "Flexural behaviour of GFRP reinforced high strength and ultra high strength concrete beams". *Construction and Building Materials, 131*, 606-617.

Grace, N. F., Sayed, G. A., Soliman, A. K., & Saleh, K. R. (1999). "Strengthening reinforced concrete beams using fiber reinforced polymer (FRP) laminates". *ACI Structural Journal, 96*(5), 865-875.

Hahn, H. T., & Tsai, S. W. (1973). "Nonlinear elastic behavior of unidirectional composite laminae". *Journal of Composite Materials , 7*(1), 102-118.

Hany, N., Hantouche, E., & Harajli, M. (2016). "Finite element modeling of FRP-confined concrete using modified concrete damaged plasticity". *Engineering Structures, 125*, 1-14.

Hibbitt, Karlsson, & Sorensen. (2004). *"ABAQUS/Standard User's Manual"* (6th Edition ed.). Pawtucket.

Hillerborg, A. (1985). "The theoretical basis of a method to determine the fracture energy GF of concrete". *Materials and Structures, 18*(4), 291-296.

Hillerborg, A., Modeer, M., & Petersson, P. (1976). "Analysis of crack formation and crack growth in concrete by means of fracture mechanics and finite elements". *Cemenet and Concrete Research , 6*(6), 773-782.

Hognestad, E. (1950). *"An experimental study of combined bending and axial load in reinforced concrete members"*. Illinois, USA: Univesity of Illinois Engineering Experiment Station.

Hognestad, E., Hanson, N. W., & McHenry, D. (1955). "Concrete stress distribution in ultimate strength design". *Journal of the American Concrete Institute , 27*(4), 455-479.

Hoque, M. M. (2006). *"3D nonlinear mixed finite-element analysis of RC beams and plates with and without FRP reinforcement"*. Winnipeg, Canada: University of Manitoba.

Hu, H., & Schnobrich, W. (1989). "Constitutive modeling of concrete by using nonassociated plasticity". *Journal of Materials in Civil Engineering, 1*(4), 199-216.

Hu, H., Lin, F., & Jan, Y. (2004). "Nonlinear FE analysis of reinforced concrete beams strengthened by fiber-reinforced plastics". *Composite Structures, 63*(3-4), 271-281.

Hughes, B., & Chapman, G. (1966). *"The complete stress-strain curve for concrete in direct tension"*. RILEM Bulletin.

Hutchinson, A. R., & Quinn, J. (1999). *"Materials, Chapter 3 in Strengthening of Reinforced Concrete Structures Using Externally Bonded FRP Composites in Structural and Civivl Engineering.* USA: Eds. L.C. Hollaway, M.B. Leeming, Woodhead Publishing, UK & CRC Press.

Hutton, D. V. (2004). *"Fundamentals of Finite Element Analysis"* (1st ed.). New York, USA: McGraw-Hill Companies.

ISIS Canada. (2007). *"Reinforcing concrete structures with fibre reinforced polymers-design manual No.3"*. University of Manitoba. Winnipig, Manitoba, Canada: ISIS Canada, Intelligent Sensing for Innovative Structures, A Canadian Network of Centres of Excellence.

ISIS Educational Committe. (2003). *"ISIS Educational Module 2: An Introduction to FRP composites for construction"*. University of Manitoba. Winnipig, Manitoba, Canada: ISIS Canada, Intelligent Sensing for Innovative Structures, A Canadian Network of Centres of Excellence.

Jirasek, M., & Bazant, Z. (2002). *"Inelastic Aanalysis of Structures"*. New York, USA: John Wiley & Sons.

Karihaloo, B. (2003). "Failure of concrete". *Comprehensive Structural Integrity, 2*(10), 475-546.

Kishi, N., Zhang, G., & Mikami, H. (2005). "Numerical cracking and debonding analysis of RC beams reinforced with FRP sheets". *Journal of Composites for Construction , 9*(6), 507-514.

Kupfer, H., Hilsdorf, H., & Rusch, H. (1969). "Behaviour of concrete under biaxial stresses". *ACI Journal Proceedings, 66*(8), 656-666.

Lee, J., & Fenves, G. (1998). "Plastic-damage model for cyclic loading of concrete structures". *Journal of Engineering Mechanics, 124*(8), 892-900.

Leung, C. K. (2001). "Delamination failure in concrete beams retrofitted with a bonded plate". *Journal of Materials in Civil Engineering, 13*(2), 106-113.

Leung, C., & Yang, Y. (2006). "Energy-based modeling approach for debonding of FRP plate from concrete subtrate". *Journal of Engineering Mechanics, 132*(6), 583-593.

Li, B., & Chua, H. G. (2009). "Seismic performance of strengthened reinforced concrete beam-column joints using FRP composites". *Journal of Structural Engineering, 135*(10), 1177-1190.

Li, V. C. (2000). "Large volume, high perfomance application of fibers in civil engineering". *Journal of Applied Polymer Science, 83*, 600-686.

Li, Z., Khulkarni, S., & Shah, S. (1993). "New test method for obtaining softening response of unnotched concrete specimen under uniaxial tension". *Experimental Mechanics, 33*(3), 181-188.

Lu, X. Z., Teng, J. G., Ye, L. P., & Jiang, J. J. (2005). "Bond-slip models for FRP sheets/plates bonded to concrete". *Engineering Structures, 27*(6), 920-937.

Lu, X. Z., Ye, L. P., Teng, J. G., & Jiang, J. J. (2005). "Meso-scale finite elmenet model for FRP sheets/plates to concrete". *Engineering Structures, 27*(4), 564-575.

Lubliner, J., Oliver, J., Oller, S., & Onate, E. (1989). "A plastic-damage model for concrete". *International Journal of Solids and Structures, 25*(3), 299-326.

Maalej, M., & Bian, Y. (2001). "Interfacial shear stress concentration in FRP-strengthened beams". *Composite Structures, 54*(4), 417-426.

Majid, G., Davood, M., & Ardalan, H. (2017). "Experimental investigation into bond behavior of FRP-to-concrete under mixed-mode I/II loading". *Construction and Building Materials, 132*, 303-312.

Malek, A. M., & Saadatmanesh, H. (1996). "Physical and mechanical properties of typical fibres and resins". (pp. 68-79). University of Atizona, Tucson, Arizona, USA: Proceedings 1st. Intern. Conf. on Composites in Infrastructure, Ed. H. Saadatmanesh, M.R. Ehsani.

Malek, A. M., Saadatmanesh, H., & Ehsani, M. R. (1998). "Prediction of failure load of R/C beams strenghened with FRP plate due to stress concentration at the plate end". *ACI Structural Journal, 95*(1), 142-152.

Malm, R. (2006). *"Shear cracks in concrete structures subjected to in-plane stresses".* Stockholm, Sweden: Royal Institute of Technology .

Malm, R. (2009). *"Predicting shear type crack initiation and growth in concrete with non-linear finite element method".* Stockholm, Sweden: Royal Institute of Technology.

Massimiliano, B., Pierluigi, C., Tommaso, D., & Giulia, F. (2017). "Intermediate debonding on crcaked steel beams reinforced with CFRP plates under fatigues". Milan, Italy: Fourth Conference on Smart Monitoring, Assessment and Rehabilitation of Civil Structures.

Mathys, S. (2000). *"Structural behaviour and design of concrete members strengthened with externally bonded FRP reinforcement".* PhD's Thesis, Ghent University, Brussel, Belgium.

Matthys, S. (1997). "Versterking van structurele betonelementen met opgelijmde vezelcomposietwapening". *(in Dutch), Infrastructuur in het Leefmilieu, Ministerie van de Vlaamse Gemeenschap, 4*(97), 274-298.

Mazzotti, C., Savoia, M., & Ferracuti, B. (2008). "An experimental study on delamination of FRP plates bonded to concrete". *Construction and Building Materials, 22*(7), 1409-1421.

M'Bazaa, I. (1995). *"Reinforcement en flexion des poutres en beton arme a l' aide des lamelles en materiaux composites: optimisation de las longueur des lamelles".* Sherbrooke, Canada: University of Sherbrooke.

Minouei, M. B. (2013). *"Finite element analysis of bond characteristics at the FRP-concrete interface".* McGill University , Montreal, Quebec, Canada.

Monteleone, A. (2008). *"Numerical analysis of crack induced debonding mechanisms in FRP-strengthened RC beams"*. Master's Thesis, University of Waterloo, Waterloo, Canada.

Mostafa, A., & Razaqpur, A. (2017). "A nonlinear model for predicting intermediate crack-induced debonding in FRP-retrofitted beams in flexure". *Composite Structures, 176*, 268-280.

Mukhopadhyaka, P., & Swamy, N. (2001). "Interface shear stress: a new design criterion for plate debonding". *Journal of Composites for Construction, 5*(1), 35-43.

Namasivayam, A., Amiya, K., Singha, R., & Joseph, T. (2013). "Retrofitting of reinforced concrete beams using fibre reinforced polymer (FRP) composites-a review". *Journal of Urban and Environmental Engineering, 7*(1), 164-175.

Ngujen, D. M., Chan, T. K., & Cheong, H. K. (2001). "Brittle failure and bond development length of CFRP-concrete beams". *Journal of Composite for Construction, 5*(1), 12-17.

Nitereka, C., & Neale, K. W. (1999). "Analysis of reinforced concrete beams strengthened in flexure with composite laminates". *Canadian Journal of Civil Engineering, 26*(5), 646-654.

Niu, H., & Wu, Z. (2005). "Numerical analysis of debonding mechanisms in FRP-strengthened RC beams". *Computer-Aided Civil and Infrastructure Engineering, 20*(5), 354-468.

Niu, H., Karbhari, V. M., & Zhishen, W. (2006). "Diagonal macro-crack induced debonding mechanisms in FRP rehabilitated concrete". *Composite Part B: Engineering, 37*((7-8)), 627-641.

Nour, A., Massicotte, B., Yildiz, E., & Koval, V. (2007). "Finite element modelling of concrete structures reinforced with internal and external fibre-reinforced polymers". *Canadian Journal of Civil Engineering, 34*(3), 340-354.

Obaidat, Y. T. (2011). *"Structural retrofitting of concrete beams using FRP-debonding issues"*. PhD Thesis, Lund University, Lund, Sweden.

Ouyang, Z. (2007). *"Durability of bond between FRP and concrete in moisture environments: experimental, numerical and analytical study"*. Milwaukee, USA: Marquette University.

Polling, R. (2001). *"Eine praxisnahe, schdigungsorientierte materialbeschreibung von stahlbeton fur strukturanalysen"*. Bochum, Germany: Ruhr-Universitt Bochum.

Pultrusions, C. (2015). *"The pultrusion process"*. Retrieved August 22nd of, 2015, from http://www.creativepultrusions.com/index.cfm/products-solutions/fiberglass-pultrusion-process/

Quayyum, S. (2010). *"Bond behaviour of fibre reinforced polymer (FRP) rebars in concrete"*. Master's Thesis, University of British Columbia, Okanagan, Canada.

Razaqpur, M. M. (2000). "3rd International conference on advanced composites materials in bridges and structures". *ACMBS-3*. Ottawa.

Reineck, K., Kuchma, D., Kim, K., & Marx, S. (2003). "Shear database for reinforced concrete members with shear reinforcement". *ACI Structural Journal, 100*(2), 240-249.

Roberts , T. M. (1989). "Approximate analysis of shear and normal stress concentrations in the adhesive layer of plated RC beams". *Structural Engineering, 67*(12), 229-233.

Roberts, T. M., & Haji-Khazemi, H. (1989). "Theoretical study of the behaviour of reinforced concrete beams strengthened by externally bonded steel plates". *87*(1), 39-55.

Ross, A., Jerome, D. M., Tedesco, J. W., & Hughes, M. L. (1999). "Strengthening of reinforced concrete beams with externally bonded composite laminates". *ACI Structural Journal, 96*(2), 212-220.

Rots, J. G., & Blaauwendraad, J. (1989). "Crack models for concrete, discrete or smeared? fixed, multi-directional or rotating? *Heron, 34*(1), 59.

Schwarz, M. M. (1992). *"Composites Materials Handbook"*. New York, USA: McGraw-Hill.

Sebastian, W. M. (2001). "Significance of midspan debonding failure in FRP-plated concrete beams". *Journal of Structural Engineering, 127*(7), 792-798.

Shah, S., Swartz, S., & Ouyang, C. (1995). *"Fracture Mechanics of Concrete: Applications of Fracture Mechanics to Concrete, Rock and Other Quasi-Brittle Materials"*. New York: Wiley.

Shahawy, M. A., Arockiasamy, M., Beitelman, T., & Sowrirajan, R. (1996). "Reinforced concrete rectangular beams strengthened with CFRP laminates". *Composites Part B: Engineering, 27*(3-4), 225-233.

Shaw, J. D. (1982). "A review of resins used in construction, Types of resin-applicsations-case histories". *Int. Journal Adhesion and Adhesive*, 77-83.

Shi, Z. (2009). *"Crack Analysis in Structural Concrete - Theory and Applications"* (1st ed.). Boston: Elsevier.

Smith, S. T., & Teng, J. G. (2002). "FRP-strengthened RC beams. I: review of debonding strength models". *Engineering Structures, 24*(4), 385-395.

Soudki, K. A. (1998). " FRP reinforcement for prestressed concrete structures". *Progress in Structural Engineering and Materials, 1*(2), 135-142.

Stoner, J. G. (2015). *"Finite element modelling of GFRP reinfoced concrete beams"*. Master's Thesis, University of Waterloo, Waterloo, Canada.

Supaviriyakit, T., Pornpongsaroj, P., & Pimanmas, A. (2004). "Finite-element analysis of FRP-strengthened RC beams". *Songkhanakarin Journal of Science Technology", 26*(4), 497-507.

Taljsten, B. (1994). *"Plate bonding strengthening of existing concrete structures with epoxy bonded plates of steel or fiber reinforced plastics"*. PhD Thesis, Lulea University of Technology, Sweden.

Taljsten, B. (1997). "Strengthening of beams by plate bonding". *Journal of Materials in Civil Engineering, 9*(4), 206-212.

Tamai, S. (1988). "Average stress-strain relationship in post yield range of steel bar in concrete". *Concrete Library of JSCE*(11), 117-129.

Tan, Z. (2002). *"Experimental research for RC beam strengthened with GFRP" [in Chinese]*. China: Tsinghua University.

TNO DIANA BV. (2015). *"DIANA"*. Deft, The Netherlands.

Triantafillou, T. C., & Deskovic, N. (1992). "Prestressed FRP sheets as external reinforcement of wood members". *Journal of Structural Engineering, 118*(5), 1270-1284.

Triantafillou, T., & Plevris, N. (1991). "Post-strengthening of reinforced concrete beams with epoxy-bonded fiber composite materials". (pp. 245-256). Nevada, USA: Advanced Composite Materials in Civil Engineering Structures, Proceedings of Specialty Conference, ASCE Materials Engineering Division.

Turon, A., Davila, C. G., Camanho, P. P., & Costa, J. (2007). "An engineering solution for mesh size effects in the simulation of delamination using cohesive zone models". *Engineering Fracture Mechanics, 74*(10), 1665-1682.

Ueda, T., & Dai, J. (2005). "Interface bond between FRP sheets and concrete subtrates: properties, numerical modeling and roles in member behavior". *Journal of Progress in Structural Engineering and Materials, 7*(1), 27-43.

Ueda, T., Sato, Y., & Asano, Y. (1999). "Experimental study on bond strength of continuous carbon fiber sheet". (pp. 407-416). Famingotn Hills (MI): In: Proc. of 4th International Symposium on Fiber Reinforced Polymer Reinforcement for Reinforced Concrete Structures, SP-188.

Vecchio, F. J., & Bucci, F. (1999). "Analysis of repaired reinforced concrete structures". *Journal of Structural Engineering, 125*(6), 644-652.

Wang, T., & Hsu, T. (2001). "Nonlinear finite element analysis of concrete structures using new constitutive models". *Computers and Structures, 79*(32), 2781-2791.

Wei, S., Xu, P., Haifeng, L., & Heping, Q. (2017). "Numerical studies on th entire debonding propagation process of FRP strips externally bonded to the concrete substrate". *Construction and Building Materials, 149*, 218-235.

Wenkenbach, I. (2011). *"Tension Stiffening in Reinforced Concrete Members with Large Diameter Reinforcement"*. Durham, UK: Durham University.

Wong, R., & Vecchio, F. J. (2003). "Towards modeling of reinforced concrete members with externally bonded fibre-reinforced polymer composites". *ACI Structural Journal, 100*(1), 47-55.

Wu, Z. S., Yuan, H., Hiroyuki, Y., & Toshiyuki, K. (2001). "Experimental/analytical study on interfacial fracture energy and fracture propogation along FRP-concrete interface". *ACI International SP-201-8*, 133-152.

Xu, T., He, Z., Tang, C., Zhu, W., & Ranjith, P. (2015). "Finite element analysis of width effect in interface debonding of FRP plate bonded to concrete". *Finite Elements in Analysis and Design", 93,* 30-41.

Yang, Z. J., Chen, J. F., & Proverbs, D. (2003). "Finite element modeling of concrete cover sparation failure in FRP plated RC beams". *Construction and Building Materials, 17*(1), 3-13.

Yingwu, Z., Xilong, C., Zhiheng, F., Lili, S., Dawang, L., & Feng, X. (2017). "Bond behaviors of FRP-to-concrete interface under the control of a novel end-anchorage system". *Composite Structures, 168*, 130-142.

Yoshizawa, H., Myojo, T., Okoshi, M., Mizukoshi, M., & Kliger, H. S. (1996). "Effect of sheet bonding condition on concrete members having externally bonded carbon fiber sheet". (pp. 1608-1616). Washington D.C.: Materials for the New Millennium Proceedings of the Fourth Materials Engineering Conference.

Yuan, H., Teng, J. G., Seracino , R., Wu, Z. S., & Yao, J. (2004). "Full-range bahvior of FRP-to-concrete bonded joints". *Engineering Structures, 26*(5), 553-564.

Zarnic, R., Gostic, S., Bosiljkov, V., & Bokan-Bosiljkov, V. (1999). "Improvemenet of bending load-bearing capacity by externally bonded plates". (pp. 433-442). London, UK: Specialist Techniques and Materials for Concrete Construction, Proceedings of the International Conference on Creating with Concrete.

Zhao, W. (1999). *"Crack and deformation behaviour of FRP reinforced concrete structures"*. PhD Thesis, University of Sheffield, Sheffield, UK.

Appendix A

Mesh Analysis

This appendix covers the results obtained from the numerical study in Chapter five. The type and number of element, used in meshing the ABAQUS models, are presented in Table A-1 through Table A-3. Moreover, the crack patterns in concrete beam was portrayed for each of the three proposed FE models, and recorded at five different loading stages. The influence of mesh density on crack evolution can be seen in Figure A-1 through Figure A-12.

Table A-1: Summary of mesh analysis for Control Beam Model

Model	Mesh Size	Element Type	Element Shape	Geometric Order	Number of Elements
Control Beam Model	(30 x 30) mm	C3D8R	hexahedral	linear	2400
		T3D2	line	linear	320
	(25 x 25) mm	C3D8R	hexahedral	linear	3848
		T3D2	line	linear	320
	(20 x 20) mm	C3D8R	hexahedral	linear	7350
		T3D2	line	linear	320
	(15 x 15) mm	C3D8R	hexahedral	linear	15734
		T3D2	line	linear	320

Table A-2: Summary of mesh analysis for CFRP Beam Model (Perfect Bond Assumption)

Model	Mesh Size	Element Type	Element Shape	Geometric Order	Number of Elements
CFRP Beam Model (Perfect Bond Assumption)	(30 x 30) mm	C3D8R	hexahedral	linear	2796
		T3D2	line	linear	320
	(25 x 25) mm	C3D8R	hexahedral	linear	4244
		T3D2	line	linear	320
	(20 x 20) mm	C3D8R	hexahedral	linear	7746
		T3D2	line	linear	320
	(15 x 15) mm	C3D8R	hexahedral	linear	16130
		T3D2	line	linear	320

Table A-3: Summary of mesh analysis for CFRP Beam Model (Cohesive Zone Model)

Model	Mesh Size	Element Type	Element Shape	Geometric Order	Number of Elements
CFRP Beam Model (Cohesive Zone Model)	(30 x 30) mm	C3D8R	hexahedral	linear	8808
		T3D2	line	linear	320
	(25 x 25) mm	C3D8R	hexahedral	linear	10502
		T3D2	line	linear	320
	(20 x 20) mm	C3D8R	hexahedral	linear	16404
		T3D2	line	linear	320
	(15 x 15) mm	C3D8R	hexahedral	linear	22524
		T3D2	line	linear	320

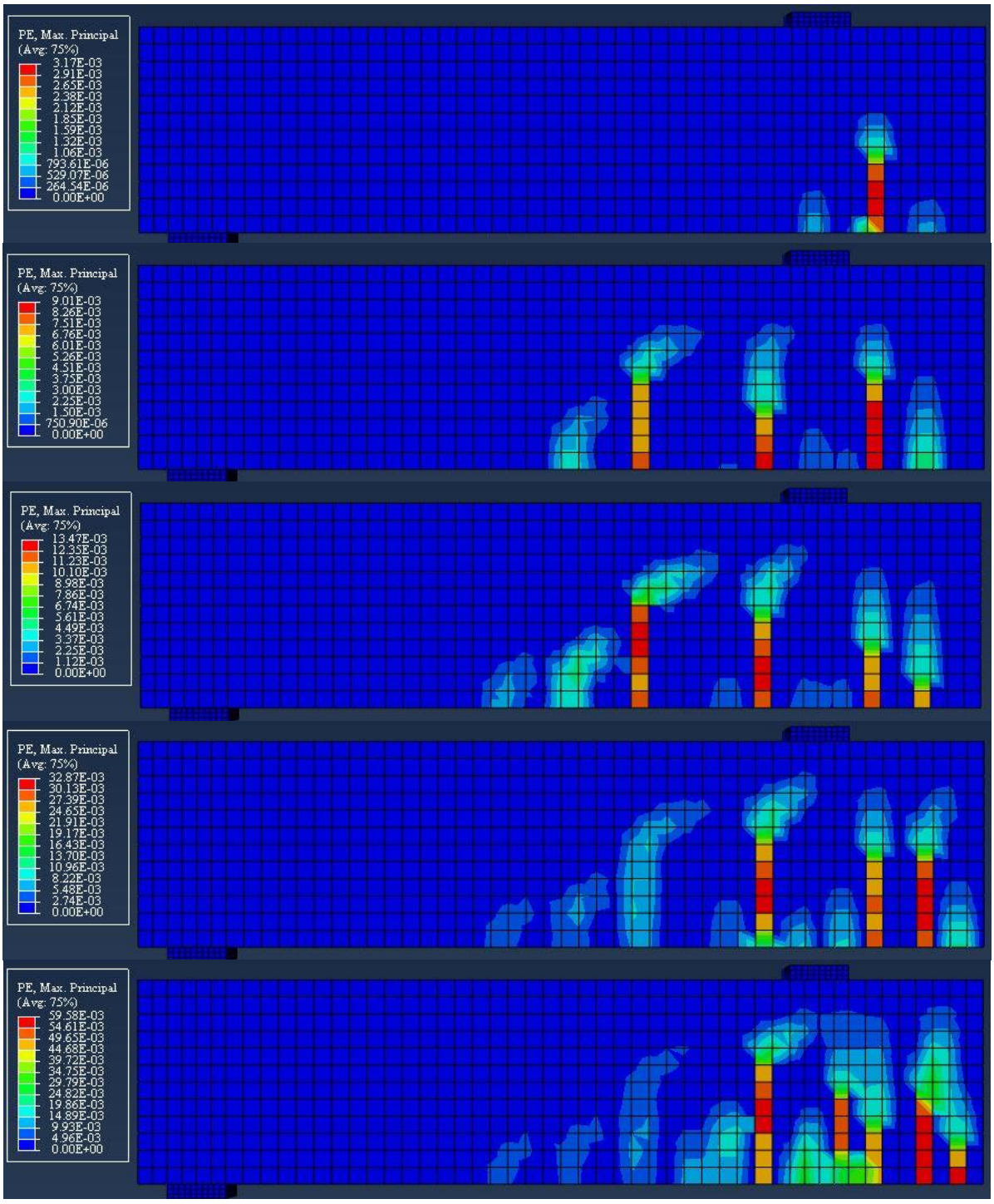

Figure A-1: Crack Pattern in Control Beam Model (mesh 30 x 30 mm)

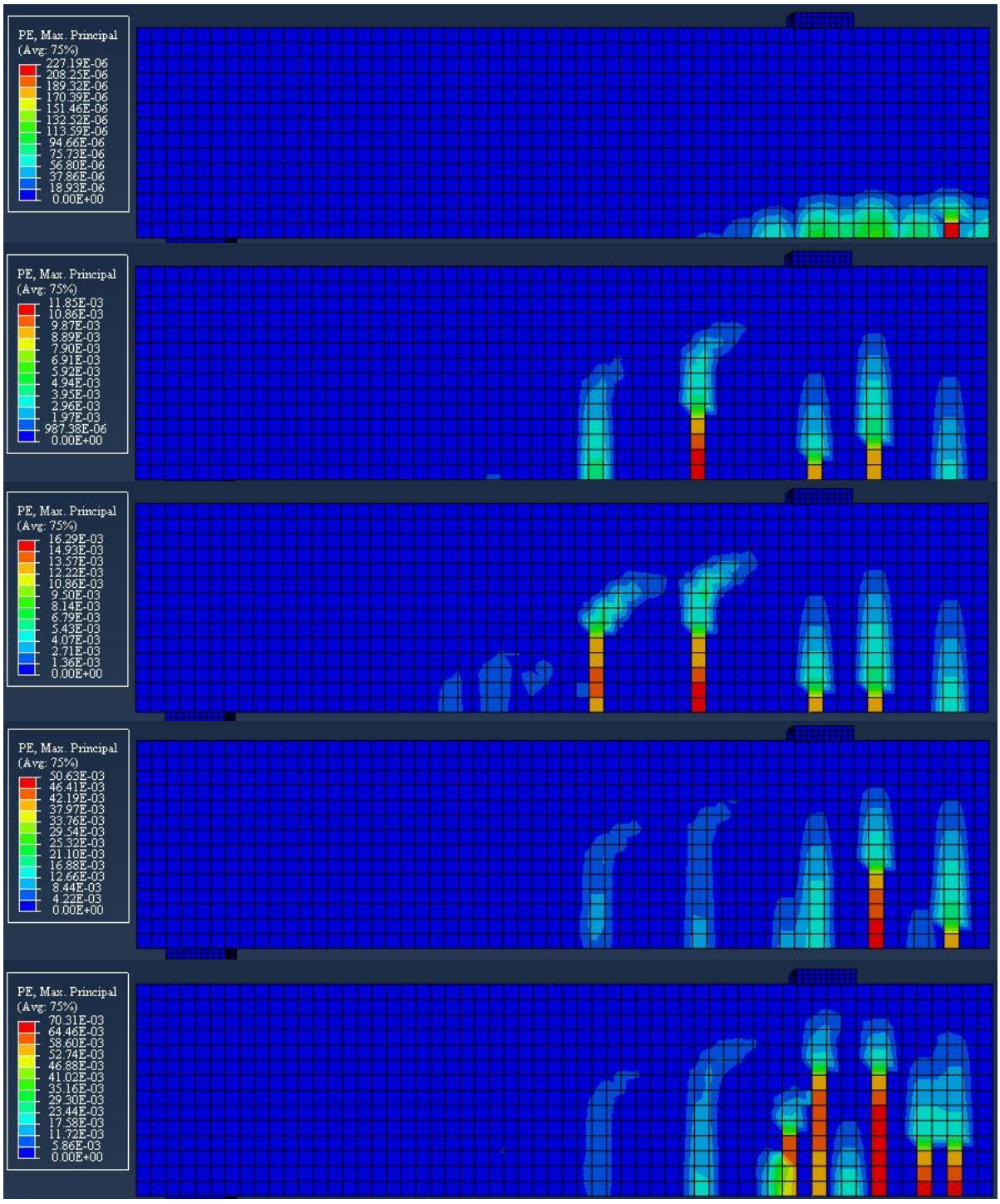

Figure A-2: Crack Pattern in Control Beam Model (mesh 25 x 25 mm)

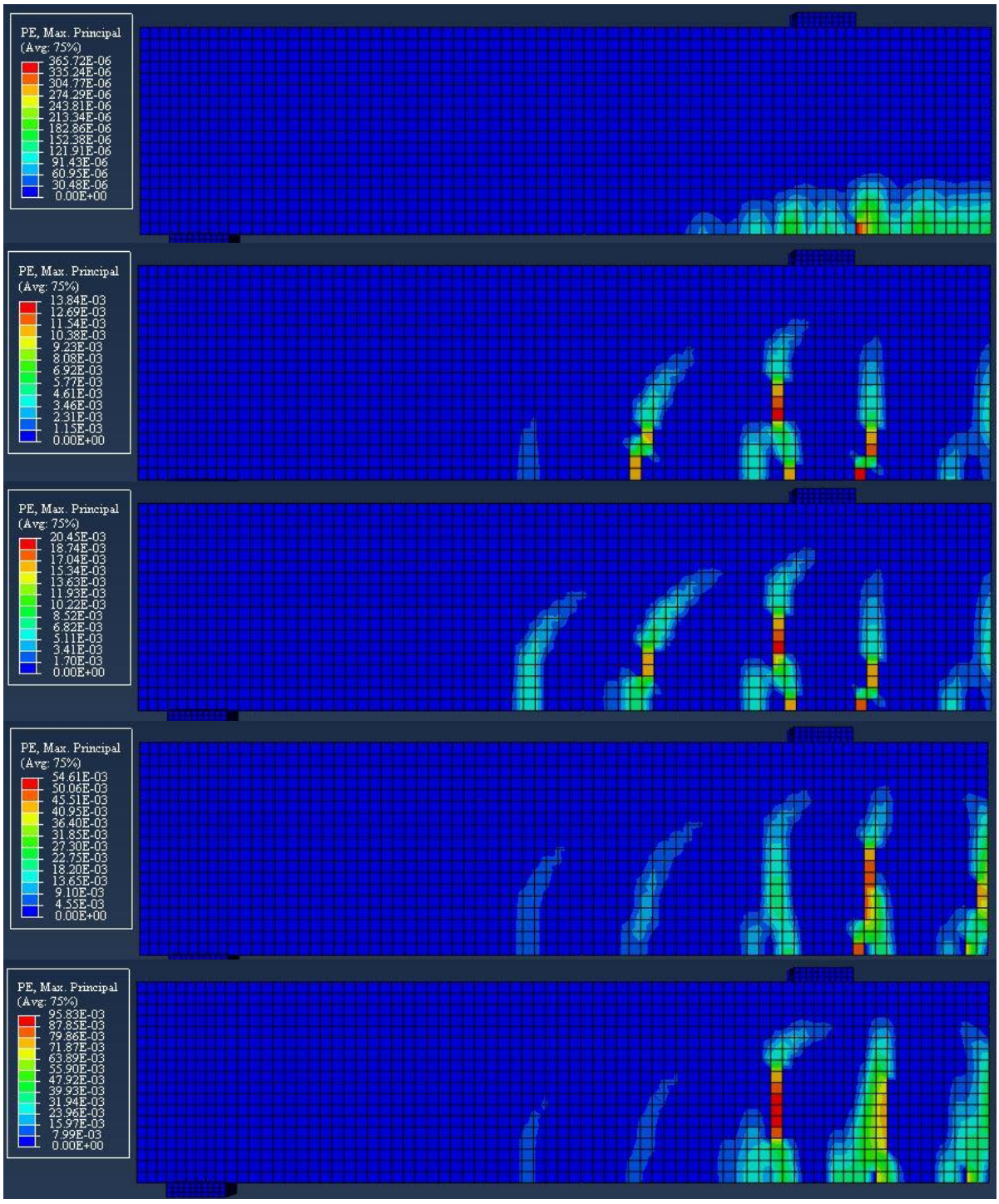

Figure A-3: Crack Pattern in Control Beam Model (mesh 20 x 20 mm)

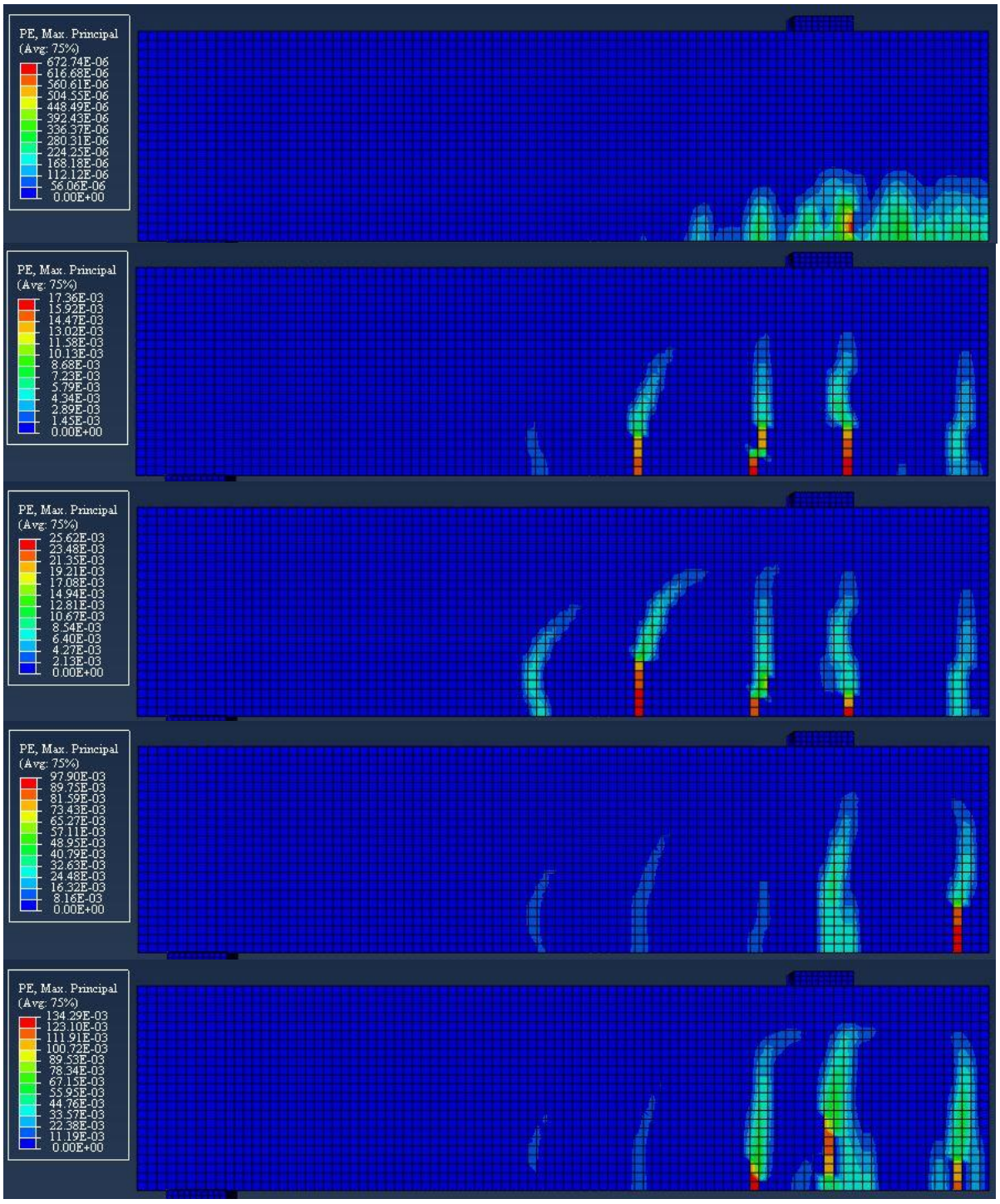

Figure A-4: Crack Pattern in Control Beam Model (mesh 15 x 15 mm)

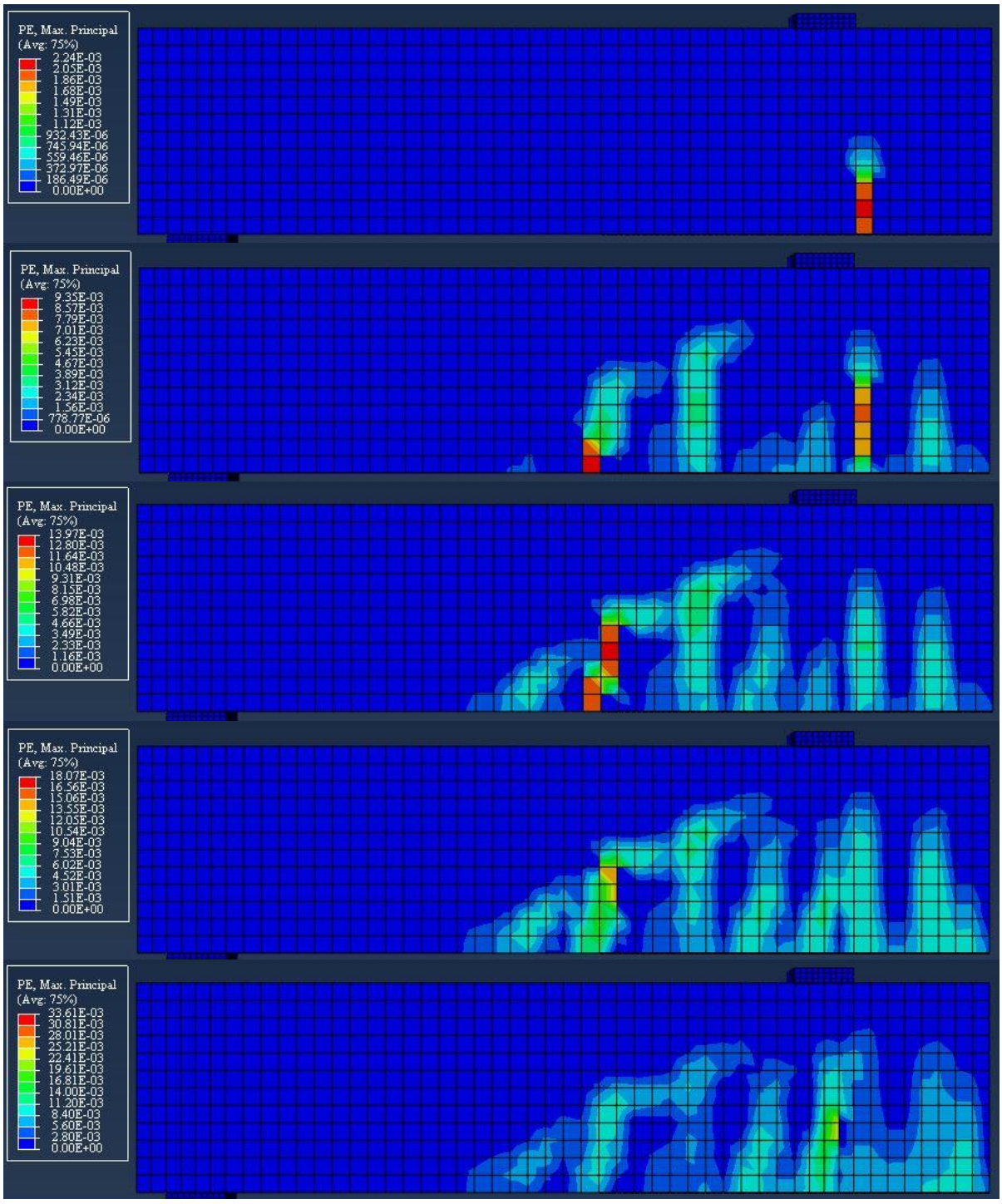

Figure A-5: Crack Pattern in CFRP Beam Model, Perfect Bond (mesh 30 x 30 mm)

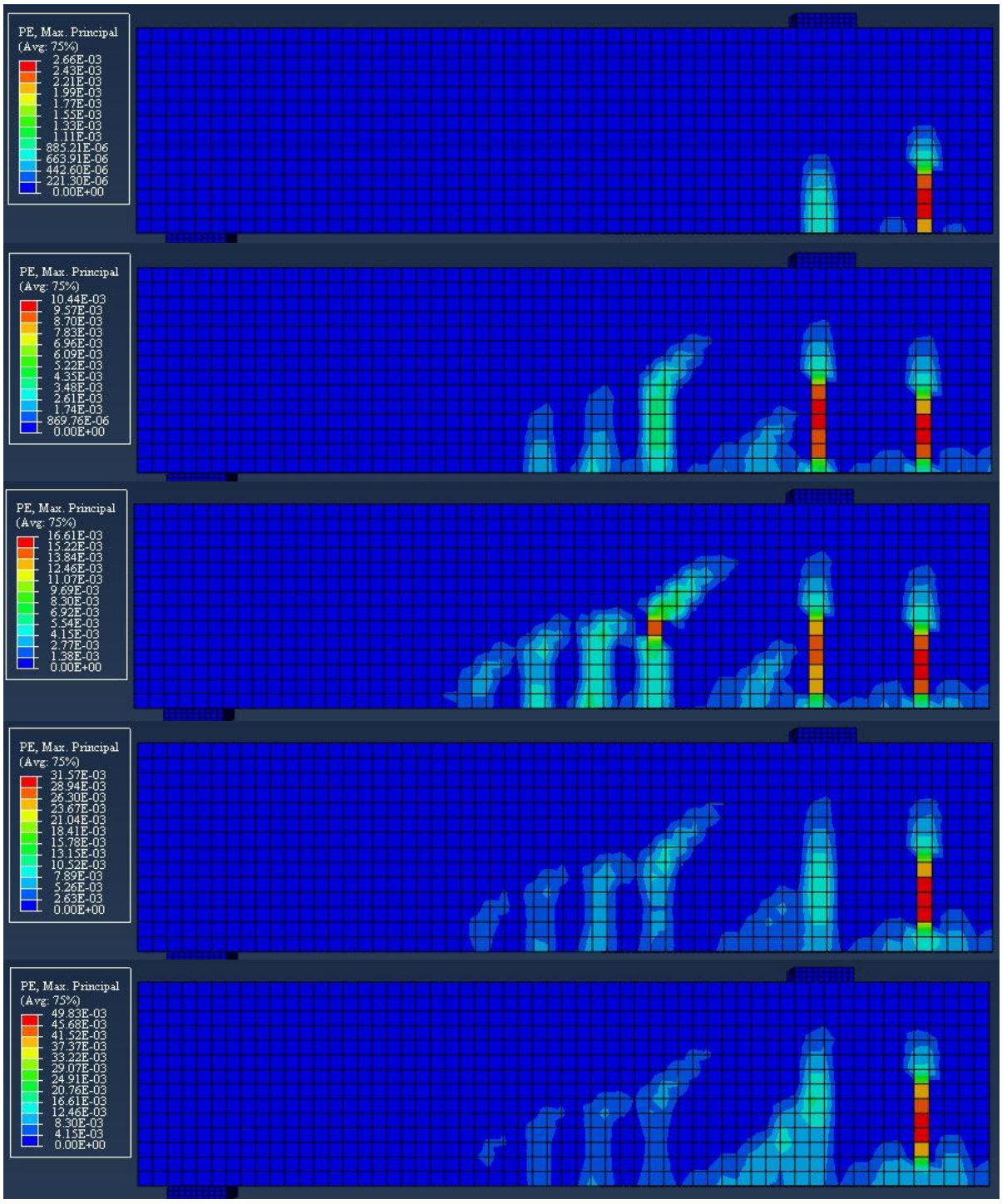

Figure A-6: Crack Pattern in CFRP Beam Model, Perfect Bond (mesh 25 x 25 mm)

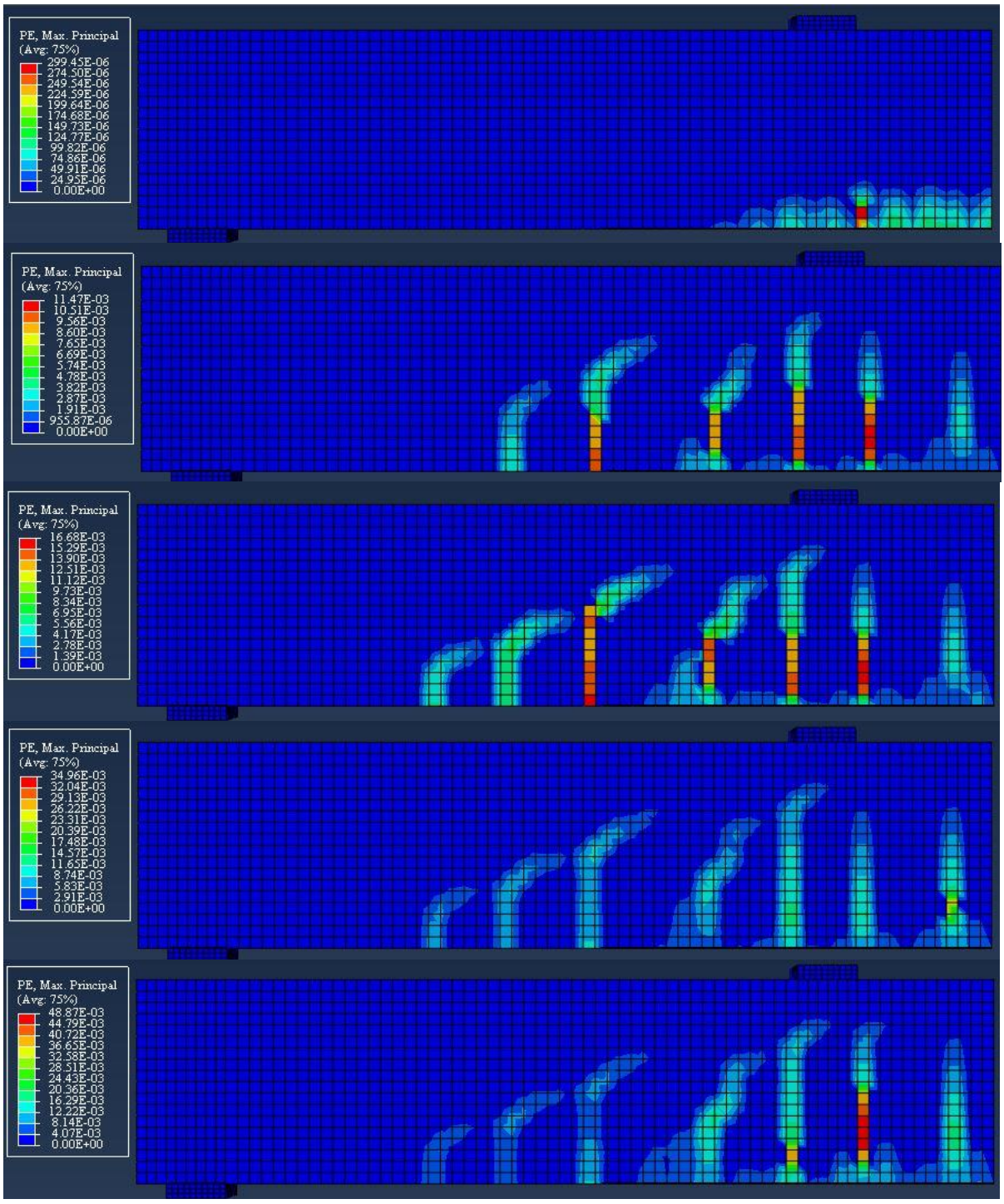

Figure_ A-7: Crack Pattern in CFRP Beam Model, Perfect Bond (mesh 20 x 20 mm)

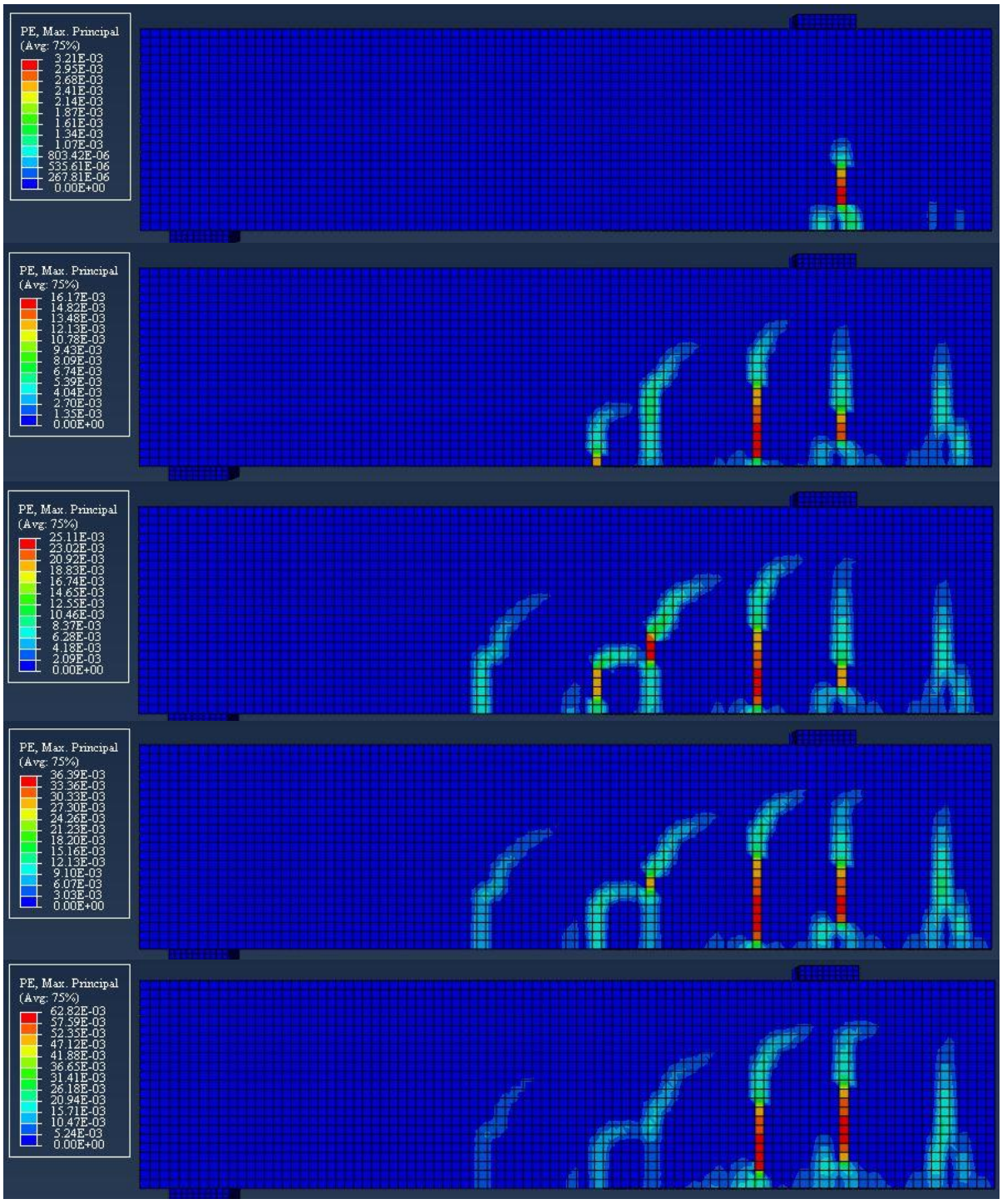

Figure A-8: Crack Pattern in CFRP Beam Model, Perfect Bond (mesh 15 x 15 mm)

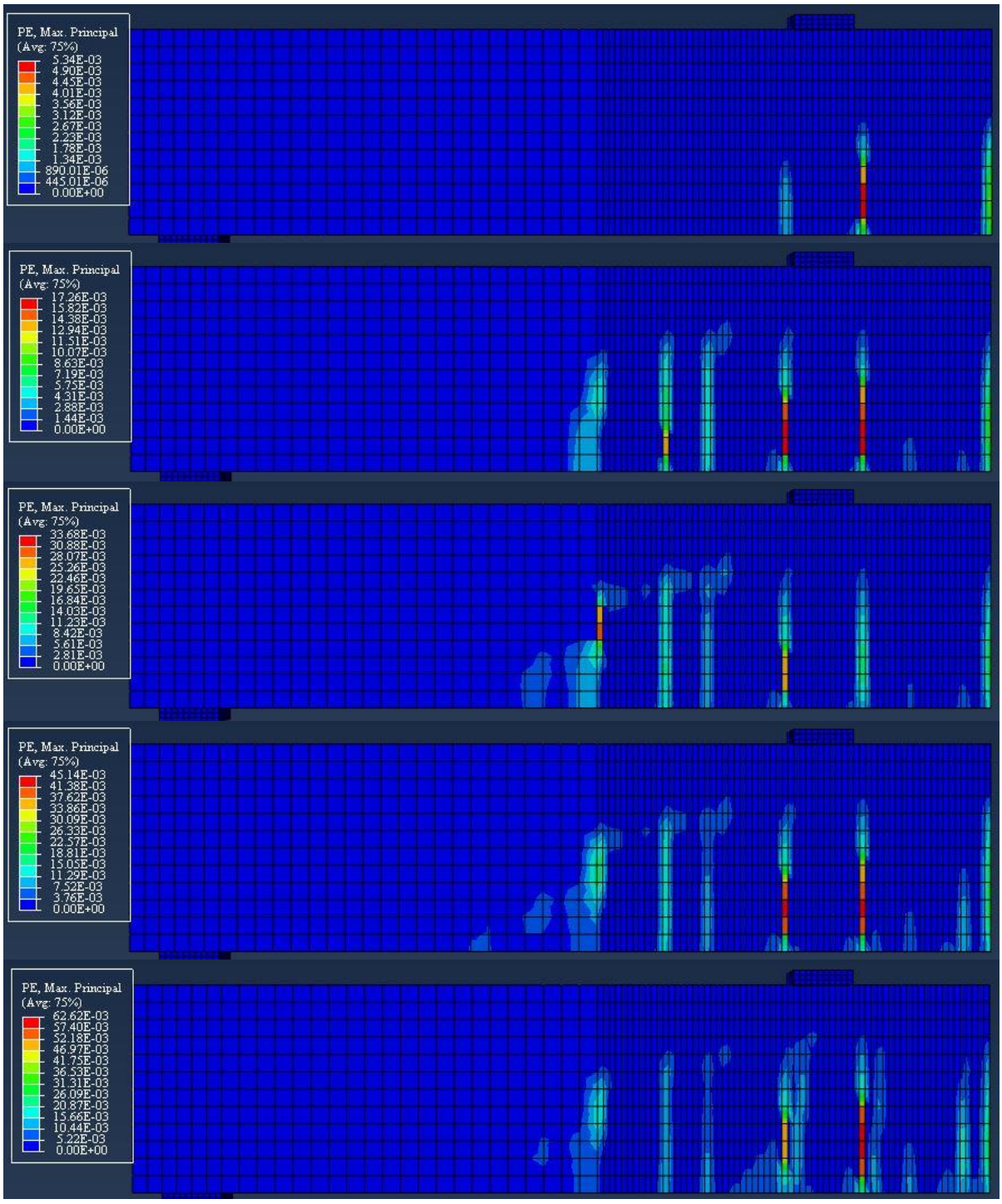

Figure A-9: Crack Pattern in CFRP Beam Model, CZM (mesh 30 x 30 mm)

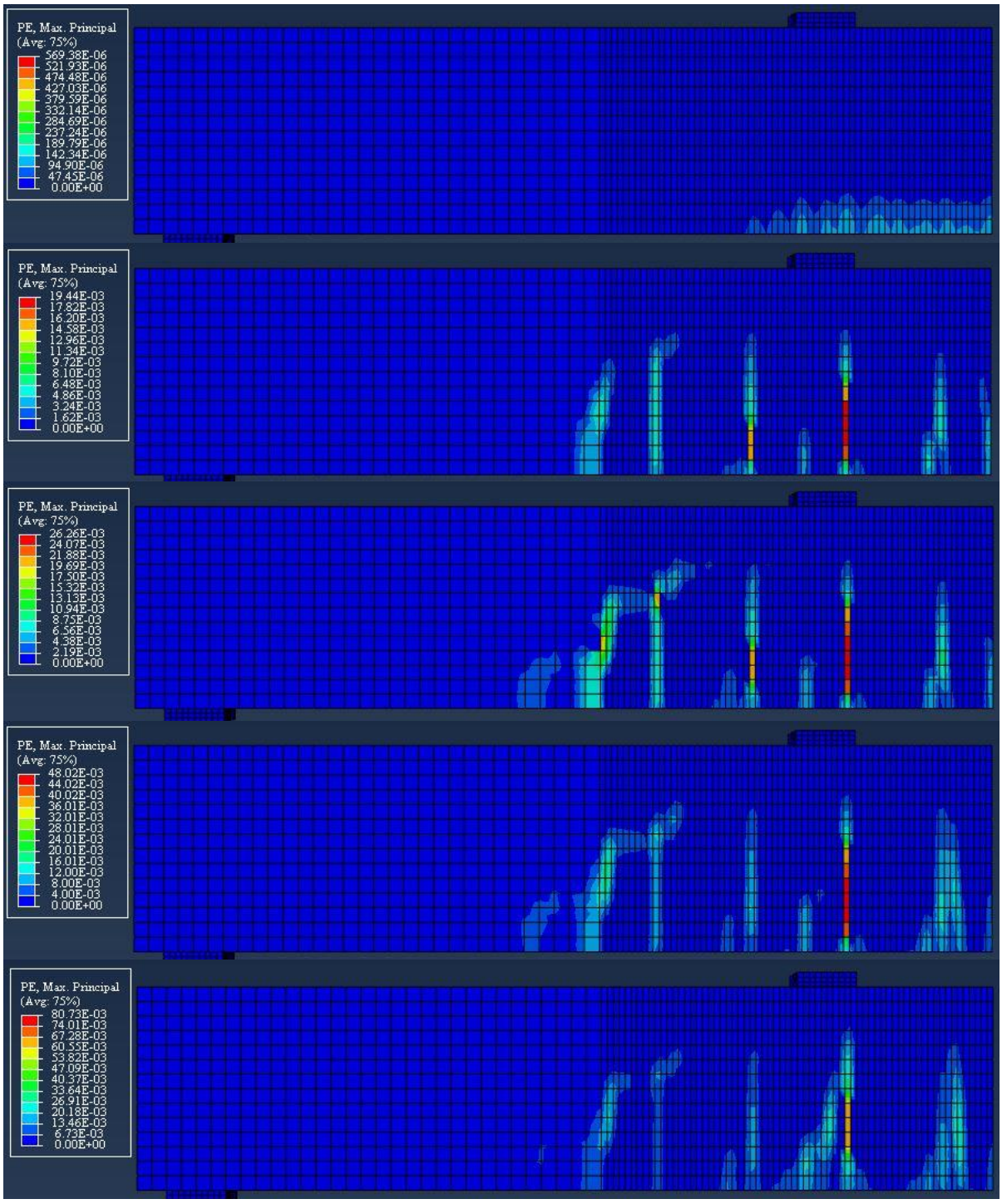

Figure A-10: Crack Pattern in CFRP Beam Model, CZM (mesh 25 x 25 mm)

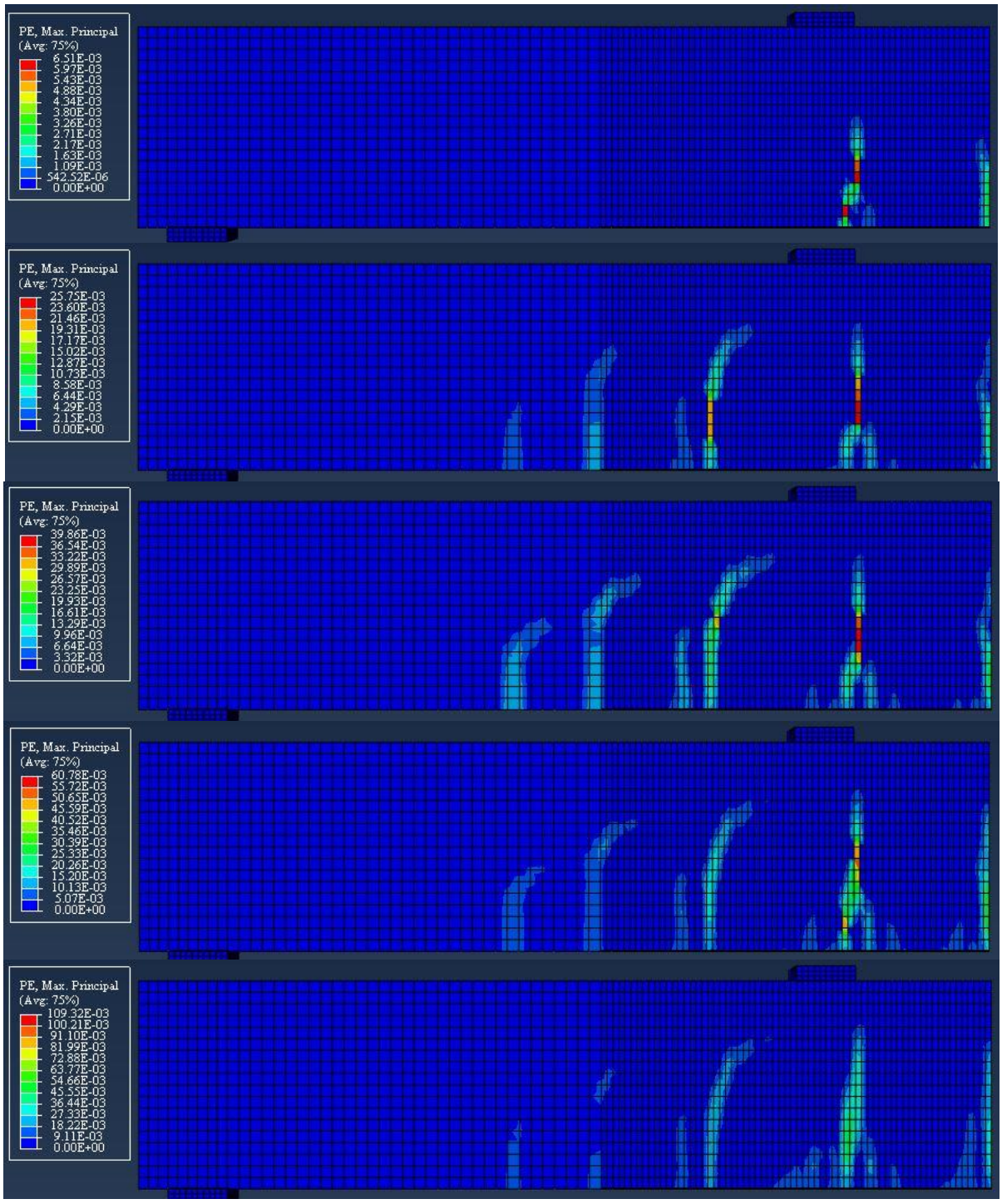

Figure A-11: Crack Pattern in CFRP Beam Model, CZM (mesh 20 x 20 mm)

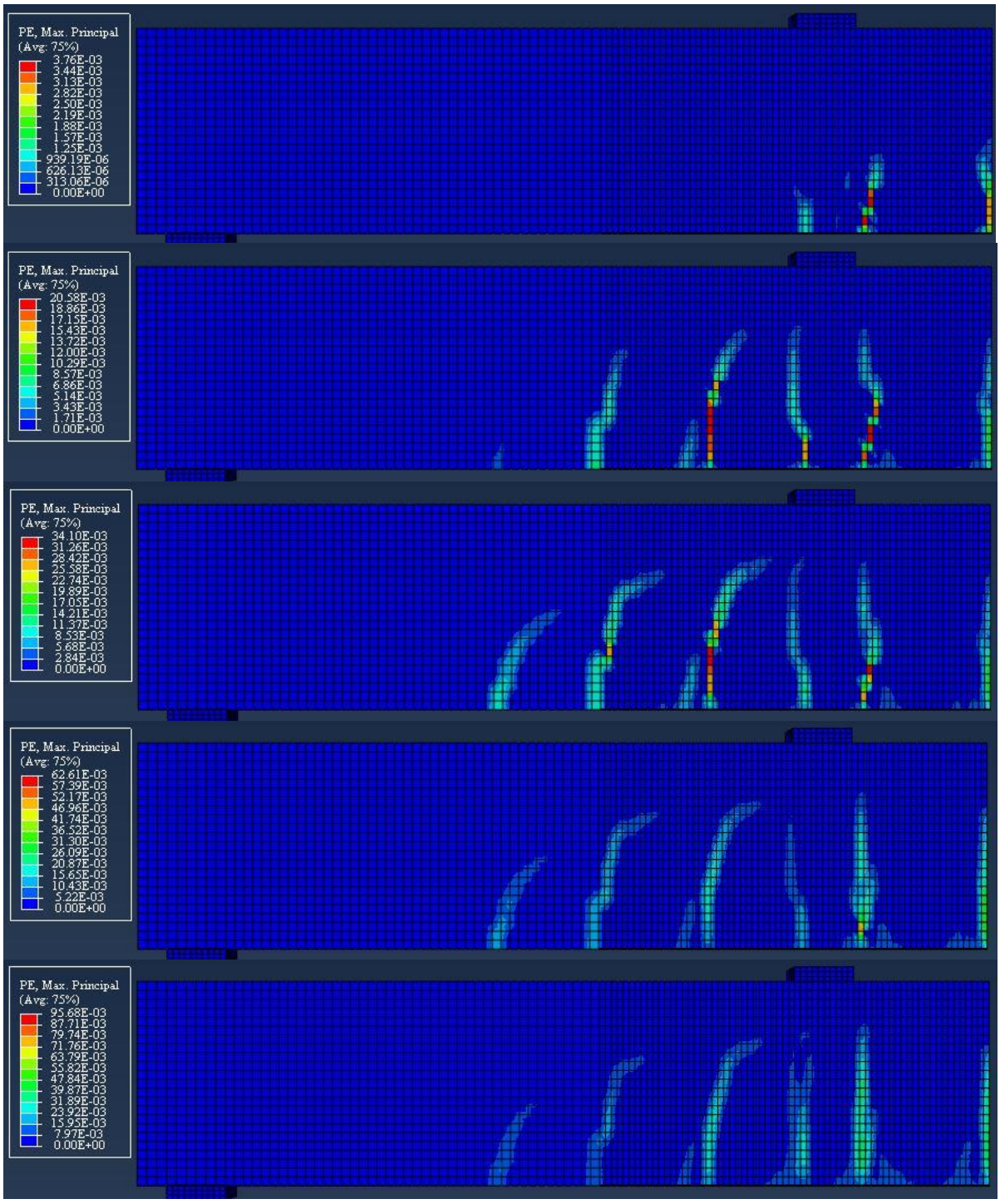

Figure A-12: Crack Pattern in CFRP Beam Model, CZM (mesh 15 x 15 mm)

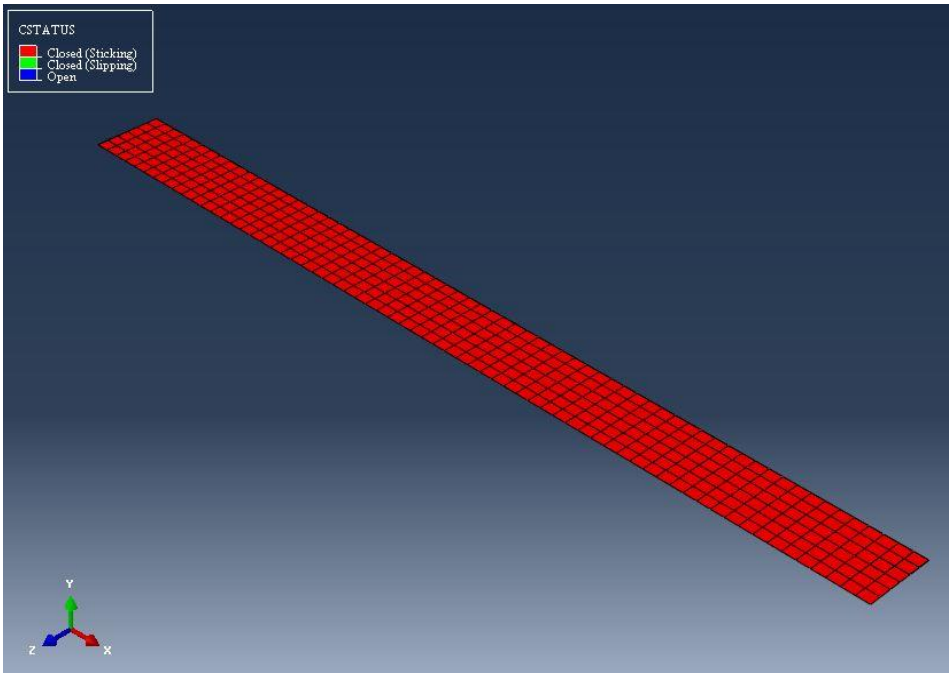

(a) Initial stage (no loading)

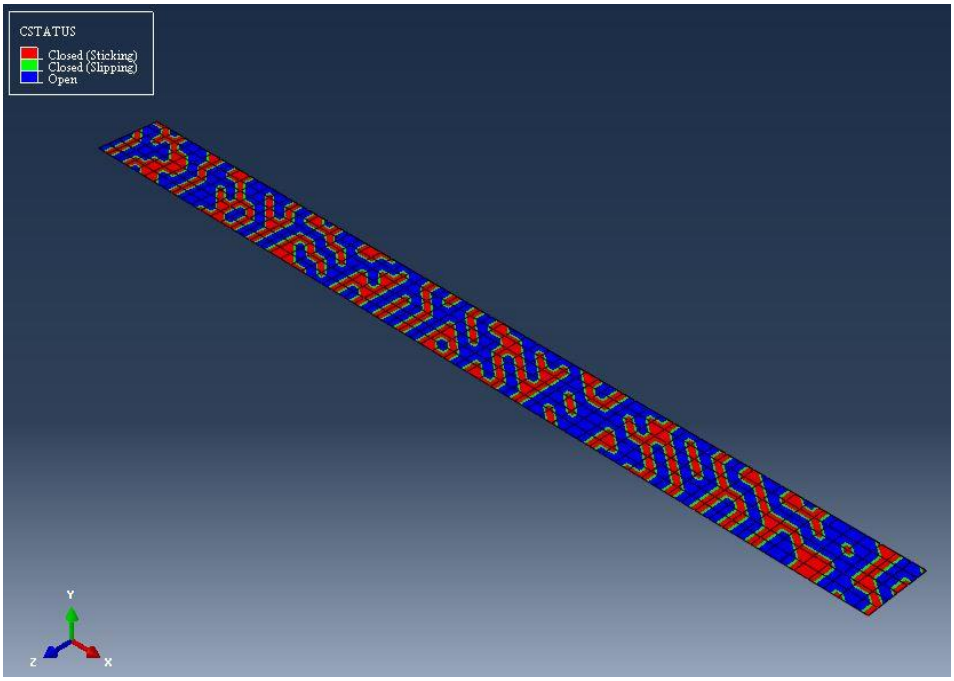

(b) Final stage (ultimate load)

Figure A-13: CFRP laminate debonding in CFRP Beam Model, CZM (mesh 30 x 30 mm)

Appendix B

Parametric Study

This appendix presents some of the results of the parametric study performed in Chapter six. The cracks pattern and evolution are depicted in Figure B-1 through Figure B-28, for every individual parameter that was studied in this analysis. This illustration was made as the load progressed at five loading interval (e.g. cracking point, beam midspan deflection of 5 mm, yielding of steel rebar point, beam midspan deflections of 12 mm and 19 mm, respectively).

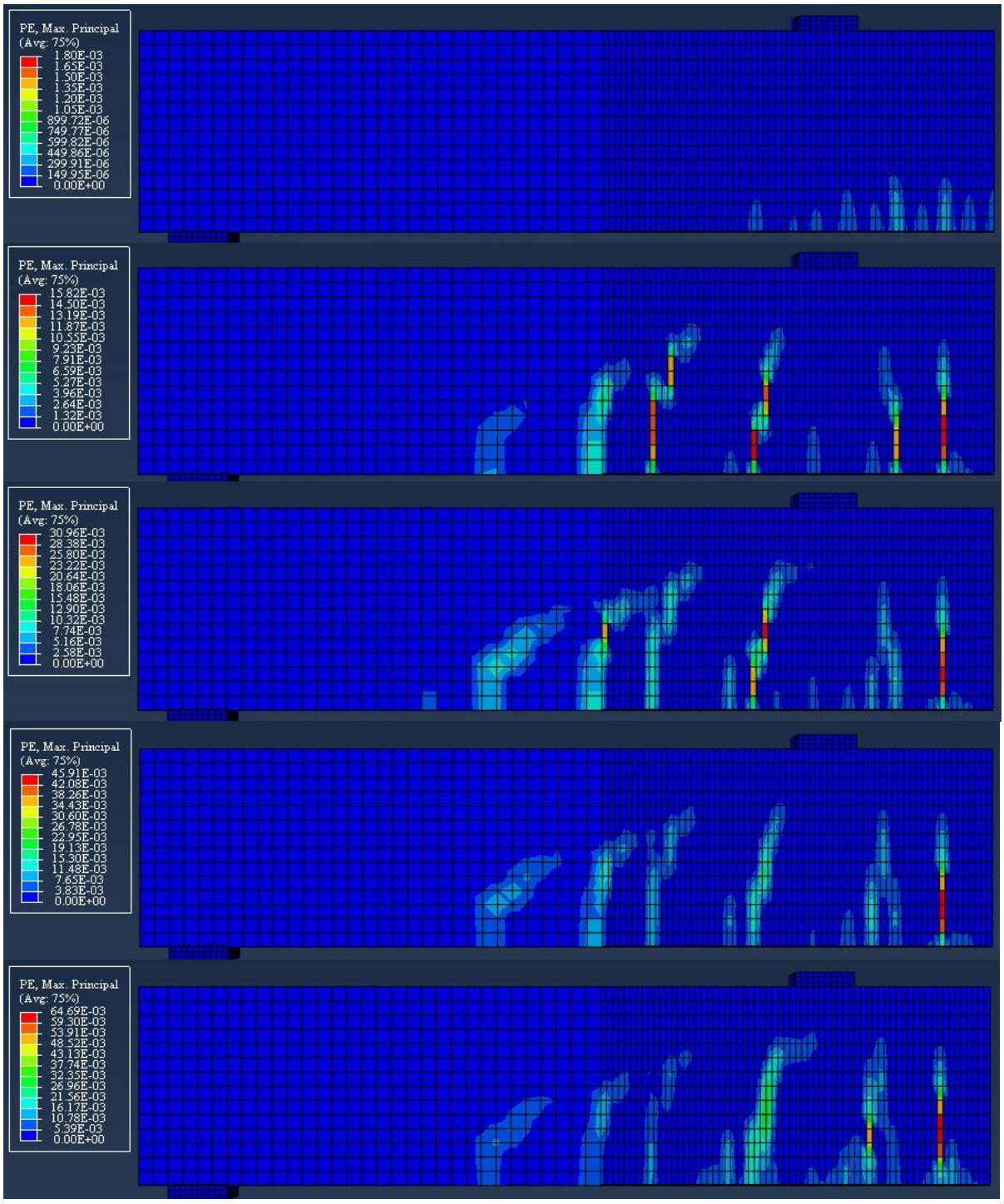

Figure B-1: Crack Pattern in CFRP Beam Model (effect of concrete compressive strength, $f_c' = 20MPa$)

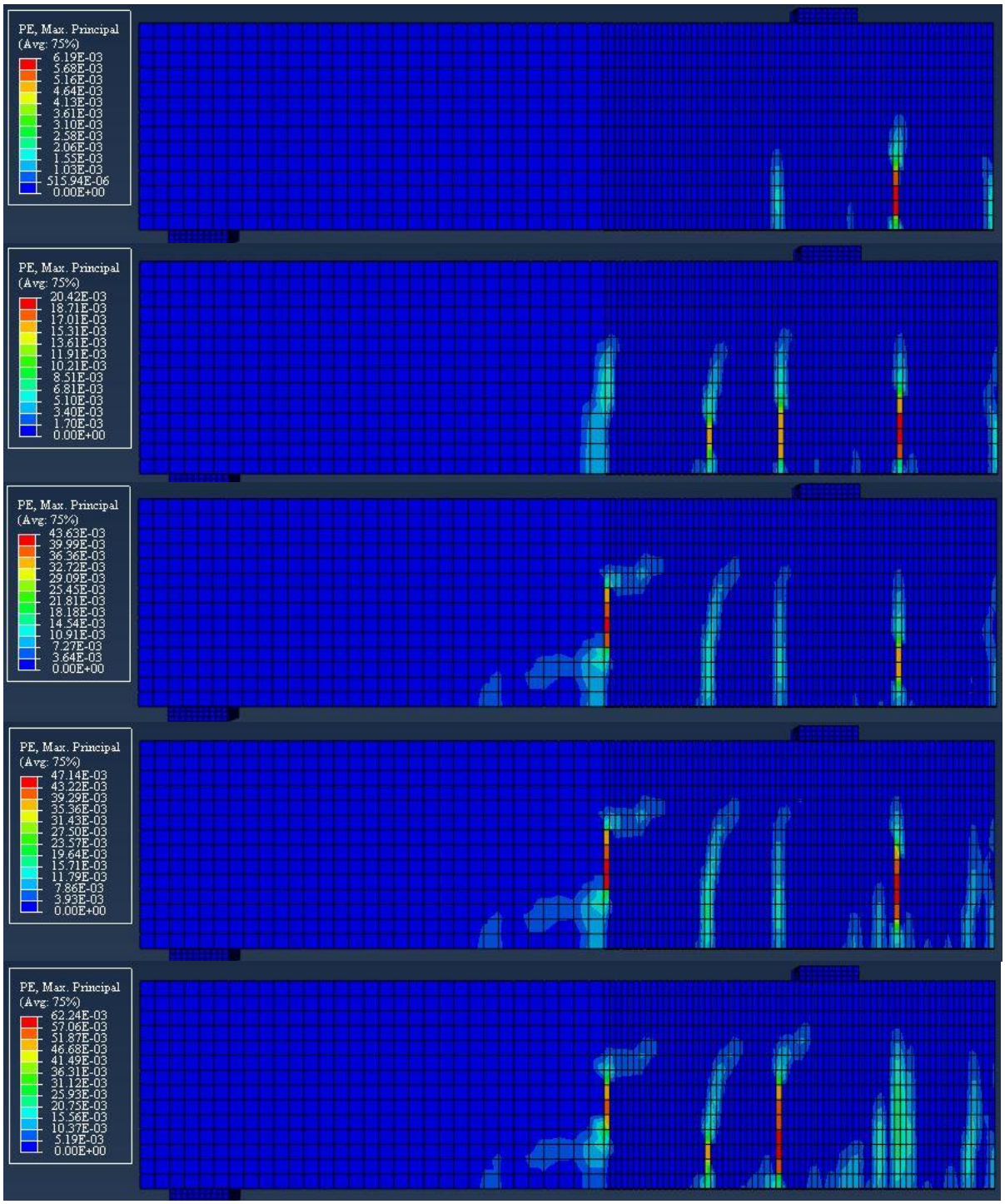

Figure B-2: Crack Pattern in CFRP Beam Model (effect of concrete compressive strength, $f_c' = 30MPa$)

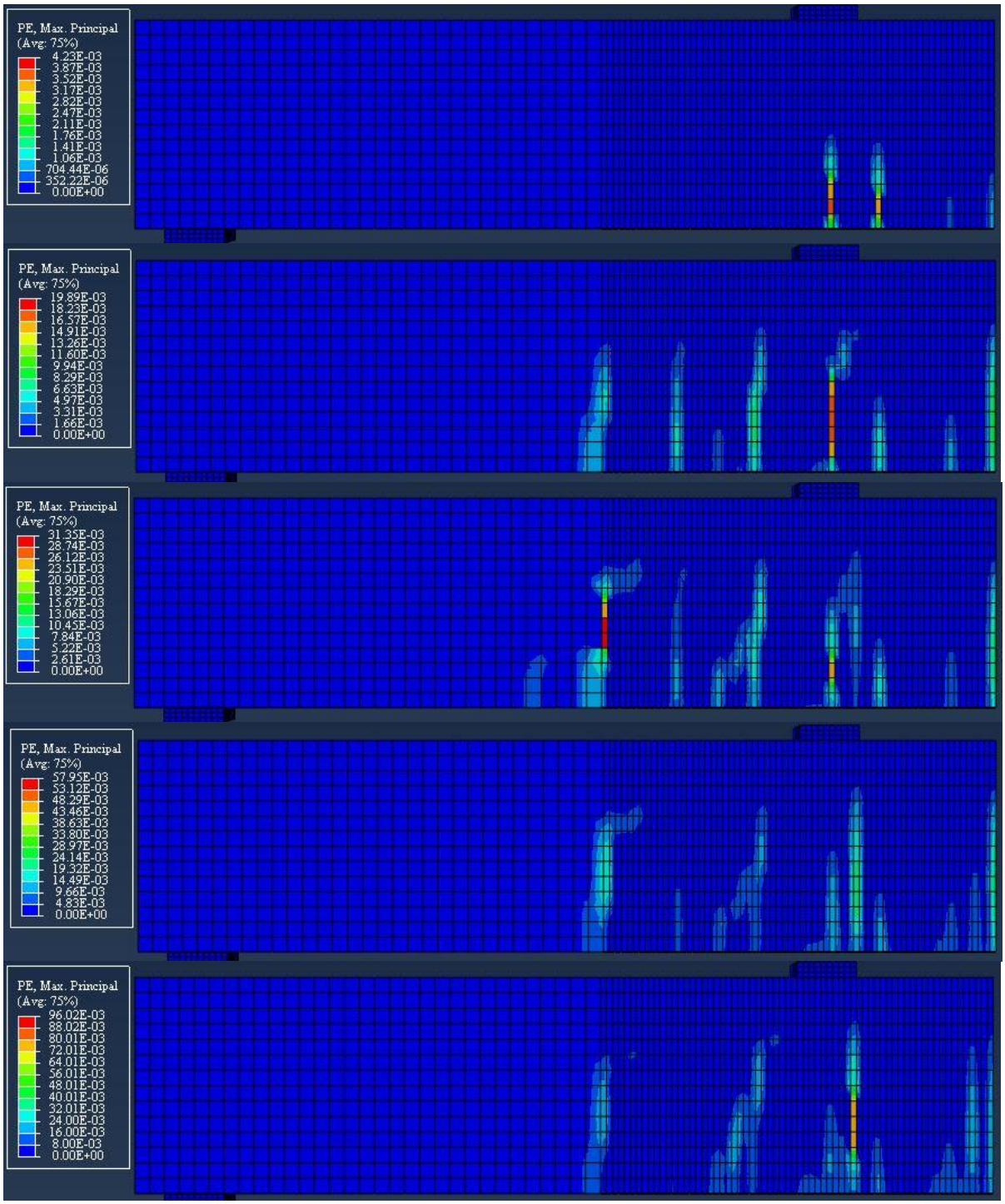

Figure B-3: Crack Pattern in CFRP Beam Model (effect of concrete compressive strength, $f_c' = 50MPa$)

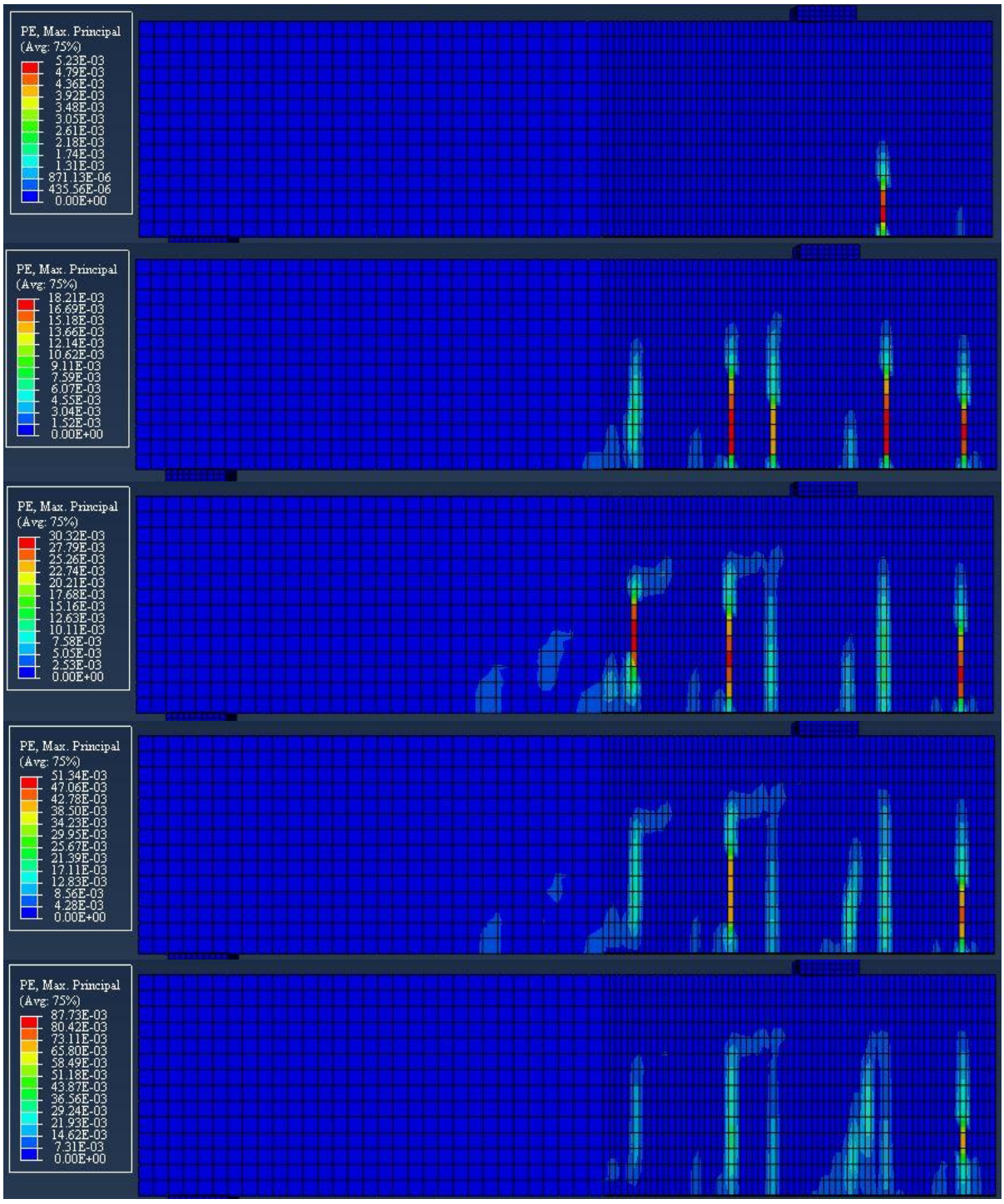

Figure B-4: Crack Pattern in CFRP Beam Model (effect of concrete compressive strength, $f_c' = 70MPa$)

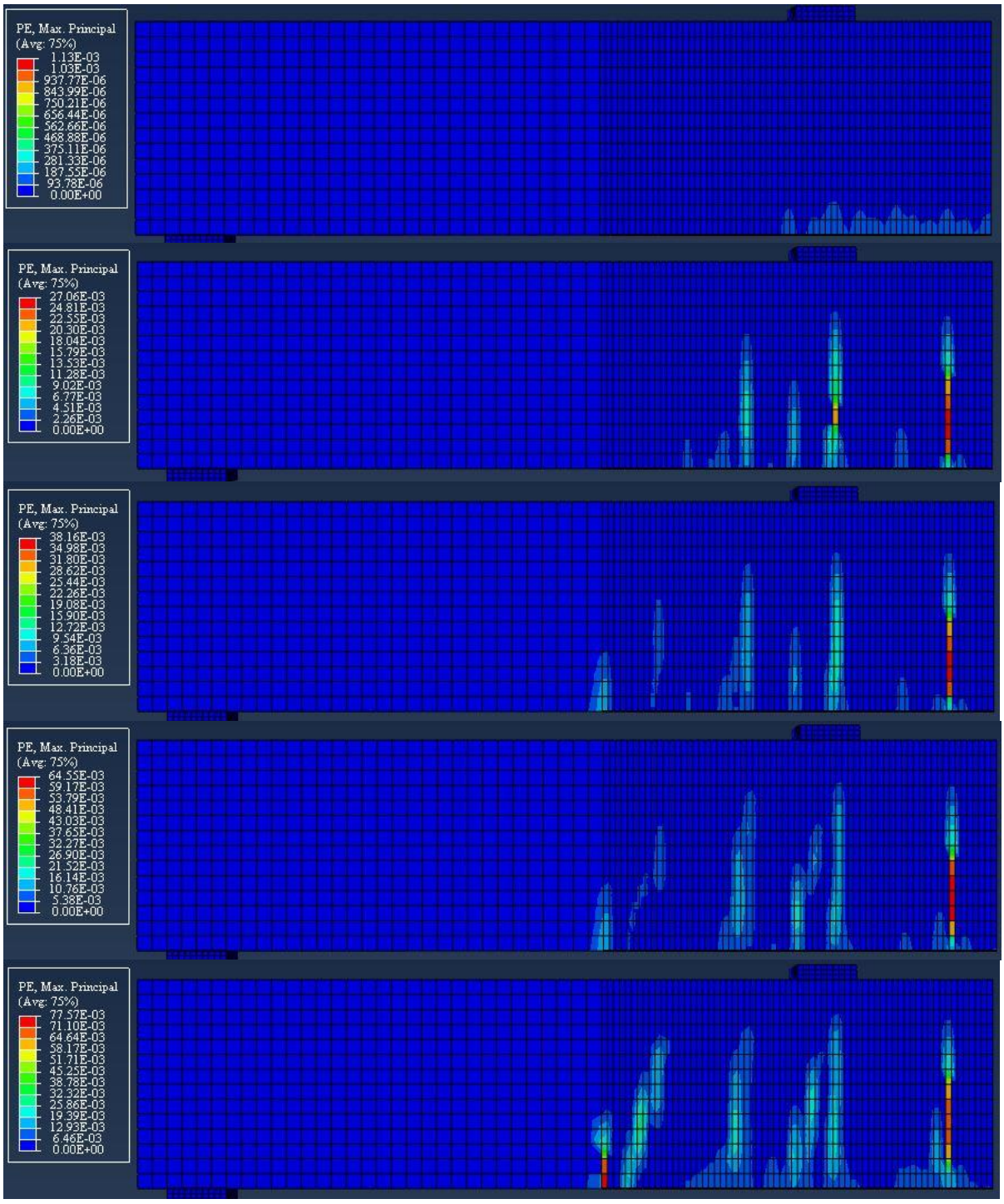

Figure B-5: Crack Pattern in CFRP Beam Model (effect longitudinal steel reinforcement ratio, $\rho = 0.0049$)

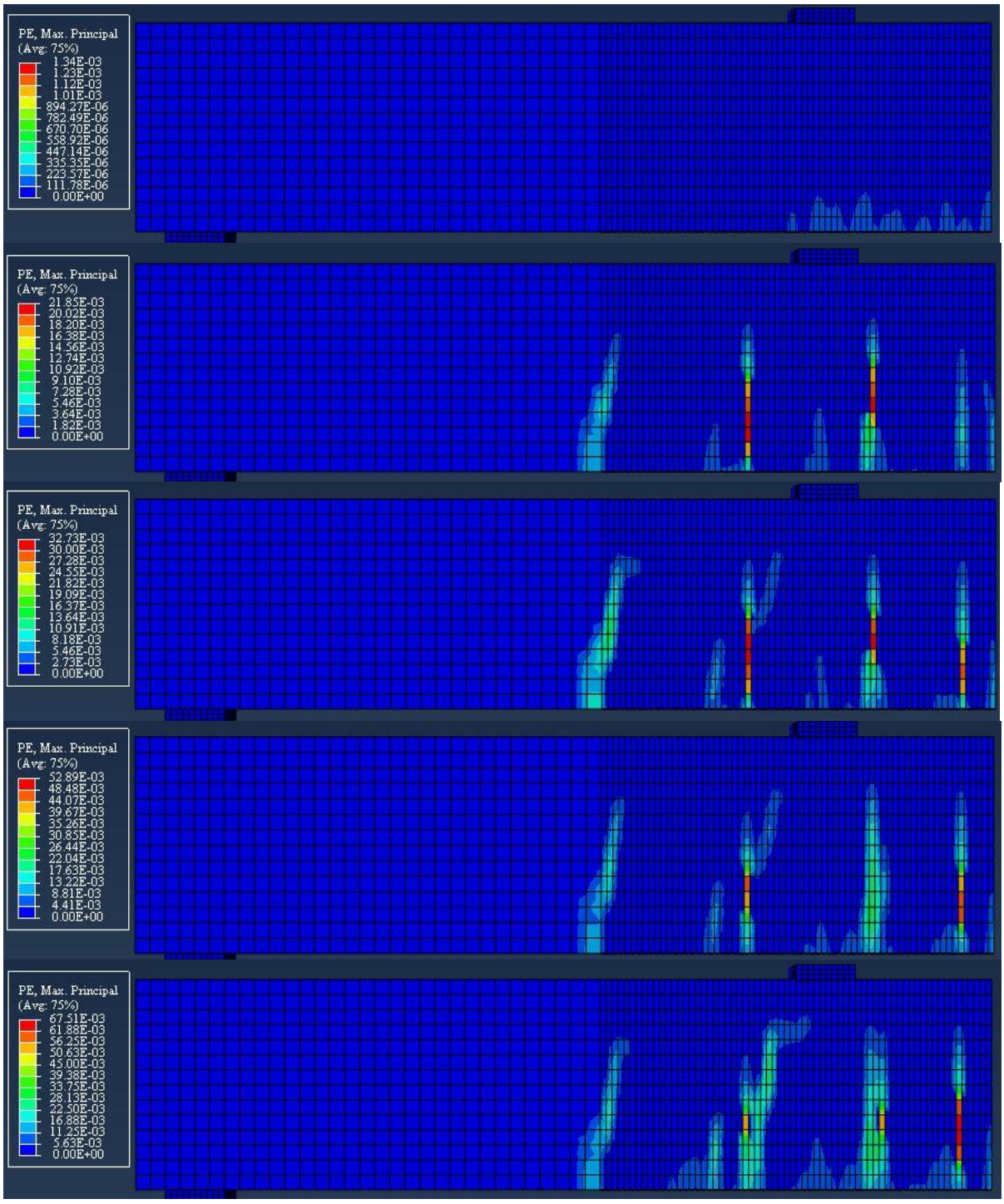

Figure B-6: Crack Pattern in CFRP Beam Model (effect longitudinal steel reinforcement ratio, $\rho = 0.0065$)

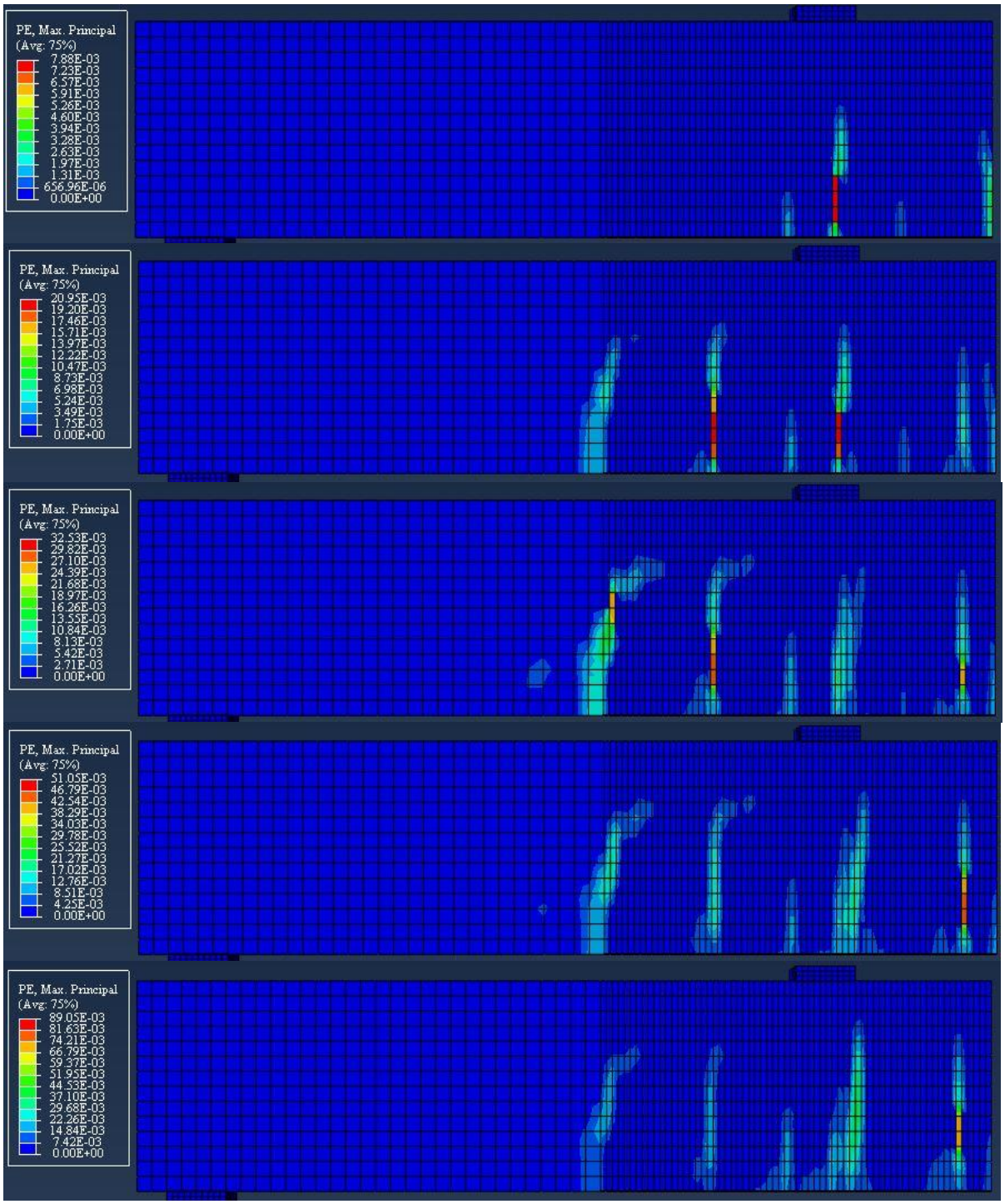

Figure B-7: Crack Pattern in CFRP Beam Model (effect longitudinal steel reinforcement ratio, $\rho = 0.0127$)

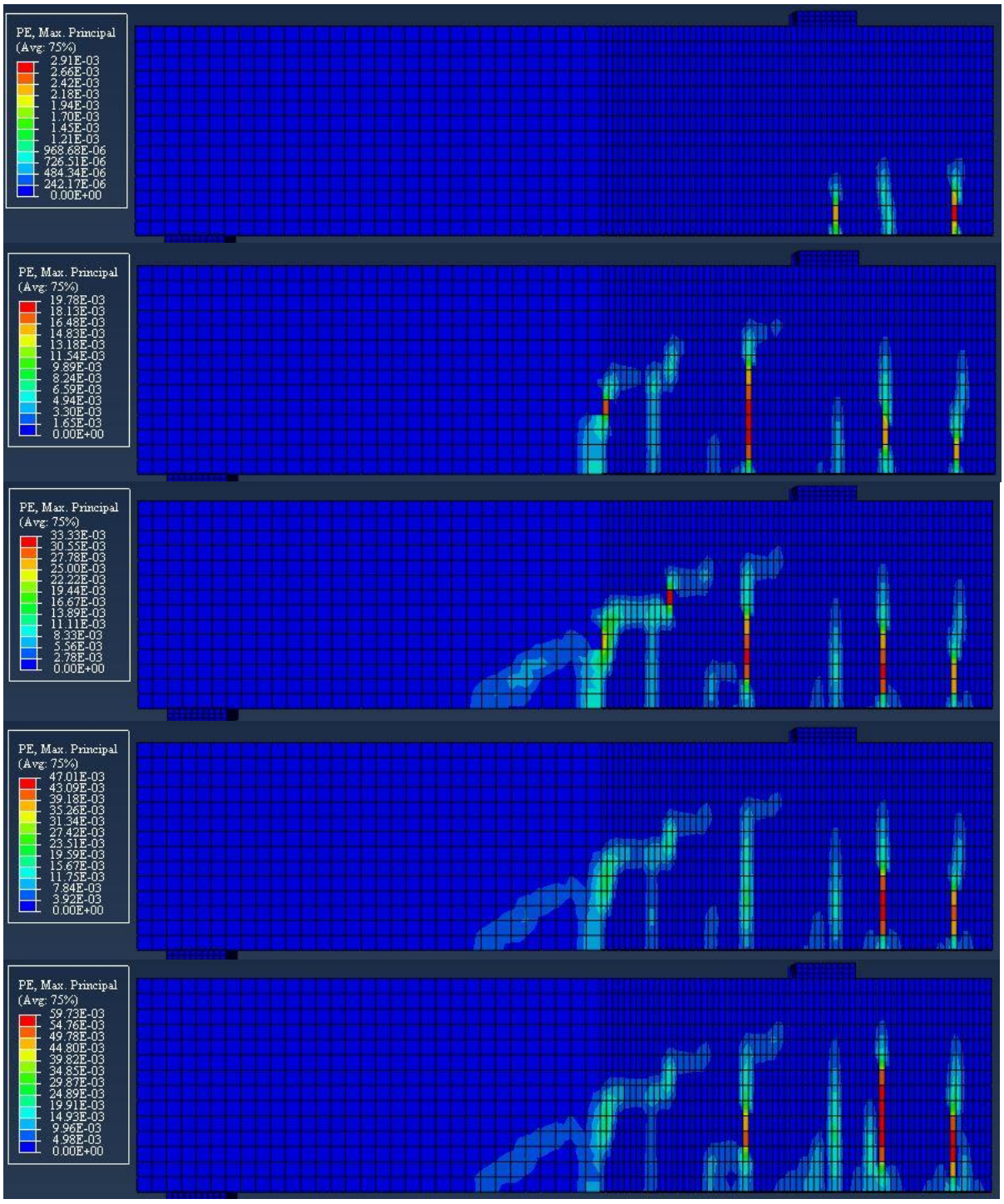

Figure B-8: Crack Pattern in CFRP Beam Model (effect longitudinal steel reinforcement ratio, $\rho = 0.0154$)

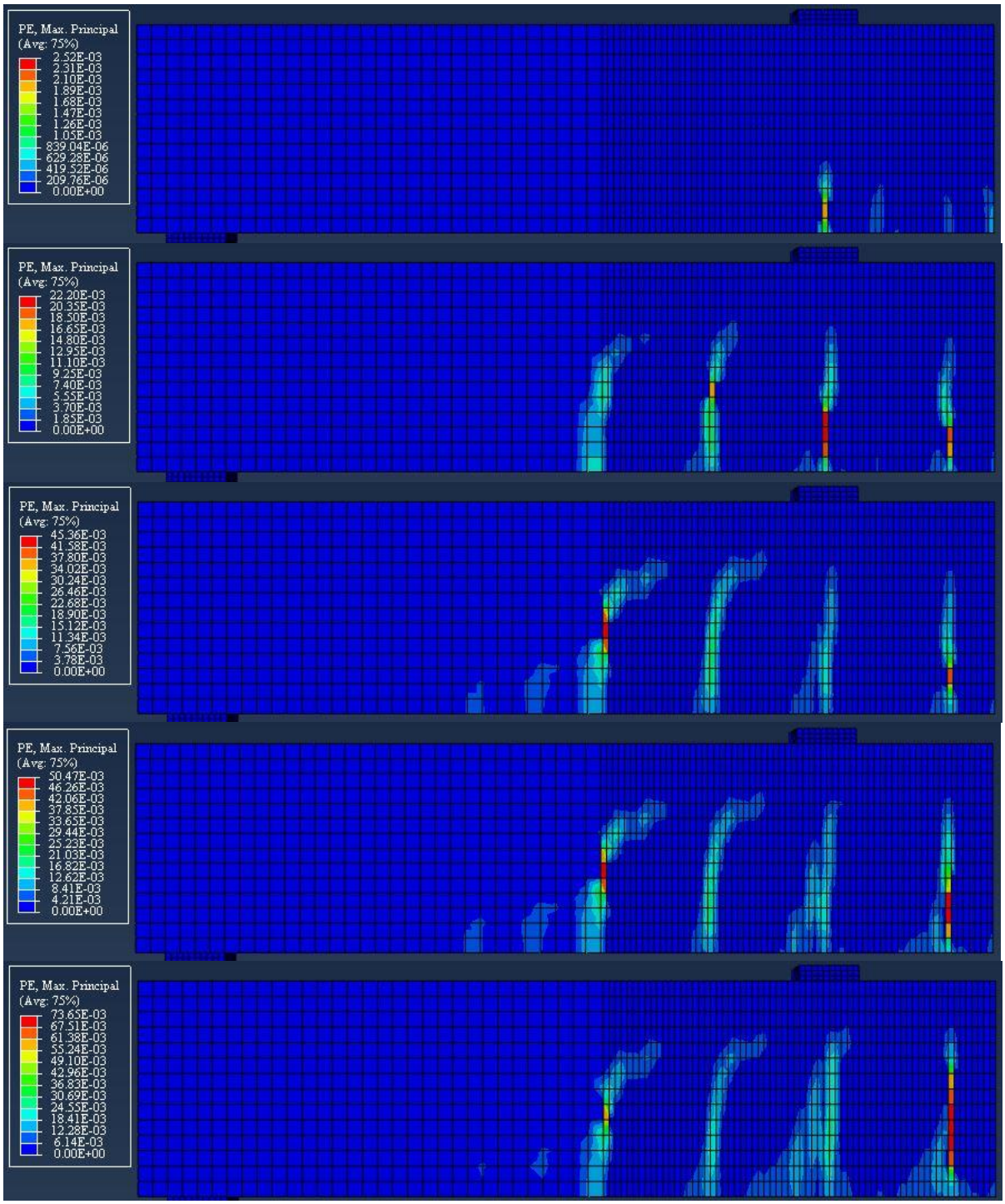

Figure B-9: Crack Pattern in CFRP Beam Model (effect of concrete plasticity parameters, $\psi = 20^o$)

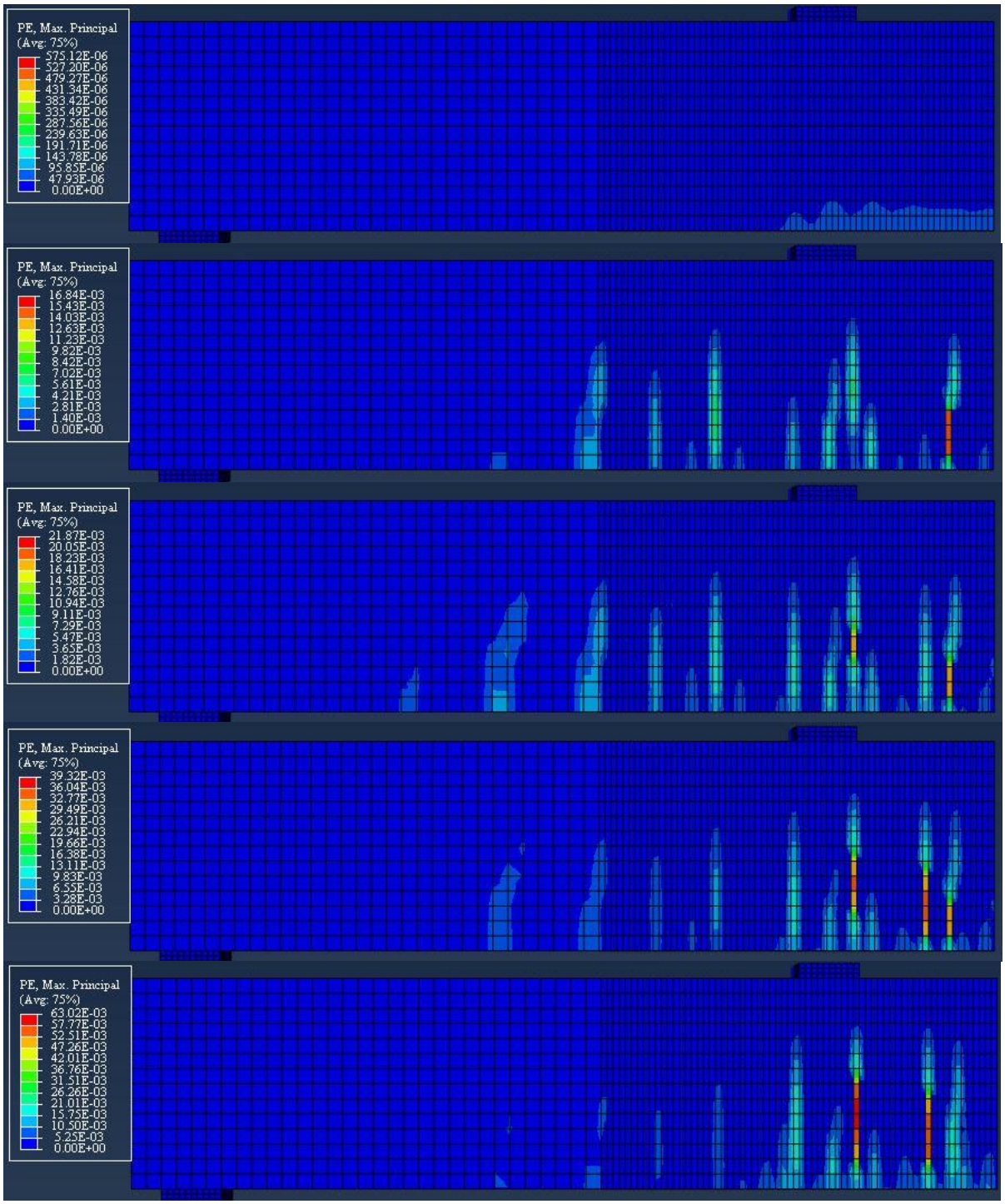

Figure B-10: Crack Pattern in CFRP Beam Model (effect of concrete plasticity parameters, $\psi = 50^o$)

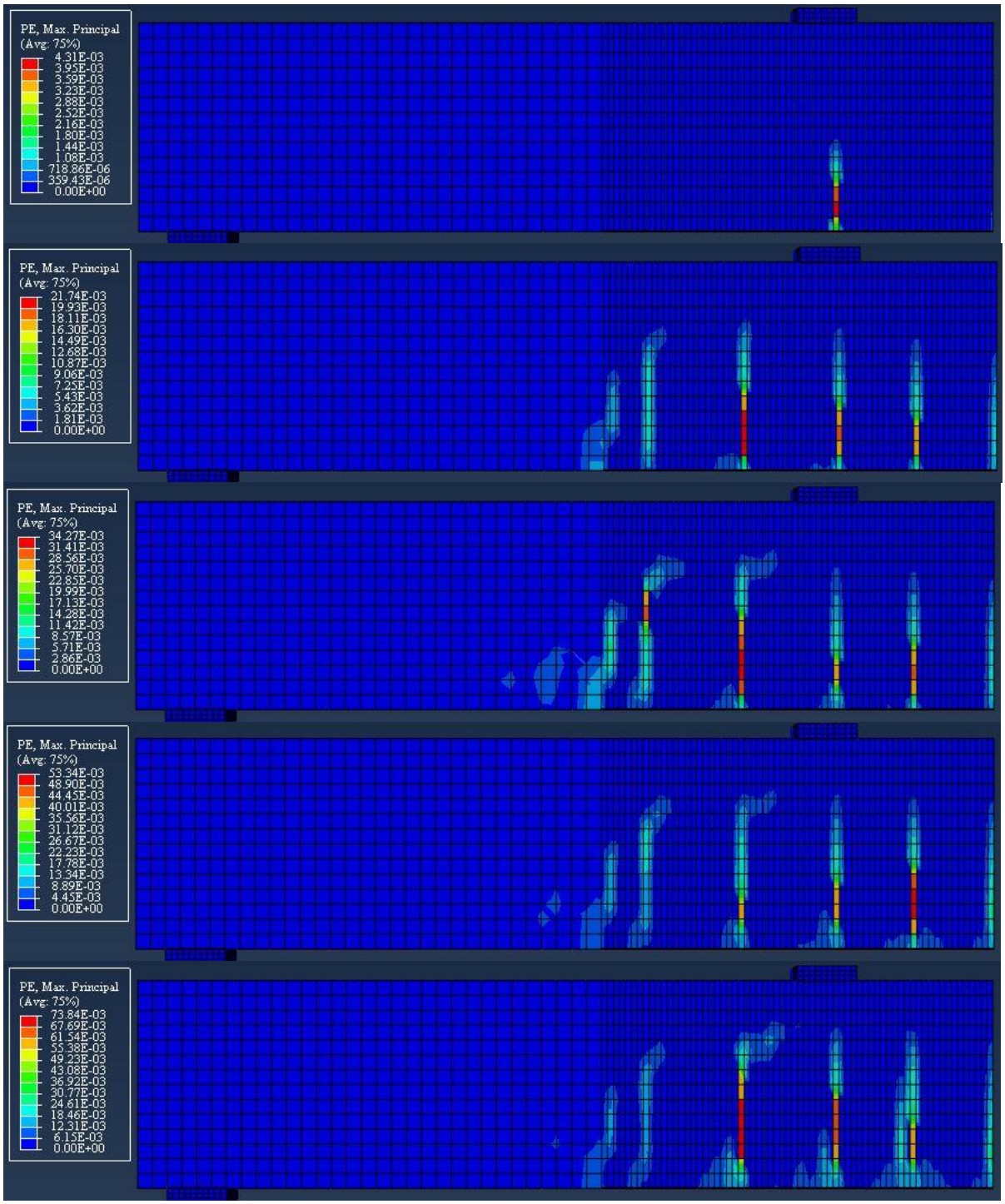

Figure B-11: Crack Pattern in CFRP Beam Model (effect of concrete plasticity parameters, $\mu = 0.00001$)

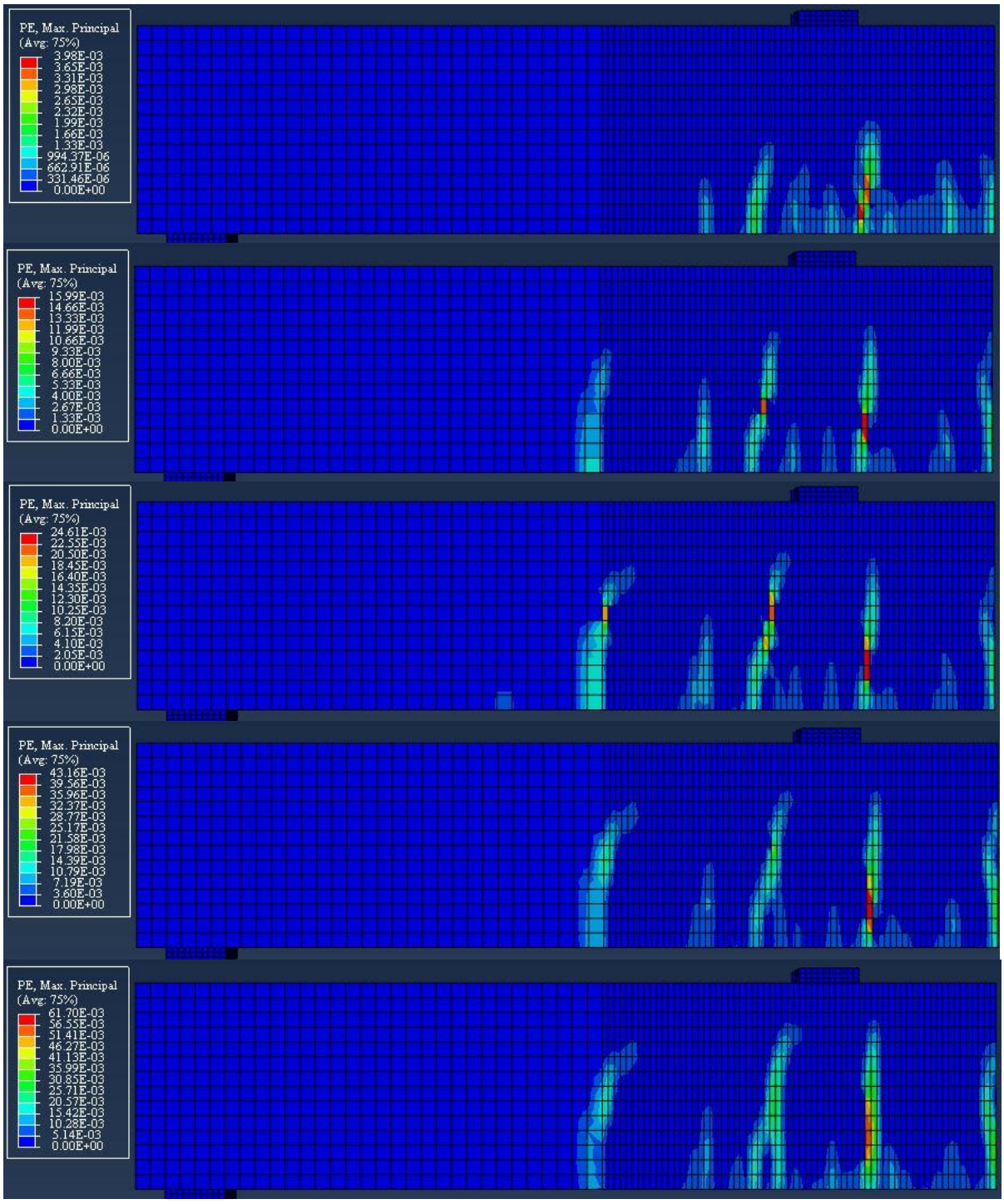

Figure B-12: Crack Pattern in CFRP Beam Model (effect of concrete plasticity parameters, $\mu = 0.001$)

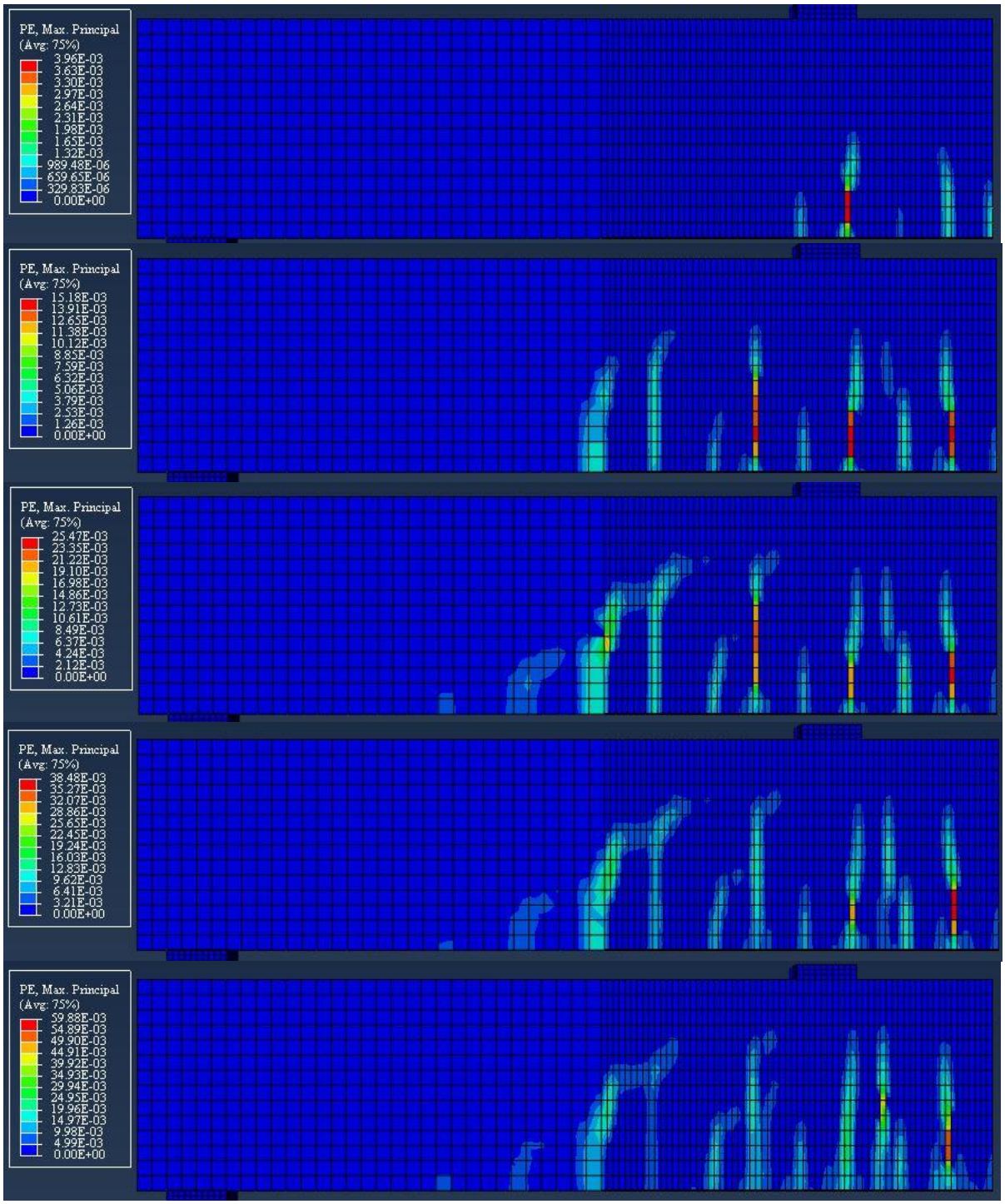

Figure B-13: Crack Pattern in CFRP Beam Model (effect of concrete plasticity parameters, No Damage)

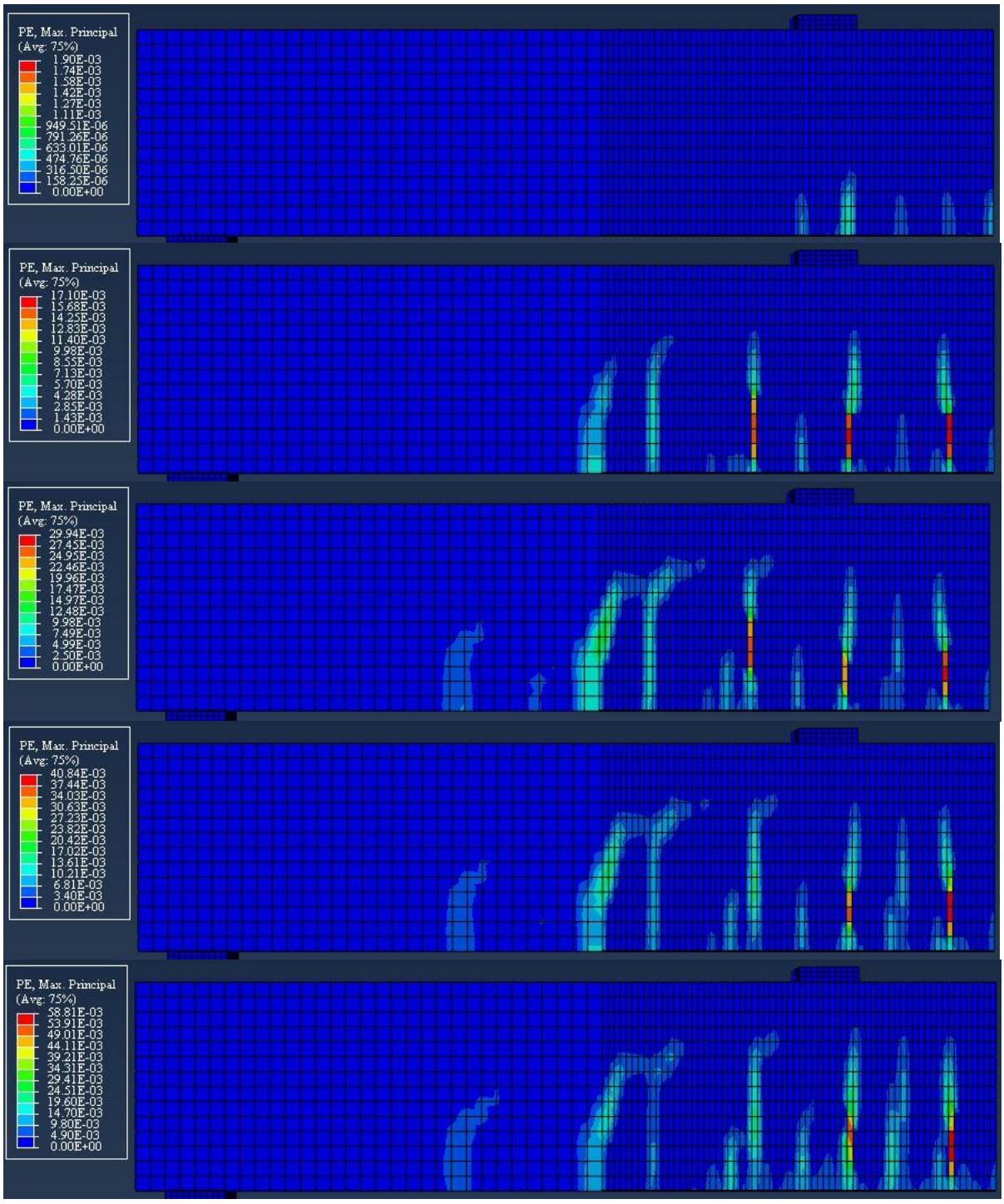

Figure B-14: Crack Pattern in CFRP Beam Model (effect of concrete plasticity parameters, Compression Damage)

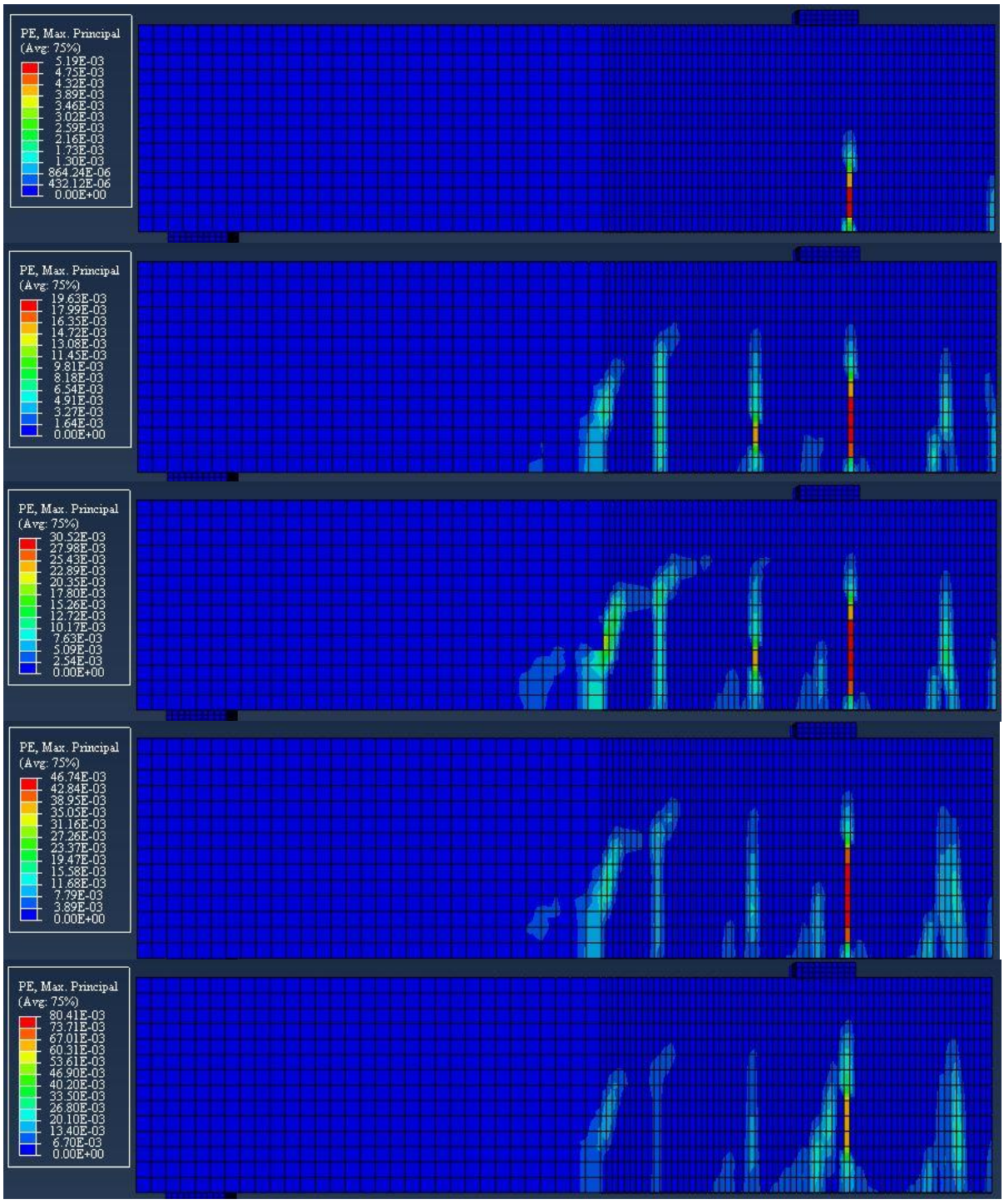

Figure B-15: Crack Pattern in CFRP Beam Model (effect of concrete plasticity parameters, Tension Damage)

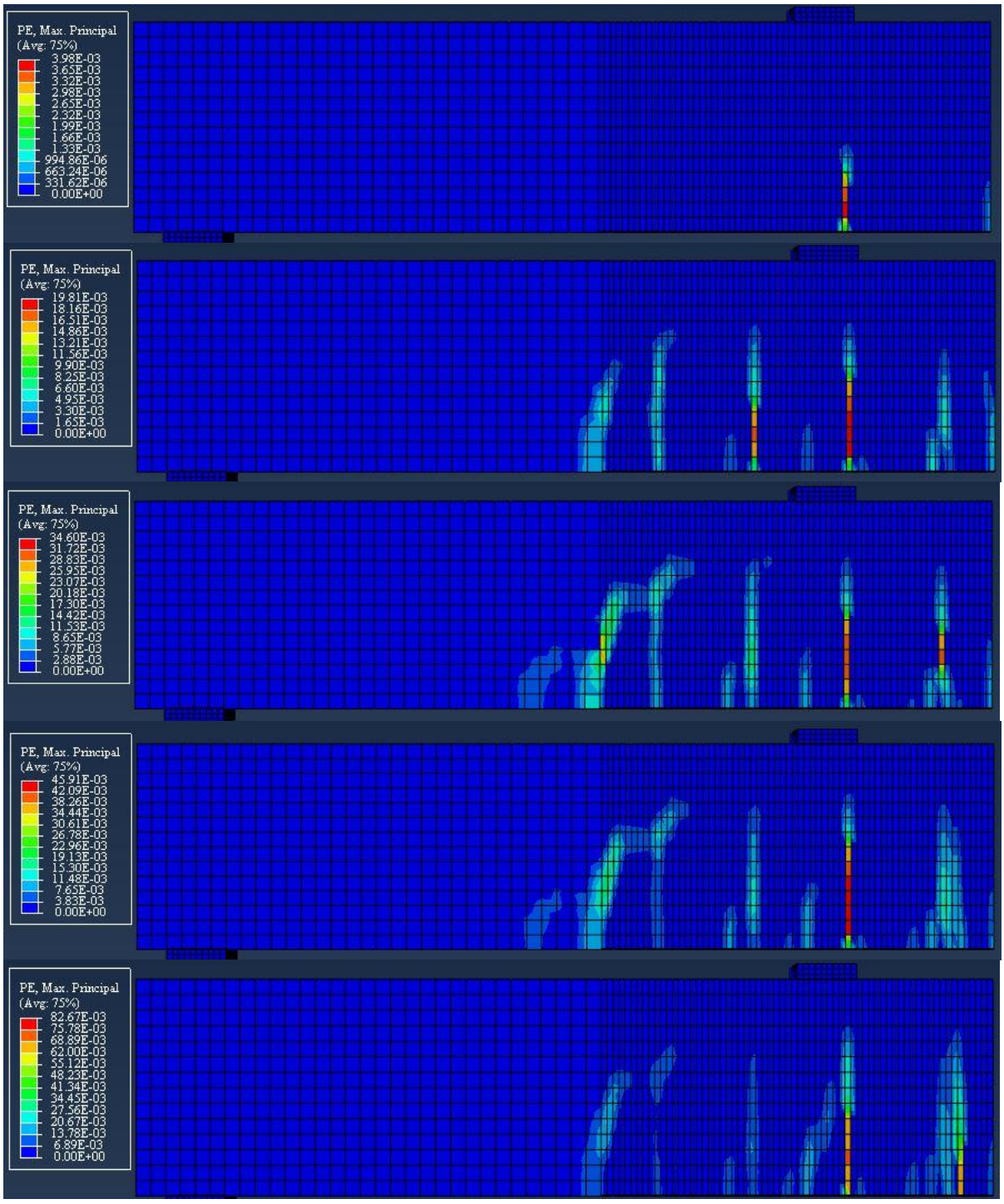

Figure B-16: Crack Pattern in CFRP Beam Model (effect of CFRP-Concrete Interfacial Bond Strength, $\tau_{max} = 1.5MPa$)

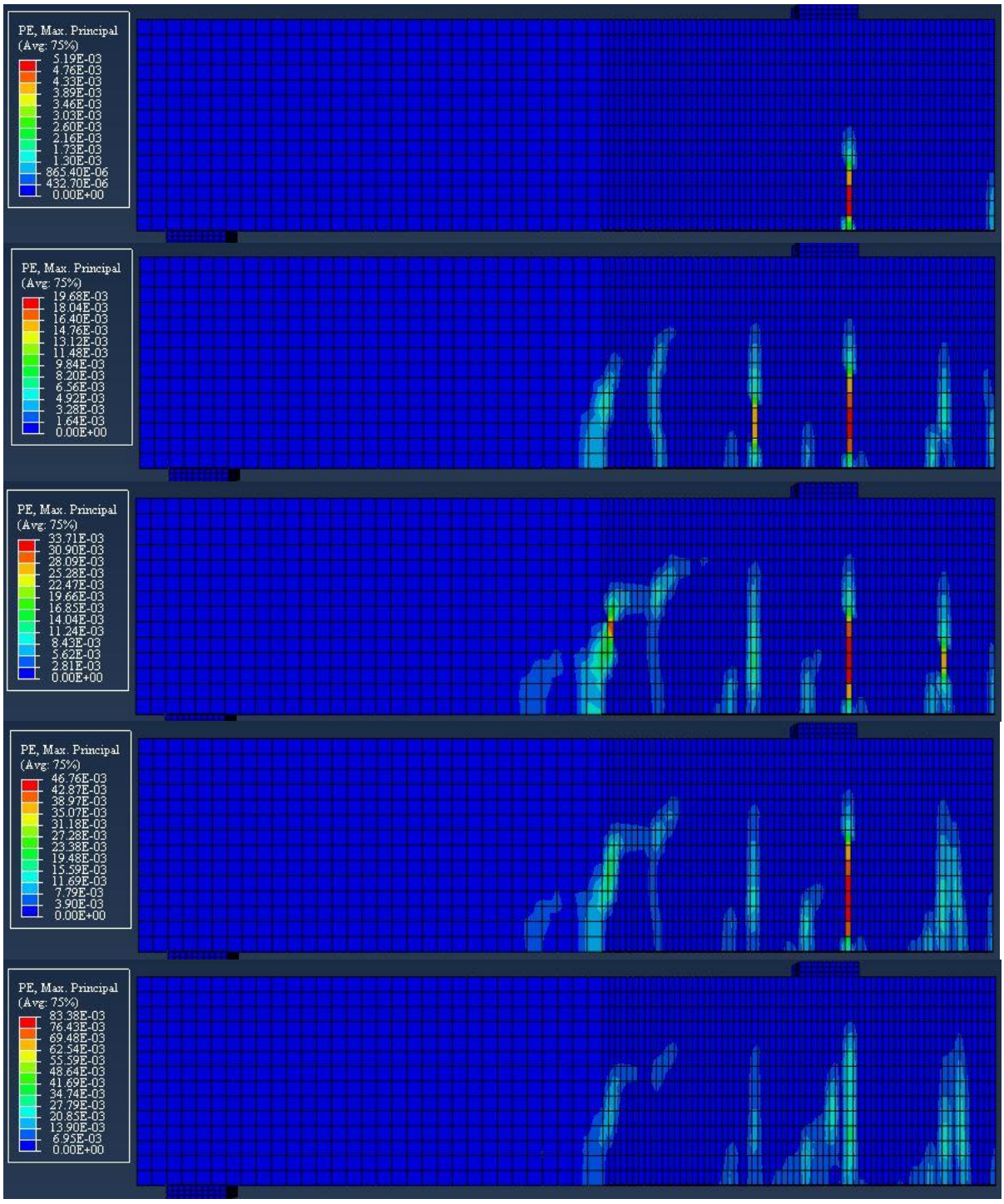

Figure B-17: Crack Pattern in CFRP Beam Model (effect of CFRP-Concrete Interfacial Bond Strength, $\tau_{max} = 3MPa$)

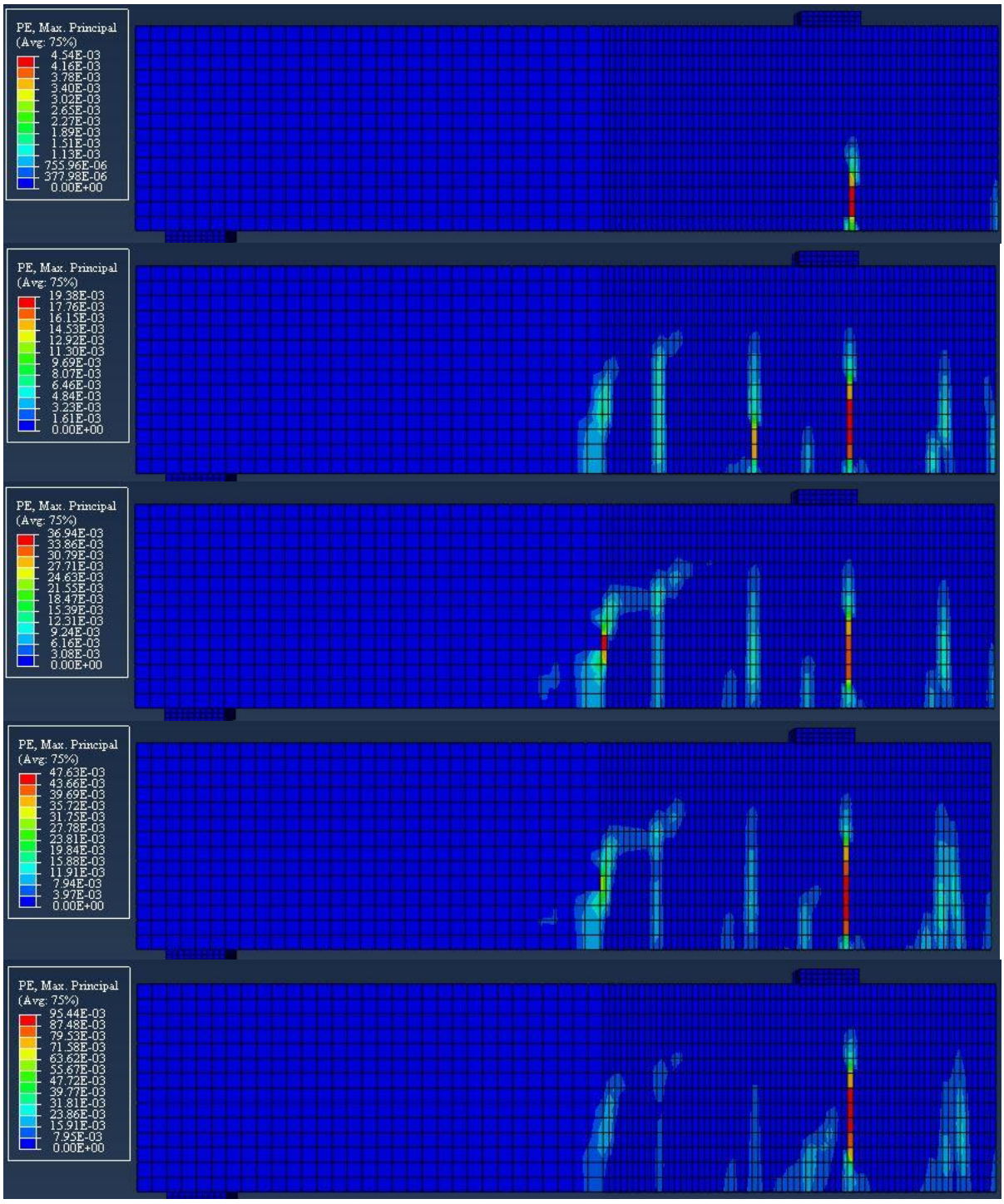

Figure B-18: Crack Pattern in CFRP Beam Model (effect of CFRP-Concrete Interfacial Bond Strength, $\tau_{max} = 7MPa$)

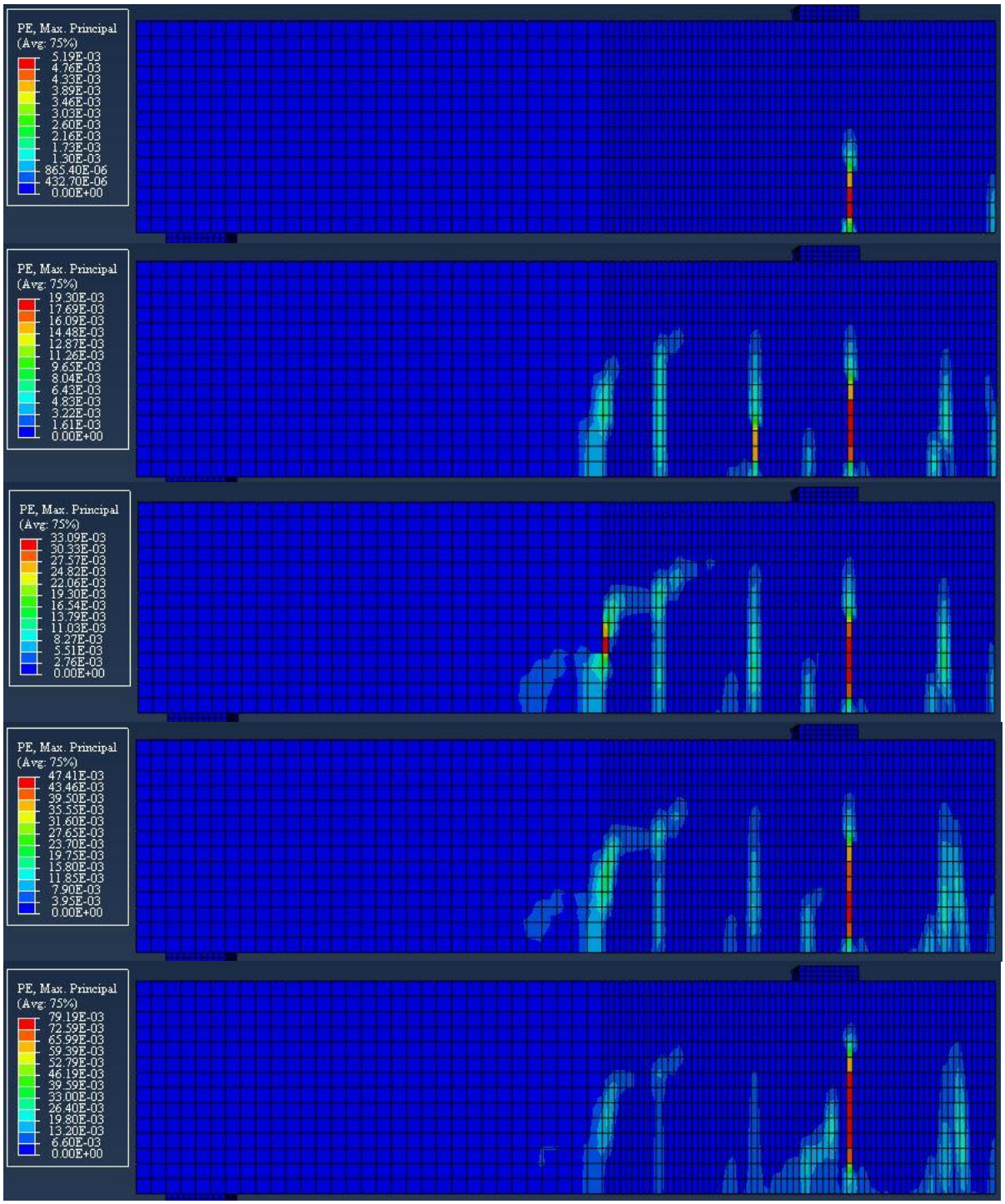

Figure B-19: Crack Pattern in CFRP Beam Model (effect of CFRP-Concrete Interfacial Bond Strength, $\tau_{max} = 10MPa$)

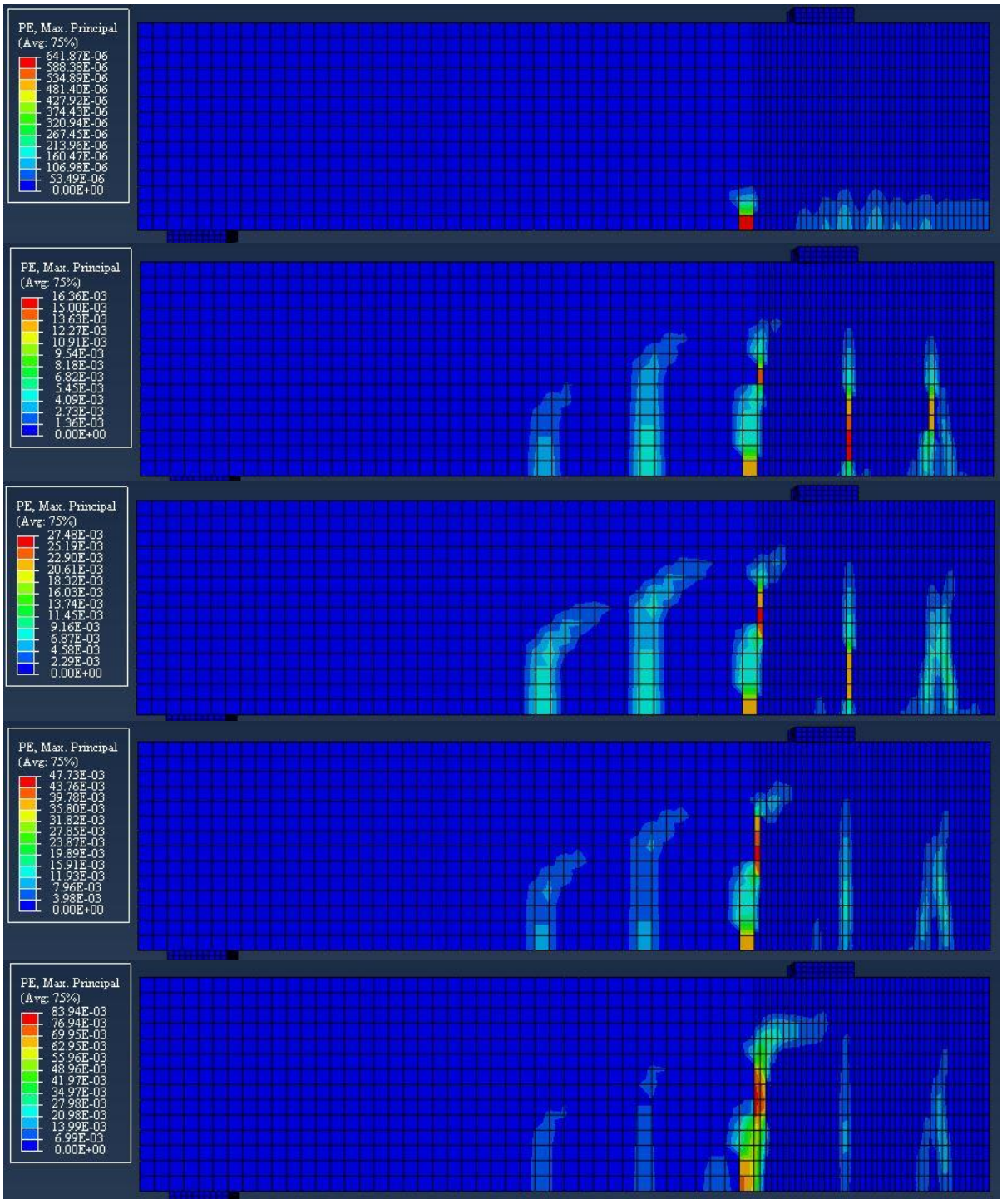

Figure B-20: Crack Pattern in CFRP Beam Model (effect of CFRP Bond Length, $L_f = 400$)

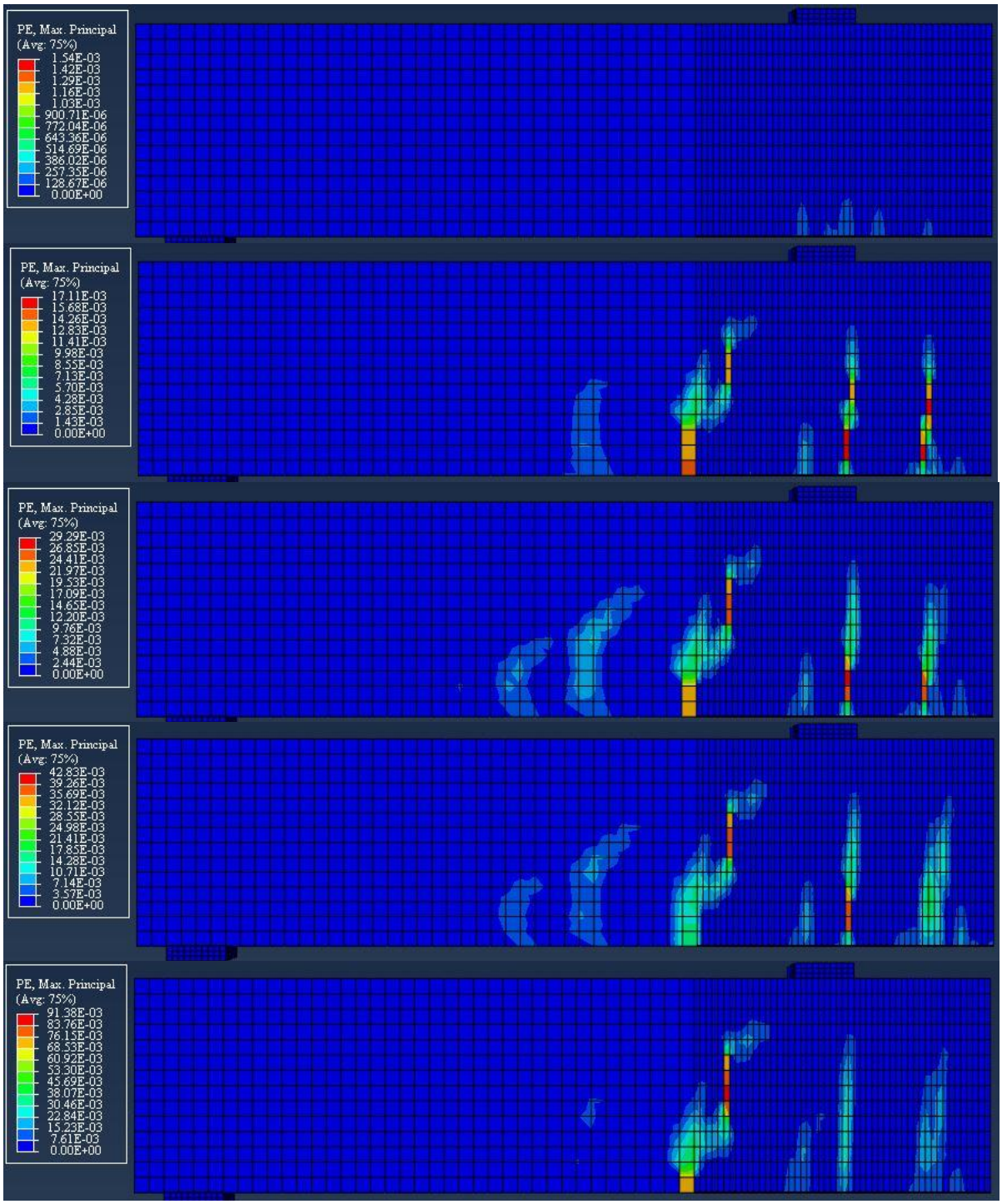

Figure B-21: Crack Pattern in CFRP Beam Model (effect of CFRP Bond Length, $L_f = 500$)

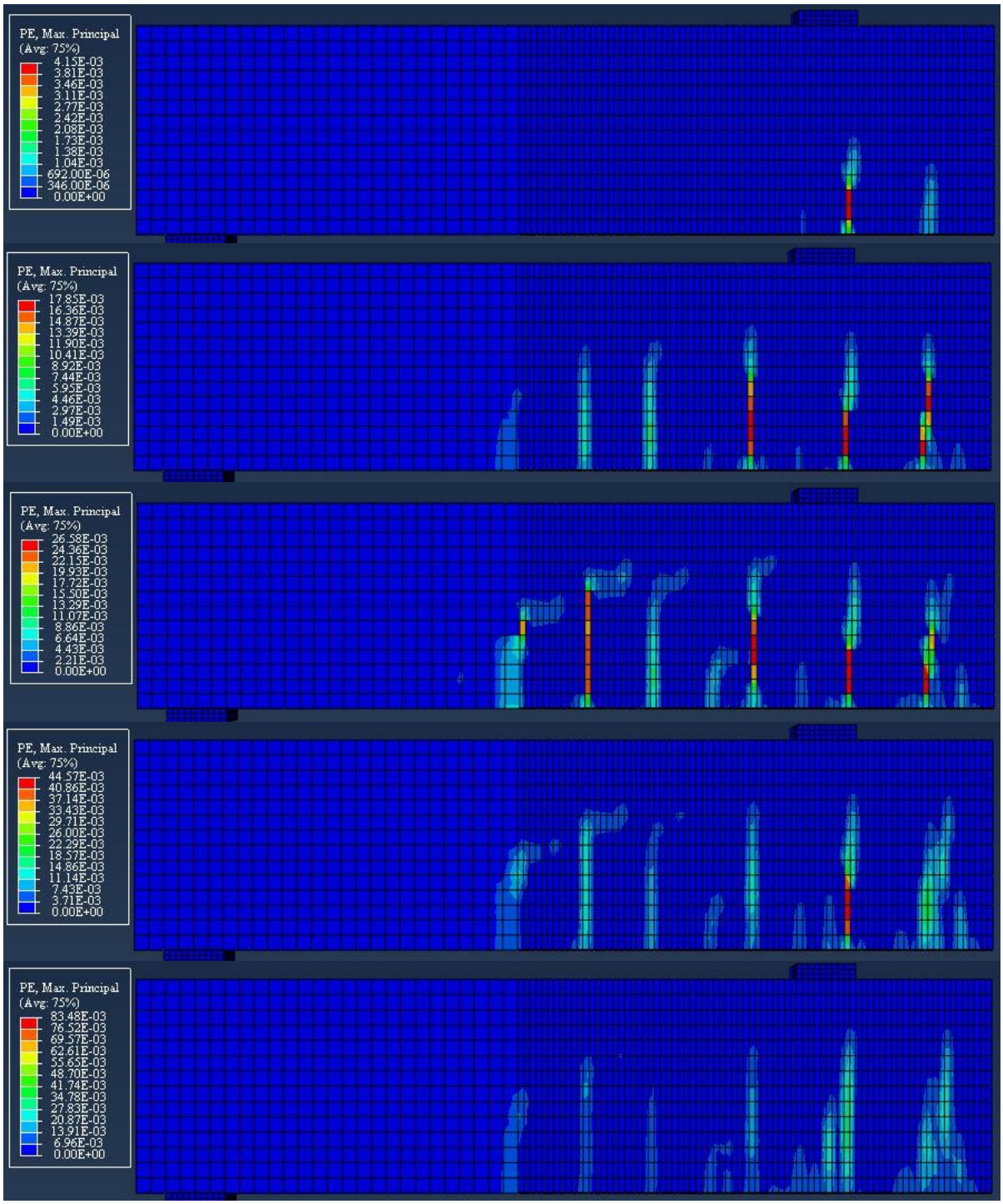

Figure B-22: Crack Pattern in CFRP Beam Model (effect of CFRP Bond Length, $L_f = 800$)

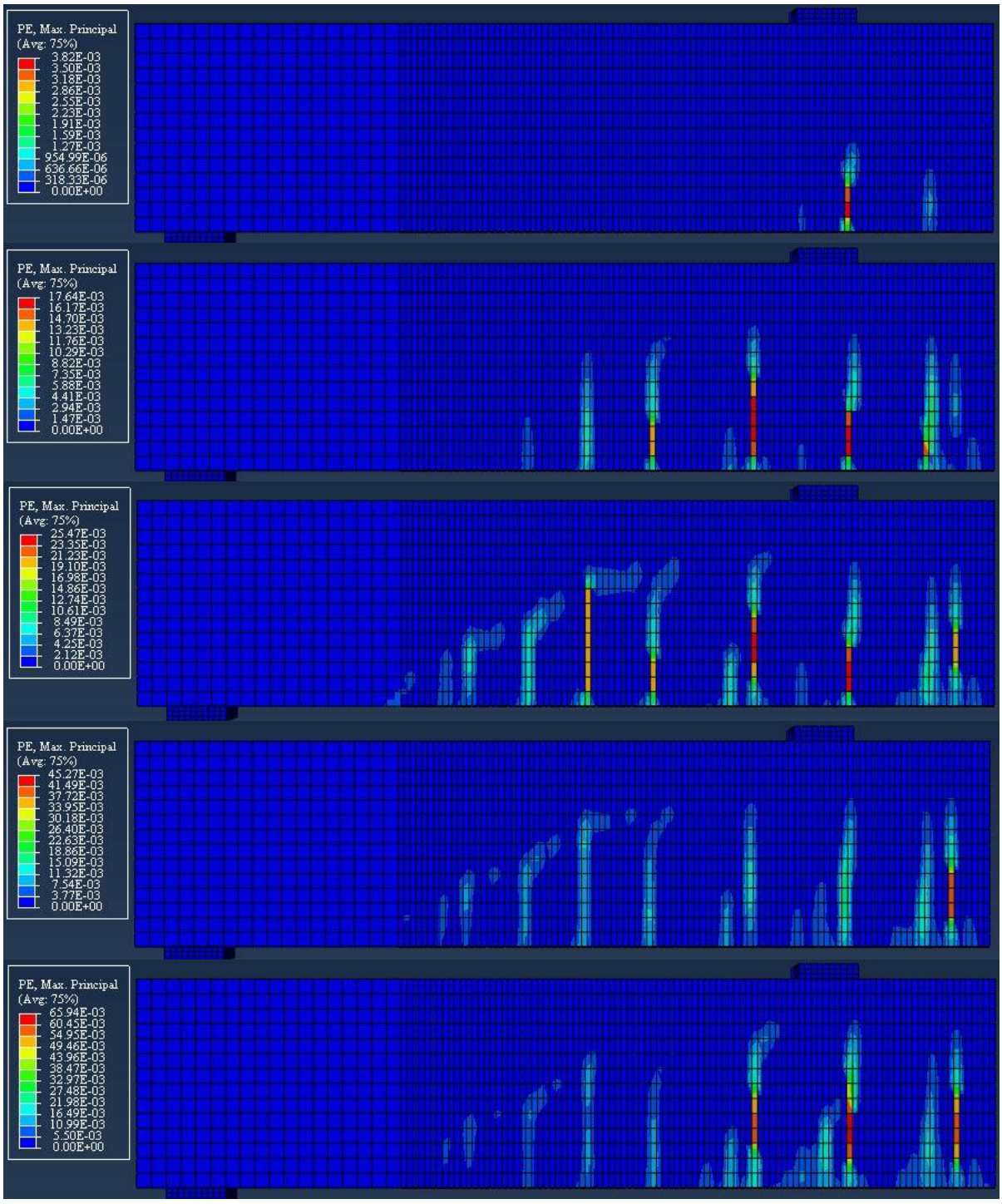

Figure B-23: Crack Pattern in CFRP Beam Model (effect of CFRP Bond Length, $L_f = 1000$)

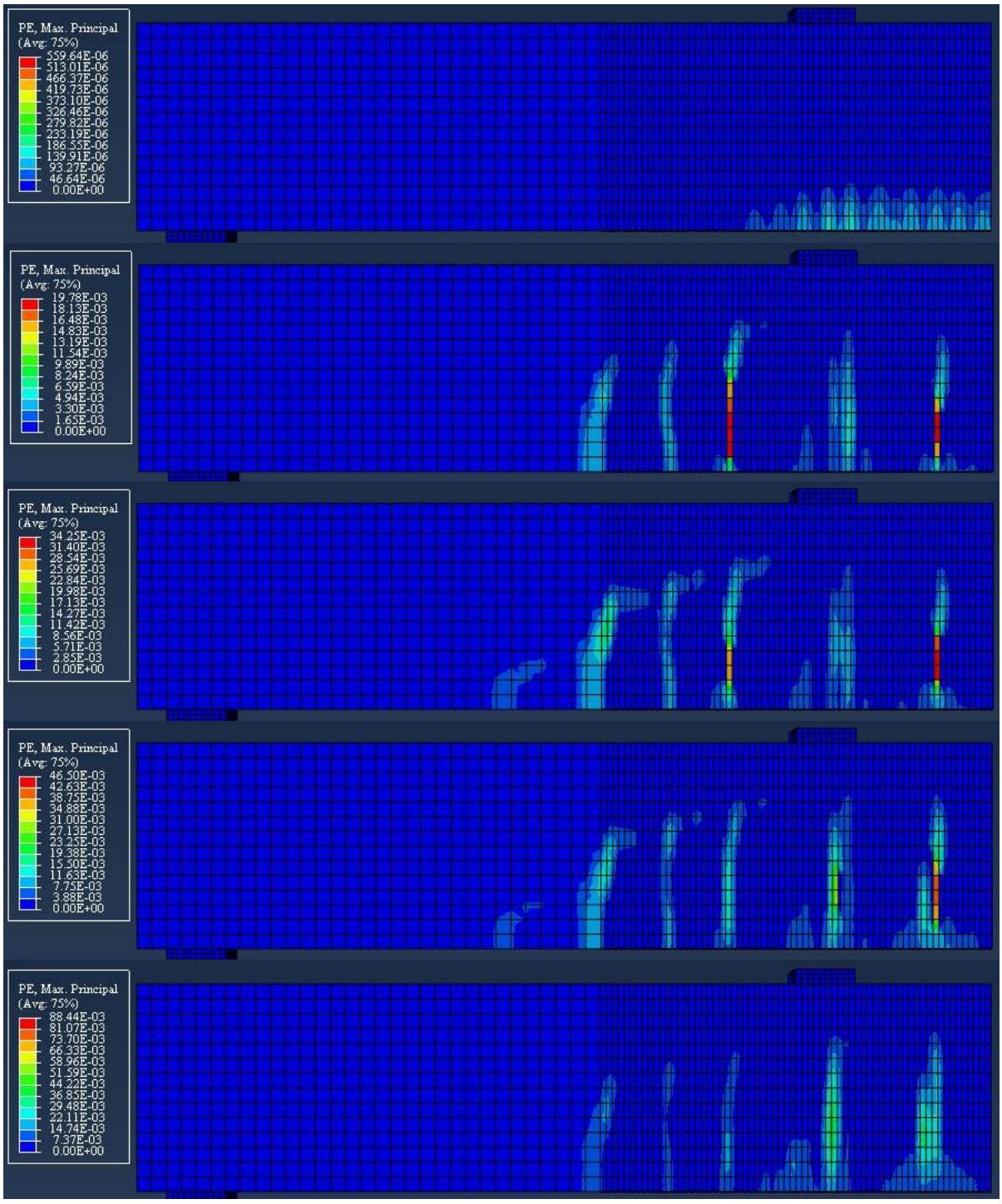

Figure B-24: Crack Pattern in CFRP Beam Model (effect of CFRP Bond Width, $B_f = 60$)

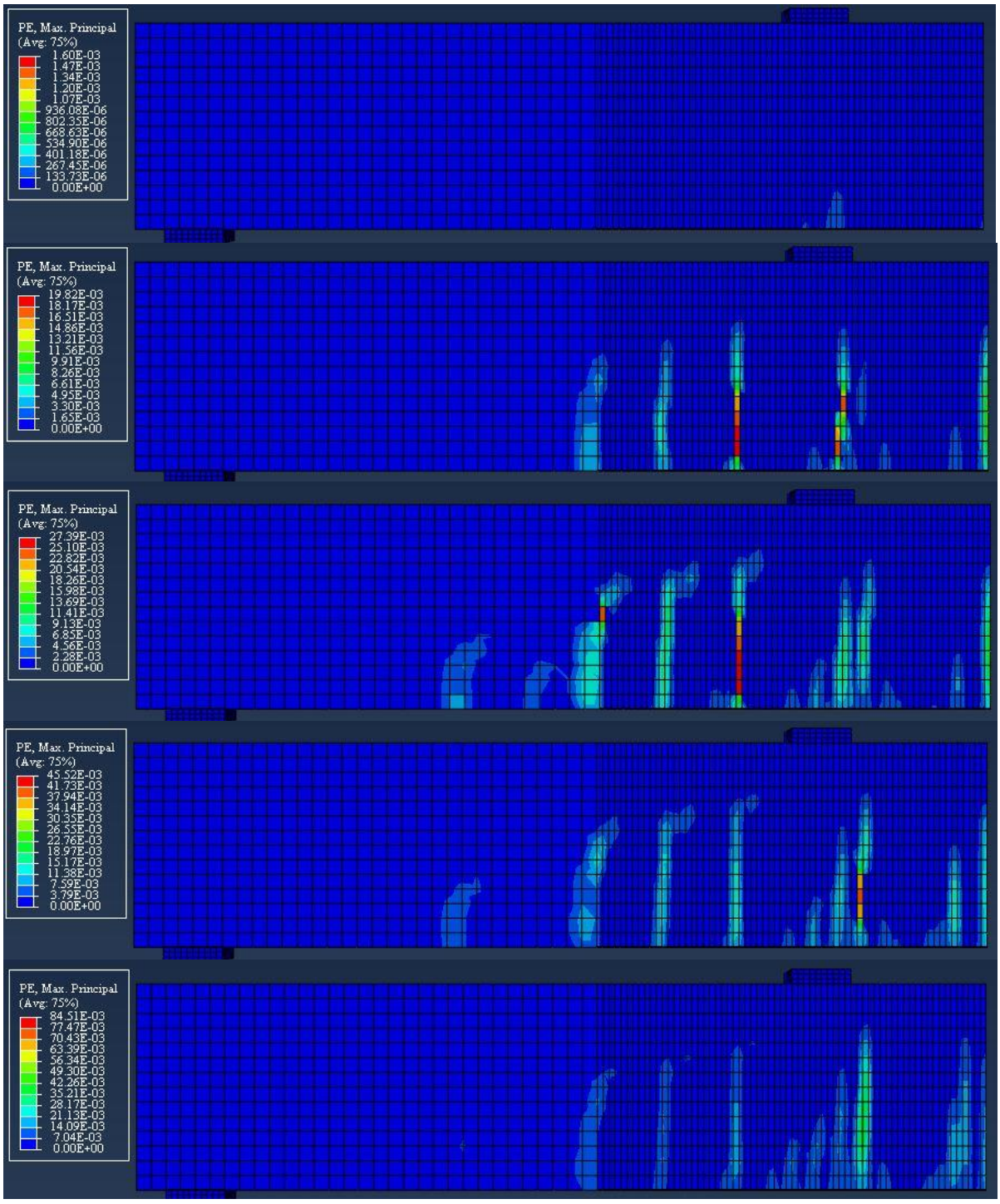

Figure B-25: Crack Pattern in CFRP Beam Model (effect of CFRP Bond Width, $B_f = 80$)

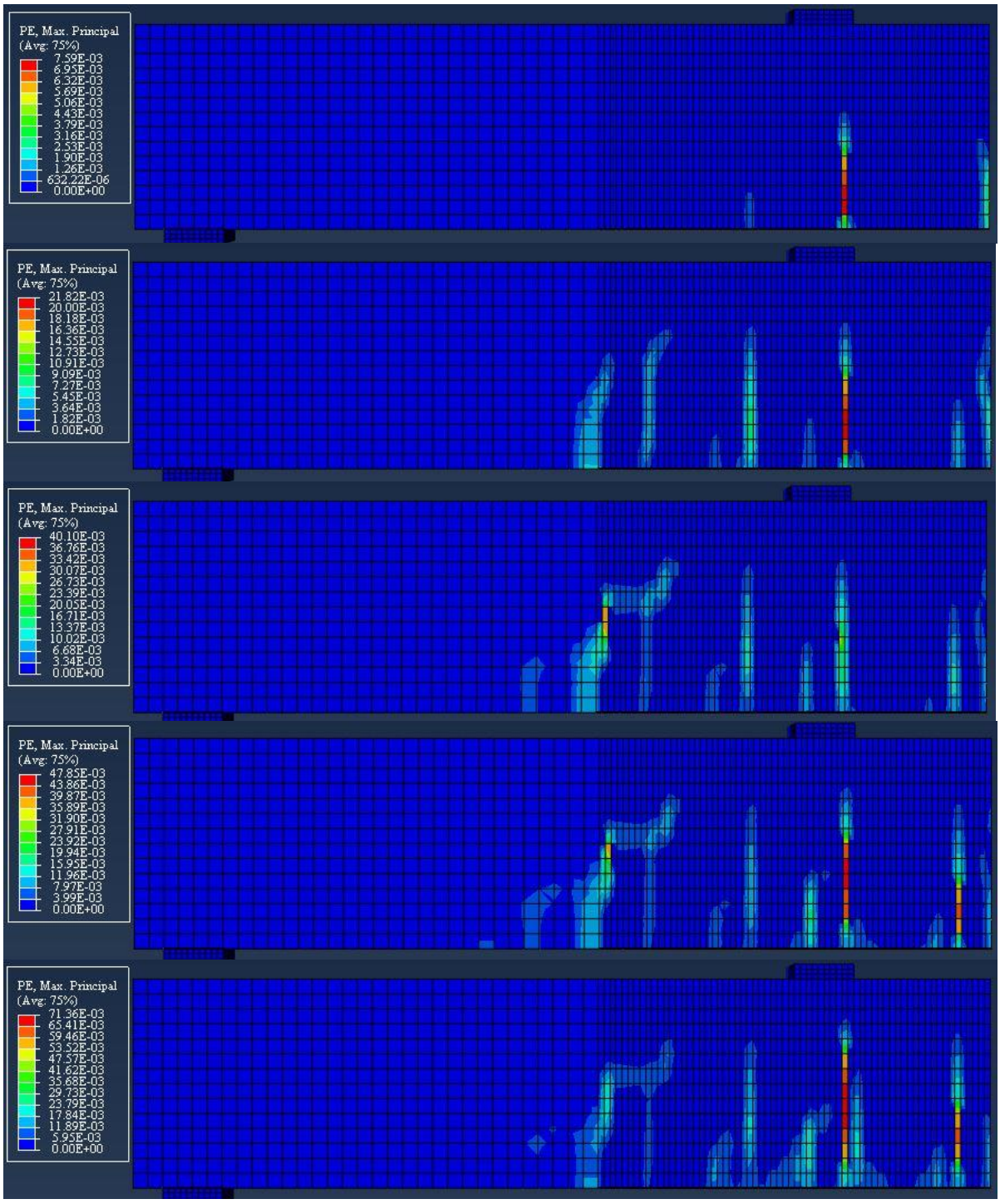

Figure B-26: Crack Pattern in CFRP Beam Model (effect of CFRP Bond Width, $B_f = 140$)

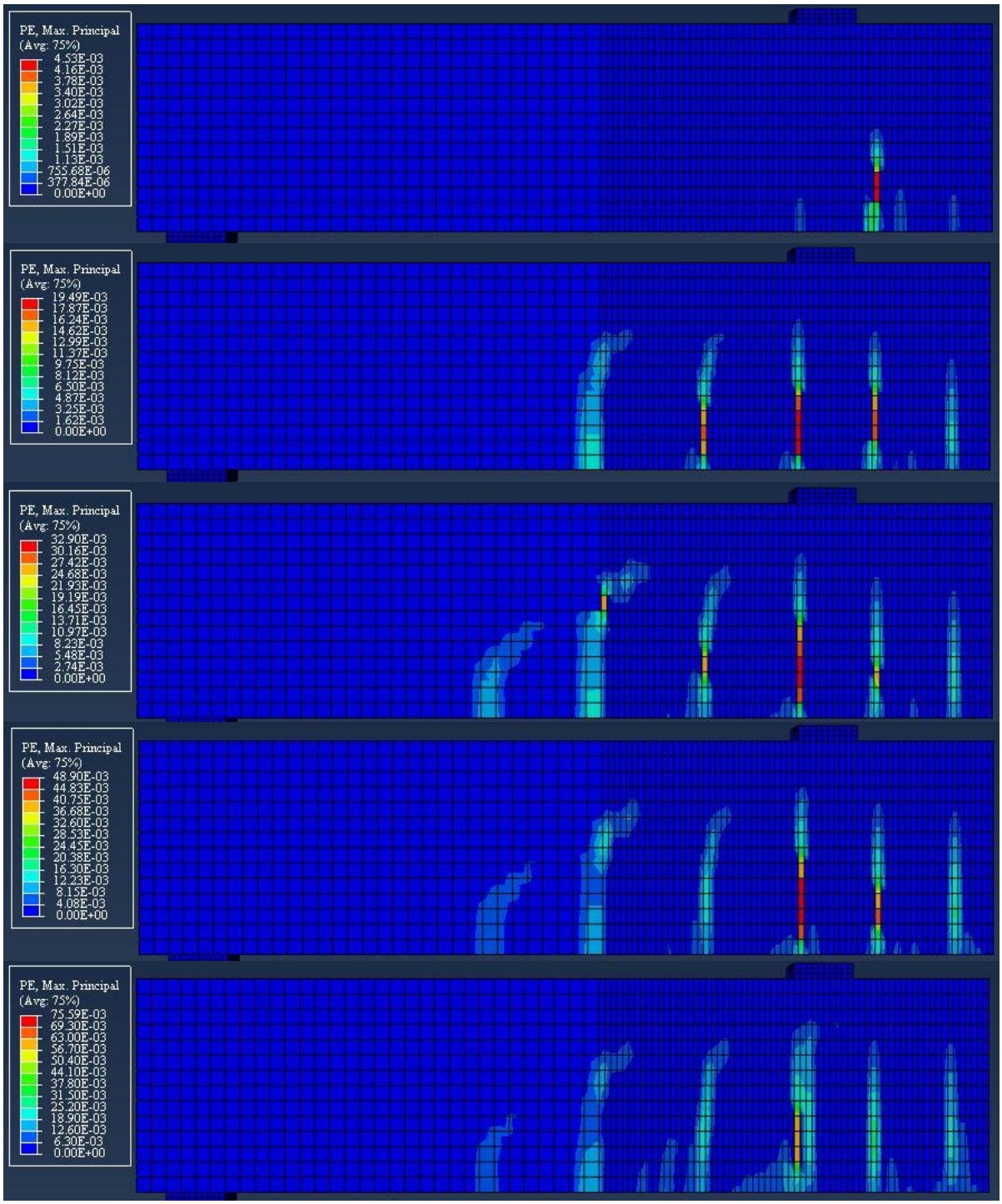

Figure B-27: Crack Pattern in CFRP Beam Model (effect of CFRP Bond Width, $B_f = 180$)

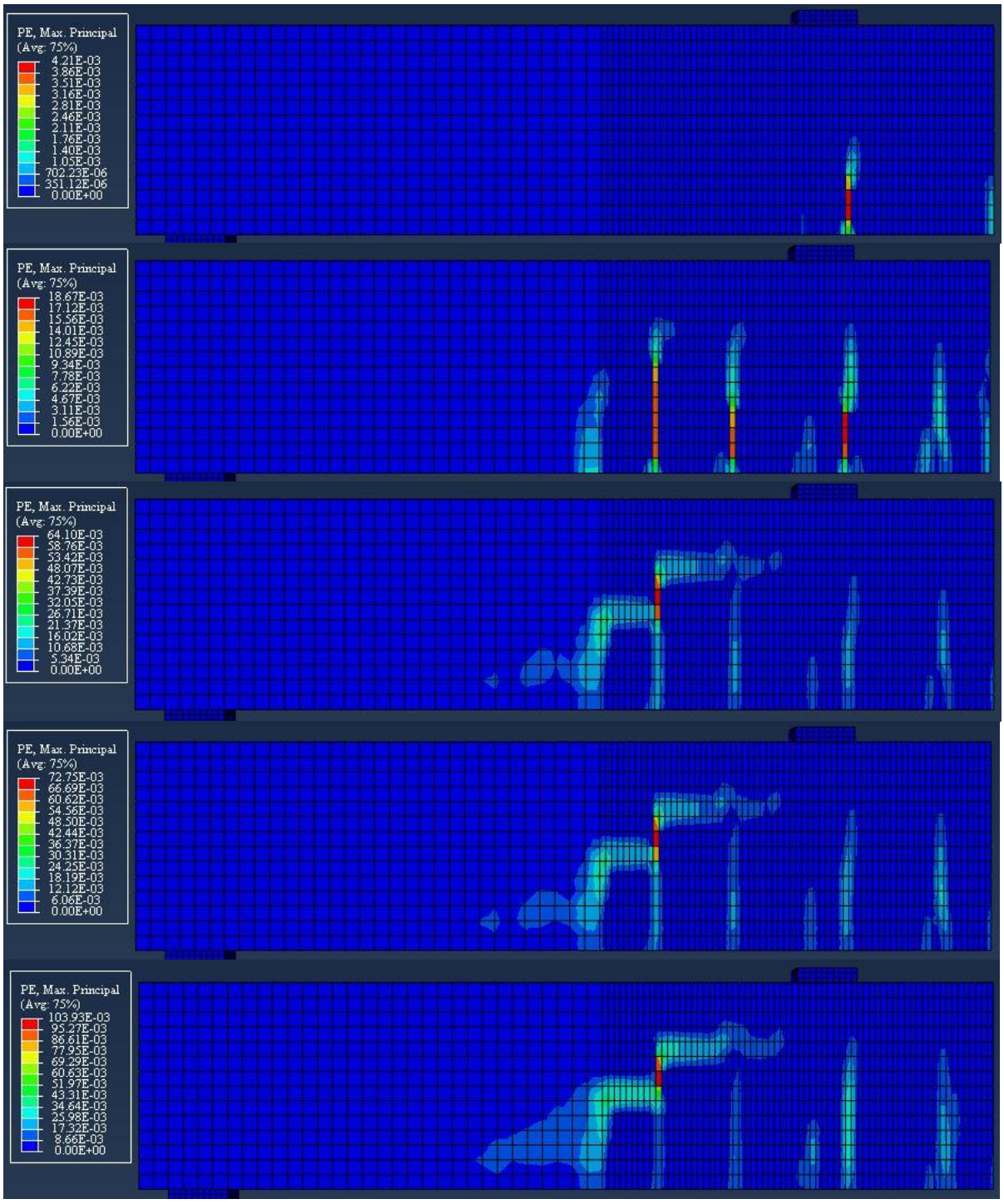

Figure B-28: Crack Pattern in CFRP Beam Model (effect of Steel Stirrups Removal)